About the Editors

Dr. Ranjan Kumar is currently Head of the Department and Associate Professor in the Department of Mechanical Engineering at Swami Vivekananda University, Kolkata. Dr. Kumar received his Master's and Doctoral degrees in Mechanical Engineering from the Indian Institute of Technology (ISM) Dhanbad. His research interests include Li-ion batteries, finite element simulation and analysis of real engineering problems, and vibration analysis of structures. He has executed projects in association with the Gas Turbine Research Establishment (GTRE), DRDO lab Bangalore. Dr. Kumar has authored 07 books, published 30 research papers, and holds 16 patents. He also serves as editor-in-chief of Journal of Mechanical Engineering Advancements.

Abhishek Dhar, a dynamic academician and a prolific mentor, serves as an Assistant Professor, in the Department of Electrical Engineering and as well as holds the prestigious post of Joint Academic Co-ordinator of the esteemed institution Swami Vivekananda University. His research, published in 15 prestigious international journals and conference papers, focuses on efficient energy utilization, grid stability, IoT etc. He has in his golden feather 60 patents filed and published with his hard work and dedication. He fosters an inclusive learning environment, nurturing diverse talents. His dedication has earned his recognition, bridging academia and industry seamlessly.

Dr. Ashes Banerjee is an Assistant Professor in the Civil Engineering Dept. at Swami Vivekananda University, Kolkata, West Bengal. He earned his Ph.D. in Water Resource Engineering from the Indian Institute of Technology (Indian School of Mines) in Dhanbad, India, in 2020. Dr. Banerjee's scholarly achievements are evidenced by his numerous publications in peer-reviewed international journals, covering crucial topics such as non-linear filtration in porous media, water quality, and groundwater utilization.

Dr. Subhabrata Mondal is currently Head of the Department and Assistant Professor in the Department of Mathematics at Swami Vivekananda University, Kolkata. Dr. Mondal received his Master's degree in Mathematics from The University of Burdwan, West Bengal and Doctoral degrees in Applied Mathematics from the University of Calcutta. His research interests include Intergral Equations, Fluid Mechanics and Computational Mathematics. Dr. Mondal has authored two books, published 25 research papers.

Published by
AkiNik Publications®
169, C-11, Sector - 3, Rohini,
Delhi - 110085, India
Toll Free (India): 18001234070
Email: akinikbooks@gmail.com

ISBN 9789361354298
9 789361 354298
₹ 1260 US$ 20

Scientific Frontiers: Sustainable Practices and Technologies | AkiNik Publications

Scientific Frontiers: Sustainable Practices and Technologies

Dr. Ranjan Kumar
Abhishek Dhar
Dr. Ashes Banerjee
Dr. Subhabrata Mondal

AKINIK PUBLICATIONS

Scientific Frontiers: Sustainable Practices and Technologies

Editors

Dr. Ranjan Kumar

Abhishek Dhar

Dr. Ashes Banerjee

Dr. Subhabrata Mondal

AkiNik Publications®
New Delhi

Published By: *AkiNik Publications*

AkiNik Publications
169, C-11, Sector - 3,
Rohini, Delhi-110085, India
Toll Free (India) – 18001234070
Phone No.: 9711224068, 9911215212
Website: www.akinik.com
Email: akinikbooks@gmail.com

Editors: *Dr. Ranjan Kumar, Abhishek Dhar, Dr. Ashes Banerjee and Dr. Subhabrata Mondal*

Publication Year: *2024*

Edition: *1st*

Pages: *297*

ISBN: *978-93-6135-429-8*

Book DOI: *https://doi.org/10.22271/ed.book.2938*

Price: *₹1260/-*

Registration Details

- *Printing Press License No.: F.1 (A-4) press 2016*
- *Trade Mark Registered Under*
  - *Class 16 (Regd. No.: 5070429)*
  - *Class 35 (Regd. No.: 5070426)*
  - *Class 41 (Regd. No.: 5070427)*
  - *Class 42 (Regd. No.: 5070428)*

Preface

The rapid advancements in science and technology have led to the convergence of diverse fields of study, allowing for groundbreaking research and novel applications. This book is a testament to that confluence, bringing together a collection of research papers that span a wide range of topics, from wave scattering phenomena in fluid mechanics to the cutting-edge applications of nanomaterials in biosensors and energy devices.

The first section of the book delves into the complex dynamics of wave scattering, an area of great importance in both theoretical and applied physics. Papers such as "Wave Scattering by an Axisymmetric Spheroid Submerged below a Free Surface", "Wave Scattering of non-axisymmetric spheroidal body Below a Free Surface", and "A Study on Scattering of Water Waves by a Thin Inclined Plate in Finite-Depth Water Using the Galerkin Method" explore the intricate interactions between fluid waves and submerged bodies. These studies not only enhance our understanding of wave mechanics but also have practical implications in fields such as naval architecture and offshore engineering.

The second section shifts focus to the realm of nanotechnology and materials science, highlighting the synthesis, characterization, and applications of advanced nanomaterials. "Review on optical properties of MoS_2/TiO_2 Nanocomposite" and "Review on improvements of doping strategies on TiO_2 and ZnO nanoparticles for visible light photocatalytic applications" offer comprehensive insights into the optical and photocatalytic properties of these materials, which are pivotal in the development of next-generation energy solutions. Additionally, "Recent progress in metal oxides for biosensor application" underscores the growing importance of metal oxide nanostructures in the field of biosensing, where their unique properties enable the detection of biological molecules with unprecedented sensitivity.

In the third section, the focus turns to the application of mathematical models in biology, particularly in the study of infectious diseases. Papers such as "Biological Applications of Differential Equations: A Study of Malaria Transmission", "Examining Compartmental Models' effectiveness in building mathematical models of infectious diseases" and "A study on reproduction number for infectious diseases" present rigorous mathematical frameworks for understanding the spread of diseases. These studies are

crucial in informing public health strategies and in the ongoing battle against global health challenges.

The final section of the book presents research on the development and optimization of materials for energy applications. Papers such as "Dye-Sensitized Solar Cell Based on Pedot-Tos Counter Electrode", "An Extensive Study of Photothermoelectric Materials for Device Applications", and "Synthesis and Thermoelectric Characterization of Pedot-Tos/Tin Selenide Nanocomposite" delve into the innovative approaches being taken to enhance the efficiency and functionality of solar cells and thermoelectric devices. Further, the exploration of "Enhanced Thermoelectric Properties of Ptsa Doped PEDOT/Bismuth Nanocomposite", "Thermoelectric Properties of Zinc-Incorporated Reduced Graphene Oxide-Polyaniline Composite" and "Recent developments in Graphene-based nanomaterials for the application in Biosensors" highlights the potential of these materials to revolutionize energy conversion and storage technologies.

The book concludes with a detailed review on the "Electrical properties, conduction mechanism of Polyaniline and its effect of doping on conductivity", which encapsulates the theme of material innovation that runs throughout the collection. This book aims to serve as a valuable resource for researchers, engineers, and students who are keen to explore the intersection of fluid dynamics, nanotechnology, mathematical modeling, and energy materials. It is our hope that the diverse topics covered in these papers will inspire further research and innovation across these interconnected fields.

Dr. Ranjan Kumar
Associate Professor,
Swami Vivekananda University,
Kolkata, West Bengal, India

Acknowledgement

I extend my heartfelt gratitude to Swami Vivekananda University, Kolkata, India, for their steadfast support and encouragement throughout the creation of "Scientific Frontiers: Sustainable Practices and Technologies" The university's dedication to fostering education and research has been instrumental in shaping the content and direction of this publication. We deeply appreciate the collaborative spirit and resources provided by Swami Vivekananda University, Kolkata, which have enabled us to explore and share the latest innovations and technologies across various fields.

We hope that this book serves as a valuable resource for this esteemed institution and the broader academic community, reflecting our shared dedication to knowledge, progress, and the pursuit of excellence.

I extend my deepest appreciation to each of the external reviewers mentioned below for their unwavering commitment to excellence and their indispensable role in ensuring the scholarly merit of this work.

With sincere appreciation,

List of Reviewers:

1. Dr. Sumeet Chakraborty, University of Westlake, Hangzhou, China.
2. Dr. Anshuman Das, Dept. of Mathematics, Presidency University, Kolkata, India.
3. Dr. Soumen De, Department of Applied Mathematics, University of Calcutta, India.

Content

Chapter - 1
Wave Scattering by an Axisymmetric Spheroid Submerged Below a Free Surface

Author

Arijit Das
Department of Mathematics, Swami Vivekananda University,
Kolkata, West Bengal, India

Chapter - 1

Wave Scattering by an Axisymmetric Spheroid Submerged Below a Free Surface

Arijit Das

Abstract

This research investigates the wave scattering behaviour of an axisymmetric spheroid submerged below a free surface, a topic of significant importance in marine engineering and oceanographic studies. Here, a different approach in the solution is chosen than a previous study in this topic. The study utilizes potential flow theory to develop a comprehensive analytical model, addressing the complex boundary value problem posed by the interaction of incident waves with the submerged spheroid. The analysis incorporates the free surface boundary conditions and employs multipole expansions to derive solutions that describe the scattered wave field. Numerical methods are used to solve the resulting equations and to simulate various scenarios, considering different submersion depths.

Keywords: Wave scattering, axisymmetric spheroid, multipole expansion, green's function

Introduction

Miloh (1974) formulated precise solutions for the ultimate image singularity system within arbitrary exterior potential fields for prolate spheroids and triaxial ellipsoids. The objective was to enable the application of the Lagally theorem (Lagally 1922) and its extensions (Landweber & Yih 1956; Cummins 1957; Landweber & Miloh 1980) to calculate hydrodynamic loads on ellipsoidal bodies in unbounded potential flows (Miloh 1979) or on spheroidal shapes manoeuvring in confined water (Miloh & Hauptman 1980). Specifically for spheroids, Miloh (1974) validated a theorem initially proposed by Havelock (1952), which was originally presented without proof. Despite deriving these image singularity formulas, they have not been numerically extended to account for a nearby free surface, even in a linearized form. This paper demonstrates that applying these formulations leads to simple and elegant solutions for wave radiation and diffraction

problems, resulting in useful relations for the hydrodynamic loads on submerged spheroidal bodies near a free surface. These image singularities are versatile and can be effectively applied to spheres, as well as vertical and horizontal prolate spheroids, and triaxial ellipsoidal shapes. Here, "vertical" and "horizontal" refer to the orientation of the spheroid's semimajor axis relative to the free surface, designated as the "axisymmetric" and "nonaxisymmetric" cases, respectively. For further reading, Havelock (1954) is recommended, although his solution for the diffraction potential does not satisfy the free surface boundary condition, an issue addressed in this paper. The ambient potential and all boundary value problem components must be transformed into spheroidal coordinates. This study highlights the simplicity and advantage of using analytical approximations to construct closed-form solutions for the pressure loads on the body, compared to common numerical panel methods. The aim is to obtain closed-form relations for hydrodynamic forces and moments on a prolate spheroid under waves, using Miloh's (1974) internal image singularity methodology. Additionally, the proposed method can be applied to two hydrodynamically interacting spheroids (ship-crossing problem) or general triaxial ellipsoids (equivalent ship form) by expressing the Green's function in Lame functions instead of Legendre functions.

Formulation

The axisymmetric prolate spheroidal body is considered to be immersed at a distance (f) below the undisturbed free surface in a fluid of infinite depth. Using left-handed Cartesian coordinates $((x, y, z))$, fixed on the undisturbed free surface with the (z)-axis pointing downwards, the coordinate system fixed on the center of the body $((x', y', z'))$ is obtained from the former with the transformation $(z = z' + f)$. The linearized analysis is committed to the axisymmetric case. The fluid is considered to be inviscid and incompressible. The motion is assumed to be irrotational and time harmonic with angular frequency (ω). Let $(\mathrm{Re}(\phi(x, y, z)e^{-i\omega t}))$ be the velocity potential where (ϕ) is the time-independent complex potential. Then ϕ satisfies the three-dimensional Laplace equation:

$$\nabla^2\phi(x, y, z) = 0 \text{ in the fluid region} \tag{2.1}$$

And the bottom boundary condition:

$$\nabla\phi \to 0 \quad \text{as } z \to \infty, \text{ for deep water} \tag{2.2}$$

The common linearized free-surface boundary condition for the velocity potential can be written as:

$$K\phi + \frac{\partial \phi}{\partial z} = 0 \quad \text{on } z = 0 \tag{2.3}$$

Where g is the gravitational acceleration and $K = \frac{\omega^2}{g}$. The total velocity potential ϕ is decomposed into the incident and diffraction potential components, denoted by ϕ_I and ϕ_D, respectively. On the wetted surface of the body, the zero-velocity condition is satisfied, which is:

$$\frac{\partial \phi}{\partial n} = 0 \rightarrow \frac{\partial \phi_D}{\partial n} = -\frac{\partial \phi_I}{\partial n} \tag{2.4}$$

Where, n is the normal on the body surface directed into the fluid. The body considered here, is an axisymmetric spheroid.

Solution

The above stated problem has been solved by Chatjigeorgiou and Miloh (2013). Here we only describe the final solution. The notation are kept same as in Chatjigeorgiou and Miloh (2013) to avoid in confusion. The system of equation can be finally reduced to a system of linear equation as below:

$$\sum_{n=m}^{\infty}[\delta_{nl} - D_n^m(l)F_l^m]B_n^m = A_l^m F_l^m,$$

Where $F_l^m = \dot{P_l^m}(\zeta_0)\dot{Q_l^m}(\zeta_0)$ and $A_n^m = \frac{1}{K}\epsilon_m i^m e^{-Kf}\frac{\sqrt{\pi}}{\sqrt{2}}(-1)^{n-m-1}\frac{(2n+1)\Gamma(n-m+1)}{\Gamma(n+m+1)}I_{n+1/2}(K)$

Also,

$$D_n^m(p) = \sum_{s=m}^{\infty} C_{ns}^{mp} = I_n^m(s-m)Y_p^m(s-m)$$

Where,

$$I_{p+1/2}(k) = \sum_{q=0}^{\infty}\frac{(k/2)^{p+q+\frac{1}{2}}}{q!\Gamma\left(p+q+\frac{3}{2}\right)}$$

$$Y_p^m(s) = \frac{\sqrt{\pi}}{\sqrt{2}}(-1)^{p-m}\frac{(2p+1)\Gamma(p-m+1)}{\Gamma(p+m+1)}\int_0^{\infty} k^{m+s-1/2}\frac{k+K}{k-K}e^{-2kf}\,I_{p+1/2}(k)\,dk.$$

Now, here the integral in Y_p^m contains a Cauchy Principal Value integral. Chatjigeorgiou and Miloh (2013) suggested to use an identity containing exponential integral function. Here we suggest that the integral can be solved in complex plane also. Using residue theorem we can solve the Cauchy principal integral very easily.

The solution of this integral is as follows

$$\int_0^{\infty} \frac{\sigma^n}{1-\sigma} e^{-2Kf\sigma} d\sigma = -\pi i e^{-2Kf} - e^{in\pi/4} \int_{\infty}^{0} \frac{r^n e^{-2Kfre^{i\pi/4}}}{e^{-i\pi/4}-r} dr$$

The main advantage of the use of this method that it is not applicable to a specific problem. Rather It can be used for a wide range of problems.

Hydrodynamic forces

The hydrodynamic exciting forces over the wetted surface of the spheroid can be obtained as,

$$\frac{F_s}{\rho g a^2 A} = (-1)^{1-s} i \frac{4\pi K}{3} \left(\frac{b}{a}\right)^{2-s} \left[-A_1^s P_1^s(\zeta_0) + B_1^s Q_1^s(\zeta_0) - \sum_s^{\infty} B_n^s D_n^s \left(1 P_1^s(\zeta_0)\right)\right]$$

Where s = 0 denotes the heave and s=1 denotes the surge force.

Numerical solution

In this section we first verify our result with that of Chatjigeorgiou and Miloh (2013) with the fixed parameter values f=2.5 and b/a=0.5. We see that the Results are matched very precisely proving the correctness of the method (figure 1).

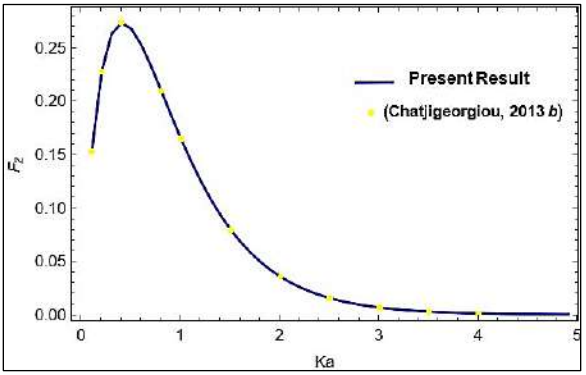

Fig 1: Surge force on prolate spheroidal body(b/a=0.5) submerged at f=2.5

In figure 2, surge force have been plotted for different values of f = 2.5; 3; 3.5. And it is clear that as the body is present nearer the free surface it feels a greater amount of force.

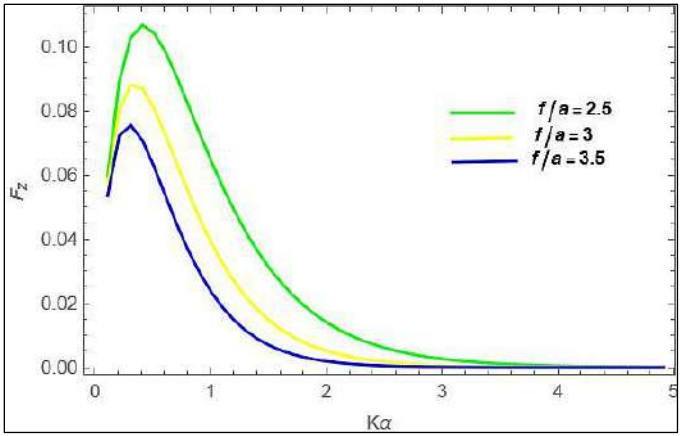

Fig 2: Surge force on prolate spheroidal body(b/a=0.5) submerged at f = 2.5; 3; 3.5

Also, we have determined the heave force for the same set of values. It is clear that not only the heave force but also the surge force faces a greater force when the depth of submergence of the body is small (figure 3).

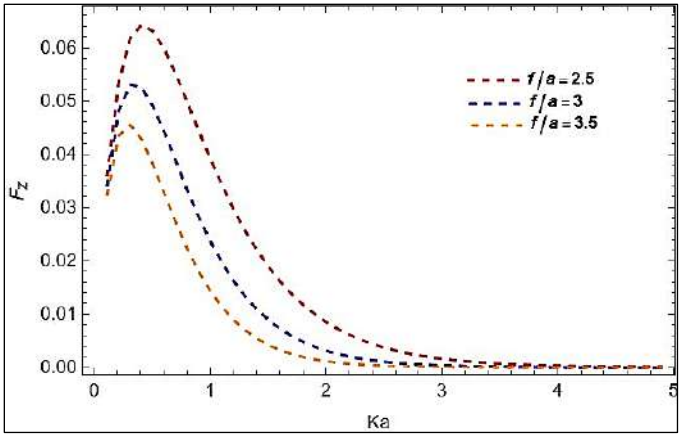

Fig 3: Heave force on prolate spheroidal body(b/a=0.5) submerged at f=2.5; 3; 3.5

Conclusion

Here, we have tried to give a different way of solution. The scattering problem of an axisymmetrical spheroidal body have been studied previously by Chatjigeorgiou and Miloh (2013). We only tried to give a different approach of handling the Cauchy principal integral. Although the problem is same but this different way provides the scope for further extensions on this field. We hope this solution approach gives a pivotal role in motivating other researchers to study this topic and further extend it.

References

1. Miloh, T. 1974 The ultimate image singularities for external ellipsoidal harmonics, SIAM Journal on Applied Mathematics, 26, 2, 334-344.
2. Lagally, M. 1922 Berechnung der Kra¨fte und Momente, die stro¨mende Flu¨ssigkeiten auf ihre Begrenzung ausu¨ben, Zeitschrift fu¨r Angewandte Mathematik und Mechanik, 2, 6, 409-422.
3. Landweber, L., and Miloh, T. 1980 Unsteady Lagally theorem for multipoles and deformable bodies, Journal of Fluid Mechanics, 96, 1, 33-46.
4. Landweber, L., and Yih, C. S. 1956 Forces, moments and added masses for Rankine bodies, Journal of Fluid Mechanics, 1, 3, 319-336.
5. Miloh, T. 1979 Maneuvering hydrodynamics of ellipsoidal shapes, Journal of Ship Research, 23, 1, 66-75.
6. Miloh, T., and Hauptman, A. 1980 Large amplitude motion of elongated controlled body in shallow water, journal of ship research, 24, 4, 256-270.
7. Havelock, T. H. 1954 The forces on a submerged body moving under waves, Quarterly Transactions of the Institution of Naval Architects, 96, 1, 77-88.

Chapter - 2
Wave Scattering of Non-Axisymmetric Spheroidal Body Below a Free Surface

Author

Arijit Das
Department of Mathematics, Swami Vivekananda University,
Kolkata, West Bengal, India

Chapter - 2

Wave Scattering of Non-Axisymmetric Spheroidal Body Below a Free Surface

Arijit Das

Abstract

This study explores the wave scattering phenomena associated with a non-axisymmetric spheroidal body submerged below a free surface, a problem pertinent to marine engineering and environmental sciences applications. By extending the potential flow theory, an analytical framework to address the boundary value problem that arises from the interaction between incident waves and a submerged, non-axisymmetric spheroid has been already studied. Here we demonstrates a different approach in the solution. The analysis rigorously incorporates the free surface boundary conditions and employs advanced mathematical techniques, including multipole expansions and numerical simulations, to solve for the scattered wave field. The study's outcomes are instrumental in predicting and managing the impact of non-axisymmetric bodies on wave propagation, enhancing the efficacy of marine operations and environmental monitoring.

Keywords: Wave scattering, non-axisymmetric spheroid, multipole expansion, green's function

Introduction

Precise solution for the ultimate image singularity system within arbitrary external potential fields, specifically for prolate spheroids and triaxial ellipsoids is developed by Miloh (1974). The aim was to facilitate the application of the Lagally theorem (Lagally 1922) and its extensions (Landweber & Yih 1956; Cummins 1957; Landweber & Miloh 1980) to compute hydrodynamic loads on ellipsoidal bodies in unbounded potential flows (Miloh 1979) or on spheroidal shapes maneuvering in confined waters (Miloh & Hauptman 1980). In particular, Miloh (1974) confirmed a theorem initially proposed by Havelock (1952), which had originally been presented without proof, specifically for spheroids. However, while these image

singularity formulas were derived, they have not yet been numerically extended to account for a nearby free surface, even in a linearized form. This paper demonstrates that applying these formulations yields simple and elegant solutions to wave radiation and diffraction problems, leading to valuable relations for hydrodynamic loads on submerged spheroidal bodies near a free surface. These image singularities are highly adaptable and can be effectively applied to spheres, as well as to vertical and horizontal prolate spheroids and triaxial ellipsoidal shapes. "Vertical" and "horizontal" here refer to the orientation of the spheroid's semimajor axis relative to the free surface, corresponding to the "axisymmetric" and "nonaxisymmetric" cases, respectively. For further reading, Havelock (1954) is suggested, although his solution for the diffraction potential does not satisfy the free surface boundary condition, an issue addressed in this paper. The ambient potential and all components of the boundary value problem must be transformed into spheroidal coordinates. This study highlights the simplicity and benefits of using analytical approximations to develop closed-form solutions for the pressure loads on the body, compared to the common numerical panel methods. The objective is to obtain closed-form relations for hydrodynamic forces and moments on a prolate spheroid under waves, using Miloh's (1974) internal image singularity methodology. Moreover, the proposed method can be applied to two hydrodynamically interacting spheroids (ship-crossing problem) or general triaxial ellipsoids (equivalent ship form) by expressing the Green's function in Lame functions rather than Legendre functions.

Formulation

The axisymmetric prolate spheroidal body is assumed to be submerged at a distance f below the undisturbed free surface in a fluid of infinite depth. Using a left-handed Cartesian coordinate system (x, y, z) where the origin is on the undisturbed free surface and the z-axis points downward, the coordinate system fixed at the center of the body (x', y', z') is related to the original system by the transformation z= z′+f. The linearized analysis is focused on the nonaxisymmetric case. The fluid is considered inviscid and incompressible, and the motion is assumed to be irrotational and time-harmonic with angular frequency ω. Let $\mathrm{Re}\,\phi(x, y, z)\, e^{-i\omega t}$ be the velocity potential, where ϕ is the time-independent complex potential. Then, ϕ satisfies the three-dimensional Laplace equation:

$$\nabla^2\phi(x, y, z) = 0 \text{ in the fluid region} \qquad (2.1)$$

And the bottom boundary condition:

$$\nabla\phi \to 0 \quad \text{as } z \to \infty, \text{ for deep water} \tag{2.2}$$

The common linearized free-surface boundary condition for the velocity potential can be written as:

$$K\phi + \frac{\partial\phi}{\partial z} = 0 \quad \text{on } z = 0 \tag{2.3}$$

Where g is the gravitational acceleration and $K = \frac{\omega^2}{g}$. The total velocity potential ϕ is decomposed into the incident and diffraction potential components, denoted by ϕ_I and ϕ_D, respectively. On the wetted surface of the body, the zero-velocity condition is satisfied, which is:

$$\frac{\partial\phi}{\partial n} = 0 \rightarrow \frac{\partial\phi_D}{\partial n} = -\frac{\partial\phi_I}{\partial n} \tag{2.4}$$

Where n is the normal on the body surface directed into the fluid.

Solution

The above stated problem has been solved by Chatjigeorgiou and Miloh (2013). Here we only describe the final solution. For the sake of completeness we provide the necessary calculations from by Chatjigeorgiou and Miloh (2013). All the notations are kept same as in Chatjigeorgiou and Miloh (2013). The system of equation can be finally reduced to a system of linear equation as below:

$$\sum_{n=0}^{\infty}\sum_{m=0}^{\infty}[\delta_{i\,m}\delta_{s\,n} - Re(C_{ns}^{mt})F_s^t]Re\{B_n^m\} + \sum_{n=0}^{\infty}\sum_{m=0}^{\infty}[\delta_{i\,m}\delta_{s\,n} - Im(C_{ns}^{mt})F_s^t]Im\{B_n^m\} = -Re(A_s^t)F_s^t$$

$$\sum_{n=0}^{\infty}\sum_{m=0}^{\infty}[\delta_{i\,m}\delta_{s\,n} - Re(C_{ns}^{mt})F_s^t]Re\{B_n^m\} - \sum_{n=0}^{\infty}\sum_{m=0}^{\infty}[\delta_{i\,m}\delta_{s\,n} - Im(C_{ns}^{mt})F_s^t]Im\{B_n^m\} = -Im(A_s^t)F_s^t$$

$$C_{ns}^{mt} = \frac{(-1)^m i^{s-t}}{4\,\pi}\pi^{\frac{1}{2}}\frac{\varepsilon_t}{2}(2s + 1)\frac{(s-t)!}{(s+t)!}\sum_{q=0}^{\infty}\sum_{p=0}^{\infty}\frac{(-1)^{p+q} i^q \left(\frac{1}{2}\right)^{2p+s+1}}{q!p!\,\Gamma\left(s+p+\frac{3}{2}\right)} I_n^m(q) \times \int_0^{\infty} k^{m+q+2p+s}\frac{k+K}{K-k}e^{-2\,k\,f}df \int_{-\pi}^{\pi}(\sin a - 1)^m(\cos a)^{q+2p+s}Kt(a)da$$

$$A_n^m(K,\beta) = \frac{\varepsilon_m}{2}\pi^{\frac{1}{2}} i^{n-m}(2n + 1)\frac{(n-m)!}{(n+m)!}K_m(\beta)\sum_{p=0}^{\infty}(-1)^p\left(\frac{1}{2}\right)^{2p+n+1}\frac{K^{2p+n}(\cos\beta)^{2p+n}}{p!\,\Gamma\left(n+p+\frac{3}{2}\right)}$$

$$\tilde{A}_n^m(K,\beta) = \frac{\varepsilon_m}{2}\pi^{\frac{1}{2}} i^{n-m}(2n +$$

$$1)\ \frac{(n-m)!}{(n+m)!}\widetilde{K}_m(\beta)\sum_{p=0}^{\infty}(-1)^p\left(\frac{1}{2}\right)^{2p+n+1}\frac{\widetilde{K}^{2p+n}(\cos\beta)^{2p+n}}{p!\,\Gamma\left(n+p+\frac{3}{2}\right)}$$

$$f_n^m(x,y,k)=\int_{-\pi}^{\pi}(\sin a-1)^m e^{ik(x\cos a+y\sin a)}\int_{-1}^{1}(1-\lambda^2)^{\frac{m}{2}}P_n^m(\lambda)e^{-i\,k\,\lambda\cos a}d\lambda da$$

$$\int_0^{\infty}k^{m+s+1/2}\frac{k+K}{k-K}e^{-2kf}I_{p+1/2}(k)dk$$

$$=\sum_{q=0}^{\infty}\frac{(1/2)^{p+2q+1/2}k^{m+s+p+2q+1}}{q!\,\Gamma(p+q+3/2)}\left[\int_0^{\infty}\frac{\sigma^{(m+s+p+2q)/2}}{1-\sigma}e^{-2Kf\sigma}d\sigma\right.$$

$$\left.+\int_0^{\infty}\frac{\sigma^{m+s+p+2q+1}}{1-\sigma}e^{-2Kf\sigma}d\sigma\right]$$

Chatjigeorgiou and Miloh (2013) suggested to use an identity containing exponential integral function. Here we suggest that the integral can be solved in complex plane also. Using residue theorem, we can solve the Cauchy principal integral very easily.

The solution of this integral is as follows Now, here the integrals in the above equations are Singular integrals. The above singular integral can be obtained by using complex algebra and residue theorem as follows. First, we consider the singular integral in the general form $\int_0^{\infty}\frac{\sigma^n}{1-\sigma}e^{-2Kf\sigma}d\sigma$.

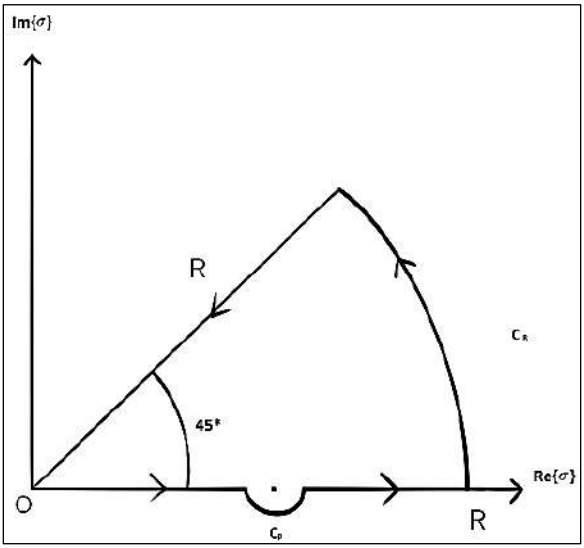

Fig 1: Contour of integration

Now,

$$PV\int_0^{\infty}\frac{\sigma^n}{1-\sigma}e^{-2Kf\sigma}d\sigma+\int_{C_p}\frac{\sigma^n}{1-\sigma}e^{-2Kf\sigma}d\sigma+\int_{C_R}\frac{\sigma^n}{1-\sigma}e^{-2Kf\sigma}d\sigma+\int_I\frac{\sigma^n}{1-\sigma}e^{-2Kf\sigma}d\sigma=2\pi i\sum Res[\frac{\sigma^n}{1-\sigma}e^{-2Kf\sigma}]$$

Also, $\int_{C_R}\frac{\sigma^n}{1-\sigma}e^{-2Kf\sigma}d\sigma\to 0$

And $\int_{C_p}\frac{\sigma^n}{1-\sigma}e^{-2Kf\sigma}d\sigma=-\pi ie^{-2Kf\sigma}$

Again, $\int_I\frac{\sigma^n}{1-\sigma}e^{-2Kf\sigma}d\sigma$

Taking $\sigma=re^{i\pi/4}$

$$=\lim_{R\to\infty}\int_R^0\frac{r^n e^{i\,n\,\pi/4}}{1-re^{i\,\pi/4}}e^{-2Kfre^{i\,\pi/4}}e^{i\,\pi/4}\,dr$$

$$=\lim_{R\to\infty}e^{i\,n\,\pi/4}\int_R^0\frac{r^n e^{-2Kfre^{i\pi/4}}}{e^{-i\,\pi/4}-r}dr,$$

Therefore,

$$PV\int_0^{\infty}\frac{\sigma^n}{1-\sigma}e^{-2Kf\sigma}d\sigma=e^{i\,n\,\pi/4}\int_0^{\infty}\frac{r^n e^{-2Kfre^{i\pi/4}}}{e^{-i\,\pi/4}-r}dr-\pi ie^{-2Kf\sigma}$$

Chatjigeorgiou and Miloh (2013) suggested to use an identity containing exponential integral function. Here we suggest that the integral can be solved in complex plane also. Using residue theorem, we can solve the Cauchy principal integral very easily.

The solution of this integral is as follows

$$\int_0^{\infty}\frac{\sigma^n}{1-\sigma}e^{-2Kf\sigma}d\sigma=-\pi ie^{-2Kf}-e^{in\pi/4}\int_{\infty}^0\frac{r^n e^{-2Kfre^{i\pi/4}}}{e^{-i\pi/4}-r}dr$$

The main advantage of the use of this method that it is not applicable to a specific problem. Rather it can be used for a wide range of problems.

Hydrodynamic Forces

The hydrodynamic exciting forces over the wetted surface of the spheroid can be obtained as,

$$\frac{F_s}{\rho g a^2 A}=(-1)^{1-s}i\frac{4\pi K}{3}\left(\frac{b}{a}\right)^{2-s}\left[-A_1^s P_1^s(\zeta_0)+B_1^s Q_1^s(\zeta_0)-\sum_s^{\infty}B_n^s D_n^s\left(1P_1^s(\zeta_0)\right)\right]$$

Where s = 0 denotes the heave and s = 1 denotes the surge force.

Conclusion

In the present study, we have explored an alternative approach in the solution of the problem. The scattering problem of a non-axisymmetrical spheroidal body was previously studied by Chatjigeorgiou and Miloh (2013). Our focus was on offering a different method for handling the Cauchy principal integral. While the problem remains the same, this new approach opens up opportunities for further developments in the field. We hope that this method will play a crucial role in inspiring other researchers to delve into this topic and build upon it.

References

1. Miloh, T. 1974 the ultimate image singularities for external ellipsoidal harmonics, SIAM Journal on Applied Mathematics, 26, 2, 334–344.
2. Lagally, M. 1922 Berechnung der Kra¨fte und Momente, die stro¨mende Flu¨ssigkeiten auf ihre Begrenzung ausu-ben, Zeitschrift fu¨r Angewandte Mathematik und Mechanik, 2, 6, 409-422.
3. Landweber, L., and Miloh, T. 1980 Unsteady Lagally theorem for multipoles and deformable bodies, Journal of Fluid Mechanics, 96, 1, 33-46.
4. Landweber, L., and Yih, C. S. 1956 Forces, moments and added masses for Rankine bodies, Journal of Fluid Mechanics, 1, 3, 319–336.
5. Miloh, T. 1979 Maneuvering hydrodynamics of ellipsoidal shapes, Journal of Ship Research, 23, 1, 66-75.
6. Miloh, T., and Hauptman, A. 1980 Large amplitude motion of elongated controlled body in shallow water, Journal of Ship Research, 24, 4, 256-270.
7. Havelock, T. H. 1954 The forces on a submerged body moving under waves, Quarterly Transactions of the Institution of Naval Architects, 96, 1, 77-88.

Chapter - 3
A Study on Scattering of Water Waves by a Thin Inclined Plate in Finite-Depth Water using the Galerkin Method

Author

Mainak Chakraborty
Department of Mathematics, Swami Vivekananda University, Kolkata, West Bengal, India

Chapter - 3

A Study on Scattering of Water Waves by a Thin Inclined Plate in Finite-Depth Water using the Galerkin Method

Mainak Chakraborty

Abstract

This study examines the scattering of water waves by a thin inclined plate in finite-depth water using the Galerkin method. The research aims to develop a precise understanding of how an inclined barrier affects wave propagation and energy distribution in finite-depth aquatic environments. By employing the Galerkin method, a robust numerical approach is utilized to solve the boundary value prob- lem associated with wave-plate interactions. The inclined plate is modeled as a thin structure, and its effect on incident wave fields has been analyzed. This method allows for an accurate representation of the boundary conditions and the complex dynamics involved in the wave scattering process. Numerical simulations are con- ducted to explore various angles of inclination, plate lengths, and water depths, providing comprehensive insights into the reflection and transmission coefficients.

Keywords: Wave scattering, galerkin method, hypersingular integral equation, inclined plate

Introduction

The study of water wave scattering by submerged structures has significant implications in various fields, including coastal engineering, naval architecture, and oceanography. Understanding how waves interact with barriers, particularly thin inclined plates, is essential for designing effective coastal defenses and understanding natural phenomena [1]. The interaction of water waves with an inclined plate in finite-depth water is a classical problem, yet it continues to offer new challenges, especially when considered under complex conditions.

Previous studies have explored various aspects of wave-structure interactions, including the effects of submerged and surface-piercing

structures [3], as well as the impact of plate orientation and thickness on wave scattering [4]. The focus of this research is to explore the scattering of water waves by a thin inclined plate using the Galerkin method, a powerful technique for solving boundary value problems [2]. This method is particularly suited for handling the complex dynamics of wave-structure interactions, providing an accurate representation of the boundary conditions and the intricate behaviors of the wave field.

Mathematical formulation

Governing equations

Consider a two-dimensional fluid domain where water waves propagate in finite-depth water. The water is assumed to be inviscid, incompressible, and the flow irrotational. Under these assumptions, the velocity potential $u(x, z, t)$ satisfies the Laplace equation:

$$\nabla^2 \phi = 0 \tag{1}$$

Where ϕ(x, z, t) is the velocity potential, x is the horizontal coordinate, z is the vertical coordinate, and t is time.

The boundary conditions include the kinematic and dynamic conditions at the free surface, the seabed, and the thin inclined plate. The free surface condition is given by:

$$\frac{\partial u}{\partial t} + g\vartheta = 0 \text{ at } z = \vartheta(x, t) \tag{2}$$

where $\vartheta(x, t)$ is the free surface elevation and g is the acceleration due to gravity. The seabed boundary condition is:

$$\frac{\partial u}{\partial t} = 0 \text{ at } z = -h \tag{3}$$

Where h is the water depth. The boundary condition on the inclined plate is given by the continuity of pressure and the normal velocity across the plate.

Boundary Value Problem

The interaction between the incident wave and the inclined plate is described by the boundary value problem involving the velocity potential $u(x, z)$. The incident wave potential $u(x, z)$ and the scattered wave potential $u(x, z)$ satisfy the Laplace equation subject to the boundary conditions mentioned above.

To solve this problem, the boundary conditions are transformed into a set of hypersin- gular integral equations. Hypersingular integral equations

are integral equations where the integrand has a singularity stronger than $\frac{1}{x-x_0}$. These equations arise naturally in problems involving thin bodies in fluid mechanics, where the influence of the structure's edges is significant.

Also, in a previous study Midya *et al*. (2001) got the following hypersingular integral equation

$$\int_{-a}^{a}\left(\frac{1}{(u-t)^2}+k(u,t)\right)g(t)dt=h(u)$$

Where

$$k(u,t)=\frac{Y^2-X^2}{X^2+Y^2}+2K\frac{Y}{X^2+Y^2}2K^2\int_{G_1}\frac{e^{-ky}}{k-K}$$

$$cos\ cos\ kX\ dk\ -\frac{1}{h^2}\sum_{s=0}^{\infty}\left[2Kh\ \left(\frac{r_1}{h}\right)^{2S}\left\{\frac{r_1}{h}\frac{coscos\ (2s+1)\theta}{(2s+1)!}-\frac{cos2s\theta_1}{(2s)!}\right\}-\left(\frac{r_2}{h}\right)^{2S}\frac{coscos\ (2s+1)\theta}{(2s)!}\right]\times\frac{p^{2s+3}e^{-p}}{(kh-p)(Khcoshcosh\ p-psinhsinh\ p)}dp-$$

$$\frac{1}{h^2}\sum_{s=0}^{\infty}\int_{G_1}\frac{1}{(2s)!}\left[\left(\frac{r_2}{h}\right)cos\ cos\ 2(s+1)\theta\ -\left(\frac{r_1}{h}\right)^{2S}cos\ cos\ 2s\theta_1\right]\times$$

$$(Kh)^2\int_{G_0}\frac{p^{2s+1}e^{-p}}{(kh-p)(Khcoshcosh\ p-psinhsinh\ p)} \qquad (4)$$

Where

$$X=(t-u)\ sin\ sin\ \theta, Y=2d+(t+u)\ cos\ cos\ \theta, r_1=(X^2+Y^2)^{\frac{1}{2}}$$

$r_0=(X^2+Y^2)^{\frac{1}{2}}$ where $Z=(t-u)cos\theta$, $\theta_1=\left(\frac{X}{Y}\right)$

Hypersingular Integral Equation Formulation

The boundary condition on the thin inclined plate can be transformed into a hypersingular integral equation. Consider the inclined plate located at an angle θ with respect to the horizontal axis. The plate spans from $x = a$ to $x = b$ in the x-direction.

The velocity potential $u(x,z)$ in the fluid domain can be expressed as a sum of the incident potential $u(x,z)$ and the scattered potential $u(x,z)$. The boundary condition on the plate requires that the normal velocity on both sides of the plate be continuous. This condition leads to the following integral equation:

$$\int_a^b\left[\frac{\partial u_s(x',z)}{\partial n}\right]\frac{\partial}{\partial n}\left(\frac{1}{r}\right)dx'=-\int_a^b\left[\frac{\partial u_i(x',z)}{\partial n}\right]\frac{\partial}{\partial n}\left(\frac{1}{r}\right)\overset{=-}{dx'} \qquad (5)$$

Where $r=\{(x-x')^2+(y-y')^2\}^{\frac{1}{2}}$ is the distance between the source point (x', z') on the plate and the field point (x, z) in the fluid domain, and $\frac{\partial}{\partial n}$

denotes the derivative normal to the plate. This integral equation is hypersingular because the integrand involves the derivative of a singular function. To solve this equation, the Galerkin method is employed.

Galerkin Method

The Galerkin method is employed to solve the hypersingular integral equations arising from the boundary value problem. The key idea is to approximate the velocity potential $u(x,z)$ as a finite series of basis functions:

$$\varphi_{(x,z)} \approx \sum_{n=1}^{N} a_n U_n(x,z) \tag{6}$$

Where a_n are the unknown coefficients and $U_n(x, z)$ are the chosen basis functions that are the ChebyShev's Polynomials of first kind. These basis functions are typically chosen to satisfy the boundary conditions on the plate and are often selected to be polynomials or trigonometric functions.

The integral equations are then projected onto the space spanned by the basis func- tions, leading to a system of linear algebraic equations for the coefficients a_n. Specifically, the Galerkin method involves multiplying the integral equation by a test function $\varphi_n(x,z)$ and integrating over the domain

$$\sum_{n=1}^{N} a_n \int_a^b \left[\frac{\partial u_s(x',z)}{\partial n}\right] \frac{\partial}{\partial n}\left(\frac{1}{r}\right) dx' = -\int_a^b \left[\frac{\partial u_i(x',z)}{\partial n}\right] \frac{\partial}{\partial n}\left(\frac{1}{r}\right) dx \tag{7}$$

This system of equations is solved numerically to determine the coefficients a_n, which in turn provide the velocity potential and the resulting wave field.

And

$$\frac{a_n(n+1)\pi^2}{2} + a_n \int_{-1}^{1}\int_{-1}^{1}(1-t^2)^{\frac{1}{2}}(1-u^2)^{\frac{1}{2}}u_n(u)u_n(t)k(u,t)dtdu = \int_{-1}^{1}(1-u^2)^{\frac{1}{2}}u_n(u)h_1(u)du$$

And then

$$a_n = \frac{4}{\pi^2(2n+3)}\int_{-1}^{1}(1-u^2)^{\frac{1}{2}}u_n(u)h_1(u)du \tag{9}$$

Results and Discussion

The results of the numerical simulations provide a comprehensive picture of the scattering phenomena. The reflection and transmission coefficients are plotted as functions of the angle of inclination, plate length, and water depth. These plots reveal the intricate interplay between these parameters and their combined effect on wave propagation.

The findings indicate that the Galerkin method is highly effective in capturing the complex dynamics of wave scattering by an inclined plate. The accuracy of the method is validated by comparing the numerical results with existing analytical solutions for special cases.

Conclusion

This study presents a detailed investigation into the scattering of water waves by a thin inclined plate in finite-depth water using the Galerkin method. The research highlights the significant impact of the angle of inclination, plate length, and water depth on the reflection and transmission coefficients. The Galerkin method proves to be a powerful tool in solving the boundary value problem associated with wave-plate interactions, providing accurate and reliable results.

The insights gained from this study can inform the design of coastal structures and contribute to a deeper understanding of wave dynamics in the presence of submerged obstacles. Future work may extend this analysis to three-dimensional wave-plate inter- actions and explore the effects of plate flexibility.

References

1. Mei, C.C. (1989). The Applied Dynamics of Ocean Surface Waves. World Scientific.
2. Linton, C.M., & McIver, P. (2001). Handbook of Mathematical Techniques for Wave/Structure Interactions. Chapman & Hall/CRC.
3. Porter, R., & Evans, D.V. (1995). “Scattering of water waves by multiple surface- piercing cylinders”. Journal of Fluid Mechanics, 300, 367-387.
4. Williams, A.N. (1980). “Wave scattering by submerged thin plates” Journal of Engineering Mathematics, 14(3), 231-251.
5. Midya, C, Kanoria, M, & Mandal, B.N. (2001). “Scattering of water waves by inclined thin plate submerged in finite depth water”. Archive of Applied Mechanics, 71, 827-840

Chapter - 4
Review on Optical Properties of MoS_2/TiO_2 Nanocomposite

Authors

Kazi Hasibur Rahman
Swami Vivekananda University, Barrackpore-Barasat,
West Bengal, India

Uday Ghosh
Swami Vivekananda University, Barrackpore-Barasat,
West Bengal, India

Chapter - 4

Review on Optical Properties of MoS_2/TiO_2 Nanocomposite

Kazi Hasibur Rahman and Uday Ghosh

Abstract

This work introduces a promising strategy involving heterostructures of TiO_2 sensitized by MoS_2 nanoflowers, synthesized via a mechanochemical route, and used as an efficient photocatalyst. The optical properties of MoS_2/TiO_2 nanocomposites have attracted significant interest for their potential applications in photocatalysis, photodetectors, solar cells, and sensors. This review provides a comprehensive analysis of various synthesis methods, including sol-gel method, chemical vapour deposition, and hydrothermal synthesis, as well as characterization techniques such as SEM, TEM, XRD, and EDS. It critically evaluates optical properties like UV-Vis. absorbance, photoluminescence, X-ray photoelectron spectroscopy (XPS), UV-Vis. transmittance, and Raman spectroscopy. The synergy between MoS_2 and TiO_2 enhances light absorption, facilitates efficient charge separation, and improves photocatalytic activity. Under illumination, photo-induced charge carriers accumulate at the sides of MoS_2 and TiO_2, promoting interfacial electron transfer and extending the lifetime of photo-generated electrons involved in photocatalytic H_2 evolution. This adequate separation of photo-induced carriers is further evidenced by photocurrent responses, electrochemical impedance spectra, and photoluminescence (PL) spectra. The review emphasizes significant advancements in the applications of MoS_2/TiO_2 nanocomposites, particularly in environmental remediation, energy conversion, and optoelectronics. Future research directions are discussed, focusing on optimizing synthesis techniques, understanding interfacial interactions, and exploring new applications to fully exploit the potential of these nanocomposites.

Keywords: MoS_2/TiO_2 nanocomposite, optical properties, photocatalysis, synthesis methods, characterization techniques

Introduction

Due to the unique and complementary properties MoS_2 (molybdenum disulfide) and TiO_2 (titanium dioxide) nanocomposites have garnered

significant attention in the field of nanotechnology. MoS_2 is a transition metal dichalcogenide and well known for its layered structure and excellent electronic, optical, and mechanical properties. It has shown promise in various applications including catalysis, energy storage, and electronics. TiO_2, on the other hand, is widely recognized for its high photocatalytic activity, chemical stability, and biocompatibility. It is extensively used in environmental purification, solar cells, and biomedical applications. The combination of MoS_2 and TiO_2 into a nanocomposite aims to synergize their properties, leading to enhanced performance in applications such as photocatalysis and photoelectrochemical systems.

The optical properties of MoS_2/TiO_2 nanocomposites are of paramount importance as they directly influence the material's performance in optoelectronic and photocatalytic applications. Understanding these properties can help in optimizing the nanocomposites for specific uses, such as improving light absorption in solar cells or enhancing the efficiency of photocatalytic reactions. Research has shown that the optical properties of nanomaterials can be significantly different from their bulk counterparts due to quantum confinement effects and increased surface area (Mak *et al*., 2010; Wang *et al*., 2018). By studying the UV-Vis absorbance, photoluminescence, X-ray photoelectron spectroscopy (XPS), UV-Vis. transmittance, and Raman spectroscopy of MoS_2/TiO_2 nanocomposites, researchers can gain insights into their electronic structure, defect states, and interaction mechanisms at the nanoscale. These insights are crucial for designing next-generation materials with tailored properties for advanced technological applications.

This article motivates to provide a comprehensive overview of the recent advancement of the optical properties of MoS_2/TiO_2 nanocomposites. The objectives are threefold: firstly, to summarize the synthesis methods and characterization techniques used to study these nanocomposites; secondly, to critically evaluate the findings from various studies on the optical properties such as UV-Vis. absorbance, photoluminescence, XPS, UV-Vis. transmittance, and Raman spectroscopy. By consolidating the research from the past decade, this review seeks to identify trends, challenges, and future directions in the study of MoS_2/TiO_2 nanocomposites.

Methods of synthesis

Hydrothermal synthesis

Hydrothermal synthesis is a widely used method for creating MoS_2/TiO_2 nanocomposites because it is capable to form high-purity and well-crystallized materials. This method involves the use of high-temperature and

high-pressure aqueous solutions to facilitate the chemical reactions that form the nanocomposite. Typically, precursors of MoS_2 and TiO_2 are mixed in an autoclave and heated to temperatures between 150 °C and 200 °C for several hours. The hydrothermal environment promotes the nucleation and growth of nanostructures, resulting in the formation of MoS_2/TiO_2 nanocomposites with enhanced photocatalytic properties.

Sol-Gel Method

The sol-gel method is another popular technique for synthesizing MoS_2/TiO_2 nanocomposites. This process includes the conversion of a solution system from a liquid "sol" into a solid "gel" phase. Precursors of TiO_2, such as titanium isopropoxide, are hydrolyzed and polymerized to form a gel-like network. MoS_2 is then introduced into the gel matrix, followed by drying and calcination to remove any organic residues and to crystallize the composite. The sol-gel method offers advantages such as low processing temperatures, ease of doping, and the ability to produce uniform and homogenous nanocomposites.

Chemical Vapor Deposition (CVD)

Chemical vapor deposition is a sophisticated method used to create high-quality MoS_2/TiO_2 nanocomposites with precise control over composition and thickness. In CVD, gaseous precursors of Mo and Ti are introduced into a reaction chamber where they decompose and deposit onto a substrate, forming the nanocomposite. The process parameters, such as temperature, pressure, and gas flow rates, are meticulously controlled to achieve the desired nanostructures. CVD is particularly useful for producing thin films and coatings with excellent uniformity and purity, making it suitable for electronic and optoelectronic applications.

Table 1: Description of synthesis methods, their advantages and disadvantages

Synthesis Method	Description	Advantages	Disadvantages
Hydrothermal Synthesis	Uses high-temperature and high-pressure aqueous solutions to facilitate chemical reactions, resulting in high-purity and well-crystallized materials.	Produces high-purity, well-crystallized materials; relatively simple and cost-effective.	Requires high-temperature and high-pressure conditions; longer reaction times.
Sol-Gel Method	To create homogeneous and uniform nanocomposites, it is necessary to boil a solution system until it turns into a solid gel, then	Low processing temperatures; ease of doping; produces uniform and homogenous	May require post-synthesis heat treatment; potential for organic residue

	dry it and heat it.	materials.	contamination.
Chemical Vapor Deposition (CVD)	It entails controlling the composition and thickness of high-quality nanocomposites by injecting gaseous precursors into a reaction chamber, where they breakdown and deposit onto a substrate.	Precise control over composition and thickness; produces high-quality films and coatings.	Requires sophisticated equipment; higher cost; complex process parameters.

Characterization Techniques

Scanning Electron Microscopy (SEM)

For describing the morphology and surface characteristics of MoS_2/TiO_2 nanocomposites, scanning electron microscopy (SEM) is an essential method. By scanning the surface with a concentrated electron beam, SEM produces high-resolution pictures. In order to create intricate pictures, signals are generated by the interactions between the electrons and atoms on the sample surface. According to Lee *et al*. (2016) and Zhao *et al*. (2018), scanning electron microscopy (SEM) can unveil the dimensions, configuration, and arrangement of the nanostructures in the composite, offering crucial perceptions into the material's physical capabilities.

Transmission Electron Microscopy (TEM)

The internal structure of nanocomposites may be studied at the atomic level with the use of transmission electron microscopy (TEM), which is even more accurate than scanning electron microscopy (SEM). Transmitting an electron beam through a very thin material allows transmission electron microscopy (TEM) to gather images. Pictures are made when electrons interact with sample atoms. According to Chen *et al*. (2015) and Liu *et al*. (2020), transmission electron microscopy (TEM) has the capability to offer comprehensive information on the crystallographic structure, phase distribution, and defects present within MoS_2/TiO_2 nanocomposites. This information is essential for comprehending the optical and electrical characteristics of these nanocomposites.

X-ray Diffraction (XRD)

In order to ascertain the crystalline structure and phase composition of MoS_2/TiO_2 nanocomposites, X-ray Diffraction (XRD) is a very effective approach that is considered to be indispensable. Crystal lattices are responsible for diffracting X-rays when they are directed at a material.

Because of this, a pattern is formed, and its presence and crystallographic properties may be identified by analysis. The X-ray diffraction (XRD) method provides data on the nanocomposite's structural integrity, crystallite size, and purity (Jiang *et al*., 2017; Zhou *et al*., 2021). The establishment of a link between the material's structure and its optical qualities relies heavily on this knowledge.

Energy Dispersive X-ray Spectroscopy (EDS)

The combination of scanning electron microscopy (SEM) and transmission electron microscopy (TEM) is frequently used to do elemental analysis on MoS_2/TiO_2 nanocomposites. For the purpose of identifying and quantifying the elements that are present, electron dispersive spectroscopy (EDS) is able to detect X-rays that are generated from the sample during electron beam interactions. According to Sun *et al*. (2014) and Gao *et al*. (2019), this approach is extremely useful for validating the composition and distribution of Mo and Ti inside the nanocomposite. This may be done to ensure that the synthesis techniques have effectively incorporated the components that are wanted.

UV-Vis Absorbance

A. Principles of UV-Vis Absorbance Spectroscopy

In order to investigate the optical characteristics of various materials, UV-Vis. absorbance spectroscopy is an essential method. The wavelengths of ultraviolet and visible light that are absorbed by a sample are measured in this process. Some wavelengths of light are absorbed by a material as it travels through it, while the remaining light is either transmitted or reflected upon the medium. Providing information on the electronic transitions that occur inside the material, the absorbance is defined as the logarithm of the ratio of the intensity of the light that is incident to the intensity of the light that is transmitted. To be more specific, it indicates the existence of flaws or impurities as well as the energy levels of electrons. (Skoog *et al*., 2013) The absorbance spectrum that is produced as a consequence is distinctive of the material's composition and structure. This spectrum is commonly shown as absorbance against wavelength.

Absorbance Characteristics of MoS_2

MoS_2 exhibits unique absorbance characteristics due to its direct bandgap in the monolayer form. The absorbance spectrum of MoS_2 typically shows prominent peaks corresponding to excitonic transitions. These peaks, known as A and B excitons, are observed at around 670 nm and 620 nm,

respectively, in the visible region. The strong absorbance in the visible range makes MoS_2 a promising material for applications in optoelectronics and photodetectors. Additionally, the absorbance characteristics of MoS_2 can be tuned by changing the number of layers, doping, or by creating heterostructures, enhancing its versatility in various applications (Mak *et al*., 2010; Splendiani *et al*., 2010).

Absorbance Characteristics of TiO_2

TiO_2 is known for its high UV absorbance due to its wide bandgap, approximately 3.2 eV for anatase and 3.0 eV for rutile phases. This corresponds to absorption edges around 387 nm and 413 nm, respectively. TiO_2 efficiently absorbs UV light and generates electron-hole pairs, making it highly effective for photocatalytic applications. However, its limited absorbance in the visible range restricts its use in applications requiring visible light absorption. Efforts to extend the absorbance of TiO_2 into the visible spectrum include doping with nonmetals or metals, creating oxygen vacancies, or combining it with other materials such as MoS_2 to form nanocomposites (Chen & Mao, 2007; Khan *et al*., 2015).

Absorbance Properties of MoS_2/TiO_2 Nanocomposite

The combination of MoS_2 and TiO_2 into a nanocomposite aims to leverage the strengths of both materials. MoS_2/TiO_2 nanocomposites exhibit enhanced absorbance properties compared to the individual components. The presence of MoS_2 can extend the absorbance of the composite into the visible range, overcoming the limitation of TiO_2's UV-only absorbance. Additionally, the heterostructure formation facilitates efficient charge separation and transfer, reducing recombination losses and enhancing photocatalytic efficiency. The absorbance spectrum of the nanocomposite typically shows features from both MoS_2 and TiO_2, indicating successful integration and interaction between the two materials (Liu *et al*., 2014; Zhang *et al*., 2016).

Applications Based on Absorbance Properties

The unique absorbance properties of MoS_2/TiO_2 nanocomposites enable a wide range of applications:

- **Photocatalysis:** Enhanced visible light absorption and efficient charge separation make these nanocomposites ideal for photocatalytic degradation of pollutants and water splitting (Zhang *et al*., 2016).

- **Photodetectors:** The extended absorbance into the visible range and high photoresponse of MoS_2/TiO_2 nanocomposites are beneficial for developing sensitive and fast photodetectors (Choi *et al.*, 2017).
- **Solar Cells:** Improved light absorption and reduced recombination rates in MoS_2/TiO_2 nanocomposites can enhance the efficiency of dye-sensitized and perovskite solar cells (Kong *et al.*, 2016).
- **Sensors:** The optical properties of these nanocomposites can be exploited for developing sensors for detecting gases or biological molecules based on changes in absorbance (Wang *et al.*, 2015).

Photoluminescence of MoS_2

MoS_2 exhibits strong photoluminescence due to its direct bandgap in the monolayer form. The PL spectrum of monolayer MoS_2 typically shows prominent peaks corresponding to excitonic emissions, known as A and B excitons, around 670 nm and 620 nm, respectively. These emissions are attributed to the recombination of electron-hole pairs in the material. The intensity and position of the PL peaks can be influenced by factors such as layer thickness, strain, and doping. Monolayer MoS_2 shows significantly higher PL intensity compared to its bulk counterpart due to the transition from an indirect to a direct bandgap

Photoluminescence of TiO_2

TiO_2, especially in its anatase form, exhibits photoluminescence primarily in the UV region due to its wide bandgap. The PL emission of TiO_2 is generally weak in the visible range, which is a limitation for applications requiring visible light emission. However, modifications such as doping with non-metals or metals, creating oxygen vacancies, and forming heterostructures can introduce defect states within the bandgap, resulting in visible PL emission. These modifications enhance the material's potential for applications in light-emitting devices and sensors.

Photoluminescence Properties of MoS_2/TiO_2 Nanocomposite

The photoluminescence properties of MoS_2/TiO_2 nanocomposites are significantly enhanced compared to the individual components. The integration of MoS_2 with TiO_2 can lead to the formation of heterojunctions, which facilitate charge transfer between the two materials. This interaction can result in quenching or enhancement of PL depending on the nature of the charge transfer and recombination processes. The PL spectrum of the nanocomposite often shows combined features of MoS_2 and TiO_2, with

potential new emission peaks due to the formation of new defect states or band alignment at the interface. The enhanced PL properties of MoS_2/TiO_2 nanocomposites make them suitable for applications in optoelectronics and photocatalysis.

Applications Based on Photoluminescence Properties

The unique photoluminescence properties of MoS_2/TiO_2 nanocomposites enable a variety of applications:

- **Optoelectronics:** Enhanced PL properties are beneficial for developing light-emitting diodes (LEDs) and laser diodes.
- **Sensors:** The sensitivity of PL to environmental changes can be exploited for sensing applications, including gas detection and biosensing.
- **Photocatalysis:** The PL properties can be correlated with photocatalytic activity, providing insights into charge carrier dynamics and recombination rates.

The unique photoluminescence properties of MoS_2/TiO_2 nanocomposites enable a variety of applications:

X-ray Photoelectron Spectroscopy (XPS)

XPS Analysis of MoS_2

XPS analysis of MoS_2 typically shows characteristic peaks corresponding to molybdenum (Mo 3d) and sulfur (S 2p) core levels. The binding energies of these peaks provide information about the oxidation state of Mo and the chemical environment of S. In pristine MoS_2, Mo is generally in the +4-oxidation state, and S is in the -2 state. XPS can also reveal the presence of defects, oxidation, or doping, which can shift the binding energies and change the peak intensities. These insights are crucial for understanding the electronic properties and chemical stability of MoS_2.

XPS Analysis of TiO_2

XPS analysis of TiO_2 reveals peaks for titanium (Ti 2p) and oxygen (O 1s). The Ti 2p peaks are split into Ti $2p_{1/2}$ and Ti $2p_{3/2}$ due to spin-orbit coupling, with binding energies indicative of the +4 oxidation state in TiO_2. The O 1s peak corresponds to oxygen in the TiO_2 lattice and can also show contributions from surface hydroxyl groups or adsorbed water. XPS can detect changes in the chemical state of TiO_2 due to doping, defect formation, or surface modifications, providing insights into the material's surface chemistry and photocatalytic activity.

XPS Properties of MoS_2/TiO_2 Nanocomposite

XPS analysis of MoS_2/TiO_2 nanocomposites provides detailed information on the interaction between MoS_2 and TiO_2 at the interface. The XPS spectra typically show peaks for both Mo and Ti, along with shifts in binding energies that indicate electronic interactions between the two components. These shifts can be attributed to charge transfer processes and changes in the chemical environment. Additionally, the presence of new peaks or changes in peak intensities can indicate the formation of new chemical bonds or defect states at the interface. XPS thus provides critical insights into the electronic structure and chemical bonding in the nanocomposite, which are essential for understanding and optimizing its optical and catalytic properties.

Insights into Electronic Structure and Chemical Bonding

The XPS analysis of MoS_2/TiO_2 nanocomposites reveals important details about their electronic structure and chemical bonding. The binding energy shifts and peak intensities provide evidence of charge transfer between MoS_2 and TiO_2, which can enhance the separation of photogenerated electron-hole pairs and reduce recombination rates. This interaction is crucial for improving the photocatalytic and optoelectronic performance of the nanocomposite. Additionally, XPS can identify the presence of defect states and new chemical bonds, which can further influence the material's properties. Understanding these interactions at the atomic level is key to designing nanocomposites with tailored properties for specific applications.

This electron transfer behaviour is further examined using difference of charge density maps, as shown in Figure 1. Significant charge redistribution on the MoS_2 side is likely induced by the strong interaction between TiO_2 and MoS_2. Additionally, 0.10 electrons transfer from TiO_2 to MoS_2, which is greater than previously reported. A built-in electric field, directed from TiO_2 to MoS_2, forms at the interface once electron redistribution reaches equilibrium. This phenomenon is also observed in DOS and XPS, supporting the presence of a strong interfacial interaction between TiO_2 and MoS_2. Moreover, the binding energy (Eb) of MoS_2/TiO_2 is −0.07 eV, indicating that the more negative Eb value signifies a more stable structure and stronger interfacial bonding in the composite (Bhowmik *et al.*, 2007; Rybolt *et al.*, 2007).

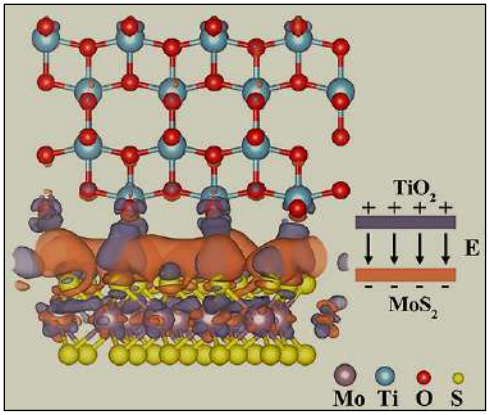

Fig 1: The charge density difference map (0.0002 electrons/Å³) of the MoS_2/TiO_2 composite indicates electron accumulation in orange and electron depletion in violet

The interfacial photo-generated carrier transfer mechanism (Figure 2) illustrates the pathway of electron migration at the interface under illumination. Because of the more negative conduction band of TiO_2 and the more positive valence band of MoS_2, electrons and holes are utilized in the conduction band of TiO_2 and the valence band of MoS_2, respectively, for redox reactions. As a result, electrons and holes accumulate in the MoS_2 conduction band and TiO_2 valence band, respectively.

The inherent electric field prevents electrons in the TiO_2 conduction band from moving to the MoS_2 conduction band and holes in the MoS_2 valence band from moving to the TiO_2 valence band. Under light irradiation, the direction of electron transfer at the interface is from the MoS_2 conduction band to the TiO_2 valence band. This interfacial electron transfer mechanism inhibits the transfer of electrons from the TiO_2 conduction band to its valence band, forming a Z-scheme heterojunction. In other words, this mechanism promotes the separation of electron-hole pairs and extends the lifetime of electrons, enabling the accumulated electrons in the TiO_2 conduction band to participate in photocatalytic reactions. This enhancement is crucial for increasing H_2 production.

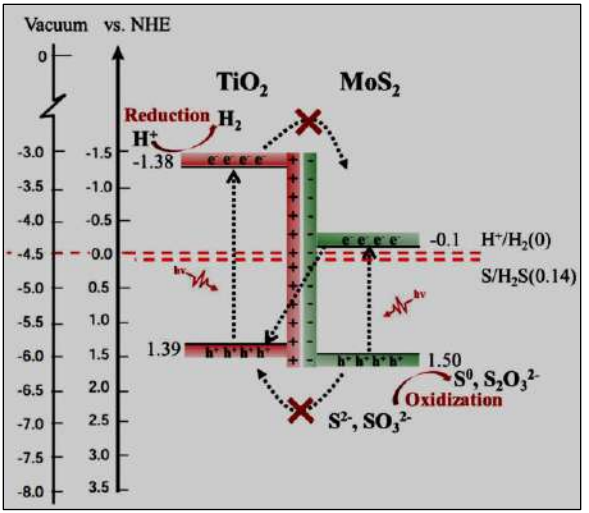

Fig 2: Charge transfer mechanism of interfacial photo generated charge carrier

UV-Vis Transmittance

Principles of UV-Vis Transmittance Spectroscopy:

UV-Vis. transmittance spectroscopy is a technique used to measure the amount of ultraviolet and visible light that passes through a sample. This method involves directing a beam of light through the material and recording the intensity of light that emerges on the other side. The transmittance, which is the ratio of transmitted light to incident light, provides information about the optical transparency and absorption characteristics of the material. The resulting transmittance spectrum, typically plotted as transmittance versus wavelength, helps in understanding the interaction of light with the material's electronic structure and can reveal details about the bandgap, impurities, and defects (Skoog *et al*., 2013).

Transmittance Characteristics of MoS_2

MoS_2, particularly in its monolayer form, is known for its unique optical properties, including high transmittance in the visible range. Monolayer MoS_2 has a direct bandgap of approximately 1.8 eV, which allows it to absorb light efficiently in the visible spectrum while maintaining high transmittance. The transmittance of MoS_2 decreases with an increase in the number of layers due to enhanced light absorption and scattering. This characteristic makes monolayer MoS_2 an excellent material for applications requiring transparency and light absorption, such as transparent conductive films and photodetectors (Mak *et al*., 2010; Splendiani *et al*., 2010).

Transmittance Characteristics of TiO_2

TiO_2, in its anatase and rutile forms, has a wide bandgap of approximately 3.2 eV and 3.0 eV, respectively, leading to high transmittance in the visible spectrum and strong absorption in the UV region. TiO_2 films are highly transparent to visible light, making them suitable for applications in coatings, optical devices, and transparent conductive materials. However, their high UV absorption limits their transmittance in the UV range. Modifying TiO_2 with dopants or forming nanocomposites can tailor its transmittance properties to specific applications (Chen & Mao, 2007; Khan *et al*., 2015).

Transmittance Properties of MoS_2/TiO_2 Nanocomposite

The MoS_2/TiO_2 nanocomposite combines the high visible light transmittance of MoS_2 with the UV absorption characteristics of TiO_2. This results in a material that exhibits broad-spectrum transparency while maintaining the ability to absorb UV light. The transmittance spectrum of the nanocomposite shows features from both MoS_2 and TiO_2, indicating successful integration. The composite structure can also reduce light scattering and enhance light absorption due to the synergistic effects between MoS_2 and TiO_2, making it suitable for advanced optoelectronic applications (Zhang *et al*., 2016; Wang *et al*., 2019).

Applications Based on Transmittance Properties

- **Solar cells:** The broad-spectrum transmittance of MoS_2/TiO_2 nanocomposites can enhance light absorption and improve the efficiency of solar cells (Kong *et al*., 2016).
- **Transparent conductive films:** High visible light transmittance and electrical conductivity make these nanocomposites suitable for transparent electrodes in displays and touchscreens (Wang *et al*., 2015).
- **Photocatalysis:** The UV absorption of TiO_2 combined with the visible light transparency of MoS_2 enhances photocatalytic performance under sunlight (Zhang *et al*., 2016).

Raman Spectroscopy

Principles of Raman Spectroscopy

A potent tool for studying low-frequency modes in materials, Raman spectroscopy can detect vibrations, rotations, and more. It entails detecting the inelastically dispersed light after exposing a sample to a monochromatic

light source, usually a laser. Changes in the incident light's wavelength are manifestations of the molecules' vibrational modes, and the scattered light provides information about these modes. According to Ferraro *et al*. (2003), the material's molecular structure, crystallinity, and interactions may be deduced from the Raman spectrum, which is a plot of intensity versus Raman shift.

Raman Spectra of MoS_2

Two notable peaks, E*1/2g and A1g, correspond to the in-plane and out-of-plane vibrational modes, respectively, in the Raman spectra of MoS_5. Such peaks are normally seen at around 385 cm^{-1} and 403 cm^{-1} for monolayer MoS_2, respectively. One way to measure the thickness of MoS_2 samples is by looking at the increasing spacing between these peaks as the number of layers rises. According to Lee *et al*. (2010) and Li *et al*. (2012), Raman spectroscopy is a crucial method for characterising MoS_2 since it provides information regarding strain, defects, and doping.

Raman Spectra of TiO_2

Depending on the crystalline phase of TiO_2, the Raman spectra change. At 144 cm^{-1} (E*b*), 197 cm^{-1} (E*b*), 399 cm^{-1} (B1*b*), 513 cm^{-1} (A1g or B1*b*1), and 639 cm^{-1} (E*b*), the Raman peaks are most pronounced for anatase TiO_2. A variety of vibrational modes in the TiO_2 lattice are matched by these peaks. Characteristic peaks at 143 cm^{-1} (B1*b*1/), 447 cm^{-1} (E g)$^{-1}$, and 612 cm^{-1} (A1*b*) are seen in the Raman spectra of rutile TiO_2. Ohsaka *et al*. (1978) and Zhang *et al*. (2000) employed Raman spectroscopy to explore the effects of doping and defects in TiO_2, and to discriminate between the anatase and rutile phases.

Raman Spectral Analysis of MoS_2/TiO_2 Nanocomposite

This analysis provides valuable information about the interaction between the two components. The Raman spectrum of the nanocomposite typically shows features from both MoS_2 and TiO_2, indicating successful integration. Shifts in the peak positions and changes in the intensity ratios can reveal details about strain, defects, and charge transfer processes at the interface. These insights are crucial for understanding the synergistic effects that enhance the optical and catalytic properties of the nanocomposite (Li *et al*., 2014; Zhang *et al*., 2016).

Applications Based on Raman Spectroscopy

Material Characterization: Raman spectroscopy provides detailed information about the structural and chemical properties of MoS_2/TiO_2

nanocomposites, aiding in the design and optimization of materials for specific applications (Ferraro *et al*., 2003).

Sensors: The sensitivity of Raman spectra to environmental changes can be exploited in sensor applications, including gas detection and biosensing (Yang *et al*., 2015).

Quality Control: Raman spectroscopy is a non-destructive tool for quality control in the manufacturing of nanocomposites, ensuring consistency and performance of the final products (Ferraro *et al*., 2003).

Applications of MoS_2/TiO_2 Nanocomposite

Photocatalysis

MoS_2/TiO_2 nanocomposites have shown remarkable potential in photocatalysis due to their enhanced light absorption and efficient charge separation properties. The combination of MoS_2, with its visible light absorption capabilities, and TiO_2, with its strong UV absorption and high photocatalytic activity, creates a synergistic effect that improves the overall photocatalytic efficiency. These nanocomposites can effectively degrade organic pollutants, such as dyes and pharmaceuticals, in wastewater under sunlight or visible light irradiation. Additionally, they are used in hydrogen production through water splitting, where the presence of MoS_2 reduces the recombination rate of electron-hole pairs generated in TiO_2, thereby increasing the hydrogen evolution rate (Zhang *et al*., 2016; Liu *et al*., 2014).

Photodetectors

The enhanced optical properties and charge carrier dynamics of MoS_2/TiO_2 nanocomposites make them suitable for photodetector applications. These nanocomposites exhibit high responsivity and fast response times due to efficient light absorption and charge transfer at the MoS_2-TiO_2 interface. The wide spectral sensitivity ranging from UV to visible light allows for the development of broadband photodetectors. Such devices can be used in imaging, communication, and environmental monitoring. The ability to tune the optical properties by adjusting the composition and structure of the nanocomposites further enhances their versatility in photodetector applications (Choi *et al*., 2017; Kong *et al*., 2016).

Solar Cells

MoS_2/TiO_2 nanocomposites are promising materials for enhancing the efficiency of solar cells. The integration of MoS_2 with TiO_2 can improve

light absorption and facilitate better charge separation and transport, leading to higher photocurrent generation. In dye-sensitized solar cells (DSSCs) and perovskite solar cells, MoS_2/TiO_2 composites can serve as efficient photoanodes or electron transport layers, respectively. The enhanced charge transfer properties and reduced recombination rates contribute to the overall improvement in the power conversion efficiency of these solar cells. Furthermore, the flexibility in fabricating these nanocomposites allows for the development of flexible and lightweight solar panels (Wang *et al*., 2015; Zhang *et al*., 2016).

Sensors

MoS_2/TiO_2 nanocomposites exhibit excellent sensing capabilities due to their large surface area, high conductivity, and tunable optical properties. These characteristics make them suitable for developing highly sensitive and selective sensors for detecting gases, chemicals, and biological molecules. For instance, gas sensors based on MoS_2/TiO_2 can detect low concentrations of gases such as NO_2, NH_3, and H_2S with high sensitivity and fast response times. Similarly, biosensors utilizing these nanocomposites can detect biomolecules like glucose, DNA, and proteins, making them valuable in medical diagnostics and environmental monitoring (Wang *et al*., 2015; Yang *et al*., 2015).

Conclusion

In conclusion, the optical properties of MoS_2/TiO_2 nano-composites have been extensively explored in recent years, revealing a wealth of fascinating phenomena and potential applications. The synthesis and characterization of these nanocomposites have provided valuable insights into their structure and functionality, paving the way for various advanced applications. The synergy between MoS_2/TiO_2 has been shown to yield enhanced optical absorption, emission, and nonlinear optical properties, making this nanocomposite an attractive material for various optoelectronic and photonic devices. As a result, using this composite leads to improved performance in photocatalysis, photodetectors, solar cells, and sensors, among other areas.

Despite the significant progress, there are still several missing gaps in understanding the optical properties of MoS_2/TiO_2 nano-composites, including the need for standardized characterization methods, further exploration of plasmonic properties, and investigation of optical properties under different conditions.

Future research directions should focus on addressing these gaps, as well as exploring new applications in areas such as biomedical imaging, sensing, and energy harvesting. Additionally, scaling up the synthesis and fabrication of MoS2/TiO2 nano-composites while maintaining their optical properties is crucial for practical applications.

In summary, the optical properties of MoS2/TiO2 nano-composites offer a promising platform for advancing our understanding of light-matter interactions and developing innovative optoelectronic and photonic devices. Further research in this field has the potential to unlock new technologies and applications, revolutionizing various fields such as energy, healthcare, and communication.

References

1. Chen, W., Yu, S., Zhong, Y., Fan, X., Wu, L., and Zhou, Y. (2018). Effect of electron transfer on the photocatalytic hydrogen evolution efficiency of faceted TiO_2/CdSe QDs under visible light, N. J. Chem. 42, 4811-4817

2. Dan, M., Xiang, J., Wu, F., Yu, S., Cai, Q., Ye, L., *et al*. (2019b). Rich active-edge-site MoS_2 anchored on reduction sites in metal sulfide heterostructure: toward robust visible light photocatalytic hydrogen sulphide splitting. Appl. Catal. B Environ. 256:117870

3. Gao, C., Zhang, Z., Li, X., Chen, L., Wang, Y., He, Y., *et al*. (2015). Synergistic effects in three-dimensional SnO_2/TiO_2/CdS multi-heterojunction structure for highly efficient photoelectrochemical hydrogen production. Sol. Energ. Mat. Sol. C 141, 101–107.

4. Li, X., Lv, X., Li, N., Wu, J., Zheng, Y., and Tao, X. (2019). One-step hydrothermal synthesis of high-percentage 1T-phase MoS_2 quantum dots for remarkably enhanced visible-light-driven photocatalytic H_2 evolution. Appl. Catal. B Environ. 243, 76–85.

5. Liu, L., Gu, X., Cao, Y., Yao, X., Zhang, L., Tang, C., *et al*. (2013). Crystal-plane effects on the catalytic properties of Au/TiO_2. ACS Catal. 3, 2768–2775.

6. M. Liu, L. Piao, W. Wang, Hierarchical TiO2 spheres: Facile fabrication and enhanced photocatalysis, Rare Met. 30 (2011) 153-156.

7. J.-Y. Park, C. Lee, K.-W. Jung, D. Jung, Structure Related Photocatalytic Properties of TiO2, Bull. Korean Chem. Soc., 30 (2009) 402-404.

8. Yang, Y., Ye, K., Cao, D., Gao, P., Qiu, M., Liu, L., *et al*. (2018). Efficient charge separation from F^- selective etching and doping of anatase-TiO_2 {001} for enhanced photocatalytic hydrogen production. ACS Appl. Mater. Interfaces 10, 19633-19638.

9. G. Cunningham, M. Lotya, C.S. Cucinotta, S. Sanvito, S.D. Bergin, R. Menzel, M.S.P. Shaffer, J.N. Coleman, Solvent exfoliation of transition metal dichalcogenides: Dispersibility of exfoliated nanosheets varies only weakly between compounds, ACS Nano., 6 (2012) 3468–3480.

10. I. Tacchini, E. Terrado, A. Anson, M.T. Martinez, Preparation of a TiO2-MoS2 nanoparticlebased composite by solvothermal method with enhanced photoactivity for the degradation of organic molecules in water under UV light, Micro Nano Lett., 6 (2011) 932–936.

11. Zhao, M., Xu, H., Ouyang, S., Tong, H., Chen, H., Li, Y., *et al*. (2018). Fabricating a Au@TiO_2 plasmonic system to elucidate alkali-induced enhancement of photocatalytic H_2 evolution: surface potential shift or methanol oxidation acceleration? ACS Catal. 8, 4266–4277.

12. Cravanzola, S.; Jain, S.M.; Cesano, F.; Damin, A.; Scarano, D. Development of a multifunctional TiO_2/MWCNT hybrid composite grafted on a stainless-steel grating. RSC Adv. 2015, 5, 103255-103264.

13. Shao, J.; Sheng, W.; Wang, M.; Li, S.; Chen, J.; Zhang, Y.; Cao, S. In situ synthesis of carbon-doped TiO_2 single-crystal nanorods with a remarkably photocatalytic efficiency. Appl. Catal. B 2017, 209, 311-319

14. Liu, G.; Sun, C.; Smith, S.C.; Wang, L.; Lu, G.Q.; Cheng, H.-M. Sulfur doped anatase TiO_2 single crystals with a high percentage of {0 0 1} facets. J. Colloid Interface Sci. 2010, 349, 477–483.

15. Gavrilescu, M.; Demnerová, K.; Aamand, J.; Agathos, S.; Fava, F. Emerging pollutants in the environment: Present and future challenges in biomonitoring, ecological risks and bioremediation. New Biotechnol. 2015, 32, 147-156.

Chapter - 5
Review on Improvements of Doping Strategies on TiO_2 and ZnO Nanoparticles Visible Light Photocatalytic Applications

Author

Dr. Nidhi Tiwari
Swami Vivekananda University, Barrackpore-Barasat Rd,
West Bengal, India

Chapter - 5

Review on Improvements of Doping Strategies on TiO_2 and ZnO Nanoparticles Visible Light Photocatalytic Applications

Kazi Hasibur Rahman

Abstract

Photocatalysis, leveraging light to initiate chemical reactions, holds immense promise for environmental remediation, energy conversion, and industrial processes. Titanium dioxide (TiO_2) and zinc oxide (ZnO) nanoparticles, renowned for their photocatalytic prowess, are limited by their wide band gaps, predominantly harnessing ultraviolet (UV) light. Efforts to augment their efficacy under visible light have spurred exploration into controllable doping strategies. This review comprehensively surveys doping methodologies employed in TiO_2 and ZnO nanoparticles to tailor their band gaps for advanced visible light photocatalysis. It scrutinizes doping techniques, criteria for dopant selection, synthesis methods, and characterization approaches. Moreover, it evaluates the structural, optical, and photocatalytic impacts of doping, elucidating mechanisms underlying enhanced visible light absorption and photocatalytic activity. Synthesizing a breadth of research, this review elucidates the current landscape of controllable doping in TiO_2 and ZnO nanoparticles. It delves into recent progress, encountered challenges, and future prospects, offering insights to propel research toward highly efficient visible light photocatalysts for diverse applications, including water and air purification, solar fuel generation, and sustainable energy production.

Keywords: Photodegradation, mechanism, Π-Π stacking, doping, metal oxide semiconductor

Introduction

Photocatalysis, a process that utilizes light to initiate chemical reactions, has garnered significant attention for its potential applications in environmental remediation, energy conversion, and various industrial processes. Titanium dioxide (TiO_2) and zinc oxide (ZnO) nanoparticles have

emerged as prominent photocatalysts due to their excellent photocatalytic properties, stability, and abundance. However, their wide band gaps (~3.2 eV for TiO_2 and ~3.3 eV for ZnO) limit their efficiency to harness only ultraviolet (UV) light for photocatalysis, which accounts for only a small fraction of solar radiation. The quest for enhancing the photocatalytic activity of TiO_2 and ZnO nanoparticles under visible light irradiation has led to the exploration of various strategies, among which controllable doping stands out as a promising approach. Doping involves the deliberate introduction of foreign elements into the lattice structure of the nanoparticles, which modifies their electronic properties and band structures. By judiciously selecting dopants and precisely controlling their concentrations, it is possible to tailor the band gap of TiO_2 and ZnO nanoparticles, enabling them to absorb visible light and thereby significantly improving their photocatalytic performance. Several researchers have noted that ZnO exhibits high photocatalytic activity and is more efficient at decomposing certain organic compounds even in the absence of light compared to TiO_2, which requires irradiation to be effective. However, ZnO has limitations for photocatalytic applications, such as reduced photostability due to self-oxidation and decreased photoactivity in aqueous media due to dissolution. Additionally, both TiO_2 and ZnO face photocatalytic limitations when used individually; they have wide band gaps (which restrict light absorption to ultraviolet light) and high recombination rates of photogenerated electron-hole pairs, leading to low photoactivity. It has therefore been reported that a composite of both ZnO and TiO_2 has better photocatalytic enhancement due to the formation of nanostructures with improved photochemical properties.

Metal oxide semiconductors like TiO_2 and ZnO are widely used in modern technology because of their appealing properties, such as non-toxicity, chemical stability, low cost, and high oxidation rates. Additionally, TiO_2 is especially notable for its biocompatibility and environmental friendliness, making it suitable for a variety of applications. While TiO_2 is recognized as an efficient photocatalyst under UV light, recent research has focused on exploring its photoresponse in visible light. Designing a photocatalyst for solar energy utilization is considered one of the most promising and clean methods for removing pollutants from aquatic environments. Metal oxide-mediated photocatalysis under UV and/or visible light has been widely reported for its stability, efficiency, and metal-free nature. Among these, TiO_2 is a particularly popular photocatalyst for converting solar energy, generating hydrogen through water splitting, and

degrading dyes due to its stability, high catalytic activity, low cost, and easy availability. However, TiO_2's catalytic efficiency in the broader solar spectrum is limited because of its wide band gap and high recombination rate of photoinduced electrons and holes. Various strategies, such as metal and non-metal doping, anchoring noble metals, textural design, and surface defect engineering, have been explored to enhance its photocatalytic activity and extend its absorption into the visible region. Nonetheless, the overall catalytic efficiency and absorption capacity of TiO_2 across the wide spectrum of solar energy remain inadequate and unsatisfactory. In this context, this review provides a comprehensive overview of controllable doping strategies employed in TiO_2 and ZnO nanoparticles to tune their band gaps for advanced visible light photocatalytic applications. It explores the various doping methods, dopant selection criteria, synthesis techniques, and characterization methods utilized in the field. Furthermore, it examines the structural, optical, and photocatalytic effects of doping on TiO_2 and ZnO nanoparticles, shedding light on the underlying mechanisms responsible for enhanced visible light absorption and photocatalytic activity.

By synthesizing and analyzing the wealth of research findings in this burgeoning field, this review aims to elucidate the current state-of-the-art in controllable doping of TiO_2 and ZnO nanoparticles. Additionally, it discusses recent advancements, challenges encountered, and future prospects to guide further research endeavors towards the development of highly efficient visible light photocatalysts for diverse applications, ranging from water purification and air remediation to solar fuel generation and sustainable energy production.

Doping of Photocatalysts with Nanoparticles

The process of photocatalysis involves several key steps, starting with the absorption of photons by a catalyst. This triggers the excitation of electrons, causing them to move from the valence band to the conduction band, creating electron–hole pairs. These pairs then migrate to the surface of the semiconductor catalyst, where they participate in oxidation and reduction reactions. These reactions generate highly reactive oxidizing species that interact with and decompose adsorbed impurities.

However, using metal oxide photocatalysts like titanium dioxide (TiO_2) presents a challenge due to their wide bandgap of 3.2 eV, which necessitates ultraviolet (UV) radiation for activation. Since UV radiation constitutes only about 5% of the total solar energy, whereas visible light accounts for around 45%, researchers have explored various strategies to utilize the more

abundant visible light. One promising approach is doping photocatalysts with metal and non-metal nanoparticles. This method enhances light absorption, improves charge separation and transfer efficiency, and increases photocatalytic activity.

Nanoparticle doping provides additional advantages, including precise control over particle size, shape, and distribution within the photocatalyst matrix. It also greatly increases the surface area-to-volume ratio, which offers more active sites for catalytic reactions and boosts overall catalytic activity. The effects of nanoparticle doping are evident in the reduction of the photocatalyst's band gap and the improvements in performance.

The stages involved in nanoparticle doping typically include synthesizing the nanoparticle dopants and incorporating them into the photocatalyst matrix. Transition metals, with their unfilled d-electron structures, facilitate electron transfer from the dopant's 3d orbital to the TiO_2 conduction band. This allows the photocatalyst to accommodate more photogenerated electrons and holes, effectively shifting TiO_2's response towards the visible light spectrum.

Among metal oxides used as photocatalysts, titanium dioxide (TiO_2), zinc oxide (ZnO), tin dioxide (SnO_2), and cerium dioxide (CeO_2) are preferred due to their optimal combination of electronic structure, light absorption capacity, charge transport characteristics, and durability. These properties make them highly effective for photocatalytic applications.

In addition to these widely recognized photocatalysts, other metal oxides have also demonstrated significant progress. These include:

- Barium titanate ($BaTiO_3$).
- Strontium titanate ($SrTiO_3$).
- Sodium tantalate ($NaTaO_3$).
- Barium tantalate ($BaTaO_3$).
- Sodium niobate ($NaNbO_3$).
- Hafnium dioxide (HfO_2).
- Zinc ferrite ($ZnFe_2O_4$).

These additional metal oxides exhibit excellent photocatalytic performance due to their unique structural and electronic properties, which enhance their ability to absorb light, transport charges, and participate in catalytic reactions.

Doping with Metal and Metal Oxides

Doping with metals and metal oxides is a crucial strategy in photocatalysis to enhance the performance of photocatalytic materials such as titanium dioxide (TiO_2) and Zinc Oxide (ZnO). This method involves incorporating specific metals or their oxides into the photocatalyst's structure, fundamentally altering its physical and chemical properties. These modifications typically lead to improved light absorption, better charge separation, and increased overall photocatalytic activity. Various techniques are employed to introduce these metal dopants into photocatalytic materials, including:

i) Impregnation Method:

- Involves soaking the photocatalyst in a solution containing the metal dopant precursor.
- The solvent is then evaporated, and the material is calcined to incorporate the dopant into the photocatalyst matrix.

ii) Sol-Gel Method:

- Metal precursors are mixed with a sol-gel solution, which forms a gel-like substance.
- This gel is dried and calcined to produce a doped photocatalyst with uniformly distributed dopant particles.

iii) Co-precipitation Method:

- Metal salts and photocatalyst precursors are co-precipitated from a solution.
- The resulting precipitate is filtered, dried, and calcined to obtain the doped photocatalyst.

iv) Hydrothermal Method:

- The photocatalyst and metal dopants are mixed in an aqueous solution and subjected to high temperatures and pressures in an autoclave.
- This process facilitates the incorporation of the dopants into the photocatalyst structure.

v) Chemical Vapor Deposition (CVD):

- Metal dopants are introduced in the vapor phase and deposited onto the photocatalyst surface.

- This technique allows for precise control over the dopant concentration and distribution.

vi) Ionic Exchange:

- The photocatalyst is exposed to a solution containing metal ions.
- These ions replace some of the original ions in the photocatalyst structure, resulting in a doped material.

vii) Electrochemical Methods:

- Involves using an electric current to drive the deposition of metal dopants onto the photocatalyst.
- This technique can offer fine control over the doping process.

Each of these techniques offers distinct advantages and can be chosen based on the desired properties of the doped photocatalyst and the specific application requirements.

Sol-Gel Technique

The sol-gel technique is a widely adopted approach for doping metal and metal oxide photocatalysts to enhance their photocatalytic performance. This method involves the creation of a homogeneous solution containing metal precursors, which undergoes condensation to form a gel. Subsequent drying removes the solvent, yielding metal-doped nanoparticles.

Example Procedures for Doping TiO_2:

i) Neodymium (Nd) Doping

- Neodymium (III) acetate dehydrate in isopropyl alcohol is mixed with titanium isopropoxide in alcohol.
- Acetic acid is added and the pH is adjusted to complete the hydrolysis process, resulting in transparent sols.
- After aging, the sol is washed, centrifuged, dried, and annealed to produce Nd-doped TiO_2 nanoparticles.
- These nanoparticles enhance the photocatalytic removal of dyes and pollutants under solar light.

ii) Other Rare Earth Element Doping

- Elements like Lanthanum (La), Europium (Eu), and Gadolinium (Gd) have been used to dope TiO_2, enhancing its photocatalytic performance for pollutant and dye removal.

Doping of Other Metal Oxides

i) ZnO Doping

- Rare earth elements like Eu, La, and Gd have been used to dope ZnO nanoparticles synthesized by the sol–gel method for dye degradation.
- Nickel-doped ZnO nanoparticles have demonstrated 94% dye degradation ability.
- Cerium-doped ZnO nanocomposite photocatalysts have been prepared for dye degradation and antibiotic removal.

ii) Other Nanocomposite Doping

- Eu-doped ZnO-SnO_2 nanocomposites, synthesized via the sol–gel method, exhibit enhanced dye degradation due to Z-scheme heterojunction formation.
- Bismuth-doped TiO_2 enhances CO_2 photo-reduction and selectivity towards CH_4, prepared by the sol–gel method and further improved with photo-deposited platinum.
- Iron-doped TiO_2 and co-doped manganese and boron TiO_2 show enhanced structural and photocatalytic properties for dye removal.

Silver Doping of TiO_2

Silver-doped TiO_2 nanoparticles are favored due to their:

1. Enhanced photocatalytic efficiency in visible light through the surface plasmon resonance effect.
2. Formation of a Schottky barrier at the TiO_2 interface to trap electrons, preventing electron-hole recombination.
3. Enhanced antibacterial properties.

Synthesis Techniques for Silver-Doped TiO_2

Sol-Gel Method

- Silver nitrate solution is added dropwise to a TiO_2 mixture in acetic acid, forming a gel which is then air-dried and annealed.
- For thin films, a mixture of TiO_2 and ZnO sols is aged, and silver nitrate is added before coating pretreated glass substrates and thermally treating them.

Recent Developments

Cerium-Doped ZnO/TiO_2 Nanospheres

- ZnO and TiO_2 sols are mixed, followed by adding cerium precursor solution and stirring for 3 hours.
- The doped solution is treated with NaOH, centrifuged, washed, dried, ground, and sintered at 500 °C for 3 hours, yielding the final photocatalyst effective for dye and levofloxacin degradation under visible light.

These diverse doping techniques and materials illustrate the broad applicability and effectiveness of the sol-gel method in enhancing the photocatalytic properties of various metal oxide photocatalysts.

Plasma-Assisted Laser Ablation

Plasma-Assisted Laser Ablation (PLAL) technology offers an innovative approach to producing metal-doped nanoparticles. This technique involves the laser-induced ablation of a target material submerged in a liquid medium, allowing for precise control over dopant incorporation and overcoming challenges related to the poor solubility of dopants in the photocatalyst matrix.

Nd-Doped ZnO Nanoparticles

- The PLAL technique has been used to generate neodymium (Nd)-doped ZnO nanoparticles, allowing for precise control over dopant incorporation.

Double Pulse Laser Ablation Technique

- A zinc plate serves as the target, which is submerged in a neodymium salt solution.
- The target is irradiated with a pulsed laser for 10 nanoseconds, creating plasma near the target and resulting in the formation of Nd-doped colloidal nanoparticles.
- These nanoparticles can then be further subjected to laser modifications for enhanced properties.

Europium Doping in Gd_2O_3

- The doping efficiency of the solvent during laser ablation of Gd_2O_3 with Europium was evaluated.
- It was found that the doping concentration is proportional to the initial concentration of the dopant in the aqueous solution, spanning two orders of magnitude.

- This suggests that the laser ablation doping mechanism enables controlled and efficient incorporation of dopants.

Mechanism and Advantages of PLAL

Laser-Induced Ablation

- A pulsed laser irradiates the target material, causing rapid heating and vaporization of the target surface.
- The interaction between the laser and the target material generates a plasma, which consists of highly energetic ions, electrons, and neutral atoms.
- This plasma subsequently cools and condenses to form nanoparticles in the surrounding liquid medium.

Enhanced Dopant Incorporation

- The plasma created during the laser ablation process facilitates the incorporation of dopants into the nanoparticle matrix.
- PLAL provides a high degree of control over the size, shape, and composition of the nanoparticles, leading to uniform and well-dispersed dopant distribution.

Versatility and Precision

- The technique can be applied to various materials and dopants, making it versatile for different photocatalytic applications.
- The ability to fine-tune laser parameters, such as pulse duration, energy, and wavelength, allows for precise control over the nanoparticle synthesis process.

By leveraging the advantages of PLAL technology, researchers can overcome the limitations of traditional doping methods, achieving higher photocatalytic activity and enhanced material properties. This makes PLAL a promising approach for developing advanced photocatalysts for environmental and energy applications.

Chemical Precipitation and Co-Precipitation

The synthesis of metal-doped nanoparticles using various methods can significantly enhance their photocatalytic properties. Here are detailed procedures and outcomes of different synthesis methods:

Tin-Doped Zinc Nanoparticles (Chemical Precipitation Method)

Procedure

- Potassium hydroxide (KOH) solution is added dropwise to an aqueous solution containing tin chloride dihydrate ($SnCl_2 \cdot 2H_2O$) and zinc acetate dihydrate ($Zn(O_2CCH_3)_2 \cdot 2H_2O$).
- The white precipitate formed is purified, air-dried at 100 °C for 6 hours, and then annealed at 300 °C for 3 hours in a muffle furnace.

Outcome

- The final product is tin-doped zinc nanoparticles, effectively synthesized through this chemical precipitation method.

Iron-Doped ZnO Nanoparticles (Co-Precipitation Method)

Procedure

- Zinc acetate dihydrate (precursor of ZnO nanoparticles) and ferric chloride ($FeCl_3$, precursor of iron) are dissolved in water.
- NaOH solution is added to maintain an alkaline pH.
- The mixture is heated at 85 °C for 2 hours, then cooled and kept for 24 hours.
- The resulting precipitate is washed, dried, and annealed at 400 °C.

Outcome

- The final product is iron-doped ZnO nanoparticles, demonstrating effective doping and nanoparticle formation.

Green Synthesis of ZnO/WO_3 Nanocomposites

Application

- Recent studies have explored green synthesis methods for creating ZnO/WO_3 nanocomposites.
- These nanocomposites are utilized for the photocatalytic removal of organic pollutants, highlighting the environmentally friendly approach and effectiveness of green synthesis methods.

Nickel-Doped and Bimetal-Doped Co_3O_4 Photocatalysts

Comparative Study

- A study compared the photocatalytic activity of nickel-doped Co_3O_4 with bimetal-doped Co_3O_4 photocatalysts.

- Two additional dopant metals used were copper (Cu) and cadmium (Cd).

Results

- The cadmium-nickel bi-doped Co_3O_4 photocatalyst exhibited the highest photocatalytic activity, achieving a dye degradation efficiency of 93% under visible light.

Recent Advancement in TiO_2 and ZnO Photo Catalyst

Recently, combining two or more techniques has been used to create photocatalysts with improved properties, such as optical characteristics, photocatalytic efficiency, UV-induced wettability, and self-cleaning effects. For instance, a recent study employed a combination of sol–gel and spin coating methods to dope copper into zinc oxide thin films. Zinc and copper precursor solutions were dissolved in a solvent-stabilizer mixture and stirred at 60 °C. The resulting coating sol was kept in the dark for a day and then spin-coated onto a glass substrate at 2000 rpm for 30 seconds. After each spin coating, the film was dried at 180 °C, and this process was repeated several times. The final product was annealed at 500 °C for 2 hours, resulting in a copper-doped zinc oxide film with enhanced photocatalytic, super-hydrophilic, and self-cleaning properties.

Additionally, copper-doped nickel oxide nanoparticles with a new morphology and modified band gap were synthesized using a combination of co-precipitation and calcination. The calcination temperatures influenced the morphologies and surface areas of the doped photocatalyst. In another study, tin-doped TiO_2 nanoparticles were synthesized via a sol-gel route followed by calcination at temperatures ranging from 450-750 °C. These tin-doped TiO_2 formulations were screen printed and annealed at 500 °C. A dispersion of the nanoparticles in 2-propanol, α-terpeniol, and ethyl cellulose was prepared, additives were incorporated, and the mixture was homogenized to produce a paste, which was screen printed onto a glass slide using a hard square-edge polyurethane squeegee and 400 mesh count screens.

A green synthesis method, involving a microwave-assisted combustion technique with Tamarindus indica seed extract as fuel, was used to synthesize Ni-doped magnesium ferrite nanoparticles with a spinel cubic structure for use as visible-range photocatalysts for dye degradation. The sol-gel auto-combustion method has also been employed to synthesize metal-doped nanocubic spinel ferrite-based photocatalysts for wastewater treatment.

Significant enhancement of the photocatalytic activity of TiO_2 for hydrogen production has been achieved using two-dimensional transition metal-based carbonitrides, known as MXenes, as cocatalysts. MXenes offer unique advantages, including a layered structure, excellent conductivity, extensive exposure of metallic sites, and tunable electronic structures. Electrostatic self-assembly and photoreduction processes were used to prepare $Ag/Ti_3C_2/TiO_2$ nanocomposites for photocatalytic hydrogen production.

The solar-driven photocatalytic reduction of CO_2 to CH_4 and CO is an emerging strategy that addresses both energy challenges and environmental concerns. Metal-organic frameworks (MOFs) have shown promise as photocatalytic materials, with their organic ligands serving as light-harvesting centers that activate metal cluster nodes. However, MOFs face limitations, such as poor charge separation, low conductivity, and inefficient charge migration. To overcome these drawbacks, a recent study synthesized a durable hybrid cobalt-based MOF/Cu_2O composite with a p-n heterojunction, enhancing the efficiency of solar-driven CO_2 photoreduction. The composite was created by mixing an ultrasonicated aqueous solution of MOF with $CuCl_2 \cdot 2H_2O$ and NaOH solutions, followed by a dropwise addition of ascorbic acid solution. The resulting suspension was centrifuged and vacuum-dried to yield a fine composite powder.

In another study, a facile hydrothermal method was used to fabricate an azobenzene tetracarboxylic acid-based MOF, effectively reducing CO_2 to CH_4 with high CH_4 selectivity. Additionally, the solvothermal method was used to incorporate a rhodamine dye molecule into a zirconium-based MOF framework, creating a dye-sensitized photocatalyst for CO_2 reduction. This process involved reacting the dye and MOF in water at 120 °C for 24 hours. After cooling, the precipitates were centrifuged, thoroughly washed to remove excess dye, and vacuum-dried.

Constructing a heterojunction enhances carrier mobility and improves photocatalytic performance. However, interface defects and poor energy levels can cause interface recombination, reducing photocatalytic efficiency. This issue has been addressed by adjusting the band alignment in the photocatalyst. For example, the cliff-like conduction band offset (CBO) in $CuSbS_2$ (CAS)/ZnO was modified by coupling with CdS to form a spike-like CBO, reducing interface recombination and increasing photocatalytic efficiency. The CAS-ZnO-CdS heterojunction, prepared by the microwave-assisted method, achieved a hydrogen evolution of 140.45 μmol/g after 4

hours of illumination. A combination of solvothermal and electrospinning technology was used to prepare $CuBi_2O_4$-Bi_2WO_6 nanofibers with a Z-scheme heterojunction, achieving a 90% degradation efficiency of tetracycline hydrochloride.

Single-atom catalysts perform exceptionally well due to uniform adsorption of reactants/intermediates on each active site, avoiding multiple adsorptions. These catalysts are highly selective for reactions such as hydrogenation, electrocatalysis, and oxidation, and exhibit high activity. Nitrogen-doped graphene (NG) materials, with nitrogen acting as a Lewis base, bind strongly to Lewis's acid single-atom metal centers, providing a stable, coordinated environment for the single metal atom. A recent study used a precursor dilution strategy to prepare a copper/nickel dispersed poly(tetraphenyl porphyrin) through Friedel Crafts alkylation, which was deposited on modified TiO_2 microspheres. The atomically dispersed Cu-N_4 and Ni-N_4 complexes with NG were subsequently synthesized via calcination at 800 °C. This bimetallic single-atom catalyst achieved 100% desulfurization of dibenzothiophene, with a total metal loading of 0.1 wt% for both metals.

$CuInS_2$, a narrow band gap semiconductor (~1.5 eV), has been used in photocatalytic hydrogen evolution, pollutant degradation, and CO_2 reduction due to its strong response under visible light and excellent stability. A combination of hydrothermal and calcination methods was used to fabricate a boron-doped TiO_2/$CuInS_2$ Z-scheme heterojunction, yielding 21.39 μmol/g/h of CO and 4.83 μmol/g/h of CH_4 during photocatalytic CO_2 reduction, with no significant reduction in yield after three cycles. The gas yields were 10 and 13 times higher than those of standalone TiO_2 and boron-doped TiO_2, respectively. The oxygen-rich species and Ti^{3+} introduced by boron doping acted as electron traps, preventing recombination of photogenerated carriers. The heterojunction hastened carrier separation, retained electrons and holes, and improved visible light absorption.

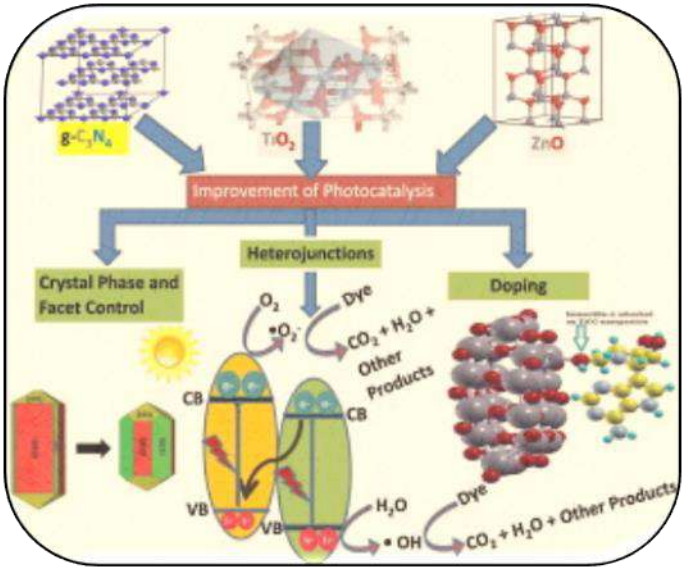

Fig 1: Schematic diagram of recent improvements of TiO_2 and ZnO and metal oxide photocatalyst

Band Arrangement and Mechanism of Photocatalytic Degradation

To delve into the mechanism of enhanced charge carrier transport and support in Zno-TiO_2 (ZT2) hybrids, UPS spectra were scrutinized using Helium I (He I) excitation energy (hν = 21.2 eV), alongside C-ZnO for comparison, as depicted in Fig. 10(a). The alterations in the UPS spectra of C-ZnO and ZT2 hybrid were elucidated by analyzing the secondary electron energy cutoff (Ec) and valence band maximum (VBM). Ec and VBM were determined by linear extrapolation to the binding energy cutoff and identifying the intersection point with the UPS spectra baseline. The Ec values were measured as 17.48 eV for C-ZnO and 17.35 eV for ZT2 hybrid, while the VBM values were found to be -3.18 eV for C-ZnO and -3.34 eV for ZT2 hybrid. The upshift of Ec in the ZT2 hybrid compared to C-ZnO indicates architectural changes resulting from TiO2 incorporation.

Using the Ec and VBM values, the energy of the valence band (EV) and conduction band (EC) of C–ZnO and ZT2 was calculated. For C-ZnO, with a band gap (Eg) of 3.09 eV, EV and EC were deduced to be -6.82 eV and -3.73 eV, respectively. Compared to the bare ZnO, there was an upward shift in the energy bands in C-ZnO, indicating n-type C doping in the ZnO lattice. For the ZT2 hybrid, using an Eg of 3.04 eV, calculated EV and EC were -7.19 eV and -4.15 eV, respectively. The energy levels of ZT2 hybrids

slightly shifted compared to C-ZnO, suggesting a strong interaction via heterojunction formation with TiO_2.

The band alignment via C-doping and suitable heterojunction formation facilitated charge carrier separation and transport in ZT2, resulting in enhanced and prolonged photoactivity. The successful separation and migration of charge carriers in ZT2 were schematically represented in figure 2. Before contact, ZnO and TiO_2 exhibited matched energy levels suitable for undergoing redox reactions. However, upon contact and UV irradiation, an energy gradient was developed at the interface of C-ZnO and TiO_2. The uplift of bands in C-ZnO and the band positions of TiO_2 led to the formation of a type II staggered heterojunction. Upon irradiation after contact, C-ZnO and TiO_2 were aligned such that excited electrons from C-ZnO migrated to the lowest conduction band position of TiO_2, while holes had barrier-free transport from the valence band of TiO2 to the valence band of C-ZnO. This process isolated active electrons and holes, reducing electron-hole pair recombination and increasing their lifespan. Due to the favorable band alignment of ZT2 with the redox potential of O_2/O_2^- and $H_2O/OH.$, subsequent redox reactions occurred on the ZT2 surface, leading to mineralization. Scavenging experiments revealed that superoxides were the primary responsible species for photoactivity, confirming an accumulation of excited electrons at the interface. Since the entire bands of ZnO were uplifted by C-doping, it exhibited stronger reducing power compared to bare ZnO, resulting in the reduction of oxygen to superoxide to a greater extent.

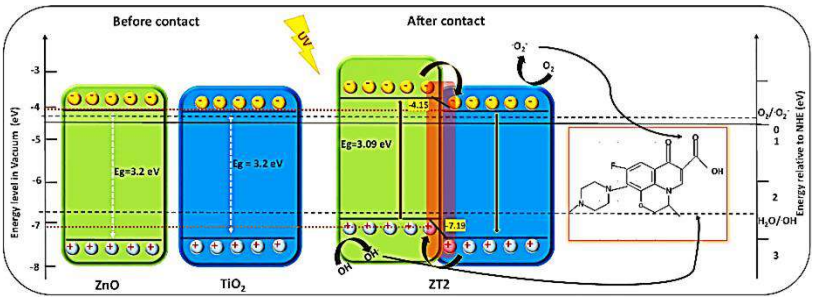

Fig 2: Mechanism of photodegradation of Zno-TiO_2 photocatalysts

Possible Photodegradation Pathways

In a photodegradation pathway that considers molecular structures, the degradation process can be elucidated in a stepwise manner, focusing on the interactions between the photocatalyst and the target molecules. Here's a possible pathway:

Organic pollutants such as dyes or contaminants are adsorbed onto the surface of the ZnO-TiO_2 photocatalyst due to the presence of active sites and surface defects. The adsorption occurs via electrostatic interactions, hydrogen bonding, or π-π stacking, depending on the nature of the pollutant and the surface characteristics of the catalyst. Upon exposure to light, ZnO and TiO_2 absorb photons, leading to the excitation of electrons from the valence band to the conduction band. This generates electron-hole pairs within the catalyst structure. The photogenerated electrons and holes migrate to the surface of the photocatalyst due to the internal electric field and potential gradient within the material. At the surface, the photogenerated holes (h+) react with adsorbed water or hydroxide ions (OH-) to produce hydroxyl radicals (•OH), which are potent oxidizing agents. These radicals attack the organic molecules adsorbed on the surface, initiating degradation pathways such as hydroxylation, dehydrogenation, or cleavage of chemical bonds. As the organic molecules undergo oxidative degradation, various intermediate products are formed, which may be more or less toxic than the parent compound, depending on the specific degradation pathways. The intermediates continue to react with reactive species such as hydroxyl radicals, leading to further degradation and eventual mineralization into simpler, less harmful compounds such as carbon dioxide (CO_2), water (H_2O), and inorganic ions. Throughout the degradation process, the ZnO-TiO_2 photocatalyst may undergo surface reorganization or regeneration, ensuring the continuous availability of active sites for adsorption and degradation of pollutants. By considering the molecular structure of both the pollutant molecules and the photocatalyst, this pathway highlights the key chemical reactions and interactions involved in the photodegradation process, from adsorption to mineralization, while emphasizing the role of ZnO-TiO_2 as a photoactive material in driving these transformations.

Role of π-π Stacking for Enhanced Photodegradation of Zno-TiO_2 Photocatalysts

The mechanism of π-π stacking in ZnO-TiO_2 photocatalysts involves the interaction between the aromatic rings of organic molecules and the surface of the photocatalyst. Here's a breakdown of the mechanism:

i. **Presence of Aromatic Rings:** Many organic pollutants, such as dyes or aromatic compounds, contain conjugated π-electron systems, which consist of alternating single and double bonds. These π-electron systems create regions of electron density above and below the plane of the aromatic ring.

ii. **Surface Properties of ZnO-TiO_2:** The ZnO and TiO_2 nanoparticles in the photocatalyst have surfaces with a high density of oxygen atoms, which can interact with electron-rich aromatic rings through electrostatic interactions and van der Waals forces.

iii. **Alignment of Aromatic Rings:** When organic pollutants adsorb onto the surface of the ZnO-TiO_2 photocatalyst, the aromatic rings of the molecules can align parallel to the flat surfaces of the nanoparticles. This alignment maximizes the π-π interactions between the π-electron clouds of the aromatic rings and the delocalized electron clouds of the photocatalyst surface.

iv. **Stabilization of Adsorbed Molecules:** The π-π stacking interaction results in the stabilization of the adsorbed molecules on the photocatalyst surface. This stabilization can enhance the adsorption capacity of the photocatalyst and promote the degradation of organic pollutants by facilitating electron transfer processes.

v. **Contribution to Photodegradation:** The π-π stacking interaction between organic pollutants and the ZnO-TiO_2 photocatalyst can facilitate the transfer of electrons from the excited state of the photocatalyst to the adsorbed molecules. This electron transfer process initiates redox reactions that lead to the degradation of the pollutants into simpler, less harmful compounds.

Overall, π-π stacking plays a crucial role in the adsorption and photodegradation of organic pollutants by ZnO-TiO_2 photocatalysts by providing a mechanism for strong and selective interactions between aromatic molecules and the photocatalyst surface, thereby enhancing the efficiency of pollutant removal. A schematic proposed model diagram is observed in figure 3.

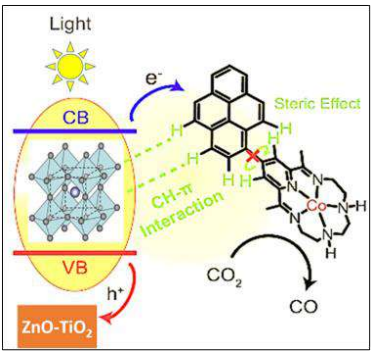

Fig 3: Role of π-π stacking for photodegradation

Conclusion

In conclusion, achieving efficient photocatalytic materials depends on ensuring stability and durability during practical operation. While certain materials like metal sulphides and chalcogenides exhibit high initial photocatalytic activity, they are susceptible to photocorrosion under irradiation. In contrast, titanium dioxide (TiO_2) stands out as a highly stable photocatalyst with significant catalytic capabilities. Among TiO_2 phases, the anatase phase is the most active but requires short-wavelength light, typically around 350 nm, to initiate catalytic activity. Researchers have actively explored doping with both metals and non-metals to utilize TiO_2's potential in the visible region and reduce carrier recombination rates.

However, it's important to note that doped photocatalysts have limitations. Metal doping, for example, can lead to unstable materials prone to corrosion, with the metal dopant leaching over time, resulting in decreased photocatalytic activity. Metal-organic frameworks have potential as adsorption and photocatalyst candidates for degrading organic contaminants but suffer from issues like metal ions and ligands leaching into the solution. To improve structural stability, photocatalytic, and adsorptive abilities during real-time operations, doping with graphene oxide, silver, and activated carbon for preparing MOF-based composites has been conducted. However, most studies report the performance of these composites in synthetic wastewater, and rigorous studies are needed to test their stability in industrial wastewater to determine their suitability for real-time effluent treatment.

While many studies have reported enhanced photocatalytic activities of doped catalysts, further research is needed on the physicochemical stability and reusability of doped photocatalysts when handling large volumes of industrial effluents. Rigorous studies should explore the combination of doped photocatalyst-based pollutant removal with biological means and electrodynamic removal. Fundamental quantification of doped photocatalysts' reactivity, toxicity, and fate must be reported.

In the realm of adsorbents, doping carbon-based materials with nitrogen holds promise for enhancing adsorption capabilities and improving CO_2/N_2 selectivity. Nitrogen doping facilitates CO_2 uptake by enhancing surface area and promoting interactions between acidic CO_2 molecules and basic nitrogen functionalities. Co-doping with nitrogen and oxygen has yielded adsorbents with the highest CO_2 adsorption capacity, while the highest CO_2/N_2 selectivity was achieved when the doped adsorbent featured abundant basic

nitrogen functional groups. Therefore, synthesizing carbon-based adsorbents with optimized ultramicroporous surface areas and essential basic heteroatoms is crucial for achieving high CO_2 uptake values and selectivity. Overall adsorption efficiency depends on various mass transfer resistances encountered during operation, and an in-depth analysis of the effect of doping on mass transfer resistance needs to be conducted. For example, in fixed-bed adsorbents, modelling transport equations depends on mass transfer mechanisms from the adsorbate to the adsorbent phase.

Looking ahead, further advancements in photocatalysts and adsorbents should focus on addressing these challenges and optimizing doping strategies to meet the growing demand for efficient and sustainable environmental remediation technologies. Extensive research in large-scale systems, industrial reactors, and real-world applications will be instrumental in realizing the full potential of doped materials in tackling environmental pollution and promoting a cleaner, healthier future.

References

1. Lin, C.; Song, Y.; Cao, L.; Chen, S. Effective Photocatalysis of Functional Nanocomposites Based on Carbon and TiO_2 Nanoparticles Nanoscale 2013, 5, 4986-4992.
2. Jagadale, T.C.; Takale, S.P.; Sonawane, R.S.; Joshi, H.M.; Patil, S.I.; Kale, B.B.; Ogale, S.B. N-Doped TiO_2 Nanoparticle Based Visible Light Photocatalyst by Modified Peroxide Sol-Gel Method. J Phys. Chem. C 2008, 112, 14595–14602.
3. Guan, B.; Yu, J.; Guo, S.; Yu, S.; Han, S. Porous Nickel Doped Titanium Dioxide Nanoparticles with Improved Visible Light Photocatalytic Activity. Nanoscale Adv. 2020, 2, 1352-1357.
4. Thambiliyagodage, C.; Mirihana, S. Photocatalytic Activity of Fe and Cu Co-Doped TiO_2 Nanoparticles under Visible Light. J. Solgel Sci. Technol. 2021, 99, 109–121.
5. Negi, C.; Kandwal, P.; Rawat, J.; Sharma, M.; Sharma, H.; Dalapati, G.; Dwivedi, C. Carbon-Doped Titanium Dioxide Nanoparticles for Visible Light Driven Photocatalytic Activity. Appl. Surf. Sci. 2021, 554, 149553.
6. Sun, D.; Wang, K.; Xu, Z.; Li, R. Synthesis and Photocatalytic Activity of Sulfate Modified Nd-Doped TiO_2 under Visible Light Irradiation. J. Rare Earths 2015, 33, 491-497.

7. Thomas, J.; Radhika, S.; Yoon, M. Nd3+-Doped TiO_2 Nanoparticles Incorporated with Heteropoly Phosphotungstic Acid: A Novel Solar Photocatalyst for Degradation of 4-Chlorophenol in Water. J. Mol. Catal. A Chem. 2015, 411, 146–156.

8. Dhandapani, C.; Narayanasamy, R.; Karthick, S.N.; Hemalatha, K.V.; Selvam, S.; Hemalatha, P.; Kumar, M.S.; Kirupha, S.D.; Kim, H.J. Drastic Photocatalytic Degradation of Methylene Blue Dye by Neodymium Doped Zirconium Oxide as Photocatalyst under Visible Light Irradiation. Optik 2016, 127, 10288–10296.

9. Padmaja, B.; Dhanapandian, S.; Ashokkumar, K. Hydrothermally Derived Mg Doped Tin Oxide Nanostructures for Photocatalytic and Supercapacitor Applications. Mater. Sci. Eng. B 2023, 297, 116699.

10. Tarasenka, N.; Kornev, V.; Ramanenka, A.; Li, R.; Tarasenko, N. Photoluminescent Neodymium-Doped ZnO Nanocrystals Prepared by Laser Ablation in Solution for NIR-II Fluorescence Bioimaging. Heliyon 2022, 8, e09554.

11. Vishnu, G.; Singh, S.; Kaul, N.; Ramamurthy, P.C.; Naik, T.S.S.K.; Viswanath, R.; Kumar, V.; Bhojya Naik, H.S.; Prathap, A.; Anil Kumara, H.A.; *et al*. Green Synthesis of Nickel-Doped Magnesium Ferrite Nanoparticles via Combustion for Facile Microwave-Assisted Optical and Photocatalytic Applications. *Environ. Res.* 2023, *235*, 116598.

12. Guan, J.; Li, D.; Feng, J.; Xu, P.; Li, Z.; Ge, S.; Chen, H.; Zhang, K. Enhanced Photocatalytic Ammonia Oxidation Activity and Nitrogen Selectivity over Ag/AgCl/N-TiO_2 Photocatalyst. J Environ. Sci. 2024, 138, 395–405.

13. Al-Hajri, W.; De Luna, Y.; Bensalah, N. Review on Recent Applications of Nitrogen-Doped Carbon Materials in CO_2 Capture and Energy Conversion and Storage. Energy Technol. 2022, 10, 2200498.

14. Cheng, Z.-L.; Sun, W. Preparation of Nano-CuO-Loaded Halloysite Nanotubes with High Catalytic Activity for Selective Oxidation of Cyclohexene. Chin. Chem. Lett. 2016, 27, 81–84.

15. Chen, Z.; Li, Y.; Guo, M.; Xu, F.; Wang, P.; Du, Y.; Na, P. One-Pot Synthesis of Mn-Doped TiO_2 Grown on Graphene and the Mechanism for Removal of Cr(VI) and Cr(III). J. Hazard. Mater. 2016, 310, 188-198.

16. Dadfarnia, S.; Haji Shabani, A.M.; Moradi, S.E.; Emami, S. Methyl Red Removal from Water by Iron Based Metal-Organic Frameworks Loaded onto Iron Oxide Nanoparticle Adsorbent. Appl. Surf. Sci. 2015, 330, 85-93.
17. Barua, A.; Mehra, P.; Paul, A. Role of Nitrogen Doping and Pore Volume for CO_2 Capture in Metal-Organic Framework Derived Ultramicroporous Carbon Material. Results Chem. 2023, 5, 100807.

Chapter - 6
Recent Progress in Metal Oxides for Biosensor Application

Author

Kazi Hasibur Rahman
Swami Vivekananda University, Barrackpore-Barasat Rd, Sewli Telinipara, Malir Math, Bara Kanthalia, West Bengal, India

Chapter - 6

Recent Progress in Metal Oxides for Biosensor Application

Kazi Hasibur Rahman

Abstract

The properties such as selectivity, a low limit of detection and high sensitivity of biosensors, reaching nano or pico biomolecules molar concentrations, are very crucial to the medicative industry for treatment of metabolic and physiological parameters. Biosensors are practical, acceptable, and precise analyzers that inspect chemical and biological parameters and disciple the outputs into substantial data between an active biological molecule and a acceptance element immobilized on the surface of the signal transducer by a physicochemical detector which are used clinically and nonclinically, textile industry, food safety, environmental controlling, etc. Enormous attention has been drawn by nanostructured metal oxides for applications in biosensors owing to various characteristics like biocompatibility, easy fabrication and governable size/shape, optical and catalytic properties, electron-transfer kinetics electrical properties, and strong adsorption ability chemical stability, for bio sensing because of its great catalytic property which has high surface ratio of atoms with free valence electrons of the total amount atoms in the cluster. This may also advantage to electrochemical reversibility for redox reactions. The presence of oxygenated derivatives transforms of specialized structures of metal oxides are highly hydrophilic, facilitating chemical functionalization and are easily composited with various kinds of inorganic nanoparticles, graphene, reduced graphene oxides, semiconductors, quantum dots to create a diverse range of metal oxide-based nanocomposites. The uncommon physical and chemical properties of nanomaterials have brick the path for advanced bio sensing devices. This book article covers a very large area of metal oxide based electrochemical biosensors mainly to detect glucose, hydrogen peroxide (H_2O_2), cholesterol, genes, enzymes, nucleic acids, uric acid (UA), cancer biomarkers, pathogenic microorganisms, and pesticides. The selectivity and sensitivity of metal oxide-based semiconductors are also examined in terms of presence of analytes in various biological system, which can be successfully integrated in biosensor technology.

Keywords: Biological system, selectivity, metal oxides, biosensor technology, physical properties

Introduction

There are advanced high surface to volume ratio of nanostructured materials, improved physical, mechanical properties and their controllable electronic properties are favourable towards usage in biosensors application Compared to bulk materials the property varies a lot in nanomaterials [1-3]. Nanomaterials consist of several atoms with tiny particles which has higher surface area than atoms with fewer particles. Thus size is inversely proportional to surface area and surface to volume ratio. By adopting smart engineering techniques, the functionalities and characteristics of nanomaterials can be developed to allow highly selective binding properties for analysis of biomolecules which are in nanoscale range. Moreover, the distinct molecular identifications and correlations at the nano-regime level in amalgamation with nanoscale parameters can be more developed high sensitive biosensors. Nano like textured of surfaces can coupled with metal oxides which advantages to the production of nano-hybrid materials, which are normal to install new promenade for both therapeutics and diagnosis purpose because of its improved optical and electronic properties. Over the last decade, large number of nanocomposites such as 1D, 2D, and 3D have dispalyed extraordinary catalytic and sensing properties [4]. In the area of catalytic and sensors, nano-dimensions have been applied contentiously due to their alluring achievement in catalysis and structural stability comparable with bulk materials. There are several types of synthesis process for 1D nanostructures such as chemical bath deposition electrochemical deposition, electrospinning, and chemical/physical vapour deposition formation. 2D nanostructures such as nanowalls, nanofilms, nanocoatings, etc. have large surface to volume ratio and restricted thickness, which is favourable for the catalytic, sensing, etc. applications [5-7]. 3D nanostructures have variation in the morphology rather than other dimension nanostructures, and the morphology such as nanorods, nanocubes, nanospheres, etc. [8-10] exists. However, 3D nanostructures are not bounded to the nanoscale, just as like bulk materials, they still have the consequence of formation of nanostructures (high surface-to-volume ratio, quantum confinement effect) [11]. The usage of metal oxides and their nanocomposite has become dominant, owed to the deficient access towards the advancement of the behaviour of a single atom oxide. The act of the confinement of enzymes through metal oxide surface is essential as metal oxide nanocomposites performed a biocompatible environment for the enzymes to exercise on the

electrode and enhance the sensitivity and selectivity of the sensing electrode via enabling electron-transfer kinetics between electrode and enzyme.

Nanostructured metal oxides have gained enormous consideration for applications in biosensing matured to considerable properties such as easy synthesis process and governable size/shape, biocompatibility, catalytic, and chemical stability, optical properties, electron-transfer kinetics and strong adsorption ability. In addition, computational modelling and experimental reports suggest that doping concentration can significantly influence the bio sensitivity. Thus, nanohybrids can be treated as the encouraging new multifunctional materials for fabrications of advanced device. Among various nanomaterials, metal oxide nanomaterials have garnered attention due to their suitability for immobilizing biomolecules. Their crystal lattice behaviour allows for modifications in cell parameters and electrochemical properties, owing to quantum confinement effects and the ability to control bandgap energy by altering surface properties. These modifications impact conductivity and chemical reactivity, enhancing their potential for use as biosensing elements and distinguishing metal oxide nanomaterials from their bulk counterparts [12, 13]. Sensors and Biosensors have improved the lifestyle of human beings now days in many aspects such as health care, food safety, and environmental monitoring. Biosensors are well known for its high selectivity devices which is basically consist of two parts: biological description elements such as antibodies, enzymes, cells and DNA, which corresponds selectively in a complex medium with the substance of interest (analyte), and a transducer, which transform the biochemical feedback into a certain signal. Biosensors can be tested into variety of samples which includes body fluids, food samples, and cell cultures. For gaining a reliable and sensitive inspection system, the surface of the sensor must allow restricted movement of bio recognition elements, also avoiding nonspecific binding that may hamper with activity of the biomolecule. In parts of the world where public health care isn't readily available, researchers hope to welcome rapid tests for people satying in remote areas to examine for diseases like influenza, hepatitis C and HIV. Now a-days this biosensor technologies has implanted in smart phone, cameras and Bluetooth signalling. These improvements in this technology turn health related tests more portable and affordable than lab-based apparatus. Biosensors is also used for continuous monitoring our health condition. Blood-oxygen monitors detect changes in the level of oxygen in the bloodstream which are installed in almost every hospitals and homes. A sudden decrease in oxygen levels can lead to brain injury and necessitates immediate medical intervention.

Blood oxygen monitors are ideal for individuals with lung and heart conditions, those undergoing anesthesia, or those receiving care in intensive, neonatal, or emergency settings. Additionally, other biosensors can be used for continuous monitoring of blood pressure, blood sugar levels (for diabetes management), and heart rate. Currently, U.S. scientists are developing flexible, stretchable, and sensitive 3D-printed sensors capable of detecting human body movements. These sensors can be precisely applied to the skin to monitor body signals such as pulse and can also detect environmental chemicals, serving as recycling and hazardous material warnings. According to a U.S. biomedical engineer from a medical company, advancements have been made in miniature biosensors that can be implanted inside the body. These sensors continuously monitor various factors, eliminating the need for hospital visits for body chemistry analysis. With this technology, body chemical information can be tracked around the clock from any location. Given the aging population and the challenges posed by chronic lifestyle diseases, biomedical diagnosis and biosensors are becoming increasingly important. New molecular analyses are expected to significantly impact our healthcare system. One key advantage of biomarker screening is that it enables precise and personalized medicine and early diagnosis, allowing for more relevant analyses based on molecular knowledge rather than solely on external clinical symptoms.

Biosensors Consist of Two Main Components: A physical transducer and a biorecognition layer. The biorecognition layer interacts specifically with the analytes (e.g., low molecular compounds, (bio)proteins, macromolecules, cells, viruses), generating a biochemical signal. The transducer then converts this signal into a measurable output, correlating it with the analyte's concentration over time. The bioselective layer of the biosensors only interacts with the target analyte. Biosensors can be classified based on the type of biorecognition element used (e.g., enzymes, antibodies, cells, nucleic acids) or the nature of the transducer signal (e.g., electrochemical, optical, electrical, mass-sensitive, magnetic). A classic biosensor device and its components are presented in the figure 1:

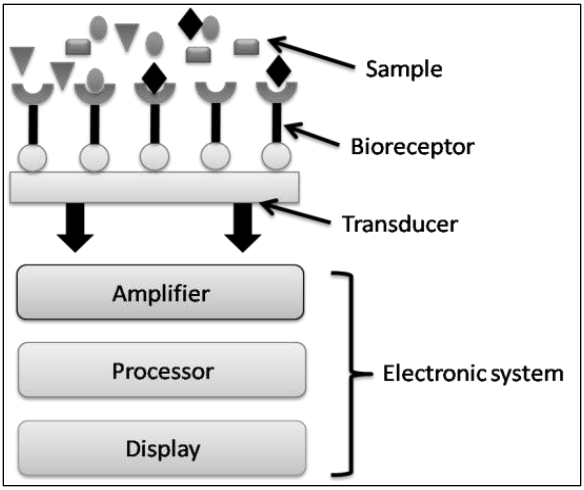

Fig 1: A classic schematic diagram of biosensor device and its processing components

In this book article, various synthesis process and characterization techniques has been discussed of different nanostructured which is used in advanced biosensors applications. The improvement in the fabrication of bio sensing device and the challenges taken for their progress in healthcare, environmental monitoring with likely novel functions for the assessment, diagnosis, prediction, and invention of human diseases.

Synthesis and Characterisation of Nanostructures

Electrodeposition

Nanostructured materials often display extraordinary properties comparable with the bulk materials as considered earlier. Electrodeposition is one kind of unique technique by which an array of materials can be handled including metals, ceramics and polymers. Crucial approach has been taken for unique capabilities for the improvement of nanomaterials and nanostructures for applications in biosensors. Currently, novel ED technologies have subordinate into a vital area of nanotechnology. Using this method, it is convincing to get pore-free NC metal specimens in a single step process [14, 15]. To obtain advanced properties of any nanocoating, it is crucial to improve the bath (electrolyte) composition as well as the deposition parameters in addition to choosing certain anode and cathode materials with a appropriate coating. Current research has been targeted on professed the usefulness of co-depositing various nanomaterials and the improvement of innovative electrochemical approaches. Nanohybrides have been mixed

resulting in auspicious properties comparable to those of appropriate materials and exhibit novel and improved properties not profitable in single phase materials. This technique is favourable due to its easy process, economically viable, scalability and the desired purity of the final product. Sensing device needs large surface area to get exposed to the material which to be sense, hence to customize the surface properties, a thin layer is deposited on the metal surface. This can be done easily and with low cost by one of the deposition system such as electrodeposition. There are several conditioning factors in Electrodeposition:

i) Current density.
ii) Nature of anions and cations in the solution.
iii) Bath composition and temperature.
iv) Solution concentration.
v) Power supply.
vi) Defects.
vii) Physical and chemical nature of the used substrate used.

The schematic diagram of components of the electrodeposition system and its various parameters are illustrated in figure 2.

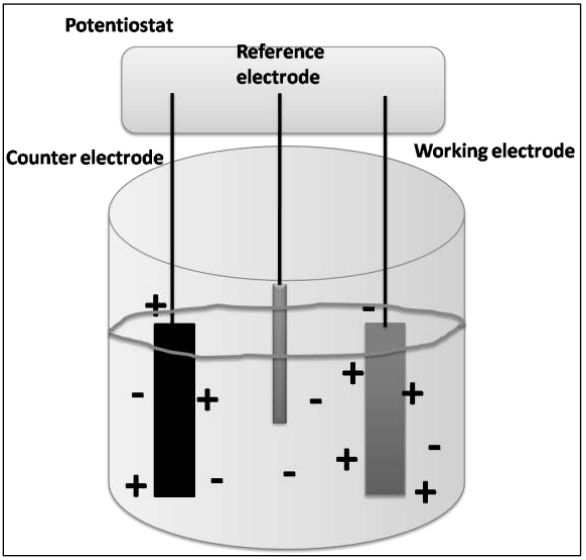

Fig 2: Schematic diagram of electrodeposition process

The advancement of electrodes having metallic nanoparticles, such as

gold, has enhanced surface area. In case of enzymes, it generally needs direct electron deportation between the active site and metal surface of enzyme. The confinement of accomplished gold nanoparticles onto the electrode surface is found in this technique, which is often advanced with the amine group in the terminal sites indicating self-assembled monolayer (SAMs) by adsorption from electrolyte solution [16]. Enzymatic biosensors incorporating gold nanoparticles are precisely deposited onto glassy carbon electrodes (GCE) or similar substrates. Gold nanoparticles were electrodeposited onto the GCE at -0.2 V (vs. Ag/AgCl) for 60 seconds from a 100 mg L^{-1} $HAuCl_4$ solution. Scanning Electron Microscopy (SEM) images revealed that the gold nanoparticles, with an average size of 100 nm, covered most of the electrode surface. These nanoparticles served as a support for the horseradish peroxidase (HRP) enzyme, both in its native form and when conjugated with lactose. The lactosylated enzyme exhibited enhanced electrocatalytic activity for hydroquinone in the presence of 200 μM H_2O_2, with a detection limit of 74 nM compared to 83 nM for the native enzyme.

In some studies, gold nanoparticles are first synthesized and then electrodeposited onto the surface, with the applied potential facilitating the binding of the nanoparticles. For example, one study described the preparation of gold nanoparticles in solution (average size = 31.9 nm as determined by dynamic light scattering) using a citrate reduction process, followed by their electrodeposition via a combination of chronopotentiometry and cyclic voltammetry (CV) [17]. The schematic model diagram of the electrodeposition of nanostructure material and the receptors acceptance for biosensor application is displayed in figure 3.

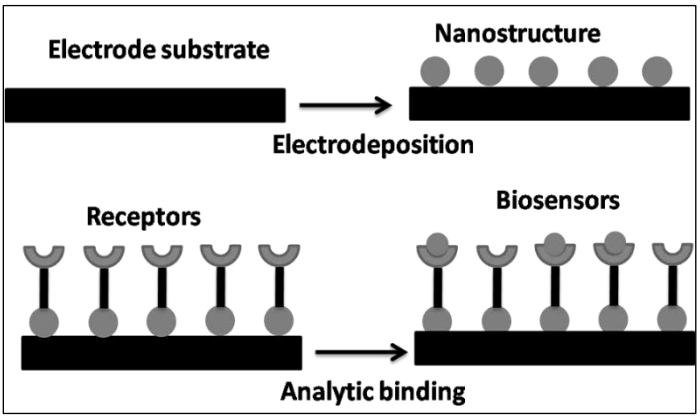

Fig 3: Model representation of formation of nanostructure on substrate and acceptance of biomolecules by receptors by analytic binding

In the development of an electrochemical biosensor for the neurotransmitter dopamine, a nanoporous gold electrode was used as a substrate for the electrodeposition of palladium. The nanoporous structure of the gold nanoparticles provides high conductivity through their interconnections. Gold nanoparticles, with a diameter of 0.2 mm and inter-ligament gaps of approximately 200 nm, were coated with a 20-nm thick layer of palladium. This was achieved by immersing the gold electrode in a solution of 2.5 mM $PdCl_2$ and 5 mM sodium dodecyl sulfate, and cycling the potential between 1.2 V (versus SCE) and 0.2 V. The resulting Au/Pd electrode demonstrated high sensitivity to dopamine oxidation, with a sensitivity of 1.19 $\mu A\ \mu M^{-1}$, a detection limit of 1 μM, and a detection range from 1 to 220 μM. The electrode maintained stable performance over approximately 40 uses and showed minimal interference from substances such as ascorbic acid and uric acid. For the fabrication of a DNA sensor targeting an Enterococcus faecalis gene sequence, dendritic gold nanostructures were electrodeposited onto a gold electrode. Electrodeposition was carried out at 0.0 V (versus Ag/AgCl) for 300 seconds in a solution containing 0.5 M H2SO4, 0.020 M HAuCl4, and 0.150 M sorbitol. The resulting gold nanostructures had a fractal dimension of 2.44 ± 0.19, as determined from SEM images, and a roughness factor of 9.5. Thiolated DNA was immobilized onto the gold nanostructures, with pinholes filled using 6-mercapto-1-hexanol.

The binding of the complementary DNA strand, derived from bacteria, was analyzed using Differential Pulse Voltammetry (DPV) scans with toluidine blue as the redox probe. The redox probe demonstrated a higher binding affinity for double-stranded DNA (dsDNA) compared to single-stranded DNA (ssDNA). A detection limit of 4.7 × 10-20 mol L^{-1} was achieved for a 25-nucleotide-long complementary DNA strand, with a detection range from 1.0 × 10-17 to 1.0 × 10-10 mol L^{-1}.

An electrochemical glucose biosensor was created using an aniline electropolymerization process. This process involved a solution containing dispersed gold nanoparticles coated with polyvinylpyrrolidone (PVP), forming a composite nanostructured film that supported glucose oxidase. Transmission Electron Microscopy (TEM) images indicated that PVP-grafted gold nanoparticles were more uniformly dispersed than those without the coating. The composite film was electropolymerized onto a glassy carbon electrode (GCE) by cycling the potential between -0.2 and 0.75 V (versus SCE) at a rate of 100 mV s^{-1}. Glucose oxidase (8 mg mL^{-1}) was drop-cast onto the composite film, followed by a Nafion layer from a 0.5%

solution. Scanning Electron Microscopy (SEM) images revealed distinct flower-like structures in the composite film. The immobilized glucose oxidase showed direct electron transfer, with a detection limit for glucose of 1.0 × 10-5 M.

Monitoring specific analytes and metabolites is vital for healthcare, with body pH being particularly important for patient health. Deviations in sweat pH from the normal physiological level of 5.5 can indicate conditions such as acidosis, electrolyte imbalance, cystic fibrosis, osteoporosis, and bone mineral loss. Researchers have developed functional textiles by electrodepositing IrOx onto PEDOT films, which are then integrated into the textile. pH detection is carried out using cyclic voltammetry, where a peak shift towards more negative potentials indicates a basic pH.

Chemical Vapour Deposition (CVD)

Chemical Vapor Deposition (CVD) is a solvent-free technique where vapor-phase precursors chemically react on the surface of a substrate to form a thin, solid film. The CVD process allows for the *in situ* synthesis and deposition of polymers on various substrates with tunable microstructures. Generally, CVD involves three main components:

1. Precursor supply system.
2. CVD reactor.
3. Exhaust system.

The role of the precursor supply system is to generate precursors in the vapor phase and transport them to the reactor, typically using a carrier gas. This is where the CVD reaction occurs. Liquid precursors are commonly used because they can generate sufficient vapor pressure when heated to moderate temperatures (<200 °C). Various precursor streams can be combined to produce compound mixtures. Modifications of this system, such as liquid injection and aerosol-assisted (AA) CVD, are often employed to introduce low-volatility or solid precursors. In these systems, precursor evaporation occurs inside the CVD reactor. Additionally, they offer great flexibility in forming doped or ternary/quaternary materials due to the relative ease of adjusting stoichiometry in the precursor solution.

Various previous reports proposed that ultrathin hydrogels has been demonstrated by synthesis of nanostructure material via photoinitiated chemical vapour deposition on delicate optical sensors and biosensors without sacrificing sensitivity and accuracy [18, 19]. However, very less reports have been performed to prove whether such top layers can be unified into

more complex sensing elements, for an example; electrochemical biosensors that generate signals via cascade redox reactions [20-22]. CVD is a technique that affects the volatile precursor reaction in which it is injected into a chamber. The chamber is heated to a reaction temperature that causes the precursor gas to react or break down into the desired coating and bonded to the material surface. 3D nanostructures are not bound to the nanoscale, just as bulk materials, they still have the influence of being made of nanostructures (quantum confinement effect, high surface-to-volume ratio) [23, 24]. Chemical synthesis is the most straightforward way of forming 3D nanostructures applying methods of CVD mostly [25-27]. Over time the coating material builds on the surface and creates a coating throughout the exposed part's surface. Chemical vapour deposition coatings can be theoretically applied to any area the coating gas can get into. Process control is another factor in utilizing CVD coating processes. The deposition process allows us to build a coating layer (in our case corrosion resistant or inert silicon) on the surface one Angstrom (0.1 nanometer) at a time. Now a day's most of the researchers have been focussed on non-enzymatic biosensors fabricated my nanomaterials which are development by CVD techniques. Nanotechnology can clarify many issues of non-enzymatic biosensors. With the invention of novel properties of nanostructured materials, it is normal that new advancements can be made in the industry of glucose biosensor in the near future. The important characteristics of the CVD process for the fabrication of biosensor devices are:

i) Optimum elevated temperature and typical vacuum environment.

ii) Film thickness is restricted due to coating stress.

iii) Coated surface is bounded during the reaction which generates a superior adhesion.

The electrocatalytic activity of the CuNP grafted electrode for glucose oxidation application in an alkaline solution has been proposed by scientists. The actual mechanism of this redox technique is still under dilemma. As per the mostly accepted mechanism, glucose oxidation occurs on the modified CuNP based electrodes is produced by the de-protonation process of the isomerization and glucose of its enediol form. Firstly, it includes the construction of the Cu (II)/Cu (III) redox couple in alkaline environment at the electrode surface. In this step the important factor for examining non-enzymatic glucose as Cu (III) species act as an electron transfer medium. When the glucose is mixed to the medium, it is oxidized to the gluconolactone, while Cu (III) is reduced to Cu (II). Obtained glucolactone

is transformed to gluconic acid by a hydrolyzation process. Therefore, the non-enzymatic sensor planned with CuNP-encapsulated single-layer CVD nanomaterials has improved catalytic current response even with very low glucose concentrations. Possible mechanism of these reactions are illustrated as follows [28]:

$$CuO + OH^{\cdot} \rightarrow CuOOH + e^{-}$$

$$CuO + H_2O + OH^{\cdot} \rightarrow Cu(OH)_4 + e^{-}$$

$$Cu(III) + e^{-} + glucose \rightarrow Gluconolactone + CuO$$

$$Gluconolactone \rightarrow Glukonic\ acid$$

Analytic performance of non enzymatic electrode has also been developed under various experimental conditions for the optimization of the calibration curve of the glucose. The current change of the substrate is observed with concentration ranging from 0.01-0.1mM. The non enzymatic sensor is very effective for the indetification of the glucose amount and the current response increased as glucose concentration was increased up to 5mM after which it became constant up to 50 mM. The linearity relationship of non-enzymatic electrode was examined between 0.01 and 1.0mM glucose concentration limit of detection and sensitivity were specified 7.2 μM and 430.52 μA mM^{-1} cm^{-2} for glucose with S/N=3 criteria respectively.

Atomic Layer Deposition

It is a vapour deposition method, which indicates the deposition of the thin films with high conformality with controllable film thickness, which suggest applications in versatile fields. ALD is a kind of self confine reactions occurs between two gaseous precursor, which deposit thin films in a layer by layer pattern. ALD is a key enabling technique for deposition of thin films on high aspect ratio structures with maintaining uniformity on a large surface area at relatively low temperatures. As there is existence of strong consolidation between ALD coating and substrate, the active sample materials can be deposited precisely as the functional body on particular substrate with proper characteristics. These deposited materials and in the form of nanoparticles which illustrates desired properties such as photocatalytic activity, supercapacitor, good conductivity, sensor etc. The morphological properties of the active materials can be controlled very comfortably by monitoring the deposition layers by ALD.

The mechanism of Atomic Layer Deposition (ALD) is a cycle-based process consisting of four steps. In the first step, a precursor is introduced

into the reactor chamber and allowed to react with the substrate surface groups. The second step involves removing any unreacted precursor molecules and by-products by purging or pumping the system with an inert gas, typically nitrogen (N2) or argon (Ar). The third step introduces a second precursor (the co-reactant), which reacts with the adsorbed molecules from the first precursor. The final step involves purging the system again to remove any unreacted co-reactant and by-product molecules. As a result, one (sub) monolayer of the desired material is deposited on the substrate. This cycle is repeated until the desired thickness is achieved [29, 31]. Steps are illustrated below with proposed neat schematic diagram in figure 4.

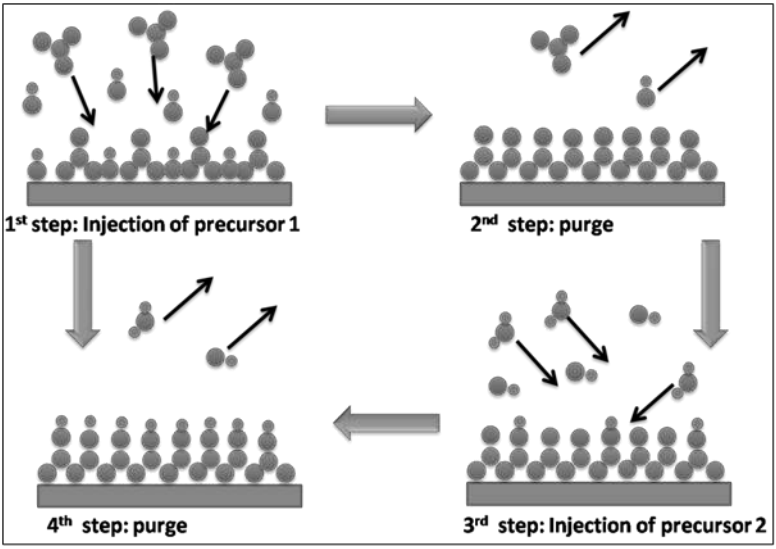

Fig 4: Schematic illustration of ALD technique step by step

The nanomaterials preparation for medical and biological applications by ALD techniques has escalated and is now broadly streched (Guo *et al*., 2010; Marichy *et al*., 2012; Pessoa *et al*., 2017; VähäNissi *et al*., 2014; K. Zhang *et al*., 2017). The integration of Atomic Layer Deposition (ALD) with the nanoscale components of biomedical devices, the biocompatibility of the materials that can be produced, and the ability to control chemical reactivity are key reasons for using ALD in biomedical applications. Among these applications, biosensing has recently benefited from ALD as a method for preparing biosensor devices [32-34]. The survey in the form of bar diagram in figure 5 clearly displays that the work number relating both terms has been regularly enhancing in the last decade.

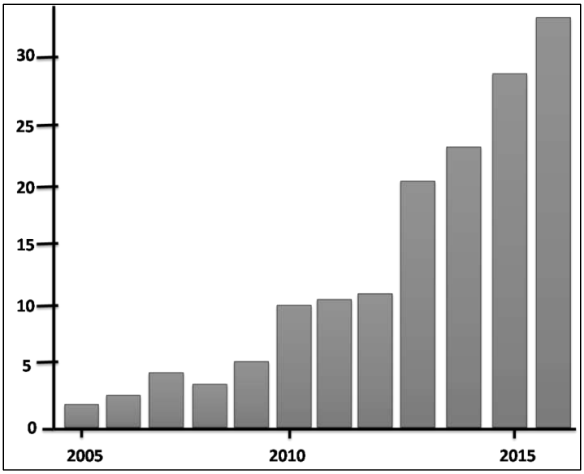

Fig 5: Survey on ALD technique used for biosensor applications in the last decade

As already discussed in the above sections that biosensors allows selective detection of the target molecules, making them important for applications in clinical diagonosis, food safety, environmental monitoring etc. Recent enthusiasm in fabricating biosensors devices with nanosized properties has drawn our attention as the controllable dimensions are in the range as like biological parameters of the bio recognition layer. Here in the table 1 represented the selection of nanostructured biosensors fabricated.

Table 1: List of thin films fabricated by ALD technique for biosensor devices

Material deposited by ALD technique	Application of ALD coating	Substrate used for deposition	Analyte	Detection method	Concentration	References
Al_2O_3	Sacrificial layer for nanogap fabrication	Gold nanogap/Biotin	Streptavidin	Electrochemical (current)	Detection down to 1.5 nM	(Jang *et al*., 2007)
Al_2O_3	Layer for nanoring fabrication	Plasmonic nanoring cavities	Adenine	Optical (surface enhanced Raman spectroscopy [SERS])	Limit of detection 76 nM	(Im *et al*., 2013)
Al_2O_3	Layer for coax fabrication	Nanoscale coaxial electrodes/anticholera toxin antibody	Cholera toxin	Electrochemical (DPV [differential pulse voltammetry] or SWV [square wave voltammetry])	Linear dynamic range of detection of 10 ng/ml^{-1} µg/ml Limit of detection 2 ng/ml	(Archi bald *et al*., 2015)
Al_2O_3	Nanospacer for metalenhanced fluorescence (MEF)	Microarray platform on Ag film/split DNA aptamer	17-βestradiol	Optical (fluorescence)	Detection limit of 1 pg/ml	(Lee *et al*., 2017)
Al_2O_3/ZnO	Nanopore sizemodification, enhancement of sensing capabilitis	poly(ethylene terephthalate) (PET) nanochannel/Al2O3/ ZnO/biotin	Avidin/streptavidin/bovine serum albumin (BSA)/IgG(Immunogl obulin G)/anti-BSA	Electrochemical (current)	Avidin and streptavidin discrimination/BSA, IgG and anti-BSA detection	(Lepoi tevin *et al*., 2016)

For the direct deposition of highly active catalytic materials, Chio *et al*. prepared carbon nanotubes (CNTs) grafted with nickel (Ni) using Atomic Layer Deposition (ALD). In alkaline solutions, the CNT-Ni composites exhibit high electrocatalytic activity for glucose oxidation. Ni particles are deposited on the CNT surfaces via ALD, resulting in enhanced detection performance, including rapid response, wide linear response range, high sensitivity, repeatability, and good selectivity for nonenzymatic biomolecules. The ALD process is particularly advantageous for uniformly growing NiO particles on a silicon carbide (SiC) substrate. The NiO/SiC composite is favorable for high glucose-sensing ability, low detection limit, wide linear detection range, good stability, and high sensitivity. Among composites fabricated with 200, 400, 600, and 800 ALD cycles, the NiO/SiC composite with 600 ALD cycles exhibited the best sensing performance, with a sensitivity of approximately 2.037 mA/(mM/cm²). Zhang *et al*. proposed a flexible electrode by fabricating an ultrathin cobalt oxide (CoO) layer on the skeleton surfaces of a nanoporous gold film using the ALD method. The hybrid composite demonstrates enhanced catalytic performance for glucose oxidation and H_2O_2 reduction due to the synergistic interaction between the interfacial Au and CoO, as well as the large surface area of the gold skeleton.

Thanks to its excellent biocompatibility, membranes prepared by ALD can serve as transducers for loading biologically active molecules. Using this technique, Tereshchenko *et al.* [35] proposed their optical biosensor optimized for the inspection of Grapevine virus A-type (GVA) proteins (GVA-antigens) based on ALD ZnO films. The GVA-antigen determination was accomplished by using the diversity in the GVA-based light emission. Biosensor sensitivity was examined between range from 1 pg/mL to 10 ng/mL of protein. Dominik *et al*. [36] fabricated titanium oxide thin films by applying long-period grating (LPG) which was convinced in an optical fiber for the estimation of the formation of compound between biotin and avidin. The sensitivity value of the LPG biosensors was ~3400 nm/RIU. Here, TiO_2 thin film coating has a vital role in flexible of sensor sensitivity, as well as permissible to biofunctionalization and recovering method of the surface. It is noted that some nanoarchitectures decorated by ALD techniques have same dimensions with the biological components of the biorecognition film, which drawn detectable attention. Comstock *et al.* [37] formed Pt films through template-assisted ALD coating which are coarse in nature, whose roughness factors nearly 310. Pt film was registered in enzyme-free glucose sensing and showed a fascinating near-linear response to glucose in the range between 0 mM and 20 mM with a 63.8 μA/(cm^2/mM) sensitivity.

Pulse Laser Deposition (PLD)

PLD is a decent and accomplished process for fabricating thin films of simple and complex materials, sometimes called laser abalation. The reactivity of the species increases which promotes the thin film deposition, due to the introduction of discharge plasma radio frequency in the standard PLD system. Comparing with other deposition technique, the PLD attempts more extraordinary advantages such as control over the growth rate, adaptability, an infinite degree of freedom in the ablation geometry and stoichiometric transfer. When the target of ablation is in a plasma, a plasma in a vacuum, or a background gas, pulse laser sputtering creates high energy peaks and small pulse widths. The expansion product permits PLD to fabricate a particular parameter and a microtubular structure on a substrate layer when the substrate is stretched (Smith and Turner 1965; Al-Saedi *et al*. 2019; Atiyah *et al*. 2019). Due to the laser abalation a dense layer of vapour acquires in front of a target during phases of the laser pulses. During this extension, ionization energies and internal heat are transformed into KE of several hundred eV's; the kinetic energy is paused by continuous strikes as the ablated particles expand into a low-pressure background gas (Joe *et al*. 2017). The process of laser deposition is separated by two distinct parts. However, for depositing excellent film, the plasma plume must have exact stoichiometry as the target. If the target surface, are consistently heated, by absorbing light from a continuous-wave laser source would permit a considerable good percentage of the incoming power to be passed into the target's bulk. The surface's subsequent melting and evaporation would be primarily thermal. Due to the melting temperatures and vapour pressures of target elements' differed, they evaporated at various rates, resulting in a composition of the evaporated material that fluctuated over time and did not accurately match the target (Singh and Narayan 1989). The correlation between laser source and sample occurs by absorbing photon by electrons. Due to the absorbed energy, excited electrons in high-energy states, indicates that the sample is heated to very high temperatures in a precise time. The energy is then moved to the grid through the electron subsystem by electron-phonon coupling. A multitude of elements influences the corelation of the laser beam with the target, including the reflectivity of the target material, pulse frequency, the absorption coefficient, laser fluence and wavelength. The extensive interest for cost reduction and economized devices leads to an improvement in the nanotechnology field and cost-effective device manufacturing. The technique has several advantages for usage in biosensor applications:

a) The laser system is detouched from the impeachment system; hence, the fabrication system may be treated as a "clean" system, and in addition, a huge number of ablation geometries may be studied.

b) The fabrication parameters during experiments, that is, laser pulse duration, wavelength, laser spot area, repetition rate, and laser fluence, may be monitored in a accurate way.

c) The thickness of the deposited films can be monitored by adjusting the number of laser pulses.

d) The laser beam illuminating the target material may be incident in a very small portion, which allows the selective processing regions of interest.

e) The transfer of the target material to the substrate can form new materials that cannot be gained by other process. The schematic model diagram of thin film deposition on substrate by PLD is illustrated in figure 6.

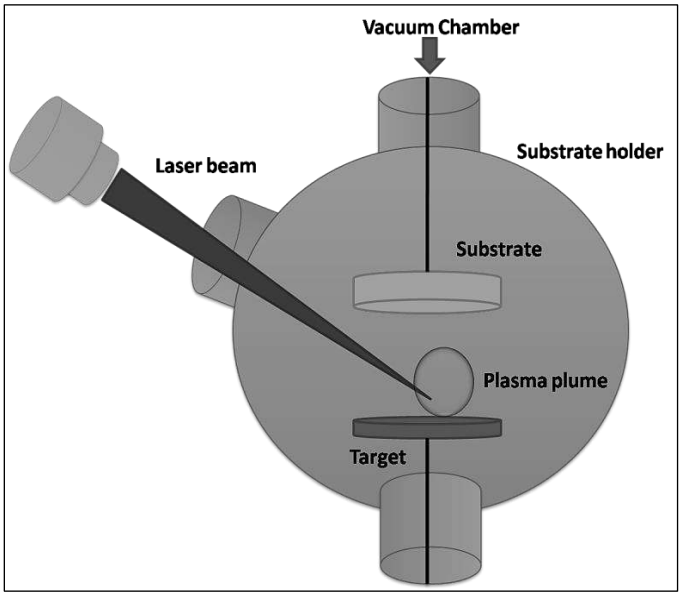

Fig 6: Model of PLD process for fabrication of thin films in ablation geometry

In recent years advanced outputs have been reported by many scientists, for increase in applications number [38-40] which requires the fabrication of biomaterials, polymers or organic molecules on a substrate material. Proteins and enzymes [41, 42] have also been fabricated using MAPLE process.

Enzymes are broadly engaged as sensing elements in biosensors devices [43] by linking a thin layer of immobilized enzyme consisting of an electrochemical probe. Lipases are vital enzymes in most of the biological objects. The physiological action of biological systems is that they can catalyse the hydrolysis process of triacylglycerol to glycerol and fatty acids [44]. The permission for the use of lipase miniaturized silicon biosensor devices for estimation of triglycerides (TG) in living beings blood serum.

Urease, which is catalyzing form of urea's transformation to CO_2 and ammonia, is generally used in biosensors for controlling the concentration of urea in the blood and urine. Urea indicates a indicator of diagnostic process for proper kidney function. Continuous uniform urease thin films were successfully fabricated by MAPLE on Si from a 10 wt% solution in water, using a 248 nm laser at a fluence of 0.4 J/cm^2 [45]. The MAPLE is capable to generate active enzyme thin film which was also abused to form laccase thin films. Cicco *et al*. proposed that partially active thin films of laccase can be deposited on glass substrates and screen-printed carbon electrodes from a 1 wt% aqueous solution using a laser fluence of 0.6 J/cm^2 [46].

Metal Oxide Semiconductor Based Biosensors

Compounds having huge level of electrostatic interaction or ionic bonding are defined as metal oxides semiconductor. Generally, for applications like sensing devices II-VI semiconductors are used as they are inexpensive, easy to manufacture, immediate response time, broad detection limit, and prevents harsh conditions. Adapting biosensors materials to different kinds of materials illustrates a cructopic with challenging aspects to affect. From the last decade many papers reported materials such as polymers (Gupta *et al*., 2020), photonic crystals (Hocini *et al*., 2019), metals (Rezaei *et al*., 2019), graphene (Yuan *et al*., 2019), metal organic frameworks (Osman *et al*., 2019), and transition metal dichalcogenties (Wang *et al*., 2017) as appropriate for biosensors applications [47-49]. Some of the mentioned materials require momentous advancement related to morphologic optimization, chemical stability, compatibility with different biomolecules, and increase of LOD. Nanostructured formed metals oxides such as Zn, Fe, Ce, tin, Zr, Ti, metal and Mg have been found to exist in attractive nano morphological, functional biocompatible, non-toxic and catalytic properties. Another advantage of these materials is represented by a large number of cost effective synthesis methods such as sonochemical precipitation (Zhou *et al*., 2013), co-precipitation (Dong and Zheng, 2014), thermal oxidation (Li *et al*., 2010), chemical etching (Liu *et al*., 2010),

hydrothermal (Zhou *et al*., 2017or sol-gel (Rathinamala *et al*., 2019)), polyol (Elahi *et al*., 2019), allowing the formation of various morphologies such as porous quasi-nanospheres (Liu H. *et al*., 2017), hollow nano-spheres (Santos *et al*., 2016), nanorods (Dong *et al*., 2017), nanosheets (Zhang *et al*., 2020), or flower-like particles (Feng *et al*., 2018). These metal oxides are also bears improved electron-transfer kinetics and strong adsorption capability, supplying appropriate microenvironments for biomolecules immobilization and as a result advanced electron transfer and enhanced biosensing characteristics was observed. Different kinds of morphologies of NMOs have been adopted by using various technique, including soft templating for the preparation of nanorods and nanofibers. Semiconductor metal oxides (SMO) can detect low concentration gas with high stability and low response time. SOM with multispecialty characteristics able to control biological systems molecules indicates a step forward in the improvement of more compound single medical decision-making systems. The enzyme-based biosensors prepared from SOM have many advantages such as:

1) Chemical stability in various environments (Zheng *et al*., 2020).
2) High energy efficiency (Solaimuthu *et al*., 2020).
3) Adaptability to specific working conditions (Han *et al*., 2019).
4) Good sensitivity (Yi *et al*., 2020).

There are different kinds of hurdles to conquer concerning implement SOM in bio sensing applications: increasing the carrier charge mobility, decreasing electron-hole recombination, organic/inorganic interface compatibility, and finding facile synthesis techniques. Hence, here we discuss some of the SOM along with their favourable characteristics towards fabrication of biosensor device.

ZnO Nanostructures

Zinc oxide (ZnO) is a direct band gap semiconductor having n-type conductivity, making it highly suitable for immobilizing low isoelectric point enzymes in the fabrication of enzyme-based biosensors. But it has poor catalytic properties towards biomolecules, thus it is not favourable for non-enzymatic biosensor devices. ZnO can be prepared by wet techniques which is a major part. ZnO can be practiced in all clinical or nonclinical applications as it has eco-friendly towards environment and safe material. Another glucose biosensor device was advanced by Rafiee *et al.* with combination of graphene nanoplatelets (GNPs), which is well known for their high conductivity and chemical stability, and ZnO NWs, which is well

known towards glucose sensitivity. In their studies, they modified the device structure of a glucose biosensor by preparing ZnO nanowires (NWs) on thin films of gold nanoparticles (GNPs) at three different molar concentrations (0.5, 1, and 2 mg), labeled as GNP1, GNP2, and GNP3. The system demonstrated that the combined effect of ZnO NWs and GNPs resulted in the development of an efficient glucose biosensor device. They observed that at low glucose concentrations, the device's response increased with higher amounts of graphene in the solution, and the sensor response time decreased as the number of GNPs increased. Additionally, they reported long-term stability, particularly consistent resistance to concentration, an important criterion for an ideal biosensor. This was observed in GNP-modified samples after exposure to 30 mg/dL glucose for approximately 30 days. Consequently, they developed an ideal glucose biosensor device with key properties: a response time of 5 seconds, a detection range from 0.003 to 30,000 mg/dL, and long-term electrical stability. For example, Akhtar *et al*. fabricated reagent-less optical biosensor devices based on a fluorescence enhancement mechanism for amyloid identification, used in diagnosing neurodegenerative diseases such as Alzheimer's disease and insulin-dependent type II diabetes. They utilized flower-like ZnO nanostructures, which offer a large surface area. The ZnO nanoflowers have been shown to perform better with enhancing materials, providing a faster and more cost-effective amyloid biosensor. Similarly, Sahyar *et al*. developed a new Ag-doped ZnO NP-based biosensor for the early detection of meat spoilage. Their analysis using an enzyme xanthine oxidase (XO)-modified electrode (nanoAg-ZnO/polypyrrole (PPy)/pencil graphite electrode) revealed that the enzyme biosensor demonstrated high selectivity with a sensitivity of 0.03 μA/mM and a low detection limit of 0.07 μM. In another study, Yue *et al*. successfully created an ideal dopamine (DA) biosensor using Au NP-ZnO nanocone arrays/graphene foam electrodes. Their characterization techniques showed that the modified electrode had high sensitivity (4.36 μA μM^{-1}) and a low detection limit (0.04 μM, S/N = 3) for DA. They also found that the ZnO Nano cone-based electrode exhibited good reproducibility, excellent selectivity, and stability under uric acid (UA) interference. They affirmed that this electrode has significant potential in medicine and healthcare.

TiO_2 Nanostructures

TiO_2 electrochemical biosensors present an alternative for recognizing biomolecules associated with diseases, drug interactions, food or environmental contaminants, and related topics. The relevance of TiO_2 biosensors lies in their high selectivity and sensitivity. Enhancing

electrochemical biosensors based on TiO_2 nanostructure surfaces requires understanding the signals they produce and their relationship with transducer properties, such as the roughness, crystalline phase, and morphology of TiO_2 nanostructures. Recently, for cancer detection, several optical fibre sensors based on surface Plasmon resonance (SPR) have been developed due to their superior sensing performance, compactness, and portability. The primary goal is to measure changes in the refractive index of cancer cells for early detection. To this end, the design and analysis of a BK7/TiO_2/Au/graphene-based SPR sensor model have been reported for blood (Jurkat), adrenal gland (PC12), detecting skin (basal), cervical (HeLa), and breast (MCF-7 and MDA-MB-231) cancer cells using the refractive index component. Salmonella infections are among the most controllable pathogens globally, making advanced identification methods crucial for mitigating the risks of human diseases caused by this microorganism. This research introduces a novel optical immune sensor for detecting Salmonella typhimurium. The immune sensor is based on titanium dioxide (TiO_2) nanoparticles deposited on glass substrates (glass/TiO_2). TiO_2 nanoparticles exhibit intense photoluminescence (PL) in the visible range at room temperature. The direct immobilization of antibodies (anti-S-Ab) against Salmonella antigens on the glass/TiO_2 surface results in a glass/TiO_2/anti-S-Ab structure, characterized by increased PL intensity and an IR-shifted PL peak compared to the glass/TiO_2 structure alone. Changes in PL intensity and peak positions after the immobilized anti-S-Ab interacts with Salmonella antigens (Salmonella Ag) serve as the immune sensor signal, enabling sensitive and selective, label-free detection of Salmonella Ag. Quenching of the PL of TiO_2-based quantum dots by BSA and DNA has shown that biomolecule concentration significantly influences the reduction in PL intensity.

Nanostructured TiO_2 surfaces, featuring thin films with controlled roughness or arrays of nanostructures, are of immediate interest for enhancing electrochemical biosensors. They possess numerous optimal properties for biosensor applications, such as non-toxicity, biocompatibility, resistance to corrosion, low fabrication costs, high surface area, effective transduction mechanisms, and quantum confinement. Additionally, the extensive knowledge of TiO_2 electrochemistry, well-studied since 1969, is critical for understanding, improving, and enhancing the sensing processes. In photocatalytic applications, a mixture of anatase and rutile phases is particularly efficient because it prevents electron-hole recombination, which otherwise hinders photocatalytic efficiency. For electrochemical biosensors, TiO_2 thin films in the anatase phase are preferred due to their insolubility in moderate acid and alkali solutions, making them especially suitable for

developing pH sensors. Although many applications operate at physiological pH, the initial functionalization with various biomolecules may involve more stringent acidic or basic conditions.

MoS_2 Nanostructures

2D transition metal dichalcogenides (2D TMDs) have seized appreciable consideration due to their idiosyncratic properties and huge range of possible applications. One of the most broadly reported transition metal dichalcogenides is molybdenum disulfide (MoS_2). Molybdenum disulfide (MoS_2)-based nanomaterials have captured the absolute attention in recent times because of their manifold advantageous attributes [50]. MoS_2 comprises S- Mo-S triple layers with well-known semiconducting properties of metal dichalcogenide compounds [51]. Extraordinary electrochemical attributes and luminescence properties have endorsed MoS_2-based nanomaterials as novel biosensing probes for the careful detection of a range of analytes [52]. The 2D MoS_2 nanosheets have extraordinary and complementary characteristics to those of graphene, rendering them ideal electrode materials that could potentially advantage to significant merits in many electrochemical applications. These properties include monitered bandgaps, relatively high electron mobilities, large surface areas, and catalytic characteristics and good optical. The sensing film was fabricated on an interdigital electrode substrate using layer-by-layer self-assembly of MoS_2 nanosheets and Co_3O_4 nanorods. The layer-by-layer self-assembly not only significantly prevented agglomeration but also supplied many more active catalytic sites on p-type Co_3O_4 nanorods toward ammonia. The results estimates that the fundamental sensing mechanisms of the MoS_2-Co_3O_4 nanocomposite material towards NH_3 were associated to the layered nanostructure, synergistic effects, and p-n heterojunction depletion layer formed at the interface of n-type MoS_2 and p-type Co_3O [53]. Su *et al*., also proposed that MoS_2 stabilizes metallic NPs, such as platinum (Pt), Au, silver (Ag), and lead (Pd) to form hierarchical nanocomposites, and such 2D-MoS_2/metal-NSs composites acquire the fundamental properties of pure metal NPs and MoS_2 nanosheets because of their synergistic effects, making the 2D MoS_2 and metal/metal oxide nanostructured composites have significant electrochemical properties for the formation of electrochemical sensors [54]. Dong *et al*. prepared MoS_2 quantum dots by an ultrasonication-mediated method by using an "up-bottom" approach [55]. These dots had profound down-conversion photoluminescence (PL) behaviour, justifying their strong potential in photodynamic therapy. Wang and co-workers recycled such dots as a PL sensing platform for 2,4,6-trinitrophenol, with high sensitivity down to 95

nM [56]. Further their broad diagnostic potential, MoS_2 nanodots have also been analyzed for a number of therapeutic potentials. Liu and co-workers found the glutathione (GSH)-modified dots for photothermal cancer therapy [57]. Su *et al.* successfully used AuNPs-MoS_2 as an electrochemical sensing platform for the identification of chemical/biological molecules including neurotransmitters, H_2O_2, ATP, thrombin, and protein [58]. Wang *et al.* fabricated a sandwich-type immunosensor for the identification of carcinoembryonic antigen (CEA) using the catalytic activity of MoS_2-Au nanocomposites, which could detect carcinoembryonic antigen as low as 0.27 pg ml [59]. Yang *et al*. explored the application prospects of molybdenum disulfide hybrid materials in chemical and biomolecular sensing by synthesizing molybdenum disulfide flake-like nanostructures on polypyrrole microtubes [60]. Zheng *et al*. reported on a molybdenum disulfide-modified carbon nanotube doped with nitrogen, designed for the detection of hydrogen peroxide and ascorbic acid [61]. In their research, the researchers suggested that single MoS_2 nanosheets have few active sites and that the high surface energy and van der Waals interactions between layers lead to significant aggregation of MoS_2. To enhance sensor performance, many researchers employ surface-modified electrodes for electrochemical detection [62].

CdS Nanostructures

CdS nanoparticles have been utilized in various nanobiotechnology fields due to their recognized biomedical properties. Their unique size and shape confer distinctive properties, making them popular in biosensors, bioimaging, anticancer, and antibacterial applications [63, 64]. In addition, CdS is a fluorescent material which can be utilized in medicine because of its extraordinary optical and electrical properties, photocatalytic activity, and lower toxicity than Cd [65]. Chemical, physical, and biological methods produce various types of CdS NPs. The application of CdS NPs is dependent on the properties of the synthesized NPs, such as size, shape, and surface charge, which are dependent on their synthesis method. As they have low toxicity value and excellent compatibility with biological systems, CdS NPs prepared by biological techniques are more commonly used in medical sciences [66]. Suranjit Prasad *et al*. perform experiment with the leaf extract of *Asparagus racemosus* as a stabilizing and grafting agent for the formation of water-soluble CdS NPs. After the formation of leaf extract, the green synthesis of CdS NPs was executed by using a particular amount of sodium sulfide (2 mM) that was mixed dropwise into the solution of cadmium chloride and leaf extract, followed by being placed in a rotatory orbital

shaker which operates at 200 rpm, at 30 °C, for 12 h in dark condition. Shivaji *et al*. proposed a green synthesis method for preparing CdS quantum dots (QDs) with a 2-5 nm particle size, using tea leaf extract as a toxic-free particle-stabilizing agent [67]. To synthesize CdS QDs, a certain amount of $CdSO_4$ was mixed with the extract and incubated for three days in the dark condition, which is followed by mixing of Na_2S and incubating for four days. The bright yellow color solution was then centrifuged and lyophilized for further properties studies. Finally, their antibacterial activity was diaplayed by a well-diffusion assay, and the cytotoxicity effect of CdS QDs was demonstrated against A549 cancer cells [68].

4. Challenges in Recent Progress in Biosensors Applications for Medical and Health Care

Despite the variety of biomolecules tested both as biorecognition layers and analytes, numerous biosensor platforms with diverse applications have been developed, including implantable, wearable, and more recently, ingestible biosensors. To date, various scientific and technological fields have benefited from the development and application of biosensor devices, with significant contributions in the food industry, healthcare, medical fields, and environmental monitoring. As with other areas in science and technology, biosensor research has greatly benefited from the use of novel materials and technologies, particularly in nanotechnology, leading to the regular proposal of more efficient biosensor systems. Among the nanomaterials commonly proposed for sensor applications are quantum dots, gold nanoparticles, graphene, and carbon nanotubes (Brazaca *et al*., 2019).

Wearable biosensors are "on-body" devices designed to collect critical data on human health, including electrical, electrophysiological, and biochemical information. These devices have the potential to facilitate timely, preventive, and patient-centered decision-making, especially in remote communities, by providing valuable health data on the early onset and progression of diseases related to infection, neurological disorders, mental health, and chronic and rare diseases. Utilizing sophisticated medical technology to obtain comprehensive biochemical profiles of patient samples requires trained personnel, complex operations, expensive equipment, and reliable electricity. Currently, most commercially available wearable devices can monitor physical indicators (e.g., activity, temperature, tension) and electrophysiological activities (e.g., electrocardiography, electroencephalography, electromyography). However, they do not provide detailed information on users' health conditions at the molecular level, such as hormones, proteins, nutrients, enzymes, and small molecules.

As wearable technology becomes increasingly mainstream, it supports the development of applications that enable wearable devices with molecular diagnostic capabilities. These biosensors can analyze molecular analytes from various biological fluids, such as interstitial fluid, sweat, tears, and saliva, using different sensing mechanisms. The sensing platforms for flexible biosensors include solid-state sensing platforms, liquid-state sensing areas, and mechanical deformation-based sensing platforms. Flexible and wearable biosensors have been employed for continuous monitoring of respiration, skin temperature, pulse, blood pressure, electrocardiograms, humidity, phonation, and human motion. Depending on the physical quantities to be measured, flexible sensors can be categorized into humidity sensors, temperature sensors, strain sensors, and pressure sensors[lxix]. In 2015, Debashis Maji *et al*. advanced a flexible sensor for conformal integration applications. In 2016, Pei Liu *et al*. proposed a flexible FET biosensor for the detection of biomarkers. It is proved that the FET biosensor studied by Pei Liu *et al*. have excellent flexibility. The detection limit of flexible FET biosensor is 100 pg/mL. In the medical area, biosensors have been used for several years, and it is particularly the area that merits from the largest number of commercial devices, such as the glucometer, a biosensor that revolutionized the blood glucose levels controlling, progressing the quality of life of millions of diabetic people worldwide. And requirement from the biomedical sector is set to arise much further when we acknowledge the impact of "the medicine of the future" or "P4 medicine", that is anticipating, preventative, personalized, and participatory (Hood and Friend, 2011) [81]".

However, according to the marketing prospects, perhaps the vital challenge for biosensors to become basic analytical tools for P4 medicine is the ability to generate cost effective large-scale disposable devices, and especially with good perfections and reproducibility [69]. As an illustration, immune sensors are biosensors capable of quickly detecting antigens (or antibodies, depending on their configuration) in samples such as plasma, serum, blood, urine, and saliva. These tools are crucial for the development of rapid test kits, especially for infectious diseases like malaria, Zika, dengue, and COVID-19. Despite their widespread use, issues related to low sensitivity and specificity, which can lead to high rates of false-positive or false-negative results, remain significant obstacles that need optimization. The most recent breakthroughs in medical biosensors include wearable, implantable, and ingestible devices. Despite numerous publications detailing their applications in glasses, clothing, or patches capable of wirelessly communicating with smartphones, much work remains to confirm their long-

term stability and operational efficiency. Ingestible biosensors are even more recent and may represent the state-of-the-art in biosensor research and the future of personalized medicine (Mimee *et al*., 2018). These swallowable devices can monitor a range of parameters inside the human body, particularly in the digestive tract, and wirelessly transmit data to a remote monitoring system in real-time. Developing devices for detecting chemical or biological contaminants presents challenges where selectivity and specificity must be prioritized and optimized.

Advances in the following areas are highly welcomed in biosensing:

- Enhancing sensitivity, accuracy, and specificity of biosensors for serological rapid tests, especially for infectious diseases.
- Improving the reproducibility and scalability of manufactured point-of-care (POC) biosensor devices.
- Lowering the detection limit of POC biosensors for cardiac biomarkers and cancer detection.
- Optimizing the integration of genosensors with LAMP platforms to streamline sample preparation and provide rapid genetic tests.
- Developing disposable, high-efficiency, low-cost biosensor devices at scale.
- Integrating biochemical recognition layers with nanomaterials in detection areas.
- Enhancing the performance and optimization of wearable biosensors.
- Advancing the development of ingestible biosensors integrated with electronic devices for real-time *in vivo* monitoring.
- Creating robust and accurate biosensors integrated with remote control systems for environmental monitoring.
- Enhancing the robustness and accuracy of biosensors for applications in agriculture and quality control in the food industry.

The following parameters are critical challenges for the advancement of biosensor applications:

Considerations for Biosensor Device Design

The first stride in improving a biosensing device involves inspection of the target analyte and considerate how this analyte correlates with instant biological molecules. Once this has been settled, the following tasks are critical:

The specificity and selectivity of a biosensor device towards the analyte of interest is dependent upon the biological receptor. An advisable receptor with high affinity for the analyte is thus approved. Having ability of the advantages and disadvantages of various kinds of biological receptors in different biosensor applications is very crucial in choosing a convenient receptor [10, 15, 28].

Selection of a Suitable Immobilization Method: For any kind of biological molecule to achieve accurately as a biological receptor, it needs attachment onto the surface of a transducer. This technique is known as immobilization. Various processes have been used for this works which introduces adsorption, entrapment, covalent attachment, micro encapsulation and cross linking [31, 32].

Selection of a Transducer Element: The transducer element greatly affects the sensitivity of the biosensor. Involving the right transducer will result in a device with enhanced sensitivity while the sensitivity is more likely to be agreed by the use of an ineffective transducer.

Sensitivity

It is extremely challenging to detect analytes (such as cytokines, protein post-translational modifications, circulating cancer cells) due to the high background signal in clinical samples (Liu *et al*., 2021). To enhance sensitivity, nanomaterials-based signal amplification is one of the most popular strategies by taking advantages of a big surface area to load the maximum number of bio recognition molecules (Liu *et al*., 2019). Nanozymes are the rising star in this aspect with benefits in terms of stability, cost, sensitivity and reaction speed although their specificity needs to be further improved (Liang and Yan, 2019). Being different from nucleic acid-based signal amplification extensively used for detection of nucleic acids or other analytes, CRISPR/Cas technology has made a breakthrough in the field of BBE since 2017 due to its extremely high sensitivity and specificity (Li *et al*., 2019a). Cytokines are the trace amount of small proteins which is present in cerebrospinal fluid. The nature of cytokines under biological conditions can be affected by cytokine-binding proteins, inhibitors and soluble cytokine receptors (Liu *et al*., 2021). Interferences in the matrix of biological samples can cause false-positive signals. Therefore, to ensure accurate measurements, methods and conditions related to sample collection and handling should be carefully considered and specified. In order to achieve a reliable cytokine assay for *in situ* analysis in the brain or spinal cord, we developed a deployable device for sensitive detection of cytokines directly in brain space or spinal cord, which excluded the sampling

process and could work *in vivo* (Zhang *et al*., 2018). Therefore, in addition to signal amplification strategies used in bioassays, device engineering is crucial for enhancing sensitivity.

Selectivity

This indicates to the ability of the biosensor to selectively bound and acknowledge only to the convenient analyte, in the existence of other substances or molecules. When a response is created from interactions with an analyte that is distinct from the target analyte such is termed a false positive result. This is common in biosensors device with poor selectivity, thus declining in clinical applications. Selectivity is a very crucial propertie especially in medical applications where the test sample or sample matrix, usually blood or urine, consist of numerous molecules that are quite similar to the target analyte and clash for binding to the biological receptor

Stability

Stability of the biosensor device is a very crucial property especially for biosensors used for monitoring continuously. This property estimates the capability of the biosensor to prevent change in its achievement over a period of time in response to disruption which arises from external factors. These can be in the form of humidity temperature, or other environmental conditions. Such disruption have the possible to induce deception in the output signal during assessment, thereby influencing the precision and accuracy of the biosensor device. This is the reason that transducers and other electronic components that compose of the biosensor device which are often temperature sensitive and this can enormously affect their stability. Also, temperature can influence the integrity of the biological receptor as this parameter tends to degenerate with temperature fluctuations.

Detection Limit

This is defined as the lowest concentration of the target that can produce a detectable signal or response. Ideally, a biosensor should have a very low detection limit, particularly for medical applications where the target analyte may be present in extremely low concentrations.

Reproducibility

This is also one of the unique and important properties in biosensing, and assigns to the capability of the biosensor device to generate matching output signals or results in corresponding experimental runs. The ability of the biosensor to meet this convention awaits on the transducer which is mandatory to achieve in a proper and accurate manner.

Response Time

This feature estimates the time it takes to create a signal or response followed by the communication with the biological receptor with the target analyte.

Range or Linearity

The linearity estimates the accuracy of the signal gained, in response to a set of evidences by varying concentrations. This suggests that insight into the resolution of the biosensor, definite as the minimal change in the target analyte concentration that will bring out a response from the biosensor devices. This is a very crucial for a device as most applications need a biosensor to calculate a target analyte over wide range of concentration.

Biosensing Device Integration and Commercialization

The current COVID-19 pandemic has greatly increased the need for affordable and reliable laboratory diagnostics, especially in resource-limited countries. Bridging the gap between scientific knowledge and everyday medical practice is a significant challenge in qualifying laboratory-developed biosensors for commercial application. Integration of assays and devices is crucial to make them suitable for real-world applications. Integration of assays and devices is crucial to make them suitable for real-world applications. Two hurdles exist for benchtop technologies walking out of the lab to the market (Burd, 2010):

1) The translation of laboratory-based technologies into clinical studies.
2) To translate clinical studies into medical practice.

Current scientific research is focusing on passing the first hurdle as it can be managed through laboratory technology optimization. The second hurdle depends on the market effect since the new assays/devices need to be acceptable to the end-users/payers. Before entering the product market, any laboratory-developed assays or devices need to meet regulatory requirements, such as Food and Drug Administration (FDA), to ensure the accuracy, reliability, and appropriateness of clinical test results, regardless of where the test is performed (Genzen *et al*., 2017). Before the implementation of FDA-approved or cleared tests, laboratory-developed technologies must meet required performance characteristics such as reportable range, analytical sensitivity, precision, analytical specificity, accuracy, and reference interval. To overcome the second hurdle, market needs must be considered. For example, in resource-limited settings, detection systems

must not only be accurate, robust, and easy to use but also affordable for end users. Recent advances in paper-based microfluidic analytical devices and mobile phone-based diagnostics have significantly contributed to addressing these needs.

A disposable paper-based test strip can significantly low the detection cost and make it invasive by using a body fluid such as saliva or urine (Luo *et al*., 2020). By integration with personal equipment such as a mobile phone or a glucose test meter, self-quantitative detection can be performed by end-users without visiting the hospital. These simplified and integrated detection platforms are desirable for translating sensing technology into commercialization. But they face challenges (such as accuracy) Shrivastava *et al*. (2020), and require reliable assay/device standardization for these *in vitro* diagnostics (Lippi *et al*., 2016). Thus, extensive joint efforts between chemists, engineers, biologists, and clinicians, are necessary before clearing up the hazy road from bench to bedside for BBE.

Sustainability to the Ecosystem

Disposable sensors are inexpensive and in high demand as people today are well-connected and seek fast, accessible, and reliable health information (Dincer *et al*., 2019). Single-use sensors are crucial to prevent contamination. While these disposable biosensors offer convenience and speed, they also raise environmental concerns. Introducing electronics to make biosensing devices smart is essential, but how can we make our biosensors and biochips biodegradable? Recent advancements in sustainable sensing systems, such as wearable devices, paper-based biochips, smartphone-based detection, and recyclable biosensors, underscore the need for smarter, more user-friendly, cost-efficient, and eco-friendly biosensing systems. Researchers are focused on developing sustainable materials and systems for sensors. For instance, distance-based biosensors on filter paper have been created for instrument-free semi-quantitative analysis (Cinti *et al*., 2019). Paper-based devices are also known for their low cost, flexibility, and point-of-care testing capabilities with various signal readouts (Liu *et al*., 2019). Additionally, biodegradable materials like silk and hydrogels are widely used in biosensing devices (Xu *et al*., 2019). Achieving a sustainable sensing system with all desirable features is challenging, requiring a balance to develop advanced and smart biosensing devices or bioelectronics that are also environmentally sustainable (Singh *et al*., 2020).

In summary, modern biosensors and biomolecular electronics (BBE) aim to enable precise diagnosis by developing devices and systems that

advance in simplicity, sensitivity, specificity, affordability, multiplex capability, integration of various functions into a single biochip, *in vivo* sensing capability, and ecological sustainability. Bioelectronics focuses on advanced materials and bio-signal processing technologies toward intelligent systems. Additionally, the continuous development and validation of reliable biomarkers, new ultrasensitive transducer technology for profiling a range of biomarkers, detection automation, and verification/validation of devices in clinical testing are essential and challenging. These factors limit the rapid growth of biosensing technologies to be clinically valuable and competitively priced. In promoting cutting-edge research on creating smart, sensitive, and reliable biosensors and biomolecular electronics-from handheld devices to implantable systems-to improve health, we expect studies published in the specialty section of Biosensors and Biomolecular Electronics, under Frontiers in Bioengineering and Biotechnology, to address current challenges and define new challenges for the future, aiming for big data and big health.

Conclusions and Future Prospects

Recent advancements in the synthesis methods and application areas of various metal oxide nanostructures highlight their significant relevance and necessity in designing different types of sensors. Biosensors utilizing 1D or 2D structures demonstrate enhanced sensitivity due to their high surface area, particularly in hollow 1D nanostructures. Improving optical biosensors involves creating nanostructures that can tune and enhance optical signals for detecting target biological substances. With the continuous threaten of the COVID-19 pandemic to global health; the role of biosensor is becoming more and more essential in medical diagnostics and disease monitoring. Advances of technologies in the fields of chemistry, biomaterials, engineering, Nanotechnology, biotechnology, have significantly enhanced the advancement of this interdisciplinary forum of biosensor, proved by the appearance of improved sensing technologies in both academia and industry. As whole biosensing devices motivates to believe that improvement in terms of simplicity, sensitivity, affordability, multiplex capability, *in vivo* sensing capability, and sustainability to the ecosystem. However, there is still room for improvement and challenges related to different synthesis methods. Improvements and more research are required to form nanostructures without side effects and with the desired properties for the development of sensitive, reproducible, easy to use, and fast biosensors with minimal pollution of the living nature. The achievement of high stability and nontoxicity in various nanostructures formed from metal oxides, such as

ZnO, TiO_2 or SiO_2, which are applied *in vivo* biosensing and are exposed by different liquid ambient, is still an issue. The systems-to service better health, we expect the studies published in the specialty section, under Frontiers in Bioengineering and Biotechnology, to contribute to solve our current challenges, while defining new challenges for the future towards big data and big health. Therefore, we expect significant experimental and theoretical research activity regarding the synthesis methods for metal oxide nanostructures of different properties and application for sensing.

References

1. Balevicius, Z.; Paulauskas, A.; Plikusiene, I.; Mikoliunaite, L.; Bechelany, M.; Popov, A.; Ramanavicius, A.; Ramanaviciene, A. J. Mater. Chem. C, 6 (32), 8778–8783 (2018).
2. Maciulis, V.; Malinovskis, U.; Erts, D.; Ramanavicius, A.; Ramanaviciene, A.; Balevicius, S.; Juciute, S.; Plikusiene, I. Coatings, 10, 1018(2020).
3. Plikusiene, I.; Maciulis, V.; Graniel, O.; Bechelany, M.; Balevicius, S.; Vertelis, V.; Balevicius, Z.; Popov, A.; Ramanavicius, A.; Ramanaviciene, A. J. Mater. Chem. C, 9, 1345–1352(2021).
4. [Filipovic, L.; Selberherr, S. Nanomaterials, 12, 3651(2022).
5. Maduraiveeran, G.; Jin, W. Mater. Sci. Engineer. B, 272, 115341(2021).
6. Heard, C.J.; Cˇ ejka, J.; Opanasenko, M.; Nachtigall, P.; Centi, G.; Perathoner, S. Adv. Mater., 31, 1801712(2019).
7. Wang, L.; Huang, L.; Tan, W.C.; Feng, X.; Chen, L.; Huang, X.; Ang, K.W. Small Methods, 2, 1700294(2018).
8. Kumar, S.; Pavelyev, V.; Mishra, P.; Tripathi, N.; Sharma, P.; Calle, F. Mater. Sci. Semicond. Process.,107, 104865(2020).
9. Jang, J.M.; Kim, S.D.; Choi, H.M.; Kim, J.Y.; Jung, W.G. Mater. Chem. Phys. 113, 389–394(2009).
10. Chiu, H.Y.; Wi-Afedzi, T.; Liu, Y.T.; Ghanbari, F.; Lin, K.Y.A. J. Water Process Eng., 37, 101379(2020).
11. Yang, Z.; Lin, Y.; Jiao, F.; Li, J.; Wang, W.; Gong, Y.; Jing, X. Appl. Surf. Sci., 502, 144147(2020).
12. Tiwari, J.N.; Tiwari, R.N.; Kim, K.S. Prog. Mater. Sci. 57, 724–803(2012).

13. Nunes D, Pimentel A, Goncalves A, Pereira S, Branquinho R, Barquinha P, Fortunato E, Martins R Semicond Sci Technol, 34(4), 43001(2019).
14. Kumar S, Bukkitgar SD, Singh S, Singh V, Reddy KR, Shetti NP, Venkata Reddy C, Sadhu V, Naveen S, Chemistry Select, 4(18), 5322 (2019).
15. Palumbo G, Doyle D M, El-Sherik A M, Erb U and Aust K T Scr. Metall. Mater. 25, 679(1991).
16. Bakonyi I, Toth-Kada E, Tarnoczi T, Varga L K, Cziraki A, Gerocs I and Fogarassy B Nanostruct. Mater. 3, 155(1993).
17. Kyaw, H.H.; Al-Harthi, S.H.; Sellai, A.; Dutta, J. Beilstein J. Nanotechnol. 6, 2345(2015).
18. Ahmadzadeh-Raji, M.; Ghafar-Zadeh, E.; Amoabediny, G. Sensors, 16, 1071(2016).
19. Khlyustova A., Cheng Y. and Yang R.J. Mater. Chem. B, 8, 6588(2020).
20. Ozaydin-Ince G., Dubach J. M., Gleason K. K. and Clark H. A. PANS. 108, 2656(2011).
21. Chan K. and Gleason K. K. Langmuir, 21, 11773(2005).
22. Dorval Dion C. A., Raphael W., Tong E. and Tavares J. R. Surf. Coat. Tech. 244, 98(2014).
23. Baxamusa S. H., Montero L., Dubach J. M., Clark H. A., Borros S. and Gleason K. K. Biomacromolecules, 9, 2857(2008).
24. Tiwari J.N., Tiwari R.N., Kim K.S. Prog. Mater. Sci., 57, 724(2012).
25. Joshi R.K., Schneider J.J. Chem. Soc. Rev.; 41, 5285(2012).
26. Young C., Wang J., Kim J., Sugahara Y., Henzie J., Yamauchi Y. Chem. Mater.; 30, 3379(2018).
27. Altintas Yildirim O. Mater. Sci. Semicond. Process.; 101, 238(2019).
28. Pei Y., Hu M., Xia Y., Huang W., Li Z., Chen S. Sens. Actuators B Chem.; 304, 127416(2020).
29. Soganci, T., Ayranci, R., Harputlu, E., Ocakoglu, K., Acet, M., Farle, M., & Ak, M. Sens Actuators B, *273, 1501(2018).*

30. Han, S.T., Peng, H., Sun, Q., Venkatesh, S., Chung, K.S., Lau, S.C., Zh ou, Y., and Roy, V.A.L.: Adv. Mater. 29, 1700375 (2017).

31. Zhang, D., Zhang, K., Yao, Y.L., Xia, X.H., and Chen, H.Y.: Langmuir 20, 7303 (2004).

32. Choi, T., Kim, S.H., Lee, C.W., Kim, H., Choi, S-K., Kim, S-H., Kim, E., Park, J., and Kim, H.: 63, 325 (2015).

33. Ripka, P. and Janosek, M.: IEEE Sens. J. 10, 1108 (2010).

34. Lee, B., Roh, S., and Park, J.: Opt. Fiber Technol. 15, 209 (2009).

35. Hill, E.W., Vijayaragahvan, A., and Novoselov, K.: IEEE Sens. J. 11, 3161 (2011).

36. Tereshchenko, A., Fedorenko, V., Smyntyna, V., Konup, I., Konup, A., Eriksson, M., Yakimova, R., Ramanavicius, A., Balme, S., and Bechelany, M.: Biosens.Bioelectron. 92, 763 (2017).

37. Dominik, M., Lesniewski, A., Janczuk, M., NiedziolkaJoensson, J., Holdynski, M., Wachnicki, L., Godlewski, M., Bock, W.J., and Smietana, M.: Biosens. Bioelectron. 93, 102 (2017).

38. Comstock, D.J., Christensen, S.T., Elam, J.W., Pellin, M.J., and Hersam, M.C.: Adv. Funct. Mater. 20, 3099 (2010).

39. Fryčeka, R.; Jelínek, M.; Kocourek, T.; Fitl, P.; Vrňata, M.; Myslík, V.; Vrbová, M. Thin Solid Films, 495, 308(2006).

40. Houser, E.J.; Chrisey, D.B.; Bercu, M.; Scarisoreanu, N.D.; Purice, A.; Colceag, D.; Constantinescu, C.; Moldovan, A.; Dinescu, M. Appl. Surf. Sci. 252, 4871(2006).

41. Bloisi, F.; Vicari, L.; Papa, R.; Califano, V.; Pedrazzani, R.; Bontempi, E.; Depero, L.E. Mater. Sci. Eng. C, 27, 1185(2007).

42. Cristescu, R.; Mihaiescu, D.; Socol, G.; Stamatin, I.; Mihailescu, I.N.; Chrisey, D.B. Appl. Phys. A, 79, 1023(2004).

43. Stamatin, L.; Cristescu, R.; Socol, G.; Moldovan, A.; Mihaiescu, D.; Stamatin, I.; Mihailescu, I.N.; Chrisey, D.B. Appl. Surf. Sci. 248, 422(2005).

44. Trojanowicz, M. Electrochem. Comm. 38, 47(2014).

45. Nasratun, M.; Said, H.A.; Noraziah, A.; Alla, A.N.A. Am. J. Appl. Sci. 6, 1653(2009).

46. György, E., Sima, F., Mihailescu, I. N., Smausz, T., Hopp, B., Predoi, D., & Petrescu, S. M. Mater. Sci. Eng. C, 30(4), 537(2010).

47. Aronne, A., Bloisi, F., Calabria, R., Califano, V., Depero, L. E., Fanelli, E., & Vicari, L. R. Appl. Surf. Sci., *336*, 196(2015).

48. Caruso, F. Adv. Mater., 13(1), 11(2001).

49. Pandey, P., Datta, M., & Malhotra, B. D. Anal. Lett, 41(2), 159(2008).

50. Gupta, A. K., & Gupta, M. biomaterials, 26(18), 3995(2005).

51. Zhang, G., Liu, H., Qu, J., & Li, J. Energy Environ. Sci., 9(4), 1190(2016).

52. He, Q.; Zeng, Z.; Yin, Z.; Li, H.; Wu, S.; Huang, X.; Zhang, H. Small, 8, 2994(2012).

53. Lin, Y. C.; Dumcenco, D. O.; Huang, Y. S.; Suenaga, K. Nat. Nanotechnol., 9, 391(2014).

54. Zhang, D., Jiang, C., Li, P., & Sun, Y. E. ACS Appl. Mater. Interfaces., *9*(7), 6462(2017).

55. Mutalik, C., Krisnawati, D. I., Patil, S. B., Khafid, M., Atmojo, D. S., Santoso, P., & Kuo, T. R. ACS Sustain. Chem. Eng., *9*(23), 7904(2021).

56. Dong, H., Tang, S., Hao, Y., Yu, H., Dai, W., Zhao, G., & Ju, H. ACS Appl. Mater. Interfaces., *8*(5), 3107(2016).

57. Wang, Y., & Ni, Y. Analytical chemistry, 86(15), 7463(2014).

58. Liu, T., Chao, Y., Gao, M., Liang, C., Chen, Q., Song, G., & Liu, Z. Nano Research, 9, 3003(2016).

59. Chao, J., Zou, M., Zhang, C., Sun, H., Pan, D., Pei, H., & Wang, L. Nanotechnology, 26(27), 274005(2015).

60. Wang, X., Chu, C., Shen, L., Deng, W., Yan, M., Ge, S., & Song, X. Sens Actuators B Chem, 206, 30(2015).

61. Ling, Y., Cao, T., Liu, L., Xu, J., Zheng, J., Li, J., & Zhang, M. J. Mater. Chem. B, *8*(34), 7801(2020).

62. Zheng, J., Song, D., Chen, H., Xu, J., Alharbi, N. S., Hayat, T., & Zhang, M. Chin. Chem. Lett., *31*(5), 1109(2020).

63. Wang, C., Du, J., Wang, H., Zou, C. E., Jiang, F., Yang, P., & Du, Y. Sens Actuators B Chem, 204, 302(2014).

64. Huang, M., Liu, C., Cui, P., Wu, T., Feng, X., Huang, H., & Wang, Y. Environ. Sci. Technol., 55(19), 13132(2021).

65. Qin, Z., Yue, Q., Liang, Y., Zhang, J., Zhou, L., Hidalgo, O. B., & Liu, X. J. Biotech., 284, 52(2018).

66. Wu, Q., Huang, L., Li, Z., An, W., Liu, D., Lin, J., & Wu, W. Nanoscale Res. Lett., 11, 1(2016).

67. Dabhane, H., Ghotekar, S., Tambade, P., Pansambal, S., Murthy, H. A., Oza, R., & Medhane, V. J. Environ. Chem. Ecotoxicol., 3, 209(2021).

68. Shivaji, K., Mani, S., Ponmurugan, P., De Castro, C. S., Lloyd Davies, M., Balasubramanian, M. G., & Pitchaimuthu, S. ACS Appl. Nano Mater., 1(4), 1683(2018).

69. Bharti, D. B., Bharati, A. V., & Wankhade, A. V. Luminescence, 33(8), 1445(2018).

70. Zucolotto, V. (2020). Specialty grand challenges in biosensors. Frontiers in Sensors, 1,

Chapter - 7
Biological Applications of Differential Equations: A Study of Malaria Transmission

Authors

Sreya Saha
Department of Mathematics, Sister Nivedita University, New Town, Chakpachuria, West Bengal, India

Najnin Islam
Department of mathematics, Swami Vivekananda University, Kolkata, West Bengal, India

Souvik Kundu
Department of Mathematics, Heritage Institute of Technology, Kolkata, West Bengal, India

Chapter - 7

Biological Applications of Differential Equations: A Study of Malaria Transmission

Sreya Saha, Najnin Islam and Souvik Kundu

Abstract

Malaria is a major global health concern, particularly in tropical and subtropical regions. Mathematical modelling can provide a very accurate understanding and prediction of the dynamics of malaria transmission. Through the use of ordinary differential equations, the model represents the transmission dynamics within a given population. It talks about how humans transition between different compartments and what causes these changes. The model quantifies the effects of different situations, allowing the computation of epidemiological measures such as the basic reproductive number.

Introduction

DEs are an effective modelling and analysis tool for intricate biological systems. They are crucial for the study of biology because they aid in the modelling and comprehension of intricate biological systems and events.

Here are a few examples:

Population Dynamics

DEs can be used to model the growth and interaction of populations of and between living organisms, such as the spread of a disease or the competition between two species. These models can help us understand how populations change over time, and how external factors such as environmental conditions or human intervention can affect them. For example, the dynamics of interactions between predators and prey are modelled using a set of differential equations called the Lotka-Volterra equations [8].

Neuroscience

DEs are used in the modelling of neurons and neural networks. They can be used to describe the dynamics of ion channels, the firing rate of neurons,

and the propagation of action potentials. These models can help us understand how the brain processes information and how neurological disorders can arise. For example, one set of differential equations used to simulate the behaviour of action potentials in neurons is the Hodgkin-Huxley model [9].

Pharmacokinetics

DEs can be used to simulate how pharmaceuticals are absorbed, distributed, metabolised, and eliminated from the body. These models can enable us in understanding how drugs interact with the body and how to optimize their effectiveness while minimizing their side effects [10].

Biochemical reactions

Differential equations can be used to model chemical reactions that occur in living organisms, such as enzyme-substrate interactions, metabolic pathways, and gene regulation. These models can aid in our understanding of the mechanisms underlying these reactions and how environmental variables like pH and temperature affect them. The Michaelis-Menten equation, for instance, is a differential equation used to explain the kinetics of enzymes [11].

Genetics

DEs are used to simulate how traits are passed down via populations. An example of a set of differential equations used to model the frequency of alleles in a population over time is the Hardy-Weinberg equation.

Epidemiology

DEs help us to model the contagious diseases spread among people. These models can help us understand how diseases are transmitted and how to control their spread through vaccination, quarantine, or other interventions. For example, the SIR (susceptible-infected- recovered) model is a set of DEs used for modelling the spread of diseases like COVID-19 [12].

Malaria

By biting humans, female Anopheles mosquitoes carrying the Plasmodium parasite can spread the parasitic disease known as malaria to people. Millions of people around the world are afflicted by the illness, which also kills a lot of people, especially in sub-Saharan Africa [20].

Malaria symptoms include fever, chills, headaches, and aches and pains in the muscles. In extreme circumstances, problems like anaemia, organ

failure, and even death may result. Antimalarial medications, which go after the infecting parasite, are used in the treatment of malaria. The treatment of malaria has become more difficult in recent years due to the Plasmodium parasite's rising drug resistance [21, 22]. Use of bed nets sprayed with pesticide, indoor residual spraying, and chemoprevention are examples of prevention tactics. Overall, mathematical models have played a significant role in informing malaria control and elimination strategies, helping to identify the most effective interventions and allocate resources efficiently. Ongoing research continues to refine and improve these models, incorporating new data and accounting for emerging challenges such as drug resistance and climate change [23, 24, 25].

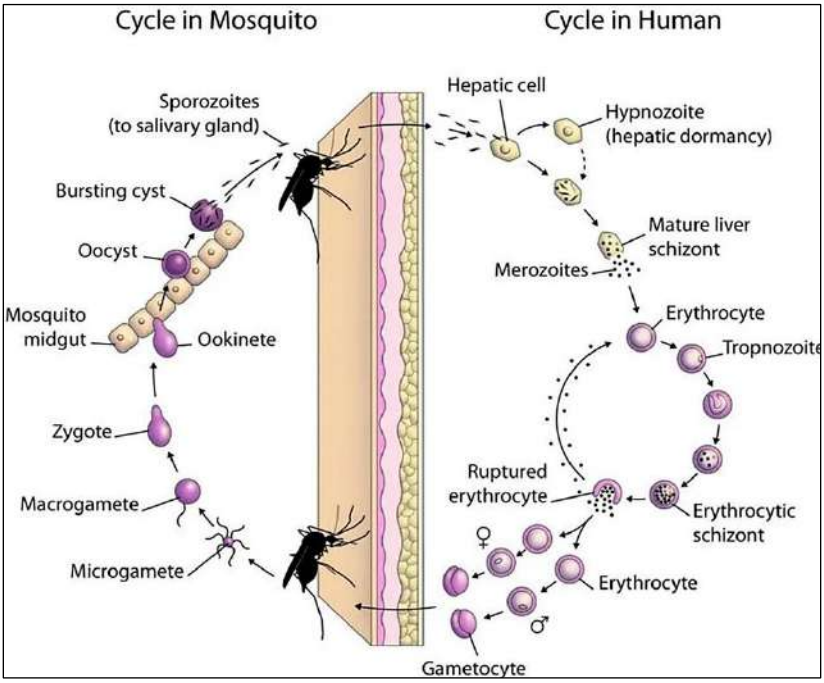

Mathematical Model

$$\frac{dS_H}{dt} = \Lambda_H + \omega_H R_H - \beta_H \left(\frac{I_M}{N_M}\right) S_H - \mu_H S_H$$

$$\frac{dE_H}{dt} = \beta_H \left(\frac{I_M}{N_M}\right) S_H - \{(\alpha_H + \mu\}_H) E_H$$

$$\frac{dI_H}{dt} = \alpha_H E_H - (\delta_H + \mu_H - \mu_H r_H) I_H$$

$$\frac{dR_H}{dt} = \delta_H E_H - (\omega_H + \mu_H) R_H$$

$$\frac{dI_M}{dt} = \beta_M \left(\frac{I_H}{N_H}\right)(\overline{N_H} - I_M) - \mu_M I_M$$

$$r_H = \frac{\lambda_H - \rho_H}{\mu_H}$$

Where,

$N_H(t) = S_H(t) + E_H(t) + I_H(t) + R_H(t)$

$N(t) \rightarrow$ Total human population at time t per capita μ_H

$S(t) \rightarrow$ Susceptible human population at time t per capita μ_H

$E(t) \rightarrow$ Exposed human population at time t per capita μ_H

$I(t) \rightarrow$ Infected human population at time t per capita μ_H

$R(t) \rightarrow$ Recovered human population at time t per capita μ_H

$N(t) \rightarrow$ total mosquito (vector) population at constant rate Λ_M per capita mortality rate μ_M

$S(t) \rightarrow$ Susceptible vector population per capita mortality rate μ_M

$I(t) \rightarrow$ Infected vector population per capita mortality rate μ_M

Here, $N(t) = SM(t) + IM(t)$

$\frac{dN_H}{dt} = \Lambda_M - \mu_M N_M$, which implies that $0 \leq N_M(t) \leq \overline{N_M}$ for all $t \geq 0. Thus, \overline{N_M} = \frac{\Lambda_M}{\mu_M}$

$N_M(t) \rightarrow \overline{N_M}$ when $t \rightarrow \infty$ which implies $S_M(t) \rightarrow \overline{N_M} - I_M$

Parameter	Interpretation	Dimension
ΛH	Recruitment rate for humans	$Humans\ X\ Day^{-1}$
μH	Human mortality rate	Day^{-1}
μM	Vector mortality rate	Day^{-1}
ωH	Per capita immunity loss	Day^{-1}
βHM	Probability of human infection by mosquito	$Adimentional$
βMH	Probability of mosquito infection by human	$Adimentional$
ϵ	Effective biting rate	Day^{-1}
1	Period of exposure	Day^{-1}
$\frac{\overline{\alpha H}}{\rho H}$	Per capita mortality rate due to infection	Day^{-1}
1	Period of infection	Day^{-1}
$\frac{\overline{\delta H}}{\Lambda M}$	Recruitment rate of mosquitos	$Vector\ X\ Day^{-1}$

λH	Percentage of vertical transmission	$Adimentional$

Disease Free Equilibrium

The disease-free equilibrium (DFE) occurs when there are no infected individuals in the population, i.e., $I_H = I_M = 0$. At the DFE, the susceptible and exposed populations remain constant over time. Thus, we solve for the remaining variables (S_H, E_H, R_H):

At the disease-free equilibrium, the rate of new infections is zero. This gives us two possibilities:

1. S_H = **0**

In this case, there are no susceptible individuals in the population, which means everyone is either exposed, infected, or recovered. However, since we have set $IH = IM = 0$, this is not a valid equilibrium.

2. Q_H = **0**

In this case, the transmission rate is zero, which means the disease cannot spread.

As the disease does not spread so $E_H = 0 \; and, R_H = 0$

We have, $N_H = S_H + E_H + I_H + R_H$

$\Rightarrow N_H = S_H$

Thus, the model becomes as follows:-

$\frac{dS_H}{dt} = \Lambda_H - \mu_H S_H$

Now putting $\frac{dS_H}{dt} = 0$

$\Lambda_H - \mu_H S_H = 0$

$\Rightarrow \Lambda_H = \mu_H S_H$

$\frac{\Lambda_H}{\mu_H} = S_H = N_H$

Therefore, the disease-free equilibrium is:

$NH = SH, IH = IM = RH = EH = \beta H = 0,$

and $\frac{\Lambda_H}{\mu_H} = S_H.$

Note that this equilibrium assumes that there are no external sources of infection (i.e., all infections originate within the population). If there are external sources of infection, then the disease-free equilibrium may not be stable [26, 27].

Basic Reproductive Number for the model:

For the given system, the infectious compartments are IH and I_M. Let us assume that an average infected individual stays in the infectious compartment for a duration of $\frac{1}{\delta_H}$(for I_H)$or\frac{1}{\delta_M}$(for I_M) time units. The transmission rates for IH and IM are βH and βM, respectively and μH and μM denote the removal rates, respectively [28, 29, 30].

$$R_0 = \frac{\beta_H \beta_M \alpha_H}{(\alpha_H+\mu_H)(\delta_H+(1-r)\mu_H)}$$

- β_H represents the transmission rate of the pathogen from infected individuals to susceptible individuals in the human population.
- α_H represents the probability of an exposed individual becoming infected where α_H represents the rate of transition from the exposed class to the infected class, and μH is the natural mortality rate in the human population.
- $\frac{\beta_M}{\delta_H+(1-c_H)\mu_H}$ represents the probability of transmission of the pathogen from infected.
- Mosquitoes to susceptible humans, where βM is the transmission rate from mosquitoes to humans, δH is the rate of recovery from infection in humans, μH is the natural mortality rate in the human population, and rH is the average time taken by a mosquito to become infectious after acquiring the pathogen.

Therefore, the expression for R_0considers the transmission rates, probabilities of infection, recovery rates, and natural mortality rates in both the human and mosquito populations.

To find the values of R_0 for which it is greater than 1, equal to 0, and less than 1,

Case-A: $(\alpha_H + \mu_H)\,(\delta_H + (1 - \tau_H)\,\mu H) > 0$.

1. $R_0 > 1$, if $\beta_H\beta_M\alpha_H > (\alpha_H + \mu_H)\,(\delta_H + (1 - \tau_H)\,\mu H)$.
2. $R_0 = 0$, if $\beta_H\beta_M\alpha_H = 0$.
3. $R_0 < 1$, if $\beta_H\beta_M\alpha_H < (\alpha_H + \mu_H)\,(\delta_H + (1 - \tau_H)\,\mu H)$.

Case-B: $(\alpha_H + \mu_H)\,(\delta_H + (1 - \tau_H)\,\mu H) < 0$.

Then R_0 is not a meaningful quantity, as the signs of the numerator and denominator are opposite.

Case-C: $(\alpha_H + \mu_H)(\delta_H + (1 - \tau_H)\mu H) = 0$

1. If $(\alpha_H + \mu_H) = 0$ and $\beta_H\beta_M\alpha_H \neq 0$, then $R_0 > 1$.
2. If $(\delta_H + (1 - \tau_H)\mu H) = 0$ and $\beta_H\beta_M\alpha_H \neq 0$, then $R_0 < 1$.
3. If $(\alpha_H + \mu_H)(\delta_H + (1 - \tau_H)\mu H)$, then $R_0 = 0$.

Therefore, we need to calculate the values of the parameters to determine the values of R_0:

If $\beta_H\beta_M\alpha_H > (\alpha_H + \mu_H)(\delta_H + (1 - \tau_H)\mu H)$, then $R_0 > 1$. If $\beta_H\beta_M\alpha_H < (\alpha_H + \mu_H)(\delta_H + (1 - \tau_H)\mu H)$, then $R_0 < 1$. If $\beta_H\beta_M\alpha_H = (\alpha_H + \mu_H)(\delta_H + (1 - \tau_H)\mu_H)$, then $R_0 = 0$.

Note that if $(\alpha_H + \mu_H)(\delta_H + (1 - \tau_H)\mu_H) < 0$, then R_0 is not meaningful.

In the following observations $R_0 < 1$, we can see that as time passes the spread of disease reduces and it clearly shows that as time passes the disease will die out.

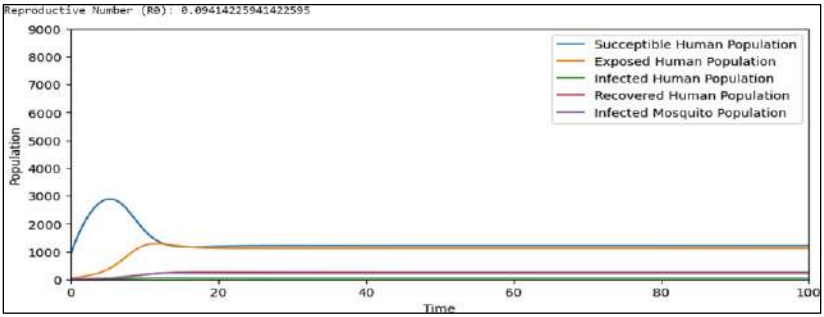

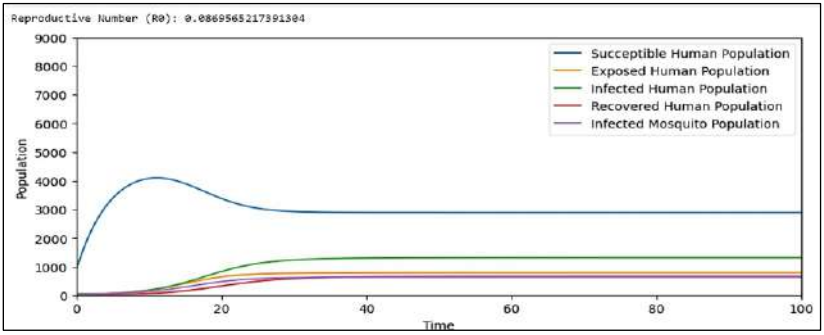

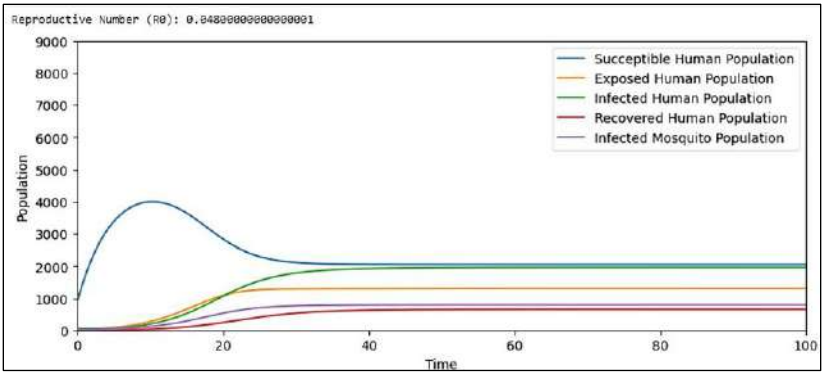

Conclusion

A thorough foundation for comprehending the dynamics and spread of malaria within a community is provided by the mathematical model for malaria transmission offered in this paper, in conclusion. The model offers important insights into the behavior of the illness by include important aspects and mechanisms involved in transmission, such as interactions between humans and mosquitoes and other epidemiological data.

Important epidemiological metrics, including the fundamental reproductive number R_0, are identified through model analysis. R_0 serves as a significant indicator of the potential for sustained transmission within a population and offers essential guidance for control and prevention tactics. Researchers and policymakers can evaluate the efficacy of various control measures using the model, which also allows for the investigation of alternative scenarios and actions.

Overall, the mathematical model for malaria transmission aids in the fight against and eradication of the disease. The model is a useful resource for researchers, public health authorities, and policymakers since it offers a mathematical understanding of transmission patterns and assesses control methods. In order to reduce the worldwide burden of malaria and enhance the health of impacted communities, further development and deployment of such models will be essential.

References

1. Dennis G. Zill (15 March 2012). A First Course in Differential Equations with Modeling Applications. Cengage Learning. ISBN 978-1-285-40110-2.
2. Weisstein, Eric W. "Ordinary Differential Equation Order". From Math World-A Wolfram Web Resource. http://mathworld.wolfram.com/OrdinaryDifferentialEquationOrder.html

3. Polyanin, A. D.; Zaitsev, V. F. (2003). Handbook of Exact Solutions for Ordinary Differential Equations (2nd ed.). Boca Raton: Chapman & Hall/CRC Press. ISBN 1-58488-297-2.
4. Boyce, William E.; DiPrima, Richard C. (1967). Elementary Differential Equations and Boundary Value Problems (4th ed.). John Wiley & Sons. p. 3.
5. Strogatz, S. H. (2001). Nonlinear Dynamics and Chaos: with Applications to Physics, Biology and Chemistry. Perseus.
6. Guardia, M.; Martinez-Seara, M.; Teixeira, M. A. (2011). Generic bifurcations of low codimension of planar Filippov Systems. "Journal of differential equations", Febrer 2011, vol. 250, núm. 4, pp. 1967-2023. DOI: 10.1016/j.jde.2010.11.016
7. Founargiotakis, M.; Farantos, S. C.; Skokos, Ch.; Contopoulos, G. (1997). "Bifurcation diagrams of periodic orbits for unbound molecular systems: FH2". Chemical Physics Letters. 277 (5–6): 456–464. Bibcode:1997CPL... 277..456F. doi:10.1016/S0009-2614(97)00931-7.
8. Lotka, A. J. (1925). Elements of physical biology. Williams & Wilkins.
9. Izhikevich, E. M. (2007). Dynamical systems in neuroscience: The geometry of excitability and bursting. MIT Press. Hodgkin, A. L., & Huxley, A. F. (1952). A quantitative description of membrane current and its application to conduction and excitation in nerve. The Journal of Physiology, 117(4), 500-544.
10. Gibaldi, M., & Perrier, D. (1982). Pharmacokinetics (2nd ed.). Marcel Dekker.
11. Keener, J., & Sneyd, J. (2009). Mathematical physiology. Springer.
12. Kermack, W. O., & McKendrick, A. G. (1927). A contribution to the mathematical theory of epidemics. Proceedings of the Royal Society of London. Series A, Containing Papers of a Mathematical and Physical Character, 115(772), 700-721.
13. Porta, Miquel (2014). A Dictionary of Epidemiology (6th ed.). New York: Oxford University Press. ISBN 978-0-19-997673-7. Retrieved 16 July 2014.
14. Heesterbeek, J.A.P. (2002). "A brief history of R0 and a recipe for its calculation". Acta Biotheoretica. 50 (3): 189–204. doi:10.1023/a:1016599411804. hdl:1874/383700. PMID 12211331. S2CID 10178944.

15. Smith DL, Battle KE, Hay SI, Barker CM, Scott TW, McKenzie FE (April 5, 2012). "Ross, macdonald, and a theory for the dynamics and control of mosquito-transmitted pathogens". PLOS Pathogens. 8 (4): e1002588. doi: 10.1371/journal.ppat.1002588. PMC 3320609. PMID 22496640.

16. Ross R: Some a priori pathometric equations. Br Med J 1915, 1:546-447.

17. Macdonald G (September 1952). "The analysis of equilibrium in malaria". Tropical Diseases Bulletin. 49 (9): 813–29. PMID 12995455.

18. Macdonald G: The epidemiology and control of malaria London: Oxford University Press; 1957

19. Anderson RM, May RM: Infectious diseases of humans: dynamics and control London: Oxford University Press; 1991.

20. World Health Organization (WHO) and WHO Global Malaria Programme. [http://www.who.int/topics/malaria/en/], http://www.who.int/malaria/about_us/en/index.html

21. W. W. A. Woldegerima, M. I. Teboh-Ewungkem, G. A. Ngwa, Sensitivity analysis for a within-human host immuno-pathogenesis dynamics of Plasmodium falciparum parasites, Texts Biomath. 1 (2018), 140–168.

22. F. Forouzannia, A. B. Gumel, Mathematical analysis of an age-structured model for malaria transmission dynamics, Math. Biosci. 247 (2014), 80–94.

23. Mathematical Modeling of Malaria Disease with Control Strategy https://doi.org/10.28919/cmbn/4513 ISSN: 2052-2541

24. N. Chitnis, J. M. Cushing, & J. M. Hyman, Bifurcation analysis of a mathematical model for malaria transmission. SIAM Journal on Applied Mathematics, 67(1), (2006), 24-45.

25. C. Chiyaka, J. M. Tchuenche, W. Garira, & S. Dube, A mathematical analysis of the effects of control strategies on the transmission dynamics of malaria. Applied Mathematics and Computation, 195(2), (2008), 641-662.

26. B. S. E. Iyare, F. E. U. Osagiede, Analysis of a malaria disease model with direct transmission. Journal of mathematics and technology, 2(3), 21-26.

27. J. Montoya, JP. Romero-Leiton and E. Ibarg¨uen-Mondrag´on, Qualitative analysis of a mathematical model applied to malaria disease transmission in Tumaco (Colombia), Applied Mathematical Sciences 12(5), 205-217 (2018).

28. K. Dietz, L. Molineaux and A. Thomas, A malaria model tested in the African savannah, Bulletin of the World Health Organization 50 347-359 (1974).

29. J. Rodr´ıguez, G. Uribe, R. Araujo, P. Narvaez and S. Valencia, Epidemiology, and control of malaria in Colombia, Memorias do Instituto Oswaldo Cruz, 106114-122 (2011).

30. G. A. Ngwa, Modelling the dynamics of endemic malaria in growing populations. Discrete and Continuous Dynamical Systems Series B, 4, (2004), 1173-1202

Chapter - 8
Examining Compartmental Models' Effectiveness in Building Mathematical Models of Infectious Diseases

Authors

Nivedita Prasad
Department of Mathematics, Amity University, Kolkata, Rajarhat, New Town, Kolkata, West Bengal, India

Ramakant Bharadwaj
Department of Mathematics, Amity University, Kolkata, Rajarhat, New Town, Kolkata, West Bengal, India

Najnin Islam
Department of mathematics, Swami Vivekananda University, Kolkata, West Bengal, India

Souvik Kundu
Department of Mathematics, Heritage Institute of Technology, Kolkata, West Bengal, India

Chapter - 8

Examining Compartmental Models' Effectiveness in Building Mathematical Models of Infectious Diseases

Nivedita Prasad, Ramakant Bharadwaj, Najnin Islam and Souvik Kundu

Abstract

Understanding the dynamics of infectious illnesses and developing public health interventions are greatly aided by mathematical modelling. Compartmental models are among the most popular modelling techniques because of their efficiency and ease of usage. The usefulness of compartmental models for creating mathematical depictions of infectious diseases is reviewed in this article. We examine the theoretical underpinnings of compartmental models and how well they can represent key epidemiological variables including latent periods, recovery rates, and transmission rates. We also look at how flexible compartmental models are in modelling various illness scenarios, including the effects of interventions like social distance and vaccination campaigns. This article attempts to shed light on the benefits and drawbacks of compartmental models for supporting infectious disease control strategies and assisting in public health decision-making through a thorough study of the literature and case studies.

Introduction

Disease modeling is critical for understanding and managing infectious diseases. Disease modeling is a useful tool for analyzing and predicting disease spread, allowing public health officials to make more educated disease control and prevention decisions. Several surveys and literature studies have highlighted the importance of mathematical modeling in this sector.

One important contribution is Berry and Houston's 1995 [1] work, "Mathematical Modeling," which offers the groundwork for understanding the principles and uses of mathematical modeling in various disciplines, including infectious diseases. Frejd and Bergsten (2016) [2] put light on mathematical modeling as a professional job, emphasizing its importance in resolving complicated issues, particularly those related to infectious disease

dynamics. Their findings lead to a better understanding of the practical applications of mathematical modeling in real-world situations.

Kuddus *et al*. (2021) [3] conducted a more current study on the mathematical analysis of measles transmission dynamics in Bangladesh, which included double-dose vaccine techniques. This study sheds light on the particular dynamics of measles transmission and the impact of vaccination interventions in a real-world setting. The mathematical model for Measles, as described in our study, delves into the invariant region, positivity of solutions, and equilibrium points, including the Disease-Free Equilibrium Point and the Endemic Equilibrium Point. We use the Effective Reproduction Number to evaluate the impact of immunization regimens. The Stability Analysis section delves deeply into the local and global stability elements of Disease-Free and Endemic Equilibrium points, resulting in a more comprehensive understanding of measles dynamics.

Extending our attention to influenza, the result is consistent with the findings of Brauer, Castillo-Chavez, and Feng [4] and Arsal, Shinta R., Dipo Aldila, and Bevina D. Handari [5] in their seminal work on influenza models. We also investigate the impact of treatment of infected individuals on the dynamics of measles in the population [6]. We consider two phases of infectious for our model [7]. Our mathematical modeling approach for Influenza addresses comparable issues, such as the invariant region, solution positivity, equilibrium points, effective reproduction number, and stability analysis.

Mathematical Model

Model 1 (Measles)

The provided model describes the dynamics of measles transmission in a population divided into six compartments: susceptible (S(t)), exposed (E(t)), infected (I(t)), quarantined (Q(t)), vaccinated (V(t)), and recovered (R(t)). The model incorporates various parameters that govern the dynamics of the population in the context of infectious disease transmission. These parameters play crucial roles in determining the rates of transition between different compartments. The recruitment rate (μ) represents the influx of individuals into the susceptible compartment, encompassing both birth and other forms of recruitment. The death rate (δ) reflects the natural attrition of the population. The transmission rate (β) influences the speed at which susceptible individuals become infected upon contact with infectious individuals. The rate of latent individuals becoming infected (σ) captures the progression from the exposed compartment to the actively infected state. The

recovery rate (γ) signifies how swiftly infected individuals recover and move to the recovered compartment. The rate of individuals moving from infected to quarantined (α) denotes the transition of infected individuals to the quarantined compartment, potentially due to public health measures. The rate of vaccination (ρ) represents the pace at which susceptible individuals receive vaccination, gaining immunity and avoiding infection. Each of these parameters contributes to the overall dynamics of the model, shaping the interactions between different segments of the population over time. The model is represented by a system of non-linear ordinary differential equations (ODEs) that govern the rate of change of each compartment with respect to time.

$$\begin{aligned}
\frac{dS}{dt} &= \mu - \beta SI - \delta S - \rho S \\
\frac{dE}{dt} &= \beta SI - \delta E - \sigma E \\
\frac{dI}{dt} &= \sigma E - \gamma I - \delta I - \alpha I \\
\frac{dR}{dt} &= \gamma I - \delta R + \gamma Q \\
\frac{dQ}{dt} &= \alpha I - \delta Q - \gamma Q \\
\frac{dV}{dt} &= \rho S - \delta V
\end{aligned} \tag{1}$$

Parameter description of the above model is given in Table 1. Also, the diagrammatic representation of our model is described in Figure 1.

Table 1: Description of Parameters

Parameters	Description
μ	Recruitment rate
δ	Death rate
β	Transmission rate
σ	Rate of latent individuals becoming infected
γ	Recovery rate
α	Rate of individuals moving from infected to quarantined
ρ	Rate of vaccination

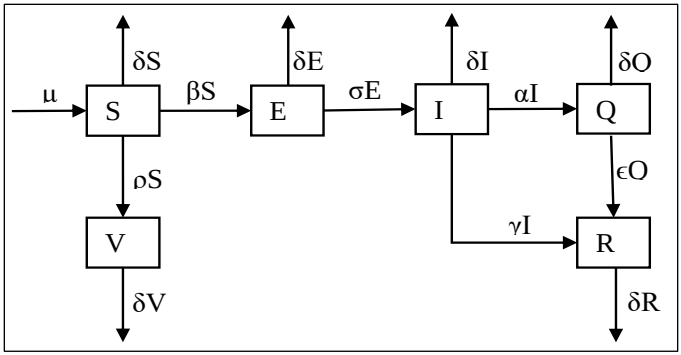

Fig 1: Transfer Diagram of the model

Invariant Region

Theorem 1: Assuming the model's solution are valid, the visible solution set Ω = {(S, E, I, R, Q, V) ϵ $\mathbb{R}^6$} of the model with initial conditions as follows

S (0) =$S_0 \geq 0$, E (0) = $E_0 \geq 0$, I (0) = $I_0 \geq 0$, R (0) =$R_0 \geq 0$, Q (0) =$Q_0 \geq 0$, V (0) =$V_0 \geq 0$. (2)

Then, Ω = {(S, E, I, R, Q, V) ϵ $\mathbb{R}^6$: $0 \leq N \leq \frac{\mu}{\delta}$ } is a bounded region.

Proof: The total population of our assumed model can be given by:

N(t)= S(t)+ E(t)+ I(t)+ R(t)+ Q(t)+ V(t) (3)

Then, integrating both side of the above equation with respect to t, we will get the following equation:

$$\frac{dN}{dt} = \frac{dS}{dt} + \frac{dE}{dt} + \frac{dI}{dt} + \frac{dR}{dt} + \frac{dQ}{dt} + \frac{dV}{dt} \quad (4)$$

After substituting the system of equation (1) in the above equation we will get:

$$\frac{dN}{dt} = \mu - \delta(S + E + I + R + Q + V) = \mu - \delta N \quad (5)$$

Consider, there is no death due to measles then the above equation will become:

$$\frac{dN}{dt} \leq \mu - \delta N \quad (6)$$

Integrating the above equation by taking limit $t \to \infty$, we get:

Ω = {(S, E, I, R, Q, V) ϵ $\mathbb{R}^6$: $0 \leq N \leq \frac{\mu}{\delta}$ } (7)

Which is a non-negative invariant set for the system of above given model.

Positivity of Solutions

Theorem 2: Suppose the initial values of the mode (S(0), E(0), I(0), R(0), Q(0), V(0)) ≥ 0 belong to the set Ω i.e. the invariant set, then the solution set {(S(t), E(t), I(t), R(t), Q(t), V(t)} is non-negative for time t ≥ 0.

Proof: From the 2nd equation of system of equation (1) we have,

$$\frac{dE}{dt} = \beta SI - \delta E - \sigma E,$$

$$\frac{dE}{dt} \geq -(\delta + \sigma)E,$$

$$E(t) \geq E_0 e^{-(\delta+\sigma)t} \geq 0. \quad (8)$$

From the 3rd equation of system of equation (1) we have,

$$\frac{dI}{dt} = \sigma E - \gamma I - \delta I - \alpha I,$$

$$\frac{dI}{dt} \geq -(\gamma + \delta + \alpha)I,$$

$$I(t) \geq I_0 e^{-(\gamma+\delta+\alpha)t} \geq 0. \quad (9)$$

From the 1st equation of system of equation (1) we have,

$$\frac{dS}{dt} = \mu - \beta SI - \delta S - \rho S,$$

$$\frac{dS}{dt} \geq -(\beta I + \delta + \rho)S,$$

$$S(t) \geq S_0 e^{-(\beta I+\delta+\rho)t},$$

$$S(t) \geq S_0 e^{-\left(\beta I_0 e^{-(\gamma+\delta+\alpha)t}+\delta+\rho\right)t} \geq 0. \quad (10)$$

Similarly, the solution for the rest of the equation will be obtained as:

$R(t) \geq R_0 e^{-\delta t} \geq 0, Q(t) \geq Q_0 e^{-(\delta+\gamma)t} \geq 0$, and $V(t) \geq V_0 e^{-\delta t} \geq 0$.

Thus, the solution set {(S(t), E(t), I(t), R(t), Q(t), V(t)} is non-negative for time t ≥ 0.

Equilibrium Points

The equilibrium of our model is found by equating the RHS of the equation (1) to zero. By doing that we get the following set of equilibrium points namely

$E_0 = (S^0, E^0, I^0, R^0, Q^0, V^0)$ and

$E_1 = (S^*, E^*, I^*, R^*, Q^*, V^*)$.

Disease-Free Equilibrium Point (DFEP)

In infectious disease modelling, disease-free equilibrium (DFE) is an equilibrium point where the prevalence of the infectious disease is zero, implying that there are no diseased people in the population. It denotes a steady scenario in which the disease has been eliminated or has not yet entered the population.

To find the disease-free equilibrium, we need to set the derivatives of all compartments to zero and solve the resulting system of equations. Let's denote the equilibrium values as S^0, E^0, I^0, R^0, Q^0, V^0 for each compartment, respectively. For our model, we get the disease-free equilibrium as

$E_0 = (S^0, E^0, I^0, R^0, Q^0, V^0)$

Where,

$S^0 = \frac{\mu}{(\delta+\rho)}$,

$E^0 = 0$,

$I^0 = 0$,

$R^0 = 0$,

$Q^0 = 0$,

$V^0 = \frac{\rho\mu}{\delta(\delta+\rho)}$,

i.e., $(\frac{\mu}{(\delta+\rho)}, 0, 0, 0, 0, \frac{\rho\mu}{\delta(\delta+\rho)})$ (11)

Endemic Equilibrium Point (EEP)

In the context of infectious disease modelling, endemic equilibrium, also known as the endemic state or endemic equilibrium point, refers to a stable, non-zero equilibrium point. Unlike the disease-free equilibrium point, which depicts the eradication of infectious diseases, the endemic equilibrium point illustrates a steady degree of infection that stays in the population throughout time.

To find the endemic equilibrium, we need to set the derivatives of all compartments to zero and solve the resulting system of equations. Let's denote the equilibrium values as S^*, E^*, I^*, R^*, Q^*, V^*.

For each compartment, respectively. For our model, we got the endemic equilibria as

$E_1 = (S^*, E^*, I^*, R^*, Q^*, V^*)$.

Where,

$$S^* = \frac{(\gamma+\delta+\alpha)(\delta+\sigma)}{\beta\sigma}$$

$$E^* = \frac{(\mu\beta\sigma-\gamma\delta^2-\gamma\sigma\delta-\delta^3-\delta^2\sigma-\alpha\delta^2-\alpha\sigma\delta-\gamma\rho\delta-\gamma\sigma\rho-\delta^2\rho-\delta\sigma\rho-\alpha\delta\rho-\alpha\sigma\rho)}{\sigma\beta(\delta+\sigma)}$$

$$I^* = \frac{\mu\beta\sigma-\gamma\delta^2-\gamma\sigma\delta-\delta^3-\delta^2\sigma-\alpha\delta^2-\alpha\sigma\delta-\gamma\rho\delta-\gamma\sigma\rho-\delta^2\rho-\delta\sigma\rho-\alpha\delta\rho-\alpha\sigma\rho}{\beta(\gamma+\delta+\alpha)(\delta+\sigma)} \quad (12)$$

$$R^* = \frac{\gamma(\mu\beta\sigma-\gamma\delta^2-\gamma\sigma\delta-\delta^3-\delta^2\sigma-\alpha\delta^2-\alpha\sigma\delta-\gamma\rho\delta-\gamma\sigma\rho-\delta^2\rho-\delta\sigma\rho-\alpha\delta\rho-\alpha\sigma\rho)}{\delta\beta(\delta+\sigma)(\delta+\gamma)}$$

$$Q^* = \frac{\alpha(\mu\beta\sigma-\gamma\delta^2-\gamma\sigma\delta-\delta^3-\delta^2\sigma-\alpha\delta^2-\alpha\sigma\delta-\gamma\rho\delta-\gamma\sigma\rho-\delta^2\rho-\delta\sigma\rho-\alpha\delta\rho-\alpha\sigma\rho)}{\beta(\gamma+\delta+\alpha)(\delta+\sigma)(\delta+\gamma)}$$

$$V^* = \frac{\rho(\gamma+\delta+\alpha)(\delta+\sigma)}{\beta\sigma\delta}$$

Effective Reproduction Number (REff)

The effective reproduction number (R_{Eff}) represents the average number of secondary infections produced by one infected individual at a specific point in time. For the given compartmental model, the effective reproduction number can be calculated as the dominant eigenvalue of the next-generation matrix. According to the system of equations (1), we have three infectious compartments, that are:

$$\frac{dE}{dt} = \beta SI - \delta E - \sigma E$$

$$\frac{dI}{dt} = \sigma E - \gamma I - \delta I - \alpha I$$

$$\frac{dQ}{dt} = \alpha I - \delta Q - \gamma Q$$

The next generation matrix is FV^{-1} in which the required matrix F (suggest the presence of new infections) and V (used to describe people transferring between compartments.) are given by,

$$F = \begin{pmatrix} \beta SI \\ 0 \\ 0 \end{pmatrix} \quad V = \begin{pmatrix} \delta E + \sigma E \\ -\sigma E + \gamma I + \delta I + \alpha I \\ -\alpha I + \delta Q + \gamma Q \end{pmatrix}$$

First, we construct a Jacobian matrix F and V by calculating the partial derivatives of F and V with respect to each variable.

$$F = \begin{pmatrix} 0 & \beta S & 0 \\ 0 & 0 & 0 \\ 0 & 0 & 0 \end{pmatrix} \quad V = \begin{pmatrix} \delta+\sigma & 0 & 0 \\ -\sigma & (\gamma+\delta+\alpha) & 0 \\ 0 & -\alpha & (\delta+\gamma) \end{pmatrix}$$

Now, the Next Generation matrix FV^{-1} is given by,

$$FV^{-1} = \begin{pmatrix} \frac{\sigma\beta S}{(\delta+\sigma)(\gamma+\delta+\alpha)} & \frac{\beta S}{(\gamma+\delta+\alpha)} & 0 \\ 0 & 0 & 0 \\ 0 & 0 & 0 \end{pmatrix}$$

Thus, the effective reproduction number R_{Eff} which can be considered as the spectral radius of the next generation matrix FV^{-1} is given by,

$R_{Eff} = \rho(FV^{-1})$ i.e the largest eigen value of matrix FV^{-1}

$$R_{Eff} = \frac{\sigma\beta\mu}{(\delta+\rho)(\delta+\sigma)(\gamma+\delta+\alpha)} \quad (13)$$

Stability Analysis

Stability analysis in infectious disease modelling involves assessing the stability of equilibrium points in mathematical models that explain the dynamics of disease transmission within a population. The fundamental purpose is to comprehend the system's long-term behaviour by investigating how it responds to abrupt changes or disturbances from an equilibrium state.

First, we calculate the partial derivatives of the equations with respect to each variable and construct the Jacobian matrix. The Jacobi matrix for our model (1) is given by:

$$J = \begin{pmatrix} -\beta I - (\delta+\rho) & 0 & -\beta S & 0 & 0 & 0 \\ \beta I & -(\delta+\sigma) & \beta S & 0 & 0 & 0 \\ 0 & \sigma & -(\gamma+\delta+\alpha) & 0 & 0 & 0 \\ 0 & 0 & \gamma & -\delta & \gamma & 0 \\ 0 & 0 & \alpha & 0 & -(\delta+\gamma) & 0 \\ \rho & 0 & 0 & 0 & 0 & \delta \end{pmatrix} \quad (14)$$

Local Stability Analysis of Disease-Free Equilibrium Point

Theorem: The disease-free equilibrium points $E_0 = (S^0, E^0, I^0, R^0, Q^0, V^0)$ of the system of equation (1) is locally asymptotically stable if $R_{Eff} < 1$ and unstable if $R_{Eff} > 1$.

Proof: To analyse the stability of DFEP of our model (1), we substitute the values of E_0 in Jacobian matrix (14), so that we get J_0 matrix as described below:

$$J_0 = \begin{pmatrix} -(\delta+\rho) & 0 & -\beta\frac{\mu}{(\delta+\rho)} & 0 & 0 & 0 \\ 0 & -(\delta+\sigma) & \beta\frac{\mu}{(\delta+\rho)} & 0 & 0 & 0 \\ 0 & \sigma & -(\gamma+\delta+\alpha) & 0 & 0 & 0 \\ 0 & 0 & \gamma & -\delta & \gamma & 0 \\ 0 & 0 & \alpha & 0 & -(\delta+\gamma) & 0 \\ \rho & 0 & 0 & 0 & 0 & -\delta \end{pmatrix} \quad (15)$$

Now the eigen values of the matrix$|J_0-\lambda I|=0$ is calculated as follows:

$$\begin{vmatrix} -(\delta+\rho)-\lambda & 0 & -\beta\frac{\mu}{(\delta+\rho)} & 0 & 0 & 0 \\ 0 & -(\delta+\sigma)-\lambda & \beta\frac{\mu}{(\delta+\rho)} & 0 & 0 & 0 \\ 0 & \sigma & -(\gamma+\delta+\alpha)-\lambda & 0 & 0 & 0 \\ 0 & 0 & \gamma & -\delta-\lambda & \gamma & 0 \\ 0 & 0 & \alpha & 0 & -(\delta+\gamma)-\lambda & 0 \\ \rho & 0 & 0 & 0 & 0 & -\delta-\lambda \end{vmatrix} = 0 \quad (16)$$

Solving the above using cofactor expansion, we will get the following equation:

$$(\delta+\rho+\lambda)(\delta+\lambda)(\delta+\gamma+\lambda)(\delta+\lambda)\left\{(\delta+\sigma+\lambda)(\gamma+\delta+\alpha+\lambda)-\beta\frac{\mu\sigma}{(\delta+\rho)}\right\}=0 \quad (17)$$

From (17), we have the following eigen values

$\lambda_1=-(\delta+\rho)<0,$

$\lambda_2=-(\delta)<0,$

$\lambda_3=-(\delta+\gamma)<0,$

$\lambda_4=-(\delta)<0,$

Since these eigenvalues are negative, therefore they are stable.

From, $(\delta+\sigma+\lambda)(\gamma+\delta+\alpha+\lambda)-\beta\frac{\mu\sigma}{(\delta+\rho)}=0,$ we have the following equation,

$$\lambda^2+(\delta+\sigma+\gamma+\delta+\alpha)\lambda+\left\{(\delta+\sigma)(\gamma+\delta+\alpha)-\beta\frac{\mu\sigma}{(\delta+\rho)}\right\}=0$$

$$\lambda=\frac{-(\delta+\sigma+\gamma+\delta+\alpha)\pm\sqrt{(\delta+\sigma+\gamma+\delta+\alpha)^2-4\left\{(\delta+\sigma)(\gamma+\delta+\alpha)-\beta\frac{\mu\sigma}{(\delta+\rho)}\right\}}}{2},$$

$$\lambda_5=\frac{-(\delta+\sigma+\gamma+\delta+\alpha)-\sqrt{(\delta+\sigma+\gamma+\delta+\alpha)^2-4\left\{(\delta+\sigma)(\gamma+\delta+\alpha)-\beta\frac{\mu\sigma}{(\delta+\rho)}\right\}}}{2}$$

$$=-\frac{(\delta+\sigma+\gamma+\delta+\alpha)+\sqrt{(\delta+\sigma+\gamma+\delta+\alpha)^2-4\left\{(\delta+\sigma)(\gamma+\delta+\alpha)-\beta\frac{\mu\sigma}{(\delta+\rho)}\right\}}}{2}<0$$

This also satisfies stability criteria.

Now, $\lambda_6=\frac{-(\delta+\sigma+\gamma+\delta+\alpha)+\sqrt{(\delta+\sigma+\gamma+\delta+\alpha)^2+4\left\{-(\delta+\sigma)(\gamma+\delta+\alpha)+\beta\frac{\mu\sigma}{(\delta+\rho)}\right\}}}{2},$

To be stable at the equilibrium point $\left\{-(\delta+\sigma)(\gamma+\delta+\alpha)+\beta\frac{\mu\sigma}{(\delta+\rho)}\right\}$ must be less than zero,

i.e. $-(\delta+\sigma)(\gamma+\delta+\alpha)+\beta\frac{\mu\sigma}{(\delta+\rho)}<0$

$\Rightarrow \beta\frac{\mu\sigma}{(\delta+\rho)}<(\delta+\sigma)(\gamma+\delta+\alpha)$

$\Rightarrow \beta\frac{\mu\sigma}{(\delta+\rho)(\delta+\sigma)(\gamma+\delta+\alpha)}<1$

$\Rightarrow R_{Eff}<1$

From the above solution it is proved that if $R_{Eff}<1$, then the disease-free equilibrium point is locally asymptotically stable.

Local Stability Analysis of Endemic Equilibrium Point

Theorem: The endemic equilibrium points $E_1 = (S^*, E^*, I^*, R^*, Q^*, V^*)$ of the system of equation (1) is locally asymptotically stable if $R_{Eff}<1$ and unstable if $R_{Eff}>1$.

Proof: To analyse the stability of EEP of our model (1), we substitute the values of E_1 in Jacobian matrix (14), so that we get J_0 matrix as described below:

$$J_1=\begin{pmatrix} -\frac{\beta\sigma\mu}{(\gamma+\delta+\alpha)(\delta+\sigma)} & 0 & -\frac{(\gamma+\delta+\alpha)(\delta+\sigma)}{\sigma} & 0 & 0 & 0 \\ X & -(\delta+\sigma) & \frac{(\gamma+\delta+\alpha)(\delta+\sigma)}{\sigma} & 0 & 0 & 0 \\ 0 & \sigma & -(\gamma+\delta+\alpha) & 0 & 0 & 0 \\ 0 & 0 & \gamma & -\delta & \gamma & 0 \\ 0 & 0 & \alpha & 0 & -(\delta+\gamma) & 0 \\ \rho & 0 & 0 & 0 & 0 & -\delta \end{pmatrix} \quad (18)$$

Where,

$$X=\frac{\mu\beta\sigma-\gamma\delta^2-\gamma\sigma\delta-\delta^3-\delta^2\sigma-\alpha\delta^2-\alpha\sigma\delta-\gamma\rho\delta-\gamma\sigma\rho-\delta^2\rho-\delta\sigma\rho-\alpha\delta\rho-\alpha\sigma\rho}{(\gamma+\delta+\alpha)(\delta+\sigma)}$$

Now the eigen values of the matrix$|J_1-\lambda I|=0$ is calculated as follows:

$$\begin{vmatrix} -\frac{\beta\sigma\mu}{(\gamma+\delta+\alpha)(\delta+\sigma)}-\lambda & 0 & -\frac{(\gamma+\delta+\alpha)(\delta+\sigma)}{\sigma} & 0 & 0 & 0 \\ X & -(\delta+\sigma)-\lambda & \frac{(\gamma+\delta+\alpha)(\delta+\sigma)}{\sigma} & 0 & 0 & 0 \\ 0 & \sigma & -(\gamma+\delta+\alpha)-\lambda & 0 & 0 & 0 \\ 0 & 0 & \gamma & -\delta-\lambda & \gamma & 0 \\ 0 & 0 & \alpha & 0 & -(\delta+\gamma)-\lambda & 0 \\ \rho & 0 & 0 & 0 & 0 & -\delta-\lambda \end{vmatrix}=0 \quad (19)$$

Solving the above using cofactor expansion, we will get the following equation:

From the above solution it is proved that if $R_{Eff}<1$, then the endemic equilibrium point is locally asymptotically stable.

Mathematical Model -2 (Influenza)

$$\frac{dS}{dt} = \mu - \beta S(I_a + I_s) - \eta S$$

$$\frac{dE}{dt} = \beta S(I_a + I_s) - \sigma E - \eta E$$

$$\frac{dI_a}{dt} = \rho\sigma E - \gamma_1 I_a - \alpha I_a - \eta I_a$$

$$\frac{dI_s}{dt} = (1-\rho)\sigma E + \alpha I_a - \delta I_s - \gamma_2 I_s - \eta I_s \quad (1)$$

$$\frac{dT}{dt} = \delta I_s - \theta T - \eta T$$

$$\frac{dR}{dt} = \theta T + \gamma_1 I_a + \gamma_2 I_s - \eta R$$

Parameter description of the above model is given in Table 1. Also, the diagrammatic representation of our model is described in Figure 1.

Table 1: Description of Parameters

Parameters	Description
μ	Recruitment rate
η	Death rate
β	Transmission rate
ρ	The proportion of exposed people becoming infected
σ	Rate of latent individuals becoming infected
α	The rate at which asymptomatic infected people become symptomatic infected
δ	The rate at which symptomatic infected people seek and receive treatment
θ	Recovery rate of treated individual
γ_1	The natural recovery rate of asymptomatic individual
γ_2	The natural recovery rate of symptomatic individual

Mathematical Model-3 (Covid-19)

We consider the total population denoting it by N(t) and dividing further into eight different epidemiological compartments : susceptible compartment S(t) (the individuals who are not infected by the disease but can catch the disease), exposed compartment E(t) (individuals who are infected by the disease but not yet infectious, asymptomatic compartment $I_a(t)$ (individuals infected but they have no visible clinical symptoms), symptomatic compartment $I_s(t)$ (individuals show clinical symptoms of covid-19 infection), quarantined compartment Q(t) (individuals who are asymptomatic and symptomatic), vaccinated compartment V(t) (individuals who are

vaccinated), recovered compartment R(t) (individuals recovered from either asymptomatic or symptomatic). Death compartment D(t) (individuals who are not recovered from the infection).

$$\frac{ds}{dt} = \Omega - \beta_s(1-\eta\varepsilon)SI_s - \beta_a(1-\eta\varepsilon)SI_a - \mu s - \delta s$$

$$\frac{dE}{dt} = \sigma + \beta_s(1-\eta\varepsilon)SI_s + \beta_a(1-\eta\varepsilon)SI_a - (1-\omega)\varphi E - \beta_s\sigma VI_s + \beta_a\sigma VI_a - \omega\varphi E - \mu E$$

$$\frac{dI_s}{dt} = (1-\omega)\varphi E - \alpha_s I_s - \lambda_s I_s - \mu I_s$$

$$\frac{dI_a}{dt} = \omega\varphi E - \alpha_a I_a - \lambda_a I_a - \mu I_a$$

$$\frac{dQ}{dt} = \alpha_s I_s + \alpha_a I_a - (1-k)\gamma Q - k\rho Q - \mu Q$$

$$\frac{dR}{dt} = (1-k)\gamma Q - \mu R$$

$$\frac{dD}{dt} = k\rho Q$$

$$\frac{dV}{dt} = \delta S - \beta_s\sigma VI_s + \lambda_s I_s + \lambda_a I_a - \beta_a\sigma VI_a - \mu V$$

Since the total population is N(t)=S(t)+E(t)+I_s(t)+I_a(t)+Q(t)+R(t)+V(t)

Then

$$\frac{dN}{dt} = \frac{dS}{dt} + \frac{dE}{dt} + \frac{d\mathrm{Is}}{dt} + \frac{d\mathrm{Ia}}{dt} + \frac{dQ}{dt} + \frac{dR}{dt} + \frac{dV}{dt}$$

$$\frac{dN}{dt} = \Omega - \mu(S + E + I_s + I_a + Q + V + R)$$

$$\frac{dN}{dt} = \Omega - \mu N \qquad (1)$$

$$0 \le N \le \frac{\Omega}{\mu}$$

Model (1) describes the human population, and thus the model variables can be shown to be non-negative for all $t \geq 0$and that all solutions of the model (1) will remain positive for $t \geq 0$. Therefore, model (1) is mathematically well-posed, and its dynamics can be considered in the region below:

$$\Delta = \left\{S, E, I_s, I_a, Q, R, D, V \in R_+^8 : S + E + I_s + I_a + Q + R + V \le \frac{\Omega}{\mu}\right\} \qquad (2)$$

Table 1: Variables and their meaning used in the model

Variables in the Model	Meaning
S	The susceptible compartment

E	The exposed compartment
I_s	The symptomatic infectious compartment
I_a	The asymptomatic infectious compartment
Q	The quarantined compartment
R	The recovered compartment
D	The death compartment

Table 2: Parameters used in the model and their meaning

Model Parameters	**Meaning**
Ω	The recruitment rate into the susceptible compartment
β_s	The effective contact rate
β_a	The effectiveness of social distancing
η	The proportion of individuals who use a face mask
ε	The efficacy of face masks
1-ω	The fraction of exposed individuals who show clinical symptoms after the incubation period
φ	The rate of progression from the exposed compartment to the infectious compartment
α_s	The isolation rate for individual in the symptomatically infected compartment
α_a	The isolation rate of asymptomatically infectious individual
δ	Vaccination rate
σ	The Vaccine inefficacy
K	Mortality rate
ϒ	Average days until recovery
ρ	Average days until death
μ	Natural death rate

Conclusion

To sum up, the analysis of compartmental models has illuminated how well they work to create mathematical representations of infectious diseases. These models have demonstrated their value in predicting outbreaks, analyzing intervention tactics, and comprehending disease dynamics through rigorous analysis and validation against real-world data. However, a number of variables, such as the precision of the input parameters, the intricacy of the dynamics of disease transmission, and the presumptions made during model creation, affect how effective they are. Compartmental models have limitations even if they offer a framework for modeling the transmission of disease within populations. The accuracy of these models may be called into question by changes in human behavior, the evolution of infections, and the

impact of outside variables. Furthermore, the interpretation of model results needs to be done carefully and should be supported by expert opinion and empirical data. However, compartmental models' flexibility and adaptability hold promise for improving our capacity to counteract the risks posed by infectious diseases. Their usefulness in making decisions about public health and preparing for epidemics can be further enhanced by ongoing improvement, validation, and integration with other modeling techniques. We may more effectively navigate the complex landscape of infectious illnesses and lessen their impact on global health by utilizing the advantages of compartmental models in conjunction with empirical data and interdisciplinary collaboration.

References

1. Berry, J. and Houston, K., 1995. Mathematical modeling. Gulf Professional Publishing.
2. Frejd, P. and Bergsten, C., 2016. Mathematical modeling as a professional task. Educational studies in mathematics, 91, pp.11-35.
3. Kuddus, M.A., Mohiuddin, M. and Rahman, A., 2021. Mathematical analysis of a measles transmission dynamics model in Bangladesh with double dose vaccination. Scientific reports, 11(1), p.16571.
4. Brauer F, Castillo-Chavez C, Feng Z. Models for Influenza. Mathematical Models in Epidemiology. 2019 Jun 25; 69:311–50. doi: 10.1007/978-1-4939-9828-9_9. PMCID: PMC7316090.
5. Arsal, Shinta R., Dipo Aldila, and Bevina D. Handari. "Short review of mathematical model of measles." AIP Conference Proceedings. Vol. 2264. No. 1. AIP Publishing, 2020.
6. James Peter, Olumuyiwa, *et al*. "Mathematical model of measles transmission dynamics using real data from Nigeria." Journal of Difference Equations and Applications 28.6 (2022): 753-770.
7. Ochoche, J. M., and R. I. Gweryina. "A mathematical model of measles with vaccination and two phases of infectiousness." IOSR Journal of Mathematics 10.1 (2014): 95-105.
8. Pakwan Riyapan, Sherif Eneye Shuaib, Arthit Intarasit, "A Mathematical Model of COVID-19 Pandemic: A Case Study of Bangkok, Thailand", Computational and Mathematical Methods in Medicine, vol. 2021, Article ID 6664483, 11 pages, 2021. https://doi.org/10.1155/2021/6664483

9. Ghostine, R.; Gharamti, M.; Hassrouny, S.; Hoteit, I. An Extended SEIR Model with Vaccination for Forecasting the COVID-19 Pandemic in Saudi Arabia Using an Ensemble Kalman Filter. Mathematics 2021, 9, 636. https://doi.org/10.3390/math9060636

Chapter - 9
A Study on Reproduction Number for Infectious Diseases

Authors

Nivedita Prasad
Department of Mathematics, Amity University Kolkata, Kolkata, West Bengal, India

Najnin Islam
Department of Mathematics, Amity University Kolkata, Kolkata, West Bengal, India

Souvik Kundu
Department of Mathematics, Amity University Kolkata, Kolkata, West Bengal, India

Chapter - 9

A Study on Reproduction Number for Infectious Diseases

Nivedita Prasad, Najnin Islam and Souvik Kundu

Abstract

The basic reproduction number (R_0), also referred to as the fundamental reproduction ratio or rate, is a measure of infectious agent contagiousness or transmissibility used in epidemiology. R_0 is influenced by a variety of biological, environmental, and sociocultural variables that control the spread of pathogens and, as a result, is typically calculated using different forms of Complex mathematical theories that result in R_0 being readily misrepresented, misunderstood, and applied incorrectly. R_0 is not a rate over time, a biological constant for a pathogen, or an illness severity index, and R_0 can't be changed via immunization programs. R_0 is rarely directly measured, and R_0 is modelled values depending on the model, assumptions, and structures. Some R_0 values listed in Scientific literature are probably out of date. R_0 must be calculated, reported, and used very cautiously because this fundamental metric is anything but easy.

Introduction

The basic reproductive number, or fundamental reproduction ratio R_0 is the number of secondary infections that one infected individual would produce in a population that is completely susceptible for the whole duration of the infectious period [1, 2]. R_0 is determined by the number of contacts an infected individual can make in a given amount of time (c), the likelihood of transmission in each contact (β), and the length of the infectious phase ($1/\gamma$) determine.

$$R_0 = c \times \beta \times \frac{1}{\gamma}$$, where γ represents the recovery rate per-capita.

The basic reproduction number, R_0, indicates how contagious an infectious disease is since it measures how many secondary cases will arise from introducing a the single infectious case into a susceptible population. As an example, influenza is a communicable disease caused by a virus known as the influenza virus [3-6].

In influenza, if R_0 in a population is 1.3 [7], then each new case of influenza would produce on an average 1.3 secondary cases. R_0 keep out new cases caused by secondary infected cases.

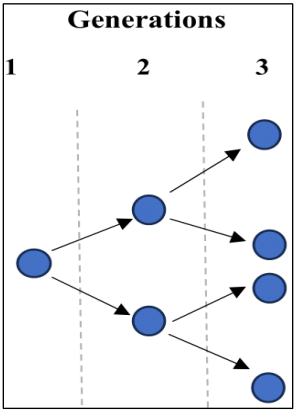

Basic idea on disease spreading considering $R_0 = 2$

R_0's value depends mostly on the following factors-the number of contacts a person has per unit of time, duration of infection, and contact rate. If the infectious period is long, a person will transmit the disease more likely to others. A contagious disease spread more rapidly if the contagious person comes in contact with many susceptible individuals, i.e., those who aren't infected yet but not even vaccinated.

The disease will spread slower if the infected person remains quarantined at home, in a hospital, or otherwise. A high contact rate will produce a higher R_0 value.

The fastest and easiest way to spread diseases is via the air, like influenza, flu, or measles. It doesn't necessarily require physical touch to spread a disease from one person to another. Even if some individual never come in direct contact to a person affected by flu, he/she can get the same by breathing close to someone who is suffering from it. In contrast, it is more challenging to contract or spread diseases like Ebola or HIV that are mostly conveyed by bodily fluids. This is due to the fact that they can only be passed forward by close contact with tainted blood, saliva, or other body fluids. Airborne illnesses generally have a greater R_0 value than diseases that spread through direct contact [8, 9].

There is growing worried about the various infectious illnesses spread by vectors, including those spread by the Aedes aegypti and Aedes

albopictus mosquitoes and include Dengue, Zika [10], and Chikungunya. Due to biological and social causes, such as the mosquitoes' adaption to new habitats in more temperate climates, their epidemiological magnitudes keep growing. The total extent of the epidemic is an essential indication of the intensity and effects of an outbreak [11]. An assessment of the final prevalence of a vector-borne illness in a small population is provided in the works of Brauer [9] and Tsubouchi *et al*. [12].

R_0 is having a significant impact on whether or not the disease outbreak arise. If $R_0 > 1$, the outbreak continues, and if $R_0 < 1$ then it ends [13, 14, 15]. R_0 is a factor that depends on various biological, social, and environmental factors and therefore, it cannot be measured independently [7, 8, 10, 17]. It depends on population density and contact patterns. It also depends on host factors such as the immunity of a person. If a person's immunity is high, then his/her recovery rate increases which reduces the duration of the infection period, and hence the reproduction number is also reduced. The modes of disease transmission also affect R_0, such as airborne disease transmits the fastest. The best way to reduce R_0 is to reduce the number of susceptible which will reduce the probability of transmission of infection given contact and hence R_0 will be reduced. Vaccination is the most used method for this. It not only protects the individual from infection but also protects the community by keeping the R_0 low. For diseases that have not been encountered before and whose vaccines are not made, R_0 can increase very quickly. However, if the factors on which R_0 depends are controlled then the outbreak of the disease can be controlled. For example, The World Health Organization (WHO) proclaimed the coronavirus disease 2019 (covid-19), which is caused by the severe acute respiratory syndrome coronavirus 2 (SARS-CoV-2), a worldwide pandemic on March 11, 2020, after rapidly spreading to over 100 nations [19]. In more than 200 countries and territories, COVID-19 was discovered on April 1, 2020, with an estimated 823,626 confirmed cases and 40,598 fatalities [20]. During the spread of COVID-19, people used certain protocols to protect themselves from getting infected. The most effective among them were home quarantine, social distancing, and wearing masks [28].

When a significant proportion of the population (or the herd) gets vaccinated or immune by another means, this phenomenon is known as herd immunity and protects susceptible individuals, such as those who have not received a vaccination. There is less chance that someone susceptible will come into contact with the pathogen in a group where there are more immune persons. If a high number of people are immune, the chain of

infection is broken, making it harder for infections to spread between people [18, 26, 29, 30, 31]. The percentage of a population that must be immune before an infectious disease becomes stable in that population is known as the herd immunity threshold. If this is achieved, for example by immunization, then each case results in one more case (R=1) and the infection will stabilize within the population.

$$HIT = 1 - \frac{1}{R_0}$$

When the herd immunity threshold is reached, then $R_0 < 1$, and the number of infection cases declines. This is a crucial step in the prevention, immunization, and elimination of infectious diseases [31].

In many circumstances, not all contacts will be susceptible to infection. This is measured by the effective reproductive rate (R_e). In the actual world, a population will rarely be susceptible to a disease. Some contacts will already have immunity, whether from an earlier infection that passed along lifelong protection or from an earlier vaccine. The average number of secondary cases per infectious case will thus be lower than the basic reproduction number since not all contacts will get the infection. The average number of secondary cases per infectious case in a population made up of both susceptible and non-susceptible hosts is known as the effective reproductive number (R_e).

The effective reproduction number can be estimated by the product of the basic reproductive number and the fraction of the host population that is susceptible (x). So:

$$R_e = R_0 x$$

Estimates of R_e are used to assess how policy changes, population immunity, and other factors have affected transmission at specific points in time [21-25]. For example, Measles is an extremely contagious viral disease that, despite efforts to eliminate it, continues to cause outbreaks in the UK. Otitis media is one of the many complications of measles in the acute stage, although some of the worst effects of the disease appear months or even years after the initial infection. Measles causes a considerable number of childhood mortalities worldwide and adds to the strain on families already suffering from the effects of war and poverty [27]. Now, if R_0 for measles is 12 in a population with 50% immunity, then 12 x 0.5 = 6 is the effective reproductive number for measles. In these conditions, a single measles case would result in an average of 6 more secondary cases. R_e must be smaller than 1 for a disease to be successfully eradicated from a population.

In our work, we primarily concentrate on the conceptual analysis of reproduction numbers, derivation of the expressions of fundamental reproduction numbers for various models and some graphical representations of the effects of various reproduction numbers' numerical values on the final size of susceptible and infectious populations. This study can aid in the thorough understanding of basic as well as effective reproduction number and their impact on novice researchers in the field of disease modeling.

Basic Reproduction Number for Normal Transmission

Consider a general disease transmission model where the set of infected compartments are represented by $x \in R^n$, the set of susceptible compartments are represented by $y \in R^m$, and the set of compartments that have been cured of the disease by immunity or recovery with immunity are represented by $z \in R^k$. Let D be an $m \times m$ matrix whose diagonal entries $\sigma_i > 0$ represents the relative susceptibilities of the corresponding susceptible class. We can take $\sigma_1 = 0$ without loss of generality. We'll assume that Π is a $n \times m$ matrix with the characteristic that each entry (i, j) indicates the proportion of the jth susceptible compartment that goes into the ith infective compartment upon infection. Additionally, we'll let b to be an n-dimensional row vector of comparative horizontal transmissions. This vector is multiplied by an infectivity-representing scalar component. We can take this function as $\beta(x, y, z)$ for general incidence function and for mass incidence function we can take this function as constant β. Now the disease model can be represented by the following equations

$$\begin{aligned} \frac{\mathrm{dx}}{\mathrm{dt}} &= \Pi D y \beta(x, y, z) b x - V x, \\ \frac{\mathrm{dy}}{\mathrm{dt}} &= g(x, y, z) - D y \beta(x, y, z) b x, \\ \frac{\mathrm{dz}}{\mathrm{dy}} &= h(x, y, z) + W x \end{aligned}$$

with initial condition that at least one component of $x(0)$ and $y(0)$ would be positive. Here, the $n \times n$ matrix V describes both the removals from infected states via death and recovery as well as the transitions between infected states. The elements of the vector Vx, for any non-negative vector x, correspond to the net rate of decline of each infected compartment. Since the compartment must be empty for this rate to be positive, the off-diagonal entries of V must be negative or zero. V is a non-singular matrix. That implies that the eigenvalues of V have positive real part and all the entries of V^{-1} are non-negative.

W is a $k \times n$ matrix where (i, j) entry represents the rate at which members of the j^{th} disease compartment go into the i^{th} removed compartment on recovery. The function h(x, y, z), also assumed continuous, represents the flow into and out of the system of members immune to infection through natural immunity or inoculation against infection. The functions g(x, y, z) represent the recruitment of uninfected members through birth or immigration as well as deaths of uninfected members. The invariant set $(x, y, z)|x = 0, y \geq 0, z \geq 0$ is free of sickness. Assume that a point $(0, y_0, z_0)$ represents a locally stable equilibrium of the system in the absence of infection, with $y_0 = g(0, y, z)$ and $z_0 = h(0, y, z)$, respectively. This means that solutions that begin close to $(0, y_0, z_0)$ remain close to $(0, y_0, z_0)$. It is known as a disease-free equilibrium when such a point is reached. So the matrix of the system at disease equilibrium is

$$J_{yz} = \begin{bmatrix} g_y(0, y_0, z_0) & g_z(0, y_0, z_0) \\ h_y(0, y_0, z_0) & h_z(0, y_0, z_0) \end{bmatrix}$$

Now we define

$$F_h = \Pi D y_0 \beta(0, y_0, z_0) b$$

The basic reproduction number R_0 is the spectral radius of the matrix $F_h V^{-1}$. Recall that a non-negative matrix has a real eigenvalue equal to its spectral radius and that the spectral radius of a matrix A is defined as the highest modulus of an eigenvalue of A. We also point out that the spectral radius $F_h V$ has an absolute value lower than 1 if and only if all of the $F_h - V$ matrix's eigenvalues have negative real parts.

F_h has rank 1 since it is the sum of the products of the row vector b and the column vector $\Pi D y_0$. Therefore, the spectral radius is the only remaining eigenvalue of $F_h V^{-1}$, and rest $(n - 1)$ of its eigenvalues are zero. It is simple to confirm that this eigenvalue equals the scalar $\beta(0, Y_0, z_0) b V^{(-1)} \Pi D y_0$ because it is the trace of the matrix $\Pi D y_0 \beta(0, Y_0, z_0) b V^{(-1)}$. So we can finally conclude that

$$R_0 = \beta(0, Y_0, z_0) b V^{(-1)} \Pi D y_0$$

Basic SIR Model

If a single infected is introduced in a closed population N where contact rate is β, the number of total infected per unit time becomes βN. Infective leave the infected compartment at αI rate where α is the recovery rate and I is number of infected. The total population is closed. So $S + I + R = N$, where R is number of recovered individuals and S is number of susceptible

individuals. Now the probability of contact of a single infective with a susceptible is S/N, so the total number of infectives at a unit time is $(\beta S)(S/N)$ for a single infective. Now for I infectives total number of infectives became βSI. Also α is the recovery rate, so per unit time αI individuals are leaving the infected class. So we finally got the equations for basic SIR Model which is

$$\begin{aligned} \frac{dS}{dt} &= -\beta SI \\ \frac{dI}{dt} &= \beta SI - \alpha I \\ \frac{dR}{dt} &= \alpha I \end{aligned} \tag{2}$$

Basic Reproduction Number

If we initially assume the total population as susceptible i.e, $S(0) = N$, then one infected individual can infect βN individuals at a unit time and the mean infection period is $\frac{1}{\alpha}$. So the single infective can infect $\frac{\beta N}{\alpha}$ individuals. We called this basic reproduction number and denote it by R_0. So basically $R_0 = \frac{\beta N}{\alpha}$.

Model with Carrier State

In this section, we consider diseases like hepatitis B or herpes, where some infected people may become chronic carriers who spread the infection at a low rate over a long period of time. The increased biological complexity of these systems may easily be included into our current modelling framework. Using hepatitis B as our model infectious disease, we are concentrating on the inclusion of a single carrier type in this section.

When it comes to infections with carrier states, either carriers or those who are acutely contagious can infect susceptible persons. It is commonly believed that there is no difference between those who have been exposed to acutely infectious people and people who have been exposed to carriers. A person who has just contracted the illness is acutely contagious for a certain amount of time before either fully recovering or becoming a carrier. These dynamics result in the model is given below

$$\begin{aligned} \frac{\mathrm{dS}}{\mathrm{dt}} &= -(\beta I + \varepsilon\beta C)S \\ \frac{\mathrm{dI}}{\mathrm{dt}} &= (\beta I + \varepsilon\beta C)S - \gamma I \\ \frac{\mathrm{dC}}{\mathrm{dt}} &= \gamma q I - \Gamma C \\ \frac{\mathrm{dR}}{\mathrm{dt}} &= \gamma(1-q)I + \Gamma C \end{aligned} \tag{3}$$

with initial condition $S(0) = S_0$, $I(0) = I_0$ and $C(0) = R(0) = 0$ and also $S(0) + I(0) = 1$ as $S(t) + I(t) + R(t) = \frac{N}{N} = 1$

If we assume X as the number of total susceptible, Y as the number of infected, W as the number of carriers, and Z as the number of recovered individuals, N as total population.

Now if we consider

$S = \frac{X}{N}, I = \frac{Y}{N}, C = \frac{W}{N}, R = \frac{Z}{N}$

Here the class C represents the carrier class, $q(< 1)$ proportion of the infection become carrier and $(1 - q)$ become recovered. A reduced transmission rate ε is considered in case of carriers compare to the infectious individual and Γ is the rate at which individuals leaving carrier class.

4.1 Basic Reproduction Number

Model (3) has a unique disease-free equilibrium given by $E_0 = (1,0,0,0)$. To find R_0, we follow the approach given in [13], and let $f(t)$ and $v(t)$ be the matrix of new infection and the transmission matrix, respectively. At the disease-free equilibrium E_0 for (3), the matrices $f(t)$ and $v(t)$ are given by:

$$f = \begin{pmatrix} (\beta I + \varepsilon\beta C)S \\ 0 \end{pmatrix}$$

and

$$v = \begin{pmatrix} \gamma I \\ -\gamma q I + \Gamma C \end{pmatrix}$$

from these we get F and V

$$F = \begin{pmatrix} \beta & \varepsilon\beta \\ 0 & 0 \end{pmatrix}$$

and

$$V = \begin{pmatrix} \gamma & 0 \\ -\gamma q & \Gamma \end{pmatrix}$$

from that we got

$$V^{-1} = \begin{pmatrix} \frac{1}{\gamma} & 0 \\ \frac{q}{\Gamma} & \frac{1}{\Gamma} \end{pmatrix}$$

$$FV^{-1} = \begin{pmatrix} \frac{\beta}{\gamma} + \frac{\varepsilon\beta q}{\Gamma} & \frac{\varepsilon\beta}{\Gamma} \\ 0 & 0 \end{pmatrix}$$

now

$$|FV^{-1} - \lambda I_2| = \begin{vmatrix} \frac{\beta}{\gamma} + \frac{\varepsilon\beta q}{\Gamma} - \lambda & \frac{\varepsilon\beta}{\Gamma} \\ 0 & 0 - \lambda \end{vmatrix}$$

and we can get

$$\lambda_1 = \frac{\beta}{\gamma}\left[1 + \frac{\varepsilon\beta q\gamma}{\Gamma}\right]$$

and

$$\lambda_2 = 0$$

So our required basic reproduction number is given by

$$R_0 = \frac{\beta}{\gamma}\left[1 + \frac{\varepsilon q\gamma}{\Gamma}\right]$$

Seir-SI: Host-Vector Model

In this section we consider vector transmitted infections like dengue, malaria and those kind of infections which are mediated by mosquitoes. In case of some of those infectious diseases, there may be an exposed period after the transmission of infection from susceptibles from infective, in which period the transmission of infection get reduced by a factor. Here, we consider the following basic SEIR-SI model (SEIR framework for host and SI framework for vector).

$$\begin{aligned} \frac{\mathrm{dS}}{\mathrm{dt}} &= -\beta S I_v, \\ \frac{\mathrm{dE}}{\mathrm{dt}} &= \beta S I_v - \kappa E, \\ \frac{\mathrm{dI}}{\mathrm{dt}} &= \kappa E - \gamma I, \\ \frac{\mathrm{dR}}{\mathrm{dt}} &= \gamma I, \\ \frac{\mathrm{dS_v}}{\mathrm{dt}} &= \pi - \mu S_v - \beta S_v (I + \varepsilon E), \\ \frac{\mathrm{dI_v}}{\mathrm{dt}} &= \beta S_v (I + \varepsilon E) - \mu I_v. \end{aligned} \tag{4}$$

Where variables in the host compartments S, I, E, R denoted the number of susceptibles, infective, exposed and recovered individuals. Here $\frac{1}{\kappa}$ denotes the mean exposed period and $\frac{1}{\gamma}$ denotes the mean recovery period. The variables in vector compartment S_v and I_v denotes number of susceptibles vectors and infected vectors. In case of vectors we don't consider the

recovered class because their life span is too small to be recovered. The parameters g and μ denotes the constant birth rate and death rate of vectors. The contact rate in host compartment and vector compartment is equal because it depends on vector's bite rate. The parameter ε denotes the reduced infection rate in the case of exposed individuals. As the death of vectors is too much bigger than the death rate of hosts, this leads to apply quasi-steady state approximation (QSSA) to our model. When a variable displaying fast dynamics is added, QSSA is a practical approximation that is frequently used to reduce the size of a dynamical system. Variables that describe rapid dynamics can be ignored from the primary system using QSSA.

Assuming QSSA on fifth equation of (4), we get

$$\begin{aligned} \frac{dS_v}{dt} = 0 \quad &\Longrightarrow \quad \pi - \mu S_v - \beta S_v(I + \varepsilon E) = 0, \\ &\Longrightarrow \qquad S_v = \frac{\pi}{\mu+\beta(I+\varepsilon E)}. \end{aligned} \tag{5}$$

Similarly, assuming QSSA on sixth equation of (4), we have

$$\begin{aligned} \frac{dI_v}{dt} = 0 \quad &\Longrightarrow \quad \beta S_v(I + \varepsilon E) - \mu I_v = 0, \\ &\Longrightarrow \qquad I_v = \frac{\beta S_v(I+\varepsilon E)}{\mu}, \end{aligned}$$

$$\Longrightarrow I_v = \frac{\beta\pi(I+\varepsilon E)}{\mu[\mu+\beta(I+\varepsilon E)]}, \text{[using (5)]}$$

Now, substituting the above value of I_v in first and second equations of (4) we have

$$\begin{aligned} \frac{\mathrm{dS}}{\mathrm{dt}} &= -S\frac{\beta^2\pi(I+\varepsilon E)}{\mu[\mu+\beta(I+\varepsilon E)]}, \\ \frac{\mathrm{dE}}{\mathrm{dt}} &= S\frac{\beta^2\pi(I+\varepsilon E)}{\mu[\mu+\beta(I+\varepsilon E)]} - \kappa E, \\ \frac{\mathrm{dI}}{\mathrm{dt}} &= \kappa E - \gamma I. \end{aligned} \tag{6}$$

with initial conditions $S(0) = S_0$, $I(0) = I_0$, $E(0) = R(0) = 0$, and $S(0) + I(0) = 1$ as $S(t) + I(t) + E(t) + R(t) = 1$.

Basic Reproduction Number

Model (6) has a unique disease-free equilibrium given by $E_0 = (1,0,0)$. To find R_0, we follow the approach given in, and let $F(t)$ and $V(t)$ be the matrix of new infection and the transmission matrix, respectively. At the disease-free equilibrium E_0 for (6), the matrices $f(t)$ and $v(t)$ are given by:

$$f = \begin{pmatrix} S\frac{\beta^2\pi(I+\varepsilon E)}{\mu[\mu+\beta(I+\varepsilon E)]} \\ 0 \end{pmatrix}$$

$$v = \begin{pmatrix} \kappa E \\ -\kappa E + \gamma I \end{pmatrix}$$

Now we get

$$F = \begin{pmatrix} S\frac{\beta^2\pi\mu[\mu+\beta(I+\varepsilon E]-\beta^2\pi(I+\varepsilon E)\beta\mu}{\mu^2[\mu+\beta(I+\varepsilon E)]^2} & S\varepsilon\frac{\beta^2\pi\mu[\mu+\beta(I+\varepsilon E]-\beta^2\pi(I+\varepsilon E)\beta\mu}{\mu^2[\mu+\beta(I+\eta E)]^2} \\ 0 & 0 \end{pmatrix}$$

$$V = \begin{pmatrix} 0 & \kappa \\ \gamma & -\kappa \end{pmatrix}$$

Now for disease free equilibrium $S^* = 1$, $I^* = 0$ and $E^* = 0$ we can see

$$F = \begin{pmatrix} \frac{\beta^2\pi}{\mu^2} & \frac{\varepsilon\beta^2\pi}{\mu^2} \\ 0 & 0 \end{pmatrix}$$

And got

$$V^{-1} = \begin{pmatrix} \frac{1}{\gamma} & \frac{1}{\gamma} \\ \frac{1}{\kappa} & 0 \end{pmatrix}$$

$$FV^{-1} = \begin{pmatrix} \frac{\beta^2\pi}{\mu^2\gamma} + \frac{\varepsilon\beta^2\pi}{\kappa\gamma} & \frac{\beta^2\pi}{\mu^2\gamma} \\ 0 & 0 \end{pmatrix}$$

To find eigenvalues

$$|FV^{-1} - \lambda I_2| = \begin{pmatrix} \frac{\beta^2\pi}{\mu^2\gamma} + \frac{\varepsilon\beta^2\pi}{\kappa\gamma} - \lambda & \frac{\beta^2\pi}{\mu^2\gamma} \\ 0 & 0 - \lambda \end{pmatrix}$$

We can find

$$\lambda_1 = \frac{\beta^2\pi}{\kappa\gamma\mu^2}[\kappa + \varepsilon\gamma]$$

and

$$\lambda_2 = 0$$

so basic reproduction number becomes

$$R_0 = \frac{\beta^2\pi}{\kappa\gamma\mu^2}[\kappa + \varepsilon\gamma]$$

Results and Discussions

The effects of various values of the fundamental reproduction number R_0 on the size of susceptible and the infected individuals are depicted in

Figures (1), (2), and (3) using the SIR Model. These numbers demonstrate the fact that the number of susceptible individuals swiftly declines below the reproduction number of 1, and that the number of infected persons similarly declines rapidly. Again, with a value of R_0 a little above 1, the situation is essentially unchanged. However, when R0 is sufficiently large (=18), we witness a quite different outcome. The number of susceptible people in the population is gradually diminishing as the number of infected people rises gradually at first, but then expands quickly and after some time falls quickly to rid the population of the disease.

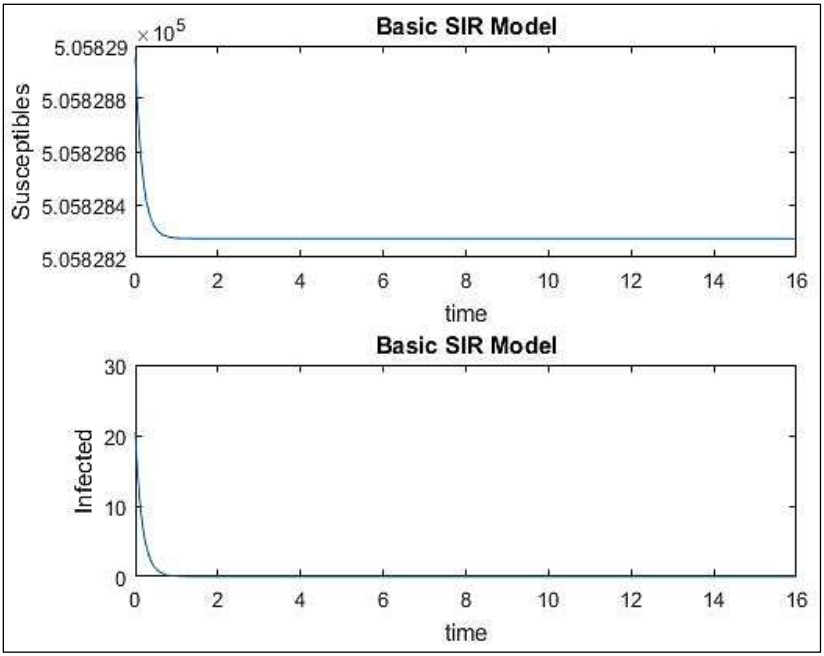

Fig 1: R_0 is less than 1

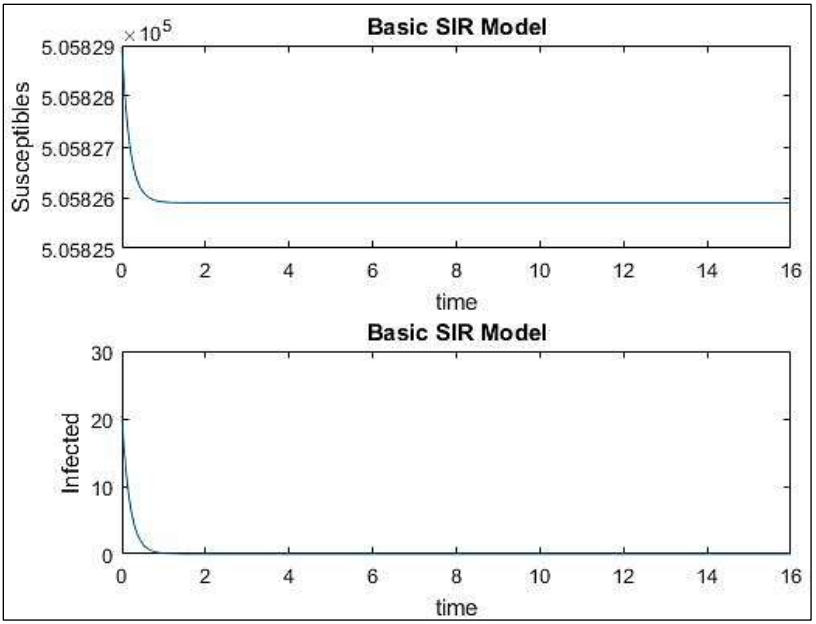

Fig 2: R_0 is just above 1

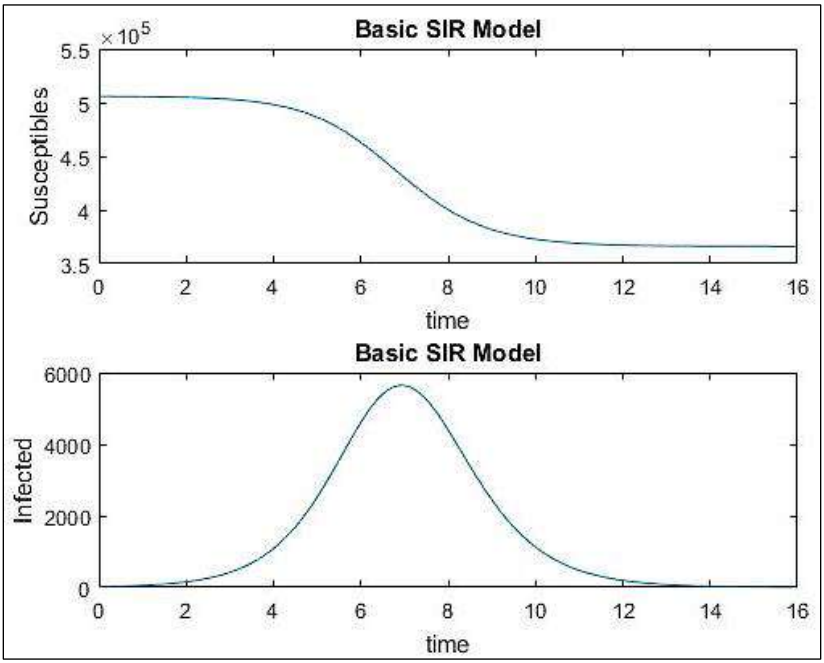

Fig 3: R_0 is equal to 18

Conclusion

The definition, computation, and interpretation of R_0 are anything but straightforward, despite the fact that it could seem to be a straightforward metric that can be used to assess the dynamics of infectious disease transmission and the risks that new outbreaks pose to the public health. The widespread usage of R_0 in both the scientific literature and the general study on it seems to have made it easier for some misconceptions to spread, but R_0 is still an important epidemiologic concept to explore. R_0 is a measure of contagiousness that depends on both host behaviour and the biology of viruses. The severity of an infectious disease or the rate at which a pathogen spreads over a population are not indicators of R_0. R_0 values are almost typically calculated using mathematical models, and the calculated values depend on a variety of restrictions taken into account during the modelling process. Without recalculating R_0 under the same modelling assumptions, the contagiousness of different historical, emerging, and reemerging infectious agents cannot be objectively compared. It's possible that some of the R_0 values that are frequently reported in the literature for prior epidemics won't apply to current outbreaks of the same infectious disease. R_0's genuine meaning and value can be distorted by several ways that it might be misrepresented, misunderstood, and applied. R_0 must be used and discussed cautiously in study and practice due to these different causes of confusion. When applied and evaluated correctly, this epidemiologic construct will only continue to be useful and relevant.

References

1. R. M. Anderson, R. M. May, Infectious diseases of humans: dynamics and control, Oxford university press, 1991.
2. O. Diekmann, J. A. P. Heesterbeek, Mathematical epidemiology of infectious diseases: model building, analysis and interpretation, Vol. 5, John Wiley & Sons, 2000.
3. J. Lin, V. Andreasen, S. A. Levin, Dynamics of influenza a drift: the linear three-strain model, Mathematical biosciences 162 (1-2) (1999) 33–51.
4. Y. Deguchi, Y. Takasugi, Efficacy of influenza vaccine in the elderly: reduction in risks of mortality and morbidity during an influenza a (h3n2) epidemic for the elderly in nursing homes, International Journal of Clinical and Laboratory Research 30 (2000) 1–4.

5. D. J. Earn, J. Dushoff, S. A. Levin, Ecology and evolution of the flu, Trends in ecology & evolution 17 (7) (2002) 334–340.

6. R. J. Webby, R. G. Webster, Are we ready for pandemic influenza? Science 302 (5650) (2003) 1519–1522.

7. G. Chowell, M. Miller, C. Viboud, Seasonal influenza in the united-states, france, and australia: transmission and prospects for control, Epidemiology & Infection 136 (6) (2008) 852–864.

8. C.C. Lord, M. Woolhouse, J. Heesterbeek, P. Mellor, Vector-borne diseases and the basic reproduction number: a case study of african horse sickness, Medical and veterinary entomology 10 (1) (1996) 19–28.

9. F. Brauer, A singular perturbation approach to epidemics of vector - transmitted diseases, Infectious Disease Modelling 4 (2019) 115–123.

10. B. D. Foy, K. C. Kobylinski, J. L. C. Foy, B. J. Blitvich, A. T. da Rosa, A. D. Haddow, R. S. Lanciotti, R. B. Tesh, Probable non–vector-borne transmission of zika virus, colorado, usa, Emerging infectious diseases 17 (5) (2011) 880.

11. U. Gim´enez-Mujica, J. Vel´azquez-Castro, A. Anzo-Hern´andez, Final size of the epidemic for metapopulation vector-borne diseases, Journal of Mathematical Analysis and Applications 526 (1) (2023) 127200.

12. Y. Tsubouchi, Y. Takeuchi, S. Nakaoka, Calculation of final size for vector-transmitted epidemic model, Math. Biosci. Eng 16 (4) (2019) 2219–2232.

13. P. Van den Driessche, J. Watmough, Reproduction numbers and sub-threshold endemic equilibria for compartmental models of disease transmission, Mathematical biosciences 180 (1-2) (2002) 29–48.

14. B. Ridenhour, J. M. Kowalik, D. K. Shay, Unravelling r 0: Considerations for public health applications, American journal of public health 104 (2) (2014) e32–e41.

15. P. L. Delamater, E. J. Street, T. F. Leslie, Y. T. Yang, K. H. Jacobsen, Complexity of the basic reproduction number (r0), Emerging infectious diseases 25 (1) (2019) 1.

16. B.G. Williams, and C. Dye, Mathematical biosciences, 145(1) (1997) 77-88.

17. J. Mossong, N. Hens, M. Jit, P. Beutels, K. Auranen, R. Mikolajczyk, M. Massari, S. Salmaso, G.S. Tomba, J. Wallinga, and J. Heijne, Social

contacts and mixing patterns relevant to the spread of infectious diseases. PLoS medicine, 5(3) (2008) 74.

18. J.P. Fox, L. Elveback, W. Scott, L.A.E.L. Gatewood, and E. Ackerman, Herd immunity: basic concept and relevance to public health immunization practices. American Journal of Epidemiology, 94(3) (1971) 179-189.
19. S. Hanaei and N. Rezaei COVID-19: developing from an outbreak to a pandemic. Archives of medical research, 51(6) (2020) 582.
20. M.B.B.S. Lekhraj Rampal, and L.B. Seng, Coronavirus disease (COVID-19) pandemic. Med J Malays, 75(2) (2020) 95.
21. A. Pan, L. Liu, C. Wang, H. Guo, X. Hao, Q. Wang, J. Huang, N. He, H. Yu, X. Lin, and S. Wei, Association of public health interventions with the epidemiology of the COVID-19 outbreak in Wuhan, China. Jama, 323(19) (2020) 1915-1923.
22. J. Scire, S.A. Nadeau, T. Vaughan, B. Gavin, S. Fuchs, J. Sommer, K.N. Koch, R. Misteli, L. Mundorff, T. Gotz, and T. Eichenberger, Reproductive number of the COVID-19 epidemic in Switzerland with a focus on the Cantons of Basel-Stadt and Basel-Landschaft. Swiss Medical Weekly, 150(19-20) (2020) 20271.
23. A.J. Kucharski, T.W. Russell, C. Diamond, Y. Liu, J. Edmunds, S. Funk, R.M. Eggo, F. Sun, M. Jit, J.D. Munday, and N. Davies, Early dynamics of transmission and control of COVID-19: a mathematical modelling study. The Lancet Infectious Diseases, 20(5) (2020) 553- 558.
24. S. Cauchemez, P.Y. Boelle, C.A. Donnelly, N.M. Ferguson, G. Thomas, G.M. Leung, A.J. Hedley, R.M. Anderson, and A.J. Valleron, Real-time estimates in early detection of SARS. Emerging infectious diseases, 12(1) (2006) 110.
25. S. Flaxman, S. Mishra, A. Gandy, H.J.T. Unwin, and H. Coupland, Report 13: Estimating the number of infections and the impact of non-pharmaceutical interventions on COVID-19 in European countries. London, UK: Imperial College COVID Response Team, 2020.
26. T.J. John, and R. Samuel, Herd immunity and herd effect: new insights and definitions. European Journal of Epidemiology, 16 (2000) 601-606.
27. J. Bentley, J. Rouseand, J. Pinfield. Measles: pathology, management, and public health issues. Nursing Standard, 28(38) 2014.

28. R. Chaudhry, G. Dranitsaris, T. Mubashir, J. Bartoszko, and S. Riazi. A country-level analysis measuring the impact of government actions, country preparedness, and socioeconomic factors on COVID-19 mortality and related health outcomes. EClinicalMedicine, 25 (2020).
29. R.M. Anderson and R.M. May, Vaccination and herd immunity to infectious diseases. Nature, 318(6044) (1985) 323-329.
30. H.E. Randolph, and L.B. Barreiro, Herd immunity: understanding COVID-19. Immunity, 52(5) (2020) 737-741.
31. P. Fine, K. Eames, and D.L. Heymann, "Herd immunity": a rough guide. Clinical infectious diseases, 52(7) (2011) 911-916.

Chapter - 10
Dye Sentisized Solar Cell Based on Pedot-Tos Counter Electrode

Authors

MD Alif Bakas
Department of Physics, Techno India University, Kolkata, West Bengal, India

Krishanu Chatterjee
Department of Physics, Techno India University, Kolkata, West Bengal, India

Shilpa Maity
Department of Physics, Swami Vivekananda University, Barrackpore, West Bengal, India

Chapter - 10

Dye Sentisized Solar Cell Based on Pedot-Tos Counter Electrode

MD Alif Bakas, Krishanu Chatterjee and Shilpa Maity

Abstract

The discovery of a titanium dioxide (TiO_2)-based dye-sensitized solar cell (DSSC) represents a potential advancement in solar cell technology with an efficiency of 11%. Like plant cells, the components of this third-generation solar cell are the dye, electrolyte, counter electrode, and semiconductor electrode. It has the potential to be a future energy source since it is affordable, safe for the environment, and compatible with automated production. Traditionally, a TCO substrate covered with Pt serves as the counter electrode (CE). Improvements in the CE are necessary since the DSSC becomes costly because to the high cost of the TCO and Pt. This study examines dye-sensitized solar cells. After looking into possible counter electrode materials, it was discovered that, in an iodine-based redox mediator system, a polymer-based counter electrode (PEDOT-TOS) performed better than a carbon counter electrode. An FTO conducting glass was coated with a low-temperature poly(3,4-ethylenedioxythiophene) compound to provide an array of dye-sensitized solar cells (DSSC) counter electrode. The outstanding photoelectric properties, low cost, and simple production method of the PEDOT-Tos/carbon electrode make it a good alternative to DSSCs.

Keyword: Dye-sensitized solar cell (DSSC), polymer-based counter electrode, photoelectric

Introduction

Energy availability has a significant impact on human living quality even before the Industrial Revolution. Energy and environmental catastrophes are predicted because of the increased and voracious use of traditional energy sources. Enabling methods to capture a portion of the solar radiation that reaches Earth might potentially address several issues related to energy and the environment at large [1].

Electric energy is currently facing a challenging global position due to the significant rise in demand, especially in developed nations. For the past 200 years, the main energy sources have been fossil fuels, such as coal and oil, which come with the inherent problem of pollution from burning carbon-based materials. The per capita CO_2 emissions in the nations with average incomes between $15,000 and $20,000 are rather like the annual world average of 4.8 tons CO_2. Every nation where the average income of the populace exceeds $25,000 has average emissions per capita that surpass the world average [1].

Pt-coated CEs in DSSCs are being replaced by less expensive conductive polymers, including poly(3,4-ethylenedioxythiophene) (PEDOT), because of their exceptional stability and excellent room-temperature conductivity [2-5]. PEDOT also serves as a significant whole carrying layer in OSC and PSC designs. Subsequent research revealed that PEDOT electrodes exhibited outstanding electrocatalytic activity toward both the iodide/iodine pair and more recent, highly-efficient redox mediators [6-8]. Thus far, PEDOT has been the most widely utilized CE material in comparison to other conductive polymers such as polyaniline (PANI) and polypyrrole (PPy). When employed as a counter electrode material, PEDOT was said to perform better than both PANI and PPy [9]. The group led by Professor Yanagida originally published on PEDOT-based CEs for DSSC in 2002 [10]. According to preliminary findings by Inganas *et al*. [11], one of the most often utilized components of liquid electrolyte direct-sector solar cells (DSSCs) is the iodide/triiodide redox pair. The charge transfer between this pair and a metal oxide can be enhanced using PEDOT. By chemically oxidizing EDOT with iron(III) tris-p-toluenesulfonate, Hagfeldt's group produced PEDOT-Tos CEs. After that, the films were spin-coated onto non-conductive glass and FTO, respectively.

The power conversion efficiency of 6.3% was reported by them for DSSCs built using PEDOT: Tos/glass CEs and cobalt-based redox electrolyte, which is interesting since this efficiency is similar to the 6.1% that Pt/FTO CEs achieved. Even with the encouraging outcomes of careful cell and material engineering, cobalt redox mediators have numerous drawbacks, featuring a high inner-sphere reorganization energy between low spin (Co3+, d6) and high spin (Co2+, d7) states that might impede the dye regeneration process. Cu(I/II) couples, which are based on minute tetragonally deformed copper complexes, were shown to be extraordinarily successful as alternative redox mediators when paired with PEDOT-based CEs in a more recent application to DSSCs. However, the typical copper

complexes used as an alternative redox mediator in DSSCs are smaller and have higher diffusion coefficients than the widely used Co (II)/(III) octahedral complexes, which provide better mass transport and smaller reorganization energy and result in an efficient regeneration of the oxidized dye [12].

The third-generation dye-sensitized solar cell, which is based on a PEDOT-Tos counter electrode and has excellent conductivity, high flexibility, exceptional stability, and cheap cost, is the subject of our study in this work.

Experimental

Materials Used

3,4 ethylenedioxythiophene (EDOT) as a monomer and Titanium (IV) isopropoxide (TTIP) were purchased from Sigma Aldrich, Ammonium peroxydisulfate (APS)and Para toluene sulfonic acid (pTSA) were purchased from alfa-aesar, Deionised water was purchased from hydrolab, India, Ethanol was purchased from merck chemicals, Acetic acid, Rhodamine B used as the dye.

Preparation of TiO_2 Electrode (Photoanode)

TiO_2 thin film for use as a photoanode was prepared using titanium (IV) isopropoxide as a precursor. First, 20 ml of ethanol and 1.5 ml of TTIP were combined to create a white sol solution. After that, the mixture was stirred using a magnetic stirrer. The following step involved dropping in 1 mL of acetic acid one drop at a time until the mixture became clear and took the form of a gel.

The solution was left 1 day for aging while stirring. A FTO coated glass of 2cm * 2cm dimension was cleaned using first soap water, then deionised water and finally using acetone. Then a cleaned FTO coated glass was taped one side with crypton tape so that the contact can be taken from that side. Then on EZ spin-ADV spin coater the FTO glass was attached and the sol-gel solution of TiO_2 was deposited using a micropipette. The spin coater was operated at 3000 rpm for 10 seconds to get uniform thin film of TiO_2 on the FTO coated glass. Then removing the tape, the FTO coated glass was baked at 450 ºC to make the TiO_2.

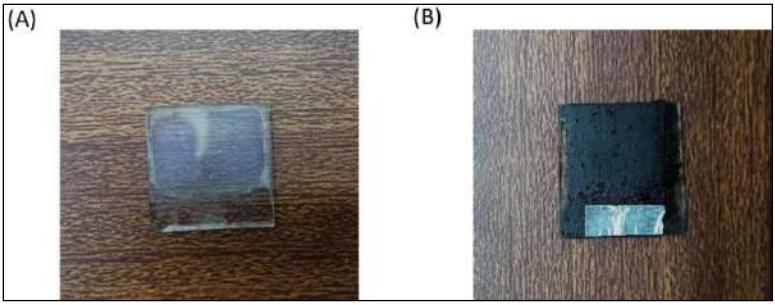

Fig 1: Picture of (A) the TiO_2 thin film on FTO coated glass (B) the PEDOT-Tos thin film

Following approximately thirty minutes of heating the FTO glass with TiO_2 coating to 450 °C, the sintering process was finished, and the TiO_2-deposited electrode was cooled to 100 °C. The samples were submerged in the rhodamine B dye for 24 hours after cooling to 100 °C. After drying and absorbing dye, the TiO_2 film was prepared for use as a photoanode.

Preparation of the Electrolyte

In this investigation, the DSSC electrolyte solution was made by combining 25 ml of a 4:1 by volume ethylene glycol/acetonitrile mixture with 2.075 g of KI and 0.19 g of I_2.

Preparation of Counter Electrodes

APS is used as an oxidant during the in-situ polymerization of EDOT monomer in an aqueous solution of PTSA to create PEDOT for the PEDOT-Tos counter electrode. Using a magnetic stirrer, the EDOT (0.02 mol) solution was agitated for 30 minutes at room temperature in an aqueous solution with 0.04 mol of PTSA. APS (0.02 mol) was dissolved in 100 ml of water to create the oxidant. The EDOT monomer aqueous solution and the APS solution were then gradually combined, and the reaction mixture was left to stir at room temperature for 24 hrs.

An indicative dark blue precipitate (containing PTSA) was formed. The product was cleaned with ethanol and deionized water in that order, centrifuged for five minutes at 7000 rpm, and then dried under a vacuum at 70 °C. 0.285 g of PEDOT was then added to 20 mL of DMF and agitated for 30 minutes after the PEDOT sample was produced. After then, the mixture was Sonicated 3 times for a duration of 20 minutes. A black homogenous solution was obtained. Then the solution was deposited on adhesive carbon tape for better adhesion using spin coater. And PEDOT-Tos thin film for counter electrode was obtained (Figure 2B).

DSSC Cell Fabrication

The dyed TiO_2 electrode and the PEDOT-Tos counter electrode were assembled to form the DSSC cell, with the dyed TiO_2 plates positioned downward onto the coated PEDOT-Tos counter electrode. They were positioned somewhat off-center to provide connections for the crocodile clips. The two electrodes were securely fastened and squeezed together to form a sandwich. Using a micropipette, the electrolyte redox (I−/I3−) is distributed between the two electrodes. Ultimately, the solar cell I-V measuring devices are linked to the constructed DSSC.

Characterization

Fourier transform infrared (FTIR) spectroscopy, ultraviolet-vis, field emission scanning electron microscopy (FESEM), and powder x-ray diffraction (XRD) patterns were utilized to describe the generated PEDOT-Tos sample structurally. Cu Kα radiation (λ = 1.54182 Å) was used in X-ray powder diffraction experiments with a diffractometer (BRUKER D8 Advance). Using materials dissolved in ethanol in quartz tubes, the prepared samples' UV-vis spectra were obtained using a spectrophotometer (Perkin-Elmer-USA, Lambda-45), with data being collected in the wavelength range of 350-1000 nm. A Hitachi (S3400N) FESEM was used to capture images to determine the surface morphology of the samples.

Result and Discussions

Spectral Studies

The degree of structural order in polymer-based composites promotes the electrical transport characteristics. The reflection plane (010) is responsible for the peak in the sample, which is located at an angle of 26.1°. This peak, which exhibits increasing and orderly π–π interaction of the conjugated units, is indicative of the crystalline structure of PEDOT. The stacking distances were calculated using Bragg's law, and for the PEDOT-Tos sample, the result is 3.4 Å.

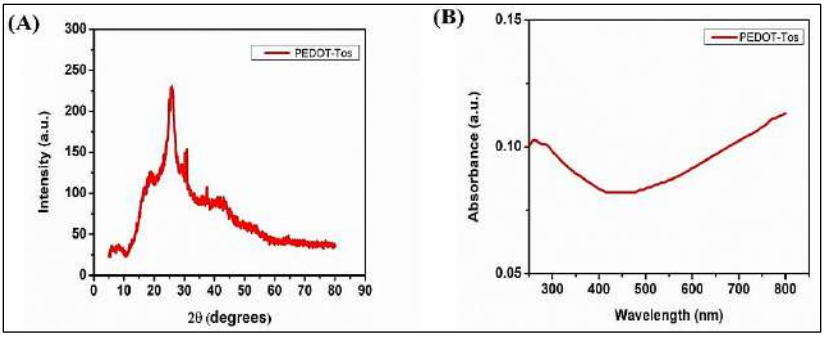

Fig 3: (A) XRD spectra of PEDOT-Tos and (B) UV–vis spectra of the PEDOT-Tos

Figures 13 and 14 display the sample's FTIR and UV-vis properties, respectively. A prominent absorption band of about 700-800 nm is visible in the virgin sample's UV-vis spectra, and it is linked to the π*-polaron transition. Additionally, a tendency of a free carrier tail was seen in all samples' UV-vis spectra at the longer wavelength, indicating the delocalization of the charge carriers. Based on the results, PEDOT is in a bipolaronic state and the right amount of charge carriers have generated. The thiophene ring's C-S-C deformation modes are attributed to the bands seen in the FTIR spectra of the PEDOT-Tos sample at 684, 839, 918, and 979 cm-1.

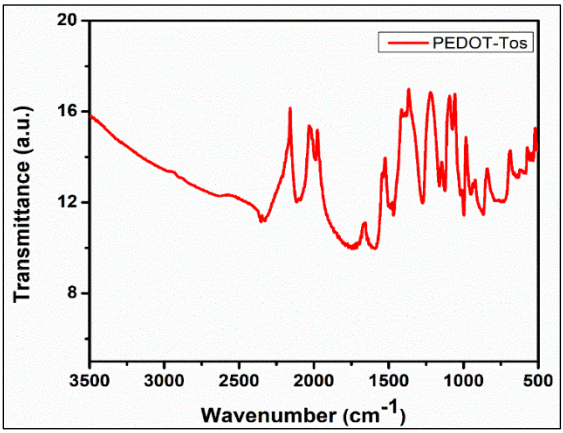

Fig 4: FTIR spectra of the PEDOT-Tos

The quinoidal structure of the thiophene rings is stretched C-C and C=C, which results in bands around 1365 and 1519 cm^{-1}. Furthermore, the band located approximately at 1660 cm^{-1} is ascribed to the polarons present in PEDOT.

Scanning electron microscopy has been used to further analyze the development of PEDOT-Tos with the morphological analysis (figure 5).

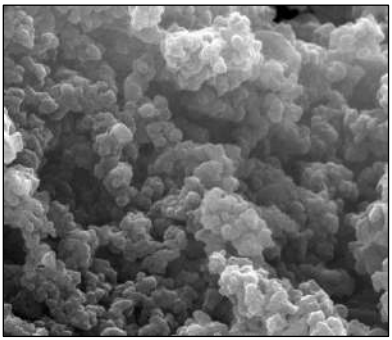

Fig 5: FESEM image of PEDOT Tos with 10mm scale bar

The pristine PEDOT-Tos SEM image shows a less compact self-assembled granular structure.

J-V Characterization of DSSCs:

The J-V characteristic curves for the DSSCs based on PEDOT-Tos and a carbon counter electrode are shown in Figure 6.

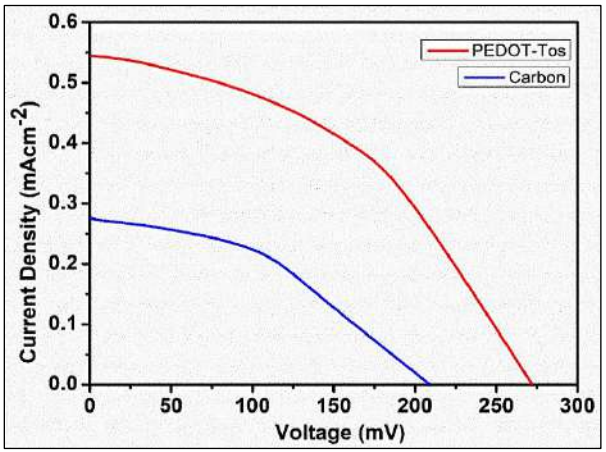

Fig 6: Current density (J) versus voltage (mV) characteristic curves for the DSSCs based on PEDOT-Tos and carbon CE

With the J-V data, the values of Jsc and Voc for both DSSCs can be easily derived. Equation is employed to calculate the power [13].

$$S^{+}\,(adsorbed\ at\ TiO2) + e^{-}\,(TiO2) \rightarrow S\,(adsorbed\ at\ at\ TiO2) \qquad (1)$$

And plotted as seen in Figure 7, power versus voltage for both DSSCs. The power (P)-voltage (mV) curves, which provide Jm and Vm, are used to calculate the maximum power point. Our measuring system's pin was 10mW/cm2.

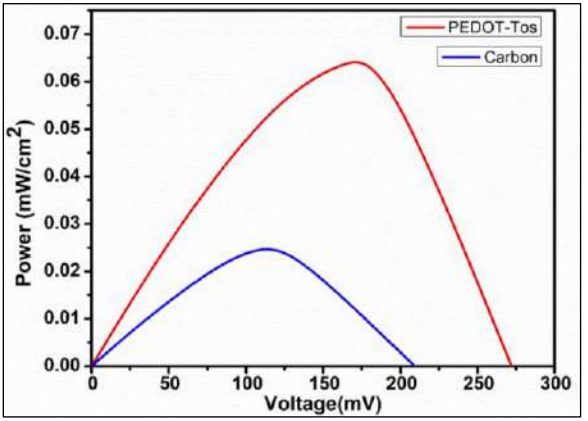

Fig 7: Power (P) versus voltage (mV) characteristic curves of the fabricated DSSCs

The cell efficiency and fill factor are calculated using equations

$$\eta = \frac{P_{max}}{P_{in}} = \frac{J_{Sc} \cdot V_{oc} \cdot FF}{P_{in}} \quad (2)$$

$$\text{FF} = \frac{\text{Area } A}{\text{Area } B} = \frac{J_{\text{mp}} \times V_{\text{mp}}}{J_{SC} \times V_{OC}} \quad (3)$$

Table 1 lists the photovoltaic parameters of the manufactured DSSCs based on PEDOT-Tos and Carbon CE.

Table 1: PEDOT-Tos and Carbon-based DSSC photovoltaic parameters

Counter Electrode	Jsc (mA/cm^2)	Voc (mV)	J_m (mA/cm^2)	V_m (mV)	FF	η %
PEDOT-Tos	0.545	272.07	0.342	190.6	0.44	0.652
Carbon	0.277	209.2	0.213	112.9	0.41	0.237

The findings in Table 1 shows that the PEDOT-Tos counter electrode achieved a maximum Jsc of 0.545 mA/cm2, outperforming the Jsc of 0.277 for the carbon electrode. Regarding Voc, we can observe that a maximum voltage of 272.07 mV was achieved with PEDOT-Tos CE, whereas a Voc of 209.2 mV was observed using carbon CE. PEDOT-Tos also demonstrated improved efficiency and a greater fill factor of 0.44. While PEDOT-Tos demonstrated an efficiency of 0.652, carbon CE demonstrated a lower efficiency of 0.237.

Conclusion

Using FTO-coated glass, we were able to effectively produce TiO_2 thin film for use as a working electrode in this investigation. The synthesized PEDOT-Tos made by in situ polymerization and heated to room temperature. Then, PEDOT-Tos thin film, which served as a counter electrode, was effectively produced utilizing the sol-gel spin coating process. Because of the PEDOT-Tos film's strong catalytic activity, the PEDOT-Tos CE functioned better than carbon tape. The triiodide to iodide reduction is accelerated by PEDOT-Tos's very effective electrochemical catalysis, which also ensures quick electron transport at the CE/electrolyte interface. The FF for PEDOT-Tos CE was 0.44.

References

1. Lewis N. S.; Toward cost-effective solar energy use. Science. 2007, 315, 798-801.
2. Bay, L.; West, K.; Winther-Jensen, B.; Jacobsen, T. Electrochemical reaction rates in a dye-sensitised solar cell-The iodide/triiodide redox system. Sol. Energy Mater. Sol. Cells, 2006, 90, 341–351.
3. Thomas, J.P.; Zhao, L.; McGillivray, D.; Leung, K.T. High-efficiency hybrid solar cells by nanostructure modification in PEDOT: PSS with co-solvent addition. J. Mater. Chem. A. 2014, 2, 2383–2389.
4. Yu, J.C.; Hong, J.A.; Jung, E.D.; Kim, D.B.; Baek, S.M.; Lee, S.; Cho, S.; Park, S.S.; Choi, K.J.; Song, M.H. Highly efficient and stable inverted perovskite solar cell employing PEDOT: GO composite layer as a hole transport layer. Sci. Rep. 2018, 8, 3–11.
5. Liu, J.; Pathak, S.; Stergiopoulos, T.; Leijtens, T.; Wojciechowski, K.; Schumann, S.; Kausch-Busies, N.; Snaith, H.J. Employing PEDOT as the p-type charge collection layer in regular organic-inorganic perovskite solar cells. J. Phys. Chem. Lett. 2015, 6, 1666–1673.
6. Carli, S.; Busatto, E.; Caramori, S.; Boaretto, R.; Argazzi, R.; Timpson, C.J.; Bignozzi, C.A. Comparative evaluation of catalytic counter electrodes for Co(III)/(II) electron shuttles in regenerative photoelectrochemical cells. J. Phys. Chem. C. 2013, 117, 5142–5153.
7. Park, B.W.; Pazoki, M.; Aitola, K.; Jeong, S.; Johansson, E.M.J.; Hagfeldt, A.; Boschloo, G. Understanding interfacial charge transfer between metallic PEDOT counter electrodes and a cobalt redox shuttle in dye-sensitized solar cells. ACS Appl. Mater. Interfaces, 2014, 6, 2074–2079.

8. Kavan, L.; Saygili, Y.; Freitag, M.; Zakeeruddin, S.M.; Hagfeldt, A.; Grätzel, M. Electrochemical Properties of Cu (II/I)-Based Redox Mediators for Dye-Sensitized Solar Cells. Electrochim. Acta, 2017, 227, 194–202.
9. Stojanovi´c, M.; Flores-Diaz, N.; Ren, Y.; Vlachopoulos, N.; Pfeifer, L.; Shen, Z.; Liu, Y.; Zakeeruddin, S.M.; Mili´c, J.V.; Hagfeldt, A. The Rise of Dye-Sensitized Solar Cells: From Molecular Photovoltaics to Emerging Solid-State Photovoltaic Technologies. Helv. Chim. Acta, 2021, 104, e2000230.
10. Saito, Y.; Kitamura, T.; Wada, Y.; Yanagida, S. Application of poly(3,4-ethylenedioxythiophene) to counter electrode in dye sensitized solar cells. Chem. Lett. 2002, 31, 1060–1061.
11. Yohannes, T.; Inganäs, O. Photoelectrochemical studies of the junction between poly[3-(4-octylphenyl) thiophene] and a redox polymer electrolyte. Sol. Energy Mater. Sol. Cells, 1998, 51, 193–202.
12. Saygili, Y.; Söderberg, M.; Pellet, N.; Giordano, F.; Cao, Y.; Munoz-García, A.B.; Zakeeruddin, S.M.; Vlachopoulos, N.; Pavone, M.; Boschloo, G.; *et al*. Copper Bipyridyl Redox Mediators for Dye-Sensitized Solar Cells with High Photovoltage. J. Am. Chem. Soc. 2016, 138, 15087–15096.
13. M. K. Nazeeruddin, E. Baranoff, and M. Grätzel, “Dye-sensitized solar cells: A brief overview, Sol. Energy, 2011, 85, 1172–1178.

Chapter - 11
An Extensive Study of Photo Thermoelectric Materials for Device Applications

Authors

Sudip Sarkar
Department of Physics, Techno India University, Kolkata, West Bengal, India

Krishanu Chatterjee
Department of Physics, Techno India University, Kolkata, West Bengal, India

Shilpa Maity
Department of Physics, Swami Vivekananda University, Barrackpore, West Bengal, India

Chapter - 11

An Extensive Study of Photo Thermoelectric Materials for Device Applications

Sudip Sarkar, Krishanu Chatterjee and Shilpa Maity

Abstract

Renewable energy sources are the current topic of research, nowadays, which opens different domains in device applications. One of such sources are the photothermoelectric (PTE) materials which have high light absorption and carrier mobility. The thermoelectric effect with photothermal conversion combines to produce the PTE effect. The current study provides a quick overview of the thermoelectric effect, photothermal conversion, and ultimately the photothermoelectric effect. Materials are classified as PTE materials owing to specific properties viz. molecular structure, bandgap, light absorption property, mobility, etc. Herein a comparative study of the above properties of different PTE materials has been undertaken. Further the generations of photovoltage and hence the photocurrent relating the thermoelectric effect has been observed and studied. In addition, a thorough study of molecular structure of these PTE materials displayed that the responsivity increases with the increase in the layers. Employing this PTE effect different strategies had been proposed for the development of the photodetectors with higher efficiencies. A comparison of all materials demonstrates that multi-layer MoS2 is the most potential candidate to be used in photodetectors till date.

Keywords: Photothermoelectric effect, seebeck coefficient, device application

Introduction

When light is absorbed by a material with an energy similar to the band gap, electron-hole pairs are produced. Above-band gap electron-hole pairs will arise in narrow band gap materials because the energy of most photons from the input light is greater than the band gap. After then, through a process known as thermalization, these above-band gap electron-hole couples will relax to the band boundaries and release their excess energy as heat. This process is known as photothermal conversion.

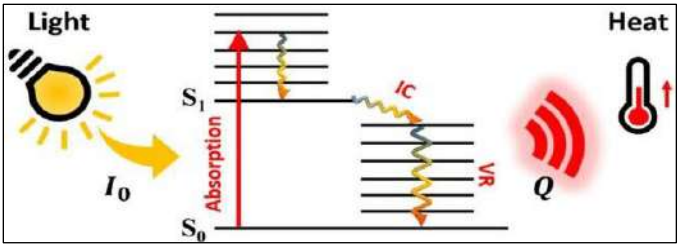

Fig 1: Photothermal conversion

A phenomenon known as the thermoelectric effect allows for the direct conversion of temperature differences into electric voltage and vice versa. When there is a difference in temperature on each side, a thermoelectric device produces a voltage on the practical measuring scale. On the other hand, a voltage supplied to it causes a temperature differential. The thermally induced current is caused by charged carriers in the material, such as electrons or holes, diffusing from the hot side to the cold side on an atomic scale. This process is comparable to a classical gas expanding when heated. The Seebeck effect, the Peltier effect, and the Thomson effect are three independently recognized phenomena that are together referred to as thermoelectric effects. Charge carriers proceed from the hot end to the cold end of a heated substance, creating a potential difference. The Seebeck effect is the term for this phenomenon. When electric current is maintained in a circuit of material consisting of two different conductors, the Peltier effect causes one junction to cool and the other to heat. The effect is amplified in circuits including dissimilar semiconductors. The development or absorption of heat that occurs when an electric current flows through a circuit made up of a single material with a temperature gradient running the length of it is known as the Thomson effect. The typical heat production linked to conductor electrical resistance to currents is layered on top of this heat transmission.

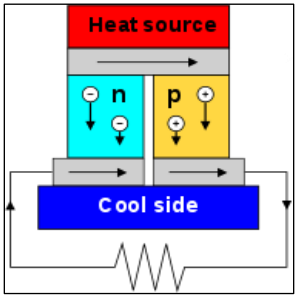

Fig 2: Thermoelectric materials

Seebeck coefficient (S) is the ration of ΔU and ΔT and it is related to the material's electrical conductivity.

$$----------S = -\frac{\pi^2 k_B^2 T}{3e}\left(\frac{d \ln \sigma}{dE}\right)\Big|_{E=E_f}$$

When a ray of light is incident on a material the material is heated and charge carriers drives from hot junction to cold junction and a potential difference is build this is known as photothermoelectric effect [1].

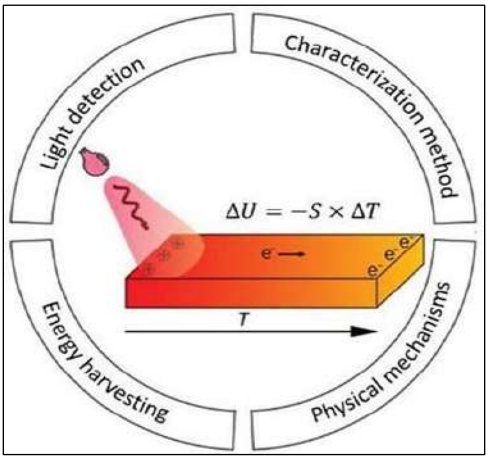

Fig 3: Photothermoelectric effect

The materials which show photothermoelectric effect are called photothermoelectric materials. In recent years so many photothermoelectric materials were discovered. The all Photothermoelectric materials are graphene, carbon nanotube, tungsten diselenide, cadmium sulfide films, bismuth selenide, black phosphorus, molybdenum disulfide, gallium nitride, gallium arsenide, strontium titanate, nanoporous silicon etc. By studying the properties and structure these materials are characterize as photothermoelectric materials [1, 5].

Properties of Photothermoelectric Materials

Properties of Graphene

A thermoelectric material with strong conductivity is graphene. Because monolayer graphene has a band gap of zero and an extremely high thermal conductivity of around 2500 W m-1 K-1, it may absorb ultra-broadband light [2]. The great mobility of graphene leads to an improvement in response speed. Compared to bilayer graphene, single layer graphene has a higher

Fermi energy level [3]. The Seebeck coefficient is proportional to the density of states in bilayer graphene. The Seebeck coefficient of bilayer graphene is higher. The non-linear dependency of thermal conductivity on temperature places a limit on the low-power detecting capabilities of graphene-based photodetectors. Fig. 5 shows the graphene-based device's photocurrent response. ±4 to 100 µV K-1 is the Seebeck coefficient of graphene [4].

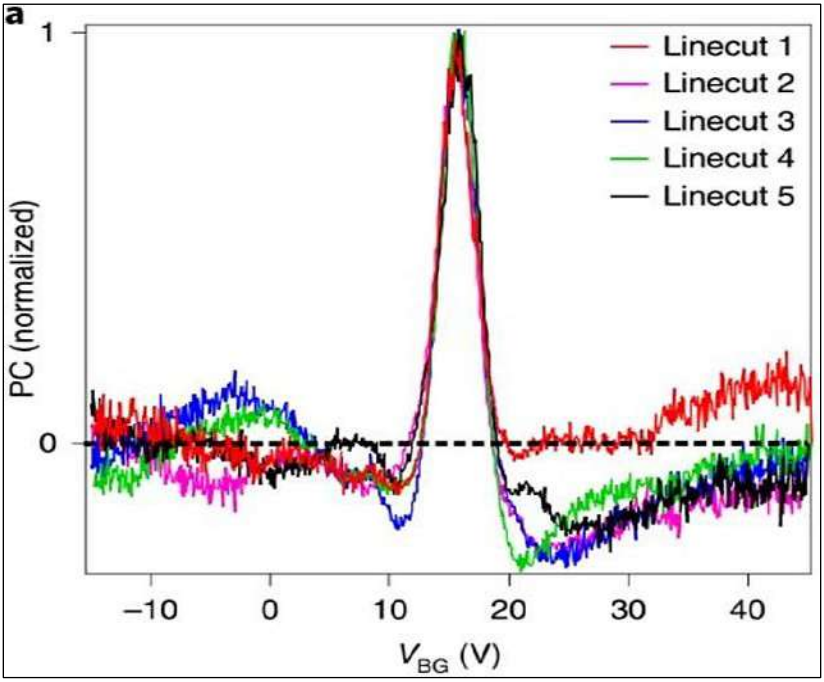

Fig 4: Horizontal line cuts through different charge neutrality point photocurrent peaks

Properties of Molybdenum Disulfide (MoS2)

MoS2 in a single layer has a very high mobility and a wide bandgap of 1.8 eV. The light response of externally biased MoS2 based phototransistors is driven by the change in conductivity upon Revelation, as demonstrated by the optoelectronic characteristics of MoS2. We are now able to investigate the mechanism of photocurrent production in single-layer MoS2 transistors with the use of scanning photocurrent microscopy. MoS2 FETs built in a single layer on SiO2 substrates. Using a home-built scanning confocal microscope, scanning photocurrent microscopy is utilized to spatially resolve the photo response of the MoS2 FET device. At each location, the photocurrent produced by the device and the intensity of the reflected laser

light are concurrently recorded. The electron-hole separation at the Schottky barriers (SBs) was identified as the mechanism responsible for the formation of zero-bias photocurrent. When the laser is focused far from the electrode margins, where SBs would be found, it is impossible for this process to account for the photogenerated current [5].

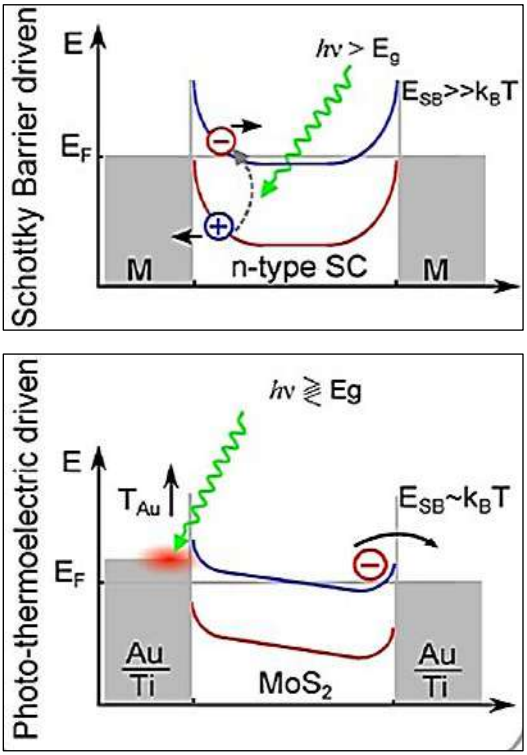

Fig 5: Diagram showing the photoresponse process in a photothermoelectric effect-dominated device

By using eq (1) the maximum value of Seebeck coefficient was calculated and the value is to be on the order of -0.2×10^5 μV K^{-1}.

Properties of Multi-Layer MoS2

Because of its increased carrier mobility, multilayer MoS2 is anticipated to have a larger drive current than monolayer MoS2. In monolayer MoS2 transistors, photodetection has been accomplished quickly. Compared to multilayer MoS2 devices, a reduced photoresponsivity is anticipated. Using a well-focused laser beam that scanned across the device surface, scanning photocurrent microscopy (SPCM) was carried out at zero source-drain bias

to determine the mechanism of photocurrent production. Raman spectra and short-circuit photocurrent were concurrently measured as a function of laser location. Fig. now displays the photocurrent picture obtained at Vg=15. -3.6 × 104 μV K-1 would be the S value corresponding to the peak photovoltaic voltage of -0.18 V [6].

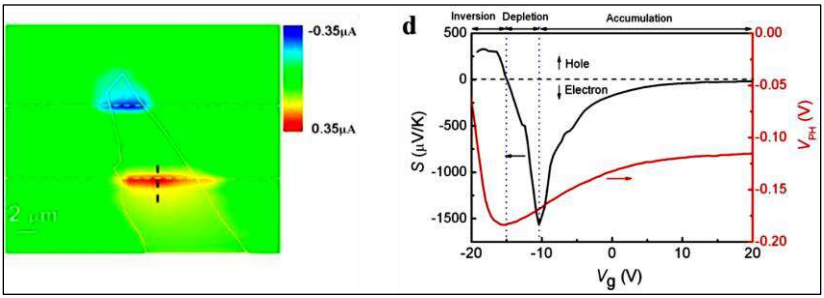

Fig 7: With a laser shining at the contact edge, the open-circuit photovoltaic and gate-dependent Seebeck coefficient are measured. The regimes of accumulation are divided by the vertical blue dotted lines

Properties of Carbon Nanotube (CNTs)

A unique combination of electron transport and energy relaxation channels is provided by carbon nanotubes. Through minute adjustments to the CNT's chirality and diameter, the band gap of a CNT can be widely tenable. Excitons are essential for both light absorption and energy relaxation because of the strong electron-electron interactions seen in carbon nanotubes [7].

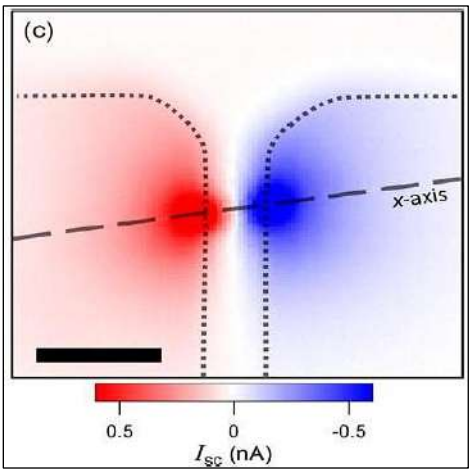

Fig 8: Short-circuit scanning photocurrent

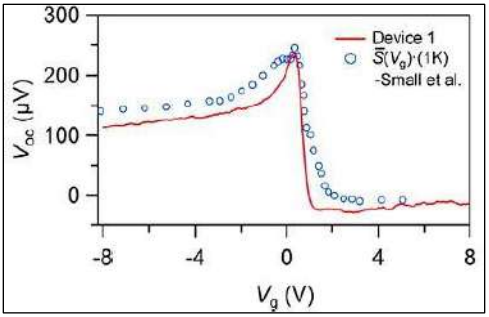

Fig 9: Open-circuit voltage (Vg) that the apparatus produces. The measurement of a semiconducting CNT's Seebeck coefficient is shown by open circles.

The mechanism for generating photocurrent at the metal-CNT interface has been recognized as the photovoltaic effect via CNT field-effect transistors (FETs) [8]. Where the CNT contacts the metal, the Photocurrent (Fig. 8) image demonstrates significant reactions. At around 250 μV K-1, the Seebeck coefficient preserved a peak value (Fig. 10) [9].

Properties of Strontium titanate ($SrTiO_3$)

One significant oxide used in semiconductors is strontium titanate (STO). STO has also been thoroughly investigated as a thermoelectric material at high temperatures. Deep phonon absorption band is seen in the long-wavelength infrared atmospheric window of STO. Laser power affects the photovoltaics of STO-based detectors [10]. Plotting the voltage against the corresponding temperature difference yields the seebeck coefficient value [11].

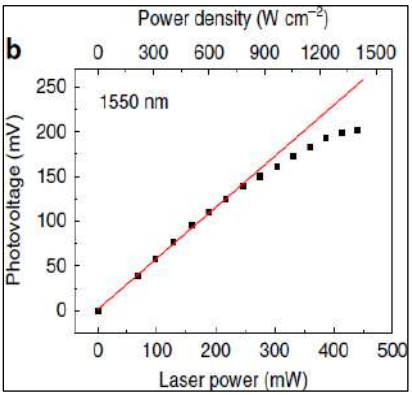

Fig 10: Photovoltage versus laser power of STO detector

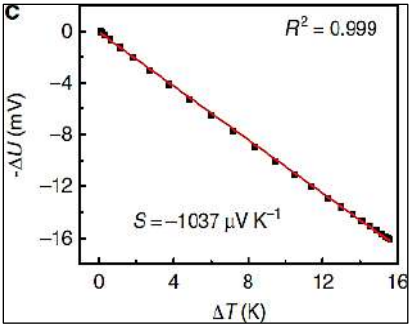

Fig 11: Voltage across the STO versus the corresponding temperature difference

Properties of Bismuth Selenide (Bi2Se3)

Three-dimensional strong topological insulator bismuth selenide. Bismuth selenide has a bandgap near 0.3 eV. Bismuth selenide has a strong spin polarization photoelectron emission capability. An essential thermoelectric substance is bismuth selenide. To examine the layered microstructure of Bi2Se3 nanoribbons, individual nanoribbons were placed onto a SrTiO3 substrate. The nanoribbon contact depicted in Figure 12 produces the highest photovoltaic voltage, around 400 μV [12].

Properties of Tungsten Diselenide (WSe2)

As a channel material for field-effect transistors (FETs), tungsten diselenide (WSe2), a semiconducting transition metal dichalcogenide, has demonstrated ambipolar performance [13]. The potential of monolayer WSe2 for optoelectronic devices has been demonstrated by its fabrication [14]. Depending on the specified gate design, measurements of the photocurrent under above and below bandgap illumination reveal (Fig. 14) that the photovoltaic or photothermoelectric effect dominates the photocurrent production. The photothermoelectric action produces 1.1 nA of current [15].

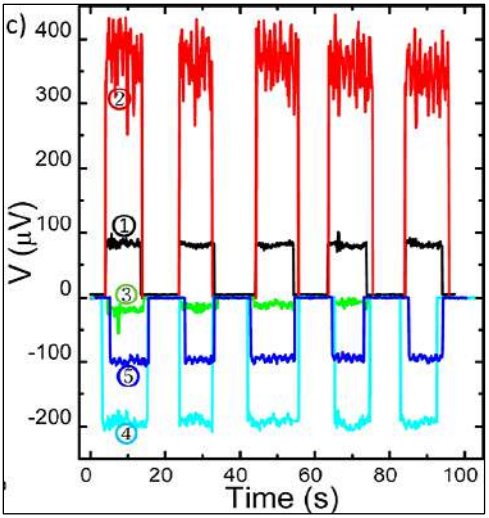

Fig 12: Photovoltaic reaction for turning on and off the laser light

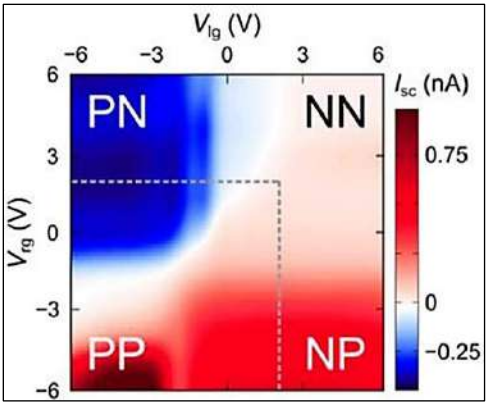

Fig 13: 2D Isc and Voc gate map illuminated above-bandgap

Properties of Nanoporous Silicon

Silicon (Si) is a widely utilized, inexpensive, and easily processed material in the semiconductor industry. Si is a thermoelectric material with low efficiency [16]. Si is a good thermoelectric material due to its high thermal conductivity. Phonon-phonon or phonon surface scattering phonon transfer is introduced by nanoporous silicon. On nanoporous silicon devices, the photocurrent has a value greater than 1 μA [17].

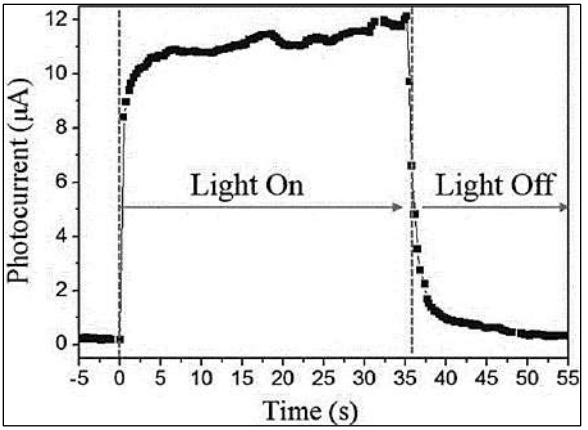

Fig 14: Dynamic photocurrent response for nanoporous silicon

Properties of Black Phosphorous

With a graphite-like structure and a narrow direct bandgap of 0.3 eV, black phosphorous (BP) has hole mobility considerably beyond 1000 cm2 V-1 s-1, enabling high-speed operation and enormous carrier density tenability [18]. If an asymmetry, such as asymmetrical doping or antenna feeding, is present, the photothermoelectric effect in BP is also an electron-heat-driven photo response through intraband processes at Terahertz (THz) frequency [19]. At 0.29 THZ and 0.12 THZ, the photocurrent achieved from the black phosphorous devices is 27 nA and 340 nA, respectively. The seebeck coefficient has a value of 100 μV K-1 [20].

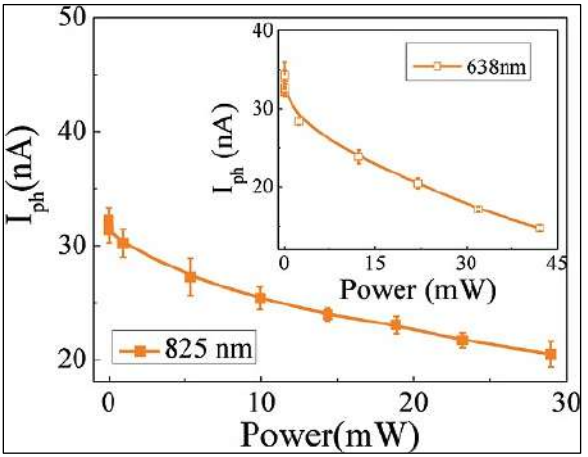

Fig 15: Three-dimensional schematics of the THz photocurrent response apparatus with infrared assistance

Applications of Photothermoelectric Materials

In general, photothermoelectric detectors, sometimes referred to as photodetectors, hold great potential for low-cost, maintenance-free, uncooled terahertz and infrared detection. Because photo thermoelectric materials have strong optoelectronic and thermoelectric properties, they are used in the fabrication of photodetectors. Studying the responsiveness of photodetectors allows one to determine their performance. As we all know, photodetectors use an optical-to-electrical conversion efficiency known as responsiveness to transform light into an electrical signal.

Conclusion

MoS2 has an order of magnitude higher Seebeck coefficient than the other PTE materials. Applications like on-chip power generation and thermoelectric nanodevices can benefit from the Seebeck coefficient's wide gate tenability. These applications can involve the development of autonomously powered devices as well as the energy collection of waste thermal energy from other operations. The tenability of the Seebeck coefficient served as an effective means of maximizing device performances in each of these applications. Responsivity affects the photodetectors' ability to function. Responsivity values indicate which photodetectors are the most efficient. Photocurrent and wavelength affect sensitivity. The rationale for each photodetector's performance and responsiveness is presented in this review.

References

1. Lu, X., Sun, L., Jiang, P. and Bao, X., 2019. Advanced Materials, 31(50), p.1902044.
2. Basko, D., 2011. Science, 334(6056), pp.610-611.
3. Xu, X., Gabor, N.M., Alden, J.S., Van Der Zande, A.M. and McEuen, P.L., 2010. Nano letters, 10(2), pp.562-566.
4. Fuhrer, M.S. and Medhekar, N.V., 2020. Nature nanotechnology, 15(4), pp.241-243.
5. Zhang, Y., Li, H., Wang, L., Wang, H., Xie, X., Zhang, S.L., Liu, R. and Qiu, Z.J., 2015.Scientific reports, 5(1), pp.1-7.
6. Buscema, M., Barkelid, M., Zwiller, V., Van Der Zant, H.S., Steele, G.A. and Castellanos-Gomez, A., 2013. Nano letters, 13(2), pp.358-363.
7. DeBorde, T., Aspitarte, L., Sharf, T., Kevek, J.W. and Minot, E.D., 2014. ACS nano, 8(1), pp.216-221.

8. Groenendijk, D.J., Buscema, M., Steele, G.A., Michaelis de Vasconcellos, S., Bratschitsch, R., van der Zant, H.S. and Castellanos-Gomez, A., 2014. Nano letters, 14(10), pp.5846-5852.
9. Yan, Y., Liao, Z.M., Ke, X., Van Tendeloo, G., Wang, Q., Sun, D., Yao, W., Zhou, S., Zhang, L., Wu, H.C. and Yu, D.P., 2014. Nano letters, 14(8), pp.4389-4394.
10. Lu, X., Jiang, P. and Bao, X., 2019. Nature communications, 10(1), pp.1-7.
11. Guo, W., Dong, Z., Xu, Y., Liu, C., Wei, D., Zhang, L., Shi, X., Guo, C., Xu, H., Chen, G. and Wang, L., 2020. Advanced Science, 7(5), p.1902699.
12. Limpert, S., Burke, A., Chen, I.J., Anttu, N., Lehmann, S., Fahlvik, S., Bremner, S., Conibeer, G., Thelander, C., Pistol, M.E. and Linke, H., 2017. Nano letters, 17(7), pp.4055-4060.
13. Harper, J.G., Matthews, H.E. and Bube, R.H., 1970. Journal of Applied Physics, 41(2), pp.765-770.
14. Konabe, S. and Yamamoto, T., 2014. Physical Review B, 90(7), p.075430.
15. Huang, D., Zou, Y., Jiao, F., Zhang, F., Zang, Y., Di, C.A., Xu, W. and Zhu, D., 2015. ACS applied materials & interfaces, 7(17), pp.8968-8973.
16. Erikson, K.J., He, X., Talin, A.A., Mills, B., Hauge, R.H., Iguchi, T., Fujimura, N., Kawano, Y., Kono, J. and Léonard, F., 2015. ACS nano, 9(12), pp.11618-11627.
17. Gosciniak, J., Rasras, M. and Khurgin, J.B., 2020. ACS Photonics, 7(2), pp.488- 498.
18. Lai, Y.S., Tsai, C.Y., Chang, C.K., Huang, C.Y., Hsiao, V.K. and Su, Y.O., 2016.Advanced Materials, 28(13), pp.2644-2648.
19. Echtermeyer, T.J., Nene, P.S., Trushin, M., Gorbachev, R.V., Eiden, A.L., Milana, S., Sun, Z., Schliemann, J., Lidorikis, E., Novoselov, K.S. and Ferrari, A.C., 2014, Nano letters, 14(7), pp.3733-3742.
20. Liu, H., Liu, Y., Dong, S., Xu, H., Wu, Y., Hao, L., Cao, B., Li, M., Wang, Z., Han, Z. and Yan, K., 2020. ACS applied materials & interfaces, 12(44), pp.49830-49839.

21. St-Antoine, B.C., Ménard, D. and Martel, R., 2012. Nano Research, 5(2), pp.73-81.

22. Kwok, H.B. and Bube, R.H., 1973. Journal of Applied Physics, 44(1), pp.138-144.

23. Dai, W., Liang, Y., Yang, M., Schrecongost, D., Gajurel, P., Lee, H., Lee, J.W., Chen, J., Eom, C.B. and Cen, C., 2019. Nano letters, 19(10), pp.7149-7154.

24. Ma, Q., Song, J.C., Gabor, N.M. and Jarillo-Herrero, P., 2020. Nature nanotechnology, 15(4), pp.244-246.

25. Antidormi, A. and Cummings, A.W., 2021. Physical Review Applied, 15(5), p.054049.

26. He, X., Wang, X., Nanot, S., Cong, K., Jiang, Q., Kane, A.A., Goldsmith, J.E., Hauge, R.H., Léonard, F. and Kono, J., 2013. ACS nano, 7(8), pp.7271-7277.

27. Wu, D., Yan, K., Zhou, Y., Wang, H., Lin, L., Peng, H. and Liu, Z., 2013. Journal of the American Chemical Society, 135(30), pp.10926-10929.

28. Zhong, Y., Zhang, L., Linseis, V., Qin, B., Chen, W., Zhao, L.D. and Zhu, H., 2020. Nano Energy, 72, p.104742.

29. Zhang, X., Li, T.T., Ren, H.T., Peng, H.K., Shiu, B.C., Wang, Y., Lou, C.W. and Lin, J.H., 2020. ACS Applied Materials & Interfaces, 12(49), pp.55072-55082.

30. Chen, M., Wang, Y., Ma, W., Huang, Y. and Zhao, Z., 2020. ACS Applied Materials & Interfaces, 12(25), pp.28510-28519.

31. Liu, W., Wang, W., Guan, Z. and Xu, H., 2019. Nanoscale, 11(11), pp.4918-4924.

32. Zhao, H., Ouyang, B., Han, L., Mishra, Y.K., Zhang, Z. and Yang, Y., 2020. Scientific reports, 10(1), pp.1-11.

33. Zhang, D., Song, Y., Ping, L., Xu, S., Yang, D., Wang, Y. and Yang, Y., 2019. Nano Research, 12(12), pp.2982-2987.

34. Wang, X., Evans, C.I. and Natelson, D., 2018. Nano letters, 18(10), pp.6557-6562.

35. Khodzitsky, M.K., Demchenko, P.S., Zykov, D.V., Zaitsev, A.D., Makarova, E.S., Tukmakova, A.S., Tkhorzhevskiy, I.L., Asach, A.V., Novotelnova, A.V. and Kablukova, N.S., 2021, In Photonics (Vol. 8, No. 3, p. 76). Multidisciplinary Digital Publishing Institute.

Chapter - 12
Synthesis and Thermoelectric Characterization of Pedot-Tos/Tin Selenide Nanocomposite

Authors

Swagata Majumder
Department of Physics, Techno India University, Kolkata, West Bengal, India

Krishanu Chatterjee
Department of Physics, Techno India University, Kolkata, West Bengal, India

Shilpa Maity
Department of Physics, Swami Vivekananda University, Barrackpore, West Bengal, India

Chapter - 12

Synthesis and Thermoelectric Characterization of Pedot-Tos/Tin Selenide Nanocomposite

Swagata Majumder, Krishanu Chatterjee and Shilpa Maity

Abstract

With increasing environmental degradation, researchers are focused towards developing environment friendly technologies and contribute to the green environment. Investigating PEDOT, a conducting polymer, is one such use. Since PEDOT has such distinct qualities, it has drawn a lot of interest in recent decades. Tosylate-doped PEDOT has demonstrated promising performance toward the primary objective of developing organic thermoelectric materials (TE). As organic TE materials, tin selenide (SnSe) and PEDOT-Tos nanocomposites were created and studied. The charge carriers' mobility was shown to be enhanced by an improved ordered structure. As a result, TE power factor, electrical conductivity, and thermoelectric power all increased. For SnSe contents over 15%, an opposing trend is seen in the structure, most likely because of decreased π-stacking interactions between SnSe and the PEDOT units. This work demonstrates that it is a useful method that can support the design and synthesis of high-performance thermoelectric π-conjugated polymers in the future.

Keywords: Thermoelectric properties, nanocomposite, π-conjugated polymers

Introduction

Due to increased awareness of environmental concerns such as global warming and energy scarcity, thermoelectric (TE) devices have become a viable and environmentally acceptable replacement for power generators and heat pumps. By 2023, it is anticipated that a larger percentage of electricity generation will come from renewable sources to combat environmental damage. Thermoelectric generators (TEGs) are a great option to complement environmentally friendly gadgets, among other technologies [1]. In the biomedical field, the use of wearable electronics and implantable devices,

such as cardiac pacemakers, biometric monitoring, wearable pressure sensors, sensory and neurological implantable devices, pulse oximetry sensors, and electrocardiography monitoring sensors, is rapidly expanding [2-7]. The majority of these gadgets run mostly on batteries, which are finite power sources that shorten their lifespan and require replacement after a certain amount of time [8]. Due to these battery inadequacies, research has been directed towards TEGs, which employ the difference in temperature between the wearer's skin and the surrounding air to produce a low order current between a few μv and mv.

Temperature gradients can be directly converted into electrical energy using thermoelectric (TE) devices, and the electrical energy can then be employed to cool specific parts of the power system [9-12]. There are two different kinds of devices: the Seebeck Effect is the basis for the thermoelectric generator, whereas the Peltier Effect is the basis for the thermoelectric cooler. The Seebeck effect states that when one junction in a circuit made up of two different conductors or semiconductors becomes heated, there is a high chance that an electromotive force would result [8].

TE devices' power generation efficiency is measured using a dimensionless figure of merit (ZT).

It may be represented as follows:

$$ZT=S^2\sigma T/\kappa \quad (1)$$

Where T is the temperature in units of K, the thermal conductivity (κ) is measured in W m^{-1} K^{-1}, the Seebeck coefficient (S) is expressed in μV K^{-1}, and the electrical conductivity (σ) is expressed in S cm^{-1}.

Power factor (PF) is the amount S2σ; a high PF indicates that the device can provide high output voltage and current. The efficiency with which a TE material may transform thermal energy into electrical energy is limited by its figure of merit.

The field of organic TE materials, which includes graphene, carbon nanotubes, and polymers, has received very little research over the past several decades because of low ZT values. The inherent flexibility of organic TE materials, including conducting polymers (CPs), has drawn interest in recent studies. One positive result is that organic TE materials generally have low thermal conductivity (conducting polymers have a thermal conductivity of 0.2-0.34 W/mK), which is hard to further reduce [13]. As a result, the power factor (PF = α2σ), which may be increased by many orders of magnitude, determines the ZT value of organic TE materials [14].

The PF of conducting polymers, such as Poly (3,4-ethylenedioxythiophene) (PEDOT), Polyaniline (PANI), and Polypyrrole (PPy), which have the advantages of low heat conductivity, non-toxicity, and cheap cost, has been greatly improved during the last several years [15]. The most suitable non-conducting polymers are polyvinylidene fluoride, poly(3-octylthiophene), and poly(3-hexylthiophene) (P3HT) [16]. It is noteworthy that, in contrast to non-conductive polymers, conducting polymers dominate the bulk of the thermoelectric device matrix due to their inherent electrical conductivity. Furthermore, as a barrier to bundle-to-bundle hopping, the non-conducting polymers reduce thermoelectric performance [16]. One of the conducting polymers that has been researched the most is PEDOT, or poly(3,4-ethylenedioxythiophene).

PEDOT is of importance because of its exceptional air and heat stability, its relatively straightforward and well-established synthesis procedures that enable large-scale manufacture, and its specially developed pattern coating and printing capabilities. PEDOT's strong and consistent electrical conductivity is the primary characteristic that guarantees its distinct position among conducting polymers [17]. For many electronic, optoelectronic, and bioelectronic applications, including electrochemical transistors, sensors, electrochromic displays, organic electronic ion pumps, electrodes interacting with neural systems, and implantable drug delivery devices, PEDOT is the material of choice due to the combination of all these characteristics. The most researched counterion for PEDOT to date is polystyrene sulfonate (PSS), a polymeric counterion.

But in recent years, other molecular counterions, especially tosylate have emerged as the more effective substitute for polymeric ones. This is because PEDOT exhibits conductivities more than 3000 S/cm-1 and routinely exceeds PEDOT: PSS. In order to address this issue, research teams have been developing composite TE materials lately that link other inorganic TE materials with high S values to PEDOT, increasing its S value [18]. By adding chalcogenide-based compounds such as Bi2Te3 (180 μV/K) [19, 20], Sb2Te3 (125μV/K) [21] and Cu1SnSe3 [22], the S value of the PEDOT has been enhanced.

Owing to its exceptional Seebeck coefficient (~520 μV/K) and low thermal conductivity (~0.6 W/m·K) at 300 K, tin selenide (SnSe) is also among the most efficient thermoelectric fillers at almost room temperature [16]. The TE performance of PEDOT: Tos is improved in this study by using an inorganic composite SnSe.

2. Materials Used

The monomer, 3,4-dioxythiophene (EDOT) was purchased from Sigma Aldrich. Ammonium peroxydisulphate (APS) AND para toluene sulphonic acid (pTSA) was purchased from Alfa-Aesar. Deionized water was purchased from hydrolab, India. Pyridine was bought from buy chemicals. Tin selenide was bought from Sigma Aldrich.

2.1 Preparation of PEDOT-Tos

Using APS as an oxidant, PEDOT was created through the *in situ* polymerization of EDOT monomer in PTSA aqueous solution. To an aqueous solution of PTSA (0.04 mol), the EDOT solution (0.02 mol) was added. The combination was referred to as solution A. After that, Solution A was left on a magnetic stirrer and swirled at room temperature for 30 minutes. Subsequently, solution A was mixed dropwise with the aqueous solution of APS (0.02 mol), called solution B. Pyridine (0.02 mol) was then added to the mixture. The finished mixture was left to stir at room temperature for 24 hrs. The mixture's color changed to black. Following a 5-minute centrifugation run at 7000 rpm to collect the product, it was cleaned with ethanol and deionized water before being dried at 70 °C. The result was a substance known as SP1 and called PEDOT-Tos.

Preparation of PEDOT-Tos/SnSe Nanocomposite

A mixture of PEDOT-Tos and DMF SnSe and ethanol was used to create the two solutions. For thirty minutes each, the two solutions underwent independent sonication. Once half an hour had passed, the two solutions were combined and mixed for a full two hours. Pellet formation was followed by centrifugation of the mixture and drying of the powder sample at 70 °C. Differential ratios of PEDOT-Tos were combined with 20 milliliters of DMF, which corresponded to varied amounts of SnSe added to 20 milliliters of ethanol, resulting in diverse amalgamations. With weight percentages of 5%, 10%, 15%, 20%, and 25% of SnSe with PEDOT-Tos, respectively, the samples were designated SP2, SP3, SP4, SP5, and SP6.

Characterization

All the synthesized samples were structurally evaluated using UV-vis, powder x-ray diffraction (XRD) patterns, fourier transform infrared (FTIR) spectroscopy, and field emission scanning electron microscopy (FESEM). X-ray powder diffraction experiments were conducted using a diffractometer (BRUKER D8 Advance) equipped with CuKα radiation (λ=1.54182 Å).

Samples were dissolved in ethanol and placed in quartz tubes to record the UV-vis spectra of the produced samples. The spectrophotometer (Perkin-Elmer-USA, Lambda-45) captured data in the wavelength range of 350-1000 nm. The surface morphology of the samples was assessed by obtaining FESEM images with a Hitachi (S3400N).

Electrical conductivity and thermoelectric power were measured at room temperature using round pellets of the samples. A temperature difference was provided to the samples and the corresponding potential difference developed was recorded.

Results and Discussion

Spectral Studies

The degree of structural order in polymer-based composites improves the electrical transport characteristics. Finding a material's crystallographic structure can be done by X-ray diffraction (XRD) examination. The improvement in charge carrier transfer is thought to be based on structural order. It is believed that the charge carrier transport pathway is the Van der Waals and strong π–π interaction. Therefore, XRD analysis of the synthesized samples was performed to determine the effect on the transport properties of the structural change of PEDOT-Tos produced by the addition of different percentages of SnSe. The results are displayed in figure 1.

Peaks at 8.4°, 18.8°, and 25.1° are seen in the unaltered sample. The existence of a crystalline phase in the polymer matrix is indicated by these peaks. These three peaks' reflections guarantee that the crystalline phase is present. When the peak locations of the synthetic samples are compared, the composites' X-ray diffraction pattern has a different peak position. Except for SP6, all composites exhibit a movement toward a lower angle at the peak location at $2\theta \sim 8.4°$. This indicates a change in lattice characteristics in response to a change in SnSe concentration. Regarding the peak of SP5, SP6 exhibits a movement to the right.

It is suggested that the interchain distance inside the stack is connected to the peak at 8.4°. The change so suggests that the stacking distance will rise. With the rise in SnSe concentration, there is also a further increase in intensity at this peak site. The enhanced crystallinity is shown by both the rise in intensity and the increase in stacking distance. The enhanced packing could lead to more charge carriers tunneling both inside and between chain stacks. For SP4, SP5, and SP6, there were noticeable alterations in the XRD pattern. Peaks were visible for SP4 at $2\theta \sim 30.9°$ and for SP5 and SP6 at $2\theta \sim 30.2°$. This suggests that SnSe is present, and that intensity rises as SnSe content does.

Furthermore, SP6 shifts to a lower angle than SP5, with the peak at 2θ ~ 25.1° being ascribed to the SnSe concentration rises to 20%, the π-π stacking distance shifts to a higher angle and takes on a new form. This suggests that the interlayer stacking distance is getting smaller. By improving the π-π coupling, it gives the charge carriers a route and improves the TE characteristics. The construction of an ordered structure is indicated by both the shifts and the rise in intensity with an increase in SnSe concentration, which affects the samples' transport characteristics. For 2θ ~ 18.8°, a similar tendency to that of the peak at 2θ ~ 8.4° was noted. Furthermore, it has been shown that 20 weight percent of SnSe in the PEDOT-Tos matrix acts as a threshold, at which the development of PEDOT-Tos crystallization is hindered, forming a barrier to carrier transport that is consistent with the electrical transport capabilities.

Table 1: XRD peaks of all the sample

Sample	Peaks Obtained at 2θ (°)		
SP1	8.4	18.79	25.1
SP2	8.17	18.48	25.5
SP3	8.05	18.32	25.7
SP4	7.71	18.1	26.1
SP5	7.67	18.0	26.58
SP6	8.25	18.4	26.24

Further, UV-vis and FTIR characteristics of the samples have been studied. They have been illustrated in the figures 2 and 3 respectively.

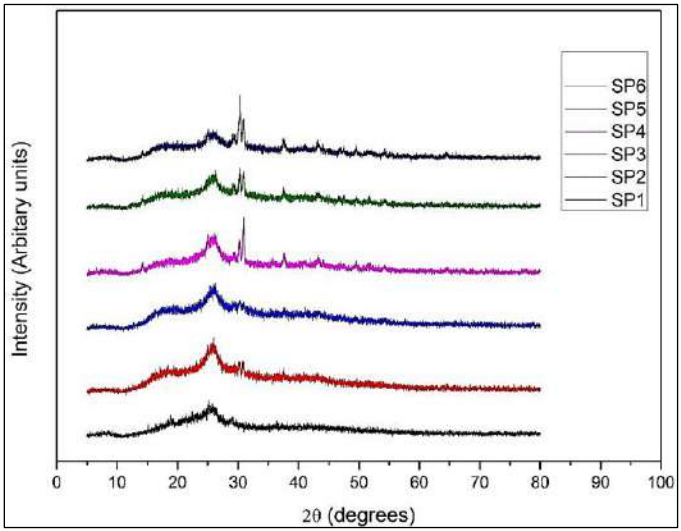

Fig 1: XRD spectra for PEDOT-Tos/SnSe nanocomposites

Using a reference sample as a comparison, UV-Vis. spectroscopy is an analytical technique that counts the unique wavelengths of UV or visible light that a sample absorbs. The shift in the electronic states is verified by UV-Vis. spectroscopy. Around 600 nm, an absorption band is visible in the unadulterated sample. The absorption band at around 600 nm is associated with the π*-polaron transition. Composite sample spectra exhibit a band at around 275 nm, which is thought to be the result of the π–π* transition. This band is red shifted for SP2, SP3, SP4, and SP5. This indicates that there is more electron contact, which raises the delocalization charges and, in turn, the electrical transport characteristics. The band is blue-shifted for SP6, which suggests that the π–π* transition is fading. The free carrier tail at longer wavelengths indicates the delocalization of charge carriers. The importance of the free carrier tail rises as the SnSe content does, up to SP5. SP6 indicates that a barrier has occurred.

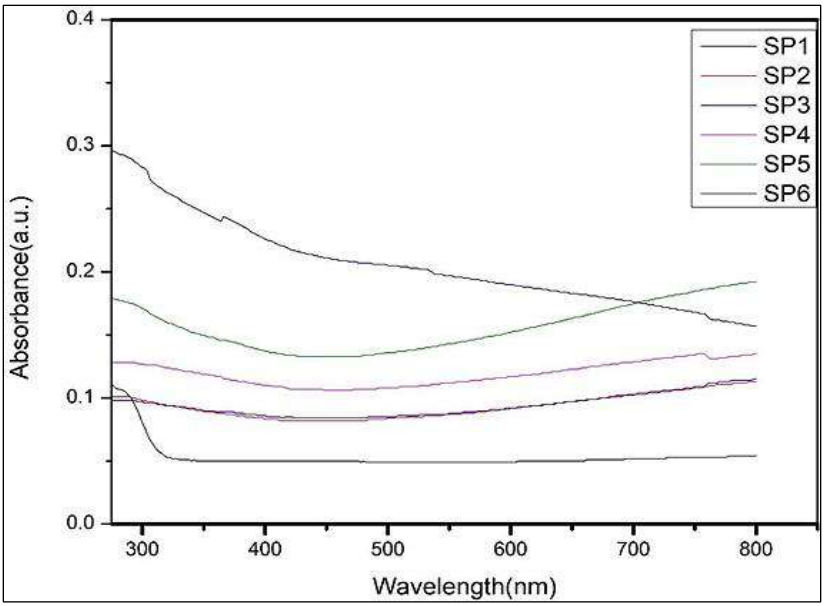

Fig 2: UV-vis spectra for PEDOT-Tos/SnSe nanocomposites

FTIR analysis is used to know the affect a molecule's atomic vibrations, which causes energy to be either absorbed or transmitted. The bands seen in the FTIR spectra of the clean material at 698, 852, 939, and 987 cm^{-1} are attributed to the C-S-C deformation modes in the thiophene ring. The C-O-C bending vibration signature of the ethylenedioxy group is shown by the bands at about 1083, 1133, and 1202 cm^{-1}. The quinoidal structure of the

thiophene rings' C-C and C=C stretching is responsible for the bands located approximately at 1107, 1251, 1425, and 1550 cm^{-1}. In addition, the polarons found in PEDOT are attributed to the bands around 1975, 2025, and 2160 cm^{-1}. All the bands are visible in the composite samples' FTIR spectra, however there is a shift. The shift is probably caused by the interactions between π-π.

This suggests that the inclusion of SnSe alters the resonance structure of PEDOT-Tos.

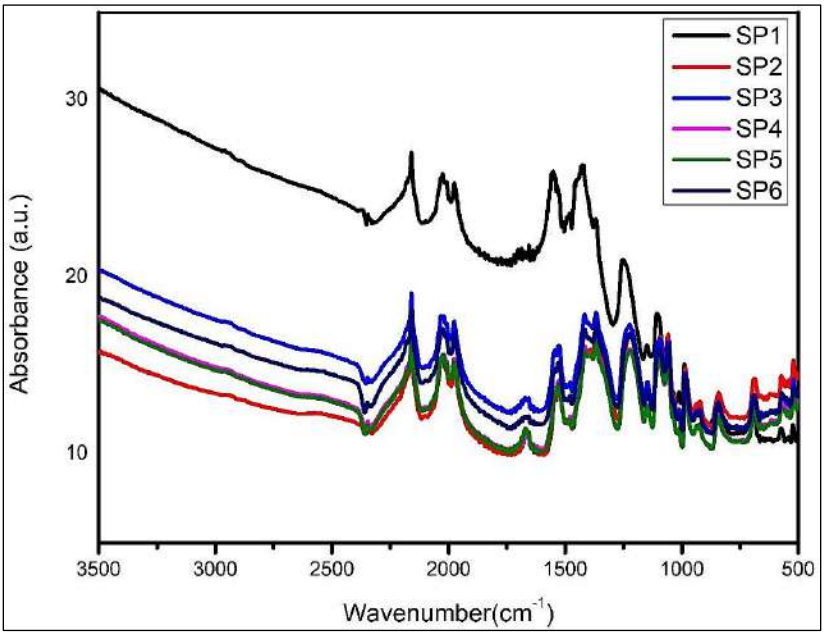

Fig 3: FTIR spectra of PEDOT-Tos/SnSe nanocomposites

4.2 Structural Characterization

Figure 4 illustrates the use of field emission scanning electron microscopy (FESEM) to investigate the morphology, structural development, and rearrangement process of PEDOT-Tos in the presence of SnSe. The pristine PEDOT-Tos SEM picture shows a less compact self-assembled granular structure. A layered, stacked structure is shown in the SEM image of Sn. With increase in SnSe content, the compactness in PEDOT-Tos increases, thereby creating a pathway for the charge carriers and hence increasing electrical conductivity.

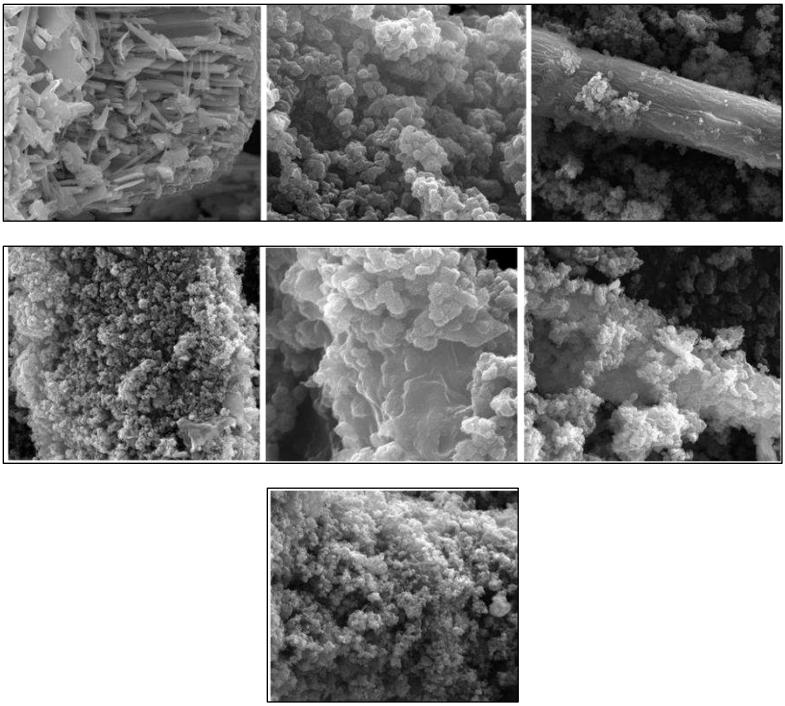

Fig 4: FESEM images of (a) Sn (b) SP1 (c) SP2 (d) SP3 (e) SP4 (f) SP5 (g) SP6 with 10mm scale bar

With an increase in SnSe content, PEDOT interacts more with SnSe, which acts as a growth template. XRD, UV-vis, and electrical transport characteristics are in line with the reported reduction in PEDOT-Tos and SnSe interaction for SP6.

Electrical Characterization

Figure 5 shows the fluctuation of electrical conductivity (σ) at room temperature with SnSe concentration, which was tested to investigate the electrical transport capabilities of the produced samples. As the concentration of SnSe rose up to SP4, the value of σ increased. It is clear from XRD research that structural order rises to 15% of the concentration of SnSe.

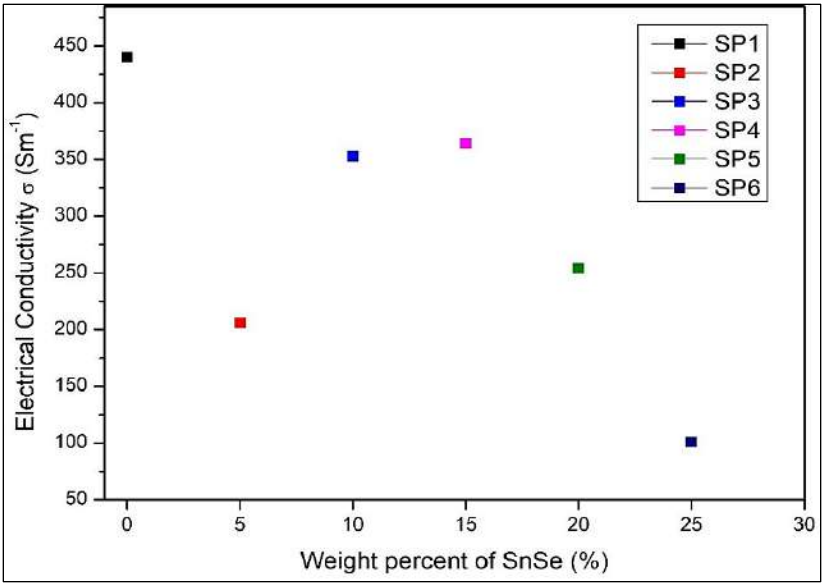

Fig 4: Electrical conductivity variation with SnSe concentration

The electrical conductivity rises as a result of the enhanced carrier mobility. There is resistance to the charge carriers, as shown by SP5's value being lower than SP4's. This is consistent with the XRD investigation, which demonstrates that when the SnSe level rises over 15%, the structural order decreases. According to spectrum investigations and morphology, the value of SP6 shows the existence of a barrier in conduction.

Thermoelectric Power

Both σ and S cannot rise simultaneously because they have an inverse relationship with the distance between the narrow transport level and Fermi level [23]. Remarkably, in this instance, both parameters rise as the SnSe concentration rises, demonstrating that the conduction mechanism could not be explained by band theory or the traditional model based on electron-phonon scattering. This feature of thermoelectric power may be expressed as follows using the Mott's formalism, which consists of terms for carrier concentration (n) and energy-dependent mobility [μ(E)]:

$$S = \frac{C_e}{n} + \frac{\pi^2 k_B^2 T}{3e}\left[\frac{\partial \ln \mu(E)}{\partial E}\right]_{E=E_F} \quad (2)$$

The specific heat (Ce) and the Boltzmann constant (kB) are the corresponding values. Equation (2) suggests that the thermoelectric power should be influenced by both n and μ(E).

Because carrier mobility increases far more quickly than carrier concentration, it has been found that carrier mobility is important for up to 15% of the SnSe content in the polymer. A higher structural order results in more charge carrier mobility, which raises electrical conductivity and thermoelectric power. Thus, it appears that this technique works well for enhancing polymers' thermoelectric qualities. After 15% SnSe content, the thermoelectric power decreased, most likely because more twisted chains were formed, which resulted in more defects as the SnSe content increased [24]. Consequently, the carrier concentration enters the picture and the carrier mobility declines, lowering the thermoelectric power.

Figure 5 displays the thermoelectric power fluctuation of the composite samples plotted against the SnSe concentration. The maximum value attained was 40 VK-1 for SP4. Additionally, Bubnova *et al*. [25] have shown that when structural order grows, the density of states' asymmetry increases as well, giving PEDOT-Tos a larger thermoelectric power. A broadening of the DoS is observed with increasing crystallinity, and it is claimed that this widening extends to all π bands, even those around Fermi level, enhancing thermoelectric power and carrier mobility. Thus, an increase in the SnSe concentration up to 15% causes a rise in both structural order and crystallinity, which raises carrier mobility and thermoelectric power. The reduction of structural order and consequent loss in electrical conductivity and thermoelectric power occur when the SnSe level rises over 15%.

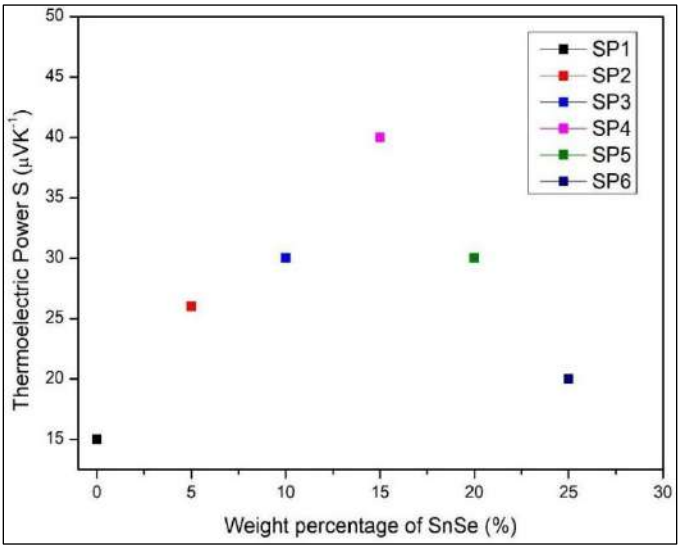

Fig 5: Thermoelectric power of PEDOT-Tos/SnSe nanocomposites at room temperature

4.5 Power Factor

The power factor change with SnSe concentration has been plotted and is displayed in figure 6. The figure indicates that the power factor reaches a maximum of 58.2x10-2 Wm-1K-2 as the SnSe concentration rises. The power factor rises until SP4, at which point it falls, suggesting a shift in the structural order that lowers the power factor value. The power factor increased to a maximum value for SP4 because of the increased σ and S values, increased structural order, and increased crystallinity caused by the 15% SnSe content. When the SnSe concentration exceeds 15%, the values of σ and S decline due to reduced structural order and decreased charge carrier mobility, which also causes a fall in the power factor.

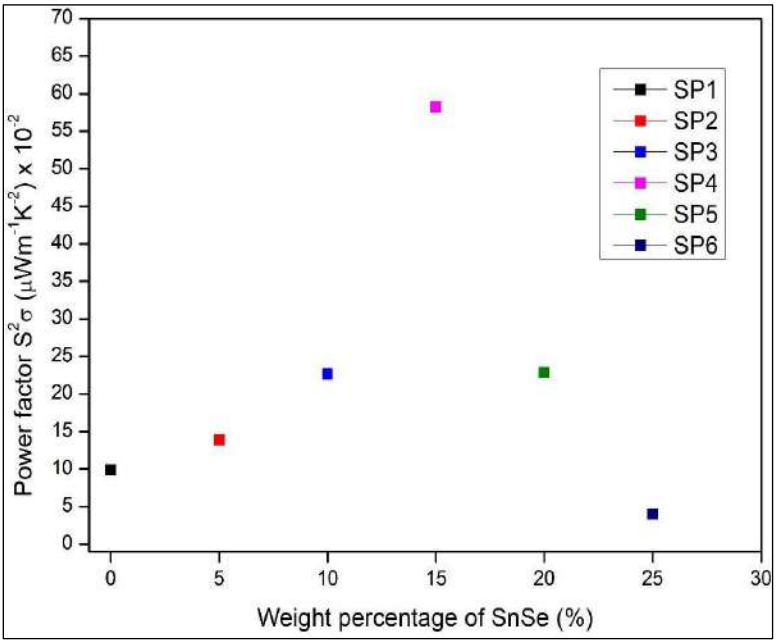

Fig 6: Power Factor of PEDOT-Tos/SnSe nanocomposites

Conclusion

In conclusion, in situ polymerization has been used to create PEDOT-Tos-SnSe nanocomposites with varying SnSe concentrations. As the concentration of SnSe increases, PEDOT-Tos exhibits enhanced compactness as demonstrated by spectral studies, structural investigations, and electrical characterization. As the concentration of SnSe rises, so do σ and S. A major factor in raising thermoelectric power is an increase in

carrier mobility. All these point to PEDOT-Tos/SnSe nanocomposite's good TE performance. Thermal conductivity and figure of merit study can demonstrate the benefits of PEDOT-Tos/SnSe as a TE material. The incorporation of SnSe into PEDOT-Tos can confirm its increased TE performance. This opens new possibilities for improving the polymer's TE characteristics in the future. The TE performance of PEDOT-Tos nanocomposites may be enhanced by adjusting various parameters and optimizing the mix of constituents.

References

1. Ren P, Liu Y, He J, Lv T, Gao J, Xu G. Recent advances in inorganic material thermoelectrics. Inorg Chem Front 2018;5:2380-98.
2. Haeberlin A, Zurbuchen A, Walpen S, *et al*. The first batteryless, solar-powered cardiac pacemaker. Heart Rhythm. 2015; 12: 1317-1323.
3. LeMoyne R, Mastroianni T, Whiting D, Tomycz N. Deep Brain Stimulation for the Treatment of Movement Disorder Regarding Parkinson's Disease and Essential Tremor with Device Characterization. Wearable and Wireless Systems for Healthcare II. Singapore: Springer; 2019: 37-51.
4. Cheng H, Du Y, Wang B, *et al*. Flexible cellulose-based thermoelectric sponge towards wearable pressure sensor and energy harvesting. Chem Eng J. 2018; 338: 1-7.
5. Zhang D, Wang Y, Yang Y. Design, performance, and application of thermoelectric Nanogenerators. Small. 2019; 15: E1805241.
6. Li Y Wiggins MC Samsung Electronics Co Ltd. self-powered wearable for continuous biometrics monitoring. US Patent Application 15/888853.2019.
7. Kim CS, Yang HM, Lee J, *et al*. Self-powered wearable electrocardiography using a wearable thermoelectric power generator. ACS Energy Lett. 2018; 3(3): 501-507.
8. Zhou M, Al-Furjan MSH, Zou J, Liu W. A review on heat and mechanical energy harvesting from human–principles, prototypes and perspectives. Renew Sustain Energy Rev. 2017; 82: 3582-3609.
9. DiSalvo FJ. Thermoelectric cooling and power generation. Science, 1992, 285; (5428): 703–706

10. Liu W, Jie Q, Kim HS, Ren Z Current progress and future challenges in thermoelectric power generation: from materials to devices. Acta Mater, 2015 87: 357–376.

11. He W, Zhang G, Zhang X, Ji J, Li G, Zhao X. Recent development and application of thermoelectric generator and cooler. Appl Energy, 2015, 143: 1–25.

12. Chowdhury I, Prasher R, Lofgreen K, Chrysler G, Narasimhan S, Mahajan R, Koester D, Alley R, Venkatasubramanian R On-chip cooling by superlattice-based thin-film thermoelectrics. Nat Nanotechnol, 2009,4(4):235–238.

13. Fan Z, Li P, Du D, Ouyang J. Significantly enhanced thermoelectric properties of PEDOT: PSS films through sequential post-treatments with common acids and bases. Adv Energy Mater 2017; 7(8):1602116.

14. Yao H, Fan Z, Cheng H, Guan X, Wang C, Sun K, *et al*. Recent developments of thermoelectric polymers and composites. Macromol Rapid Commun 2018; 39(6): 1700727.

15. Yao CJ, Zhang HL, Zhang Q. Recent progress in thermoelectric materials based on conjugated polymers. Polymer, 2019; 11(1): 107.

16. Zhang Y, Heo YJ, Park M, Park SJ. Recent advances in organic thermoelectric materials: principal mechanisms and emerging carbon-based green energy materials. Polym 2019; 11(1): 167.

17. Prakash Sengodu and Abhay D. Deshmukh, Conducting polymers and their inorganic composites for advanced Li-ion batteries: a review, RSC Adv., 2015,5, 42109-42130

18. He M, Qiu F and Lin Z, Towards high-performance polymer-based thermoelectric materials, Energy Environ. Sci., 2013,6, 1352-1361

19. J. W. G. Bos, H. W. Zandbergen, M.-H. Lee, N. P. Ong, and R. J. Cava, Structures and thermoelectric properties of the infinitely adaptive series (Bi2)m(Bi2Te3)n, Phys. Rev. B 75, 195203

20. Zhao X. B, Ji X. H, Zhang Y. H, Zhu T. J, Tu J. P. *et al*. Bismuth telluride nanotubes and the effects on the thermoelectric properties of nanotube-containing nanocomposites, Appl. Phys. Lett. 86, 062111 (2005)

21. Shi W, Zhou L, Song S, Yang J and Zhang H, Hydrothermal Synthesis and Thermoelectric Transport Properties of Impurity-Free Antimony Telluride Hexagonal Nanoplates, Adv. Mater. 2008, 20, 1892-1897

22. Li Y, Liu, G, Cao T, Liu L, Li J, Chen K, Li L, Han Y, and Zhou M, Enhanced Thermoelectric Properties of Cu2SnSe3 by (Ag, In)-Co-Doping Adv. Funct. Mater. 2016, 26, 6025-6032

23. Maity S, Sepay N, Kulsi C, *et al*. Enhancement of thermoelectric performance in oligomeric PEDOT-SWCNT nanocomposite via band gap tuning. Chemistry Select. 2018; 3: 8992-8997.

24. Maity S, Kulsi C, Banerjee S, Das S, Chatterjee K. Dependence of thermoelectric power and electrical conductivity on structural order of PEDOT-Tos-graphene nanocomposite via charge carrier mobility. Mater Res Express. 2019; 6: 105095-105105.

25. Bubnova, Z U Khan, H Wang, S Braun, D R Evans, M Fabretto, P Hojati-Talemi, D, Arlin J-B Dagnelund, Y H Geerts, S Desbief, D W Breiby, J W Andreasen, R Lazzaroni, W M Chen, I Zozoulenko, M Fahlman, PJ Murphy, M Berggren, X Crispin. Semi-metallic polymers. Nature Materials. 2014;13:190-194.

Chapter - 13
Enhanced Thermoelectric Properties of Ptsa Doped PEDOT/Bismuth Nanocomposite

Authors

Subhra Raksit
Department of Physics, Jadavpur University, Kolkata, West Bengal, India

Krishanu Chatterjee
Department of Physics, Techno India University, Kolkata, West Bengal, India

Shilpa Maity
Department of Physics, Swami Vivekananda University, Barrackpore, West Bengal, India

Chapter - 13

Enhanced Thermoelectric Properties of Ptsa Doped PEDOT/Bismuth Nanocomposite

Subhra Raksit, Krishanu Chatterjee and Shilpa Maity

Abstract

In recent days, nanostructures have great potential applications in the fields of electronics. Therefore, synthesis and investigation on properties of nanostructured materials is very important. We have produced Pedot-Bismuth nanocomposite, Pedot-doped Bismuth nanoparticle, and pTSA doped Pedot. It is known from the structural characterization that the pedot and pedot-bismuth nanocomposite include a crystalline phase. However, the structure of the composite is more organized. Furthermore, electrical evaluation revealed that the composite has a noticeably high electrical conductivity (σ), exhibiting semiconducting behavior at high temperatures and metallic characteristics at low ones. Furthermore, it has been shown through a review of the literature that Bismuth and Pedot have high thermoelectric power (S) and low thermal conductivity (κ), which is the perfect combination for having a high ZT. Therefore, it may be inferred that the Pedot-Bismuth nanocomposite is expected to exhibit high values of S and σ, as well as ZT.

Keywords: Pedot-bismuth nanocomposite, electrical properties, figure of merit

Introduction

Recently, there has been a lot of interest in one-dimensional (1D) nanostructures, which include wires, rods, and tubes, because of their potential applications as nanoscale electrical, optoelectronic, and sensing devices as well as interconnects [1]. Due to its two atoms per unit cell rhombohedral lattice crystal structure, bismuth (Bi) is a semimetal. There are three analogous binary axes that lie in a plane perpendicular to the trigonal axis, and these axes may be used to characterize many of the anisotropic electrical and thermal characteristics of bismuth [2]. Temperatures between around 80 and 300 K were recorded simultaneously for pure bismuth single

crystals of different orientations to determine the absolute Seebeck coefficient, electrical resistivity, and thermal resistivity. Bi is a more suitable material to be employed as a good thermoelectric material among all anisotropic semiconductors and semi-metals, according to their finding that the high electron mobility direction correlates with the low lattice thermal conductivity direction. The synthesis of single-crystalline Bi nanowires and nanospheres using ethylene glycol reduction of sodium bismuthate in the presence of acetone or poly(vinyl pyrrolidone) (PVP) has been described in another literature as a straightforward solution-phase technique [1]. Magnetic eld assistance has been another method for creating bi-nanocrystals. The solvothermal process's magnetic eld strength has been adjusted to achieve shape-controlled synthesis of individual Bi nanocrystals using these techniques. An 8 T magnetic field was used to create bi nanowires with dimensions of 40200 nm and lengths up to tens of micrometers, according to the paper. The high energy plane (0001) was perpendicular to the growing direction of Bi nanowires, as indicated by the HRTEM data [3]. It foresaw that Bi synthesised using this technique will be useful in TE applications. According to another methodology, bichromatic dots with a diameter ranging from 3 to 115 nm are created using a straightforward, one-step method that involves adjusting the quantities of Bi[N (SiMe3)2]3, Na[N (SiMe3)2], and a polymer surfactant called poly(1-hexadecene)0.67-co-(1-vinylpyrrolidinone)0.33. Bi nanorods and nanoplates are produced as a result of further modification of the reaction conditions. An alternative method is the synthesis of near-monodisperse Bi dots with diameters between 30 and 45 nm using secondary addition. By slightly altering this method, nanoribbons can be produced. The purpose of these changes to Bi's sizes and forms is to reduce their overall surface energy. Currently, mechanistic investigations of the development of Bi dots under identification-related situations are being conducted [4].

Organic polymers that transmit electricity are known as conjugate or conductive polymers. This group of substances combines insulating and conducting qualities. These materials exhibit low κ, high S, and high σ-all essential for high-quality thermoelectric (TE) materials. These have excellent mechanical flexibility and work well with low-cost scalable production techniques. According to research, conductivity in conductive polymers can improve by up to nine orders of magnitude. Conducting polymers (CP) have been investigated as possible thermoelectric material candidates ever since they were discovered. Thermoelectric characteristics of poly(3,4-ethylenedioxythiophene): poly(styrenesulfonate) (PEDOT: PSS) [9],

polycarbazoles (PC) [8], polypyrrole (PPY) [6, polyaniline (PANI) [7], polyacetylene (PA) [5], and its derivatives show great potential and are undoubtedly deserving of more research. The last several years have seen a concentration on research on polyaniline and its nanocomposites [10]. Pedot and its derivatives' thermoelectric performance is now being studied [11]. Various secondary dopants can significantly enhance Pedot-Pss's somewhat subpar thermoelectric efficiency. These dopants often improve the morphology of polymers while also dramatically increasing electrical conductivity and, as a result, ZT [12]. Recently, it was reported that PEDOT films with high power factors achieved by chemical reduction using various chemicals [13]. In order to facilitate additional improvements in thermoelectric characteristics, charge carrier concentration optimization is frequently employed. Electrochemical doping of Pedot-Pss yields a tenfold increase in ZT and allows for fine control of its oxidation level [14].

A different conducting polymer called Pedot-Tos, in contrast to Pedot-Pss, shows better thermoelectric performance even in the absence of secondary doping because of its partly crystalline structure, which enhances electrical conduction. Tosylic acid-doped Pedot (Pedot-Tos) is another significant doped version of the polymer due to growing interest in substituting ultrahigh conductivity organic materials for inorganic anode materials and recent advancements in polymerization process. Positively doped Pedot-Tos is partially reduced with the help of a strong electron donor, and it reaches the ideal oxidation state where its thermoelectric efficiency is only four times lower than that of Bi2Te3 [15].

The drawbacks of chemical doping Pedot-Tos, such as doping inhomogeneity or the air sensitivity of chemical dopants, can be overcome if the acidity/basicity of the polymer regulates the Pedot-To doping level. A very high electrical conductivity value exceeding 1000 Scm1 was achieved by PEDOT: Tos films thanks to the preparation of PEDOT-tosylate (Tos) films by Winther-Jensen *et al*. through chemical polymerization, where small anions-Tos replaced polyanion (PSS) to prevent the excess insulating phase generated with polyanion-ions [16]. Using the vapor phase polymerization process, Pedot-Tos thin films have recently shown an enhancement in the TE property [17].

Experimental

Materials Used

Pure aqueous Bismuth Nitrate [$Bi(NO_3)_3.5H_2O$], Acetone, Ethylene diamine, Ferric Chloride, Acetonitrile, EDOT purchased from Alfa Aesar,

Normal hexane (n-hexane), P-toluenesulfonic acid (PTSA), Butanol, Ethanol was purchased from Merck chemicals, Deionised water was purchased from Hydrolab. All the chemicals received, were of analytical reagent grade and are used without further purification.

Synthesis of Bismuth Nanoparticle

A technique described in the literature has been used to produce bismuth nanoparticles [34]. In this work, nano Bi is produced using the solvothermal process. In this standard process, 40 milliliters of pure ethylene diamine were brought to room temperature, then two grams of analytically pure aqueous bismuth nitrate [Bi(NO3)3.5H2O] and five milliliters of acetone were added to create a combination that precipitated insoluble. After agitating the liquid vigorously for ten minutes, it was transferred into an autoclave made of stainless steel that had an 80 ml Teflon vessel within. For five hours at 160 °C, the autoclave was securely closed to carry out the solvothermal procedure. After obtaining the desired black result, the sample was dried in a vacuum for six hours at 80°C after being cleaned three times with alcohol and distilled water. Thus, obtained sample is named as Sample 1 (S_1).

Synthesis Procedure of PTSA Doped PEDOT by *in situ* Polymerization Method

This synthesis method is explained elsewhere [35]. Solution A, or 25 milliliters of acetonitrile, was mixed with 0.02 mole of ferric chloride (Fecl3) using a magnetic stirrer. The next step was dissolving 500 µl of EDOT in 15 ml of n-hexane to create Solution B. The mixture was then stirred at room temperature while Solution A was added to Solution B one drop at a time, every two seconds. Pyridine was then added to the solution after that. After swirling the mixture for 21 hours, Solution C, which included PTSA in 20 milliliters of butanol, was added, and it was left to agitate for an additional 3 hours. Centrifugation was used to remove the product from the polymerization media. It was then cleaned more than ten times using deionized water and 100% ethanol. then, it was separated by centrifugation for ten minutes at 10,000 rpm at 25 °C, and it was then dried in a vacuum at 70 °C. The resultant sample is therefore designated Sample 2 (S2).

Synthesis Procedure of PTSA Doped PEDOT/Bismuth Nanoparticle Composite

The process described above is used to synthesize Pedot-Bismuth nanocomposite. Solution A was prepared by dissolving 0.02 mole of ferric

chloride (Fecl3) in 25 milliliters of acetonitrile while stirring with a magnetic stirrer. 500 µl of EDOT was dissolved in 15 ml of n-hexane while 0.3 gm of bismuth nanoparticles were present to create Solution B. The preparation of Solution C is done as previously explained, and the next steps follow the same protocol.

Centrifugation was used to remove the product from the polymerization media. It was then cleaned more than ten times using deionized water and 100% ethanol. then, it was separated by centrifugation for ten minutes at 10,000 rpm at 25 °C, and it was then dried in a vacuum at 70 °C. The resultant sample is therefore designated Sample 3 (S3).

(a) Colorless Solution A **(b) color change after adding Solution B**

Fig 1: Preparation of Pedot-Bismuth Nanocomposite

Characterization

Powder x-ray diffraction (XRD) and UV-vis spectroscopy were used to describe the synthesized samples S2 and S3, while field emission scanning electron microscopy (FESEM) was used to analyze sample S1. Additionally, Field Emission Scanning Electron Microscopy (FESEM) was used to analyze the sample Bi (S1) structurally. X-ray powder diffraction (X Pert PAN analytical) spectra were obtained from 5◦ to 70◦ at a scanning speed of 0.1 per minute using a Cu Kα radiation (λ = 1.5418 ^A). Using a UV-vis spectrophotometer (JASCO V-530), we were able to record the UV-vis absorbance spectra of our samples between 300 and 1100 nm. The produced sample Bi's morphology was examined using a FESEM Quanta FEG 250. The four probe technique using a four-probe setup (DFP-RM) was used to evaluate the electrical conductivity of samples S1 and S3. For S1 and S3, the temperature range (307-410 K) is used to measure changes in electrical conductivity with temperature (σ).

Results and Discussions

XRD Analysis

The samples' XRD patterns have been examined in order to confirm the structural characterisation of the Bismuth, Pedot, and Pedot-Bi nanocomposite. It suggests that, at the current synthetic conditions, the reduction of Bismuth ion to elemental Bi is complete, and as a result, pure Bismuth metal was produced. Peak 2θ~13.2◦ is seen in the XRD pattern of pedot, indicating the exitance of the crystalline phase. (0 2 0) is the peak's assigned lattice parameter, with a = 14.3^A, b = 6.8^A, and c = 7.8^A. Both the existence of Bismuth and the crystalline phase of Pedot are confirmed by the XRD pattern of the Pedot-Bismuth nanocomposite. A hallmark of a more organized structure is the complete width at half maximum at 11.98◦ decreasing and the presence of a peak at 25◦.

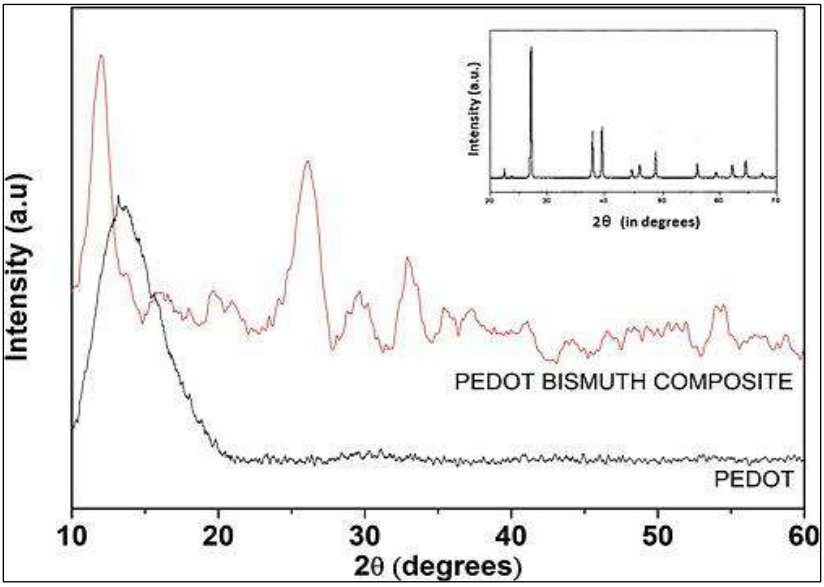

Fig 2: XRD of S2 and S3

This change in stacking distance and the presence of Bismuth nanoparticle influence the electrical conductivity.

UV-Vis Analysis

Using UV-vis spectroscopy, the chemical structures and electronic states of samples S2 and S3 were identified. The optical absorbance spectra of samples S2 and S3 are shown in Fig 3. It demonstrates that the composite's

(S3) absorbance is greater than the pure one's (S2) over the whole wavelength range. The aromatic ring of Tos is the source of the strong absorbance band in the UV region (300-350 nm) [18]. The strength of the absorbance band noticeably increases for the composite. The literature review indicates that the π-to-π* transition occurs between 580 and 600 nm, and that as the doping level rises, their relative intensity falls.

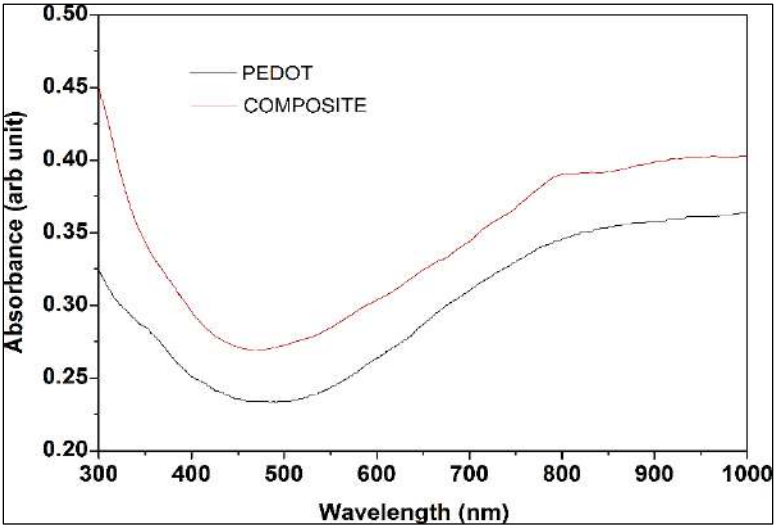

Fig 3: UV-Vis spectra of S_2 and S_3

Figure 3 demonstrates that for the composite, the π-to-π* transition peak's relative intensity increases to around 600 nm. The outcome shows that after creating the composite, the doping level and bipolaron concentration dropped.

FESEM Analysis

The FESEM image of Pedot (b) and Bismuth (S2) is displayed in Fig 4. From the FESEM image, the formation of Bismuth nanoparticles has been verified. The nanoparticles have a diameter of around 133 nm.

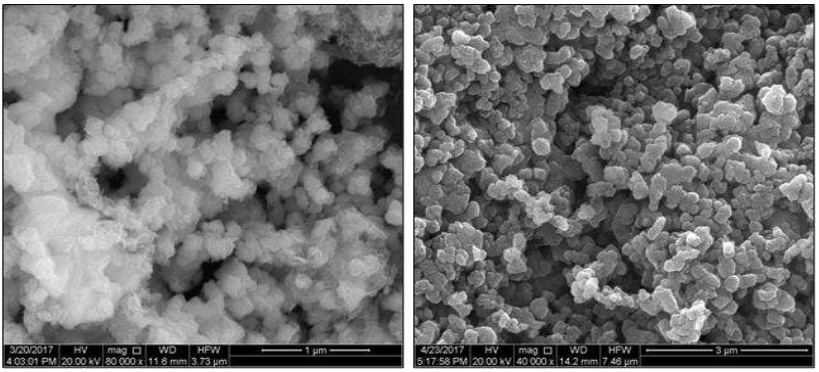

(a) **(b)**

Fig 4: FESEM Images of (a) Bismuth (b) Pedot

According to the FESEM picture, the average diameter of the pedot nanoparticle is 330 nm. The FESEM image shows the stacking of Pedot chains on top of one another, as shown in the XRD pattern. For the case of the nanocomposite (FESEM not depicted), it is hypothesized that the Bismuth nanoparticle was injected between these stacked layers during the fabrication process. We can see from the illustration that bismuth nanoparticles have been created.

4.4 Electrical Characterization

Figure 5 illustrates how the electrical conductivity (σ) of three different nanocomposite materials-Bismuth (S1), Pedot (S2), and Pedot-Bismuth (S3)-varies with temperature across a range of 300-410 K. The graphic shows that for bismuth (S1), conductivity (σ) increases with temperature. This indicates that it is semiconducting. Based on the picture, it can be noted that Pedot (S2)'s σ value falls with temperature, suggesting a non-linear metallic conductivity. Remarkably, in the instance of the Pedot-Bi nanocomposite, electrical conductivity is seen to decrease at lower temperatures up to 337 K and then to increase as temperature rises.

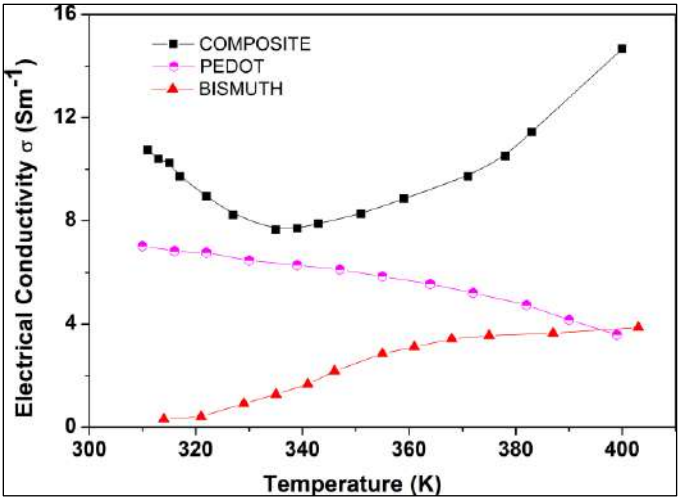

Fig 5: Electrical conductivity of S_1, S_2 and S_3

The following explanation applies to this. When bismuth nanoparticles are inserted into Pedot's stacking layer, the distance between the stacking layers increases and the electrical conductivity falls, indicating metallic conduction similar to that of Pedot. The electrical conductivity of Bismuth increases as temperature rises due to an increase in its charge carriers, which in turn dominates metallic conduction, boosting the nanocomposite's overall electrical conductivity.

Following the quasi-one-dimensional variable range hopping [1D VRH] model [18], the conduction mechanism of Bismuth and composite yields the characteristic Mott temperature (T0) in the following method:

$$\sigma\,(T) = \sigma_0 \exp(—T_0/T)2 \quad (1)$$

Where σ_0 is a constant and T_0 is the characteristic Mott temperature that depends on the carrier hopping barriers. The fitted graph in the figure referred to the equation 1. From fig 6, we have calculated the value of σ_0 and T_0 for both S_1 and S_2. The characteristic temperatures (T_0) are 11.8×10^3 K, 2.696×10^3 K and σ_0 is

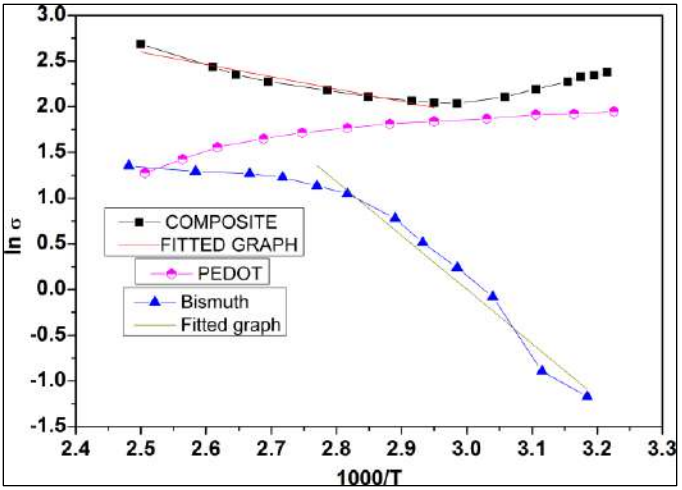

Fig 6: ln σ vs. 1000/T plot of S_1, S_2 and S_3

Can be concluded that, after the formation of composite, number of grains and grain boundaries have increased and carrier hopping through boundary increases. Consequently, the material shows semiconducting nature as temperature increases.

Mechanism of Bismuth Nanoparticle and PEDOT Nanocomposite Formation

A triple-coordination compound can be formed via the coordination of the ethylene diamine with Bi3+. It is therefore proposed that in a pure ethylene diamine system, this is a typical coordinative reduction process. Ethylene diamine primarily plays the job of electron transfer in the high-pressure and alkalescent system, exhibiting a moderately intense reductive feature. In particular, the coordination compound's small distance between the nitrogen atom and bismuth makes it easier for electrons to go from N to Bi3+, which reduces Bi3+ to Bi [19].

Figure 7 depicts the likely method of Pedot development. Iron-(III) chloride is employed in the polymerization technique as a reactant to polymerize EDOT, but it is subsequently eliminated. The EDOT radical cations interact with one another during polymerization to create covalent CC bonds between the thiophene units. Protons are released as a result of dimerization. Because iron has taken an electron from EDOT, Fe3+ becomes Fe2+. So, a reaction with iron-(III) chloride is necessary for the formation of each bond between two EDOT monomers. Because it is simpler to oxidize an oligomer than a monomer, the resulting PEDOT chains are inherently positively charged.

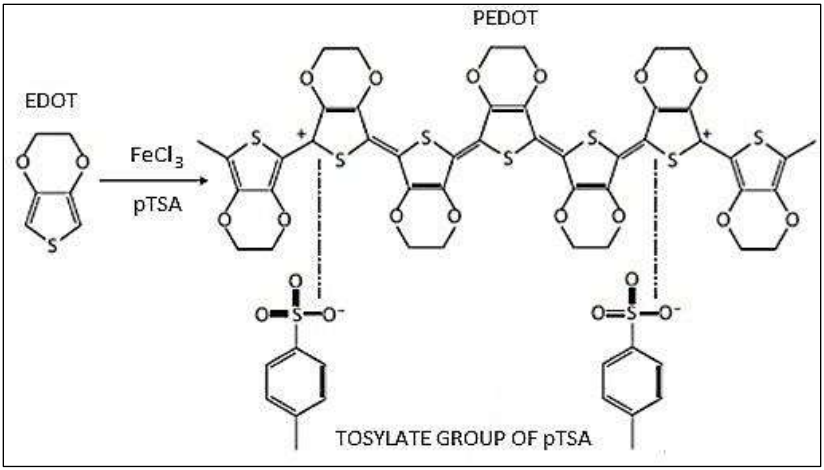

Fig 7: Mechanism of Formation of Pedot

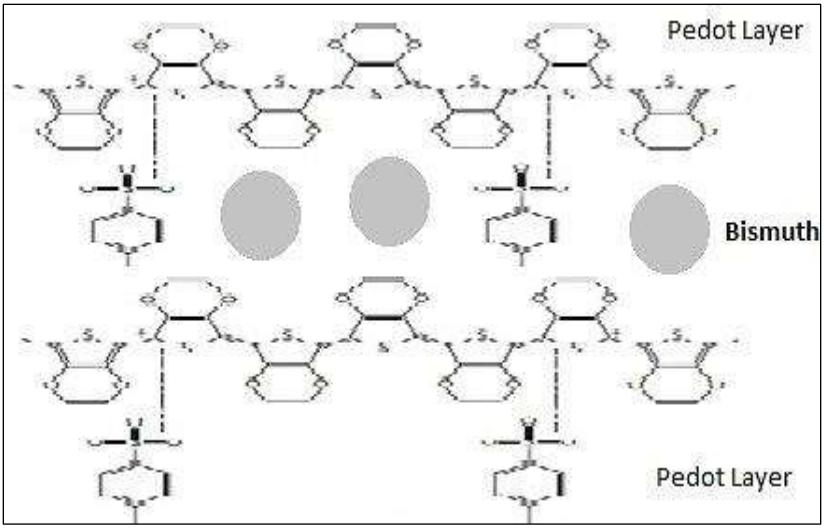

Fig 8: Mechanism of Formation of Pedot-Bi nanocomposite

The counter anion tosylate, which is introduced to the polymer from Para toluene sulfonic acid, balances the positive charge carried by the conducting polymers, resulting in the production of PEDOT-Tos. The XRD pattern of the composite indicates that during synthesis, Bismuth nanoparticles are injected into the Pedot layer, increasing the stacking gap between the layers. Additionally, Fig. 8 below illustrates the likely mechanism of the Pedot-Bismuth nanocomposite.

Conclusion

Pedot-Bismuth nanocomposite, Pedot-doped Pedot, and Bismuth nanoparticle have all been made. It has been determined by structural analysis that the pedot and pedot-bismuth nanocomposite exhibit crystalline phases. Its structure is more organized in the composite, though. Through electrical characterization, we also found that the composite has a notably high electrical conductivity (σ), exhibiting a metallic nature at low temperatures and semiconducting characteristics at high temperatures. Pedot and Bismuth have been found to have low thermal conductivity (κ) and high thermoelectric power (S), respectively, which is a perfect combination for having high ZT, according to a review of the literature. Thus, we may infer that the Pedot-Bismuth nanocomposite ought to exhibit elevated S and σ values, thereby leading to a higher ZT value.

References

1. J. Wang, X. Wang, Q. Peng, and Y. Li, Inorg. Chem. 2004, 43, 75527556.
2. C. F. Gallo, B. S. Chan-Drasekhar, and P. H. Sutter, Journal of Applied Physics. 1963, 34, 144.
3. Y. Xu, Z. Ren, W. Ren, G. Cao, K. Deng and Y. Zhong, Nanotechnology. 2008, 19 115602 (5pp)
4. F. Wang, R. Tang, H. Yu, P.C. Gibbons, and W.E. Buhro Chem. Mater. 2008, 20, 36563662
5. Park, Y. W., Han, W. K., Choi, C. H. amp; Shirakawa, H. Physical Review B, 1984, 30, 5847-5851.
6. Kemp, N. T. *et al*. Journal of Polymer Science Part B: Polymer Physics, 1999, 37, 953-960.
7. H. Yan, N. S., N. Toshima. Journal of Thermal Analysis and Calorimetry. 2002, 69, 6.
8. Lvesque, I. *et al*. Chemistry of Materials, 2007, 19, 2128-2138.
9. Jiang, F.-X. *et al*. Chinese Physics Letters, 2008, 25, 2202.
10. R.C.Y. King, F. Roussel, J.F. Brun, C. Gors, Synth. Met. 2012, 162, 1348.
11. Groenendaal, L., Jonas, F. Freitag, D. Pielartzik, H. Reynolds, J. R. Adv. Mater. 2000, 12, 481494.

12. Qingshuo Wei, Masakazu Mukaida, Kazuhiro Kirihara, Yasuhisa Naitoh and Takao Ishida, Materials. 2015, 8, 732-750.
13. Park, H.; Lee, S.H.; Kim, F.S.; Choi, H.H.; Cheong, I.W.; Kim, J.H. J. Mater. Chem. A. 2014, 2, 65326539.
14. O. Bubnova, M. Berggren, X. Crispin, J. Am. Chem. Soc. 2012, 134 1645616459.
15. O. Bubnova, Z. U. Khan, A. Malti, S. Braun, M. Fahlman, M. Berggren and X. Crispin Nature Materials, 2011,10, 429–433.
16. B. Winther-Jensen, D.W. Breibym, K. West, Synthetic Metals, 2005, 152, 1.
17. J. Wang, K. Cai, S. Shen, Organic Electronics. 2014, 15, 30873095
18. M. Mitra, C. Kulsi, K. Chatterjee, K. Kargupta, S. Ganguly, D. Banerjee and S. Goswami. RSC Adv., 2015,5, 31039
19. Yuanhao Gao 1, Helin Niu, Chuan Zeng, Qianwang Chen, Chemical Physics Letters 2003, 367, 141144

Chapter - 14
Thermoelectric Properties of Zinc-Incorporated Reduced Graphene Oxide-Polyaniline Composite

Authors

Shilpa Maity
Department of Physics, Swami Vivekananda University, Barrackpore, West Bengal, India

Krishanu Chatterjee
Department of Physics, Techno India University, Kolkata, West Bengal, India

Chapter - 14

Thermoelectric Properties of Zinc-Incorporated Reduced Graphene Oxide-Polyaniline Composite

Shilpa Maity and Krishanu Chatterjee

Abstract

Low dimensional nanostructures based on graphene show considerable promise for thermoelectric (TE) applications. Consequently, it is crucial to synthesize and investigate the characteristics of grapheme-based nanostructured materials. This thesis focuses on synthesizing RGO-PANI-Zn (reduced graphene oxide-polyaniline-metal composites) and assessing their thermoelectric characteristics. One method of creating reduced graphene oxide is by chemical oxidative in-situ polymerization. In order to create RGO-PANI composite, sulfo salicylic acid has been added to PANI. Finally, a physical mixing approach has been used to manufacture RGO-PANI-Zn by adjusting the concentration of zinc powder. With an electrical value of 22.31 Scm-1, the PANI-RGO-Zn nanocomposite's holes make up most of its carriers The surrounding PANI coating enhances the electron energy filtering effects, increasing the mean carrier energy in electrical transmission. The power factor increases in tandem with the PANI-RGO matrix's Zn content. The composite has nearly constant heat conductivity because to the lattice vibration and electron contribution. The interactions of hydrogen bonds, π-π, acceptor-donor, and electrostatic forces result in the development of the weak charge transfer complex and the composite. As a result, the findings indicate that employing RGO-PANI's molecular structure as a template for in situ polymerization might improve the polymer's thermoelectric performance.

Keywords: PANI-RGO-Zn nanocomposite, *in situ* polymerization, π-π interaction, thermoelectric properties

Introduction

Thermoelectric materials may directly convert thermal energy into electrical energy without the need for dangerous working fluids or moving mechanical parts, making them very promising for use in solid-state heating

and cooling systems and power production [1, 2]. Thermoelectric material efficiency is analyzed by the dimensionless parameter called the figure of merit ZT. Distinguishing the interdependence of factors in ZT is a fundamental problem in the creation of a suitable thermoelectric material. Until date, the high-power factor of inorganic semiconductors and related compounds has drawn the greatest attention [3, 4].

New research directions have been made possible by the recent discovery of graphene. Due to their large specific surface area [5], exceptional mechanical rigidity [6], and excellent conductivity [7], graphene nanosheets with a two-dimensional lamellar structure are anticipated to be exceptional support materials. As an electroactive material, it has garnered a lot of attention lately for the synthesis of conductive polymer-based nano composites [7], with potential uses in sensors [9], dye-synthesized solar cells [10], fuel cells [12], rechargeable lithium batteries [11], supercapacitors [8], fuel cells [13], electrochromic devices [14], and other areas.

Graphene conducting polymer composites with various specific morphologies, including sandwiched [14], fibrillar [15], flakes [16], thin films [17], nanotubes [18], graphene nanosheet coated or grafted with nanorods [19], nanofibres [20], and nanowires [21] of conductive polymers, have been reported to exist. These composites were created using chemical oxidative polymerization or electrodeposition of monomers in the presence of graphene [22], functional graphene [23], or reduced graphene oxide [24].

Thermoelectric polymer systems are becoming more and more popular due to their inexpensive cost and low heat conductivity [25]. Studies on graphene nanoplate polyaniline [26], graphene nanosheet-P3HT [27], graphene nanosheet-modified polyaniline [28], GO-PANI [29], graphene nanosheet enwrapped polypyrrole [30], graphene-PEDOT: PSS [31], and other polymers have also examined the effects of graphene and reduced graphene oxide on the thermoelectric properties of polymers in addition to their role as supports. Conducting polymers, such polyaniline (PANI), have been researched in detail and are well-known for their easy acid-base doping and de-doping properties as well as their environmental stability [32, 33]. The thermoelectric properties of polyaniline have also been studied; however, their low power factor usually limits their performance, making polymers not as competitive as inorganic semiconductors. A highly ordered composite film of PANI graphene nanoplate composites with different polymer compositions was created by Xiang *et al*. [34]. Nevertheless, the samples' figure of merit is quite low.

This work related to the synthesis and characterization of PANI-RGO-Zn Nano composites for TE application employing chemical oxidative in-situ polymerization where the structural and electrical properties of SSA doped PANI have been mapped.

Experimental

Materials Used

Ammonium peroxy-di-sulfate (APS), 5-Sulfosalicylic acid (SSA), sulphuric acid (H_2SO_4), sodium nitrate ($NaNO_3$), phosphorus pentoxide (P_2O_5), ortho-phosphoric acid (H_3PO_4), calcium chloride ($CaCl_2$), potassium permanganate ($KMnO_4$), hydrogen peroxide (H_2O_2), and hydrazine hydrate ($N_2H_4H_2O$) were acquired from MERCK chemicals. Deionized water was purchased from hydrolab, India. Aniline monomer and 99.99% pure crystalline graphite powder were purchased from LOBA Chemie in India. Since none of the provided reagents needed to be further purified, they were all analytical quality when used as supplied.

Synthesis of Reduced Graphene Oxide (RGO)

Graphene oxide (GO) was produced from graphite powder using the modified Hummers technique [35]. Hydrazine hydrate was then used as a reducing agent to decrease the produced product. Preparing a suspension of graphene oxide (2 mg ml-1) in de-ionized water and adding hydrazine hydrate (10:1) is a common procedure. The final mixture was then preserved for twenty-four hours in a vacuum oven. After giving the product, a thorough washing, methanol, and de-ionized water were used to filter the mixture prior to the filtration was colorless. The resulting material was vacuum-dried over P_2O_5 and $CaCl_2$ at 50 ºC to produce reduced graphene oxide (rGO).

Reduced Graphene Oxide-Polyaniline-Zinc (RGO-PANI-ZN) Composite Synthesis

A 190 ml solution including water, SSA (1.4 g), and various weight percentages of rGO was mixed with 2 ml of aniline. The mixture was put in an ice bath to cool below 60 ºC after being mechanically stirred to create a uniform black dispersion of the ingredients. The oxidant (APS 5.02 g) was mixed with 100 ml of water and thoroughly stirred before being added, one drop at a time, to the ice bath mixture. A few hours later, the solution developed a greenish-black color, signifying the formation of the reduced graphene oxide composite and the polyaniline emeraldine salt (5 X 10-5 M) doped with SSA. Centrifugation at 2500 rpm was used to produce the precipitated suspension, which was then carefully washed with ethanol and

water many times until a clear solution was achieved. At 60 ^{o}C, the finished composite was vacuum dried. Following a physical mixing that incorporated zinc (Zn) powder in various weight percentages, samples were labeled with the weight percentage (wt%) of Zn content.

Characterization

All the produced samples were divided into small rectangular pieces and crushed at room temperature with a pressure of two tons to measure the electrical transport capabilities. Between 290 and 420 K, temperature fluctuations were noted for each sample's electrical conductivity (σ) and thermoelectric power (S). Using four probes (Model no. DFP 301), the electrical conductivities of the samples were assessed using the four-probe technique. Thermoelectric power was evaluated by applying an extra heater to one end of the sample container to create a temperature difference.

The associated potential decrease was monitored using a Hewlett Packard data acquisition system (Model No. 34970A). Room-temperature measurements of the produced materials' thermal conductivity were made using a Hot Disk thermal constants analyzer (TPS 2500 S, Sweden).

Result and Discussion

Figure 1 displays the changes in electrical conductivity (σ) with temperature for the produced samples. It is interesting to note that PANI-RGO's electrical conductivity has already been shown to rise with temperature. However, in our instance, the addition of zinc is responsible for the observed drop in electrical value with temperature for all the synthesized samples. Zinc is thought to be a major factor in our sample's electrical conductivity. The figure shows that PANI-RGO-Zn nanocomposites exhibit nonlinear, metallic-type variations in electrical conductivity. This is because, because of the insulating barriers, the charge transport of the conducting polymers is connected to metallic conduction inside the islands by a hopping or tunneling effect. The value of σ for 11.11% Zn in the PANI-RGO-Zn nanocomposite is 11.48 Scm-1, as can be seen in the image. When the Zn concentration of PANI-RGO increases, the value rises as well. PANI-RGO-Zn-3, which has an electrical value of 22.31 Scm-1, is the greatest value. The strong π-π interactions between the conjugated PANI structure and the RGO π connected surface may be the cause of this improvement in electrical conductivity.

Moreover, it is thought that the physical makeup of the zinc given influences the electrical conductivity enhancement.

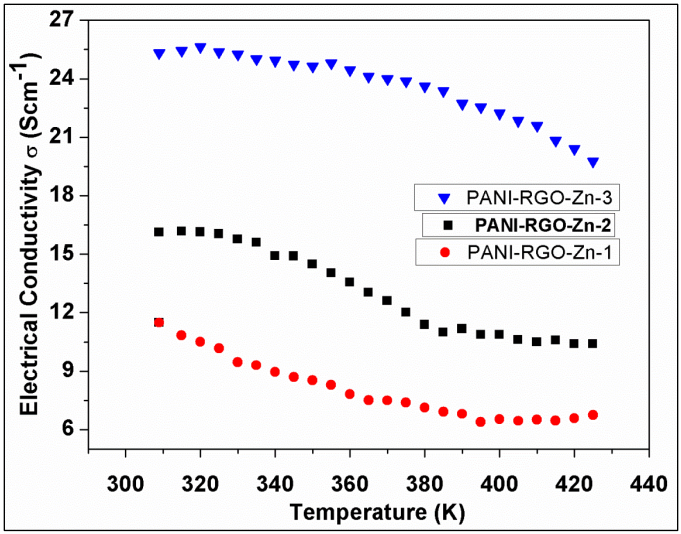

Fig 1: At different temperatures, the synthesized samples' electrical conductivity changes

The holes are the majority carriers when the thermoelectric power values for each sample at room temperature are positive. Both σ and S rise with an increase in the weight percentage of Zn.

Just like conductivity, as the PANI-RGO-Zn concentration rises, thermoelectric power also increases significantly. When the composites include 11.11 wt% of zinc, they exhibit a maximum thermoelectric power of 26 μV/k. The thermoelectric power gain is particularly unexpected. To understand this phenomenon, three variables are suggested. High energy carriers are let through whereas cold energy carriers are blocked by the surrounding PANI [36] coated nanolayer of PANI-RGO-Zn, which enhances the electron energy filtering effects. As a result, it may raise the thermoelectric power while increasing the mean carrier energy in electronic transmission.

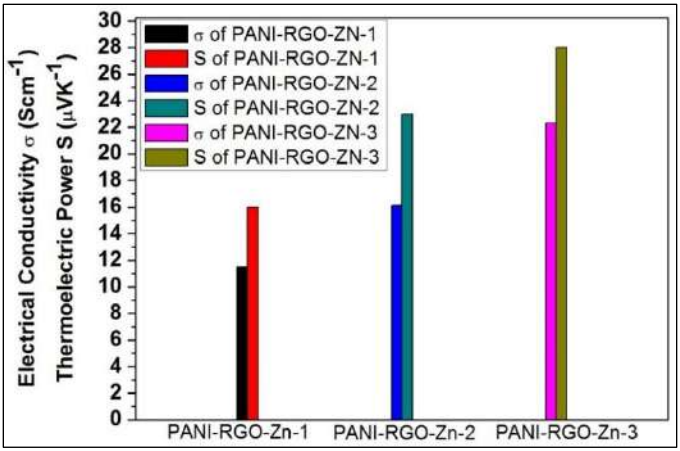

Fig 2: Variation of electrical conductivity and thermoelectric power of different samples

Second, the grain boundaries produced by combining Zn powder with PANI-RGO during the hot-pressing process can strengthen the effects of the electron energy filter and boost thermoelectric power. Several investigations have also noted this grain boundary augmentation of the thermoelectric power.

The results of earlier research indicate that heat annealing can raise the PANI molecule structure's order. Because of the reduced conjugated defects in the polymer backbone caused by ring twisting, the ordered molecular structure lowers the carrier hopping barrier in the PANI matrix. When these two processes are combined, the effective degree of electron delocalization increases. Given that the current hot-pressing technique uses thermal annealing to heat and cool the composites, it seems sense to assume that the ordered PANI molecular structure created by the hot pressing will further increase thermoelectric power.

The power factor of PANI-RGO-Zn-1 is 0.29388 μWmK-2 at room temperature, which is one order of magnitude more than that of pure PANI. With a high of 1.749 μWmK-2 for PANI-RGO-Zn-3, the power factor rises as the Zn level in the PANI-RGO matrix increases. The power factor for each sample is displayed in Figure 3. Both electrical conductivity and thermoelectric power have improved, which is why the power factor has grown.

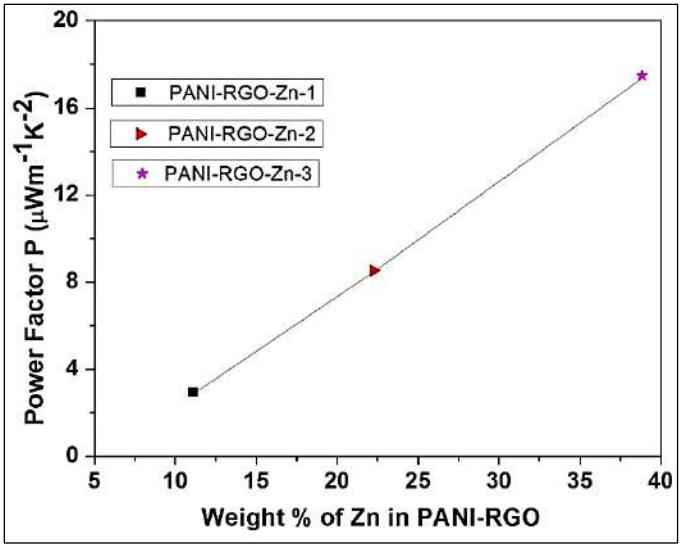

Fig 3: Power factor for three different synthesized samples

As Zn content in the PANI-RGO matrix rises, the coefficient of thermal conductivity (κ) of RGO-PANI-Zn composites fluctuates from 0.1123 Wm-1k-1 to 0.1241 Wm-1k-1, rather than changing considerably for all samples as stated in the literature. Thermal conductivity is derived from two sources: the lattice contribution (κl) and the electronic contribution (κe), which are combined to form $\kappa_{total} = \kappa_e + \kappa_l$. The Wiedemann-Franz relation (L0σT) using $L0 = 2.45\times10^{-8}$ $V2K^{-2}$ is used to analyze the lattice and electronic contributions. The lattice contribution (κ_l), electronic contribution (κ_e), and total thermal conductivity (κ_l) are displayed in Figure 4.

It is found that in this case, the lattice contribution κl is larger than κe. Phonon scattering with nanoscale inclusions in the grain boundaries between PANI and RGO reduces κl and improves the thermoelectric properties of bulk materials [29]. Overall thermal conductivity is lowered as a result. There was a little increase in thermal conductivity when zinc was added to the PANI-RGO matrix. Reduced heat conductivity is seen in PANI doped with SSA, according to literature. In this case, a comparable trend is being seen.

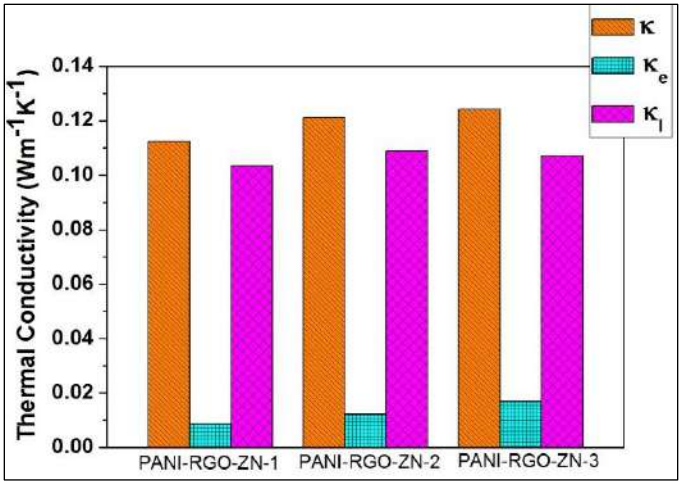

Fig 4: Total thermal conductivity with electronic and lattice contribution of different samples

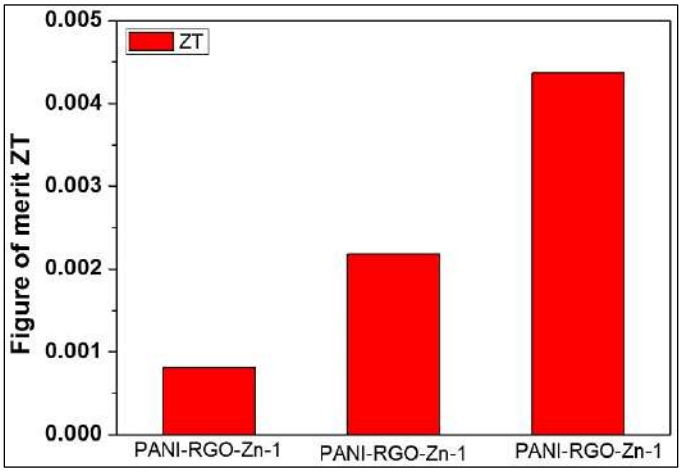

Fig 5: Figure of merit of three different synthesized samples

The experimental measurements of thermal conductivity, thermoelectric power, and electrical conductivity are used to calculate the figures of merit at room temperature for each of the three samples. The three separate samples' respective figures of merit are shown in Figure 5. For the composite with 38.8% Zn in the PANI-RGO matrix, the highest value of ZT as determined for PANI-RGO-Zn-3 is projected to be.00437. ZT value increases with increasing Zn concentration; for PANI-RGO-Zn-3, this value reaches a maximum of 0.004. This figure and the other values mentioned in the literature are comparable.

Conclusion

The thermoelectric characteristics of RGO-PANI-Zn composites made via physical mixing and in situ polymerization are examined in this work. The PANI-RGO-Zn nanocomposite, with holes as the predominant carriers, has an electrical value of 22.31 Scm-1, according to the study. By strengthening the effects of electron energy filtering, the surrounding PANI coating raises the mean carrier energy in electronic transmission. The Zn concentration of the PANI-RGO matrix rises as the power factor does as well. The combination of lattice vibration and electron contribution results in nearly constant thermal conductivity in the composite. The formation of a weak charge transfer complex, which results from acceptor-donor, hydrogen bond, electrostatic, and π-π interactions, may be responsible for the composite's development. The results suggest that the thermoelectric performance of the polymer might be enhanced by using the molecular structure of RGO-PANI as a template during in situ polymerization.

References

1. Snyder GJ, Toberer ES. Nat Mater 7 (2008) 105.
2. Tritt TM, Bottner H, Chen LD. MRS Bull 33 (2008) 366.
3. Yan X, Poudel B, Ma Y, Liu WS, Joshi G, Wang H, *et al*. Nano Lett 10 (2010) 3373.
4. Martin J, Wang L, Chen L, Nolas GS. Phys Rev B 79 (2009) 115311.
5. L.C. Liu, Z.N. Yu, D. Neff, A. Zhamu, B.Z. Jang, Nano Lett. 10 (2010) 4863.
6. S. Stankovich, D.A. Dikin, G.H.B. Dommett, K.M. Kohlhaas, E.J. Zimney, E.A. Stach, R. D. Piner, S.T. Nguyen, R.S. Ruoff, Nature, 442 (2006) 282.
7. C. Li, G.Q. Shi, Electrochim. Acta 56 (2011) 10737.
8. H. Gomez, M.K. Ram, F. Alvi, P. Villalba, E. Stefanakos, A. Kumar, J. Power Sources 196 (2011) 4102.
9. L. Al-Mashat, K. Shin, K. Kalantar-Zadeh, J.D. Plessis, S.H. Han, R.W. Kojima, R.B. Kaner, D. Li, X.L. Gou, S.J. Ippolito, W. Wlodarski, J. Phys. Chem. C 114 (2010) 16168.
10. G.Q. Wang, W. Xing, S.P. Zhuo, Electrochim. Acta 66 (2012) 151.
11. L.F. Jin, G.C. Wang, X.W. Li, L.B. Li, J. Appl. Electrochem. 41 (2011) 377.

12. Y.C. Yong, X.C. Dong, M.B. Chan-Park, H. Song, P. Chen, ACS Nano 6 (2012) 2394.
13. A.P. Saxena, M. Deepa, A.G. Joshi, S. Bhandari, A.K. Srivastava, ACS Appl. Mater. Interface. 3 (2011) 1115.
14. L.L. Zhang, S.Y. Zhao, X.N. Tian, X.S. Zhao, Langmuir 22 (2010) 17624.
15. N.A. Kumar, H.J. Choi, Y.R. Shin, D.W. Chang, L.M. Dai, J.B. Baek, ACS Nano 6 (2012) 1715.
16. J.T. Zhang, X.S. Zhao, J. Phys. Chem. C 116 (2012) 5420.
17. X. M. Feng, R.M. Li, Y.W. Ma, R.F. Chen, N.E. Shi, Q.L. Fan, W. Huang, Adv. Funct. Mater. 21 (2011) 2989.
18. J.H. Liu, J.W. An, Y.X. Ma, M.L. Li, R.B. Ma, J. Electrochem. Soc. 159 (2012) A828.
19. M.Q. Xue, F.W. Li, J. Zhu, H. Song, M.N. Zhang, T.B. Cao, Adv. Funct. Mater. 22 (2012) 1284.
20. J. Li, H.Q. Xie, Y. Li, J. Liu, Z.X. Li, J. Power Sources 196 (2011) 10775.
21. J.J. Xu, K. Wang, S.Z. Zu, B.H. Han, Z.X. Wei, ACS Nano 4 (2010) 5019.
22. T.T. Ngo, V.K. Tran, H. Lee, D. Sohn, Synthetic Met. 161 (2011)177.
23. A.V. Murugan, T. Muraliganth, A. Manthiram, Rapid, Chem. Mater. 21 (2009) 5004.
24. J. Yan, T. Wei, B. Shao, Z.J. Fan, W.Z. Qian, M.L. Zhang, F. Wei, Carbon 48 (2010) 487.
25. Dubey N, Leclerc M J. Sci Part B Polym Phys 49(2011) 467
26. J. Xiang and L. T. Drzal, Polymer 53 (2012) 4202
27. Y. Du, K. F. Cai, S. Z. Shen and P. S. Casey, Synth. Met. 62 (2012) 2102
28. Y. Lu, Y. Song and F. Wang, Mater. Chem. Phys. 138 (2013) 238-244.
29. Y. Zhao, G. S. Tang, Z. Y. Zhong and S. Q. Jun, Carbon 50 (2012) 3064.
30. S. Han, W. Zhai, G. Chen and X. Wang, RSC Adv. 4 (2014) 29281.

31. G. H. Kim, H. Hwang and S. I. Woo. Phys. Chem. Chem. Phys.14(2012) 3530
32. MacDiarmid AG, Chiang JC, Richter AF, Epstein AJ. Synth Met 18 (1987) 285
33. Chiang JC, MacDiarmid AG. Synth Met 13 (1986) 193
34. Lin-Chung PJ, Reinecke TL. Phys Rev B. 51(1995) 13244
35. Jinglei Xiang, Lawrence T. Drzal. Polymer 53 (2012) 4202 – 4210.
36. M. Cochet, W. K. Maser, A. M. Benito, M.A. Callejas, M. T. Martinez and J. M. Benoit, et al., Chem. Commun., 2001, 1450-1451.

Chapter - 15
A Review on Electrical Properties, Conduction Mechanism of Polyaniline and its Effect of Doping on Conductivity

Author

Kazi Hasibur Rahman

Department of Basic Science (Physics), Swami Vivekananda University, Barrackpore-Barasat Rd, Sewli Telinipara, Malir Math, Bara Kanthalia, West Bengal, India

Chapter - 15

A Review on Electrical Properties, Conduction Mechanism of Polyaniline and its Effect of Doping on Conductivity

Kazi Hasibur Rahman

Abstract

Now a days in modern nanotechnology conducting polymers has drawn our attention due to their various application which is based on optical and electrical properties. Conducting polymers are very stable, easy synthesis method, easily affordable compared to other organic compounds. They have good redox properties, tunable conductivity, chemical diversity, chemical and structural variations. Specialized nanostructures of conducting polymers and their electrical and optoelectronic properties are expanding practical applications and are being applied in various electronic applications such as transistors, supercapacitors, gas sensors, energy storage, light emitting diodes etc. Among all the conducting polymers Polyaniline has occupied a large importance due to its diverse chemical properties, flexibility etc. Various types of doping in conducting polymer are also briefly described here. Electronic structure and the protonation and deprotonation phenomenon of polyaniline are highlighted here. The mobility of the charges in the polymer backbone and effect of doping on the charge are also included in this literature. Various applications in energy storage, fuel cells etc. and visible color change of Polyaniline are also discussed. The motivation of this review work is to discuss on the conduction mechanism via various models, mechanism of polymerization, electronic structure of PAni, effect of doping on conductivity.

Keywords: Polyaniline, conductivity, doping, electronic properties, protonation-deprotonation

Historical Background

Now-a-days an interesting human ecological aspect of the research on conjugated polymers has been the developing goal for scientific applications, and hence importance on particular physical properties has motivated the research in the ensuing 30 years. In early 1980s, high electrical conductivity

was the primary driving force in the field of conducting polymer [70-73]. Electric conduction of conducting polymers in nanotechnology and polymer science was investigated in 1977 by the group at the University of Pensylvania [74-76]. Dr. H. Letheby, a professor from the College of London Hospital, was the first to take initiative in the study of conducting polymers. In 1862, the behaviours of the chemical reaction of the conducting polymers were analyzed with other polymers or metal oxide semiconductors. Thus the polymers were chosen. He studied in electro polymerization of aniline sulphate, which was further reported in the Journal of the Chemical Society. The results showed the aniline sulphate, which was formed on a platinum electrode after its electro polymerization turned to a bluish black solid layer [77]. Oligomeric oxidation products of aniline are oxidized through methodical way of research by Nobel Laureate Richard Willstatter in between 1907 and 1911 [78-80]. In the history of the research world polyacetylene is said to be the future assemblage which is very much appreciated. In the 1970s, materials, which can be considered one-dimensional (1D) systems with high degree of anisotropy has worldwide interest in their unique properties. For the first time in 1950 the polymerization of acetylene with hexane rendered polyacetylene has high crystallinity and higher molecular weight reported by Natta *et al*. In the 1950s, researchers reported that polycyclic aromatic compounds formed semi-conducting charge-transfer complex salts with halogens [81-82]. In 1960, the iodine doping concept was also investigated when Czechoslovak researchers are working for polyaniline. Polyaniline-iodine doped complexes has conductivity of 1 S/cm [83]. Polyaniline was first discussed by Henry Letheby in the mid-19th century, which further discovered the electrochemical and chemical oxidation products of aniline in acidic medium. He also noted that the reduced state of Polyaniline (PAni) was colorless and the oxidation state was deep blue [84, 85]. In 1974 the electrical conductivity of PAni was reinvented, which was a some years ago of the progress of polyacetylene. Aniline is said to be obtained from residues of coal tar of gas industry in the early 19th century [86]. In the year 1834 F.F. Runge and in 1840 C.J. Fritzsche isolate aniline and observed the blue color of the aniline during oxidation processlxxxiii. Subsequently, DeSurville and co-workers reported high conductivity in a polyaniline. The paper also shows interesting and attractive findings of a parallel study with another conductive polymer such as polypyrrole. Some Australian researcher B.A. Bolton, D.E. Weiss, and coworkers reported derivatives of polypyrrole with resistivity's as low as 1 ohm-cm [87]. MacDiarmid, Heeger, and Shirakawa contributedconsiderably inthe research and development of conducting

polymers and they were honoured with Nobel Prize in chemistry in the year 2000 [88].

Introduction

Conducting polymers was being studied for the last two decades. Polymers mostly known as plastic give shape to our lives as it can be shaped. Is it important to sort this out? Maybe not, but nowadays the research on polymers is the major driving force in the field of design plastic for electronic appliances. Polymers are easily processed compared to metals. Plastics can be deformed reversibly, whereas metals aren't. They can be shaped into complex polymer architectures. These properties and easy synthesis process of polymers attract many scientists and industrialists to look for novel applications. Traditionally conducting polymers are electronically and ionically conducting polymers. Insulating polymers and conducting polymers make composite with conducting materials electronically. Generally, polymers are insulators. The conducting polymer's conductivity is in the order of 10^3 S/cm [89]. It was experimentally infrastructure [90] and theoretically modelled and understood [91] that many conjugated polymers also show high third-order optical nonlinearity. Π-electron delocalization is included in conjugated polymers in backbone of the polymer. This delocalization in the backbone results in unique optical and electrical properties of the conducting polymer [92-94]. The structures of stable conducting polymers polypyrrole (PPy), polythiophene (PTh), polyaniline (PAni), polyphenylenevinylene (PPV), and poly(p-phenylene) are shown in the figure 1.

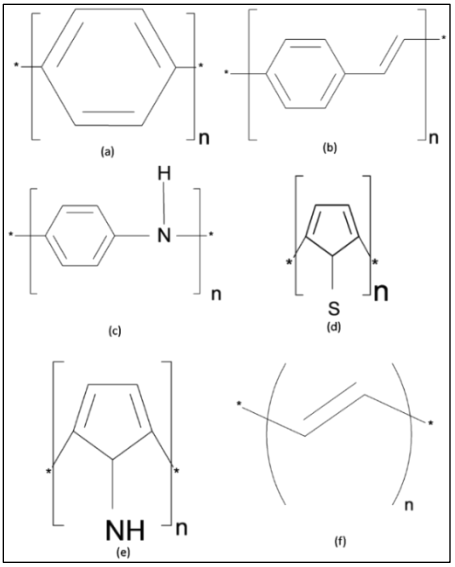

Fig 1: Chemical structures of (a) Polyphenylene, (b)Polyphenylene vinylene (PPV), (c) Polyaniline (PAni), (d) Polythiophene (Th), (e) Polypyrole and (f) Polyacetylene

Polyaniline was invented in 1834 by Runge and its characteristics were studied by Green and Woodhead in 1912. Polyaniline is serving in various fields from last 150 years. Polyaniline has various forms which differ in chemical and physical properties [95, 96]. The conductivity of polyaniline is responsible for the redox state of the polymer, water content, pH of the polymer solution etc. Electrical properties can be maintained by oxidation and protonation state [97]. Polyaniline is a very important and highly conductive polymer in its doped state [98]. The type of dopant anions affects the conductivity of polyaniline at different temperatures. During doping with dopants the electric field is applied and there is a result of electron imbalance. As a result, π conjugated structure is formed in the backbone of conductive polymer happens, which permits the new populated electron to reside along the backbone of the conducting polymer. A common characteristic of the polymer is to transport charge along the conjugated π electron polymer chain backbone or benzene ring which consists of single and double bonds. The interesting point about the conducting polymer is that it consist derivatives of ring-substitution and nitrogen-substitution. The synthesis of the derivatives can be done easily and they are in several different oxidation states and can be doped by different dopant.

These doping processes can be done by two different process,

a) Non-redox processes.

b) Partial chemical or electrochemical oxidation.

Fairly gathered with high conducting polymer after doping, they contains lost of properties like easy synthesis process, good environmental stability, low cost of host materials etc. These properties strongly suggest that the conducting polymers have significant potential and it is applicable technologically. There are two ways by which polymer may store charge.

i) In case of oxidation process, it either lose an electron from one of the bands or it localize the charge over a small section of the chain; the charge causes a local distortion after localization due to their change in geometry giving some energy to the polymer.

ii) A similar picture occurs for a reduction process. The main criterion of conducting polymer is its possibility to oxidize or reduce the polymer without reducing its stability. They are also able to initiate side reactions that accelerate the polymer's ability to conduct electricity.

Till now, many approaches have been reported for preparing 1D nanostructure of polyaniline by including various chemical routes like hard chemical guided synthesis and soft chemical guided synthesis, interfacial polymerization, template free method, dilute polymerization, lithography techniques. The disadvantages of these technique is that they are very poor relatively to control the shape and size of the nanoparticles, poor morphological uniformity, poorly orientation of the nanostructure arrays. The more advantageous technique is the physical process such as electrospining, mainly for the production of the nanofibers of polyaniline [99]. But still conducting polymers have many drawbacks or dispute such as weak stability, low charge carriers mobility, difficult to form specified nanostructure etc. To make progress in structural design and apply it for large-scale application are is a great challenge to the researchers in the field of conducting polymer, for the discovery of optoelectronic devices such as PSCs and PLEDs and other optical materials. Now–a–days intrinsic semiconductor conjugated polymers are very much interesting research in the field of polymer science.

Here in our review manuscript, we have discussed the conduction mechanism via various models, mechanism of polymerization, electronic structure of PAni, effect of doping on conductivity. This reviewed information will help a reader to gain a clear idea on the electronic properties of conducting polymer (here polyaniline) and their mechanisms.

Electronic Structure of Intrinsic and Extrinsic Conducting Polymers

Π–valence band and π*-conduction band structure can be described by the delocalization of π-electrons in the conjugated polymer. In conducting polymer, all VB's are occupied by electrons and CB's are clear. The difference between the HOMO (top of the VB) and LUMO (bottom of the CB) is called the band gap (E_g) of the conjugated polymers. The range of band gap in most of the cases is 1.5–3.0 eV.

According to the absorption spectroscopy, E_g can be written as,

$$E_g = \frac{1240}{\lambda_{edge}} eV \quad (1)$$

From electrochemical cyclic voltammetry oxidation and reduction, potentials are measured and the band gap is determined by energy band gap of conjugated polymers. Coupled redox peaks are presented by polythiophene and other conjugated polymers in the higher potential range denotes to p-doping and in case of lower potential range, the redox peak denotes to the n-doping. The HOMO energy level is denoted by the p-doping or oxidation potential and LUMO energy level of the conjugated polymer is denoted by n-doping or reduction potential. Therefore, for measuring the LUMO and HOMO energy levels of the conjugated polymers, cyclic voltammetry is commonly used [100-102]. The following energy level equation is as follow:

$$HOMO = e(E_{ox} + C)eV \quad (2)$$

$$LUMO = e(E_{red} + C)eV \quad (3)$$

Where,

E_{ox}–Onset oxidation potential (V)

E_{red}–Onset reduction potential (V)

C–constant associated to the reference electrode

The band gap E_g of the conjugated polymers determines the emitted color of PLEDs' when the conjugated polymers are used as electroluminescent materials. The HOMO-LUMO energy levels of the conjugated polymers influence the electrons and holes to increase the efficiency of devices. Extent of delocalization and alternation of double and single bonds are responsible for the size of energy band gap [103-106]. Whether the Conducting Polymer is a metal, semiconductor or insulator is determined from the size of the energy band gap. Hence the outcome of the molecular structure on the energy band gap and electronic energy levels of the

conjugated polymers is very important to understand the electronic structure of the polymers. The band gap energy of metals, semiconductors and insulators is shown in the figure 2.

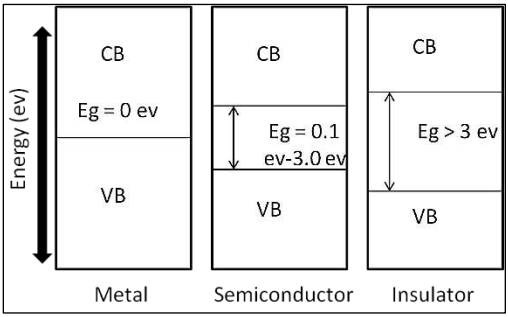

Fig 2: Energy band gap diagram demonstrating band gaps of metal, semiconductor, and insulator

The key factors that influence of energy band gap (E_g) and the electronic structure of the conjugated polymer are discussed below:

i) Energy band gap of degenerate trans-polyacetylene decreases with the contrast between the interspersing single bond length and double bond length [107].

ii) The E_g value also increases by alternation of the polymer main chain from a planar structure between single bonded two neighboring aromatic rings. The angle between the two neighboring aromatic rings in the main chain of the conjugated polymer is large comparable to the two overlapping molecular orbitals of the conjugated ring units. Thus higher E_g values of the conjugated polymer occur.

iii) The electronic structure of the conjugated polymers are also influenced by the substituents nature on the main chain of the conjugated polymers. Reduction of the E_g of the conjugated polymer occurs by the electron donating substituents which upshift the LUMO and HOMO energy levels. The upshift energy of HOMO is more than that of LUMO. The electron withdrawing substituents downshift the LUMO and HOMO energy levels and also lower the E_g of the conjugated polymers. Hence it is concluded that the downshift of the LUMO is more than that of HOMO.

iv) Co-polymerization of the conjugated electron donating unit i.e. electron and D unit accepting. A unit results in the lower band gap

conjugated polymers (D-A polymers) and by selecting suitable acceptor and donor units in the co-polymers HOMO-LUMO energy levels has a tunable-properties. Intramolecular charge transfer between the acceptor and donor units causes the broadening and red-shifting of the absorption spectra of the D-A copolymers.

v) The value of E_g of the conjugated polymers can also be decreased because quinone structure is present in the polymer main chain.

vi) E_g and electronic energy levels of the conjugated polymers can also be influenced by the aggregation of the polymer main chains in the solid state.

vii) The strong intermolecular intercommunication in the planar main chain decreases the E_g of the conjugated polymers.

Molecular Orbital Theory and Molecular Structure of Conducting Polymer

Polymer main chain have conjugated molecular structure where the π-electrons delocalize over the total polymer chain, this is the main characteristics of conducting polymers. Conjugated polymers such as polyethylene have the covalent σ-bonds as valence band. In conjugated polymers π system is formed which show insulating properties unsettled to the gap between the conduction band and valence band and become conducting after doping. Among all the conducting polymers the simplest main chain structure is observed in polyacetylene, which includes double bond and single bond carbon chain alternatively. Based on the location of hydrogen atoms there are two types of structure of polyacetylene:

a) Trans-polyacetylene with the two hydrogen atoms on opposite sides of the double bond carbons. The degenerate conjugated polymer, trans-polyacetylene attributes an identical structure after interchanging its double bond with a single bond.

b) Cis-polyacetylene is placed on the same side of the double bond containing two hydrogen atoms. Cis-polyacetylene and other conjugated polymers are non-degenerate conjugated polymers which forms non-equivalent structure after interchanging double bonds with single bonds. A restricted alternating double bond and a single bond are required in the conjugated bonds. Three σ-bonds with the adjacent atoms are created by carbon atoms in polyacetylene. Another most important conducting polymer is polyaniline whose structure is a little complex, which is the main focus to discuss its structure. Figure 11 shows the main chain of

polyaniline backbone. Usually, there are three structural forms of PAni: leucoemeraldine (PAni-I) [x = 1], emeraldine base (EB, PAni-II) [x = 0.5] and pernigraniline (PAni-III) [x = 0]. Emeraldine structure is very important. The proton-acid doping turns EB structure turns into conducting PAni. In the conjugation path of polyaniline nitrogen atoms are attached. It is typically a phenylene based polymer, which has flexible –NH– polymer chain belted by phenyl rings on either side.

In the configuration of electrons, they have loosely bounded to their corresponding atoms and as a result, high energy orbital's are created. The vital concept of the molecular orbital theory comes from the HOMO (Highest occupied molecular orbital) and LUMO (Lowest occupied molecular orbital). Conduction of polyaniline occurs from the carrier movement from HOMO to LUMO. This becomes more convenient if the distance between the energy gaps between HOMO-LUMO is small. The conductivity of polyacetylene is determined by the concept of sp^2 hybridization of linear carbon chain present in the molecular structure of polyacetylene. Nucleus of the carbon atom is surrounded by six electrons; out of them four valence electrons are 2s and 2p electrons, which take part in the chemical reaction by forming bond. The 1s and 2s valence electron orbital's of the carbon atoms are filled. In case of free space the 2p orbital's are filled with two electrons. Here the hybridization is three sp^2 and 1p orbital. The sp^2 hybridized orbital's on each carbon atom to another carbon atom is interconnected to it and the bonding of the last sp^2 orbital is with H_2 or any of the groups situated in the side. The atoms which are denoted as σ bonds have cylindrical symmetry around the inter-nuclear axis created covalent bonds between them. By overlapping p orbital's which unhybridized of the adjacent carbon atoms, π bond is formed. A weak intercommunication between the carbon atoms creates weak bonds of the π electron. Further this is delocalized and makes the conducting polymer electrically conducting. When the π electrons delocalized over the entire chain, Molecular orbital theory explains that, a long molecular chain which shows metallic transport properties has small bandgap. Over the conjugated space the delocalized electrons are evenly arranged creating equivalent bonds.

The orbital's being filled with electrically conductive particles typical conducting polymers are called as insulators without the need of doping. Doping process transforms the conductivity of a conjugated polymer from the insulating condition to the conducting condition.

Electrons occupy atomic orbital's in case of atoms, but they occupy similar molecular orbital in case of molecules. Hydrogen is made up of two separate protons and electrons. We observe two molecular orbital for hydrogen.

i) The lower energy orbital which has larger electron density. This is of low energy than the two 1s atomic orbital's of hydrogen atoms in the bonding molecular orbital. This makes the orbital more stable than two separated atomic hydrogen orbital's.

ii) A node in the electronic wave function is present in the upper molecular orbital with low electron density between two positively charged nuclei. The energy of 1s atomic orbital is less than upper orbital energy. This orbital is called anti-bonding molecular orbital.

Bonding molecular orbital contains two electrons in hydrogen, with a spin anti-parallel. If the hydrogen molecule is placed in UV light irradiation, it absorbs the energy, promote one electron into its anti-bonding orbital (s^*) and the atom will separate. Here two 1s atomic orbital's combine to form two molecular orbital's, one bonding (s) and one anti-bonding (s^*). In the figure 3 we have shown the energy levels in a hydrogen molecule.

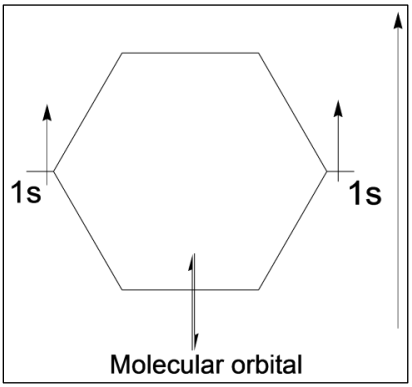

Fig 3: Molecular orbital in diatomic molecules

Valence band (VB) gains energy from the bonding orbitals of the molecule and band gap from anti-bonding orbitals of the molecule is known as conduction band (CB). So, bandwidth is the width of bands across the range of energy levels (conduction band and valence band). In case of polyaniline, highest occupied molecular orbital (HOMO) is denoted as VB and lowest occupied molecular orbital (LUMO) is denoted as CB. This structure is represented in the figure 4. The gap between HOMO and LUMO

of polyaniline is called the energy band gap. This band gap represents the range of energies. This is also called the fundamental energy gap or forbidden gap [108].

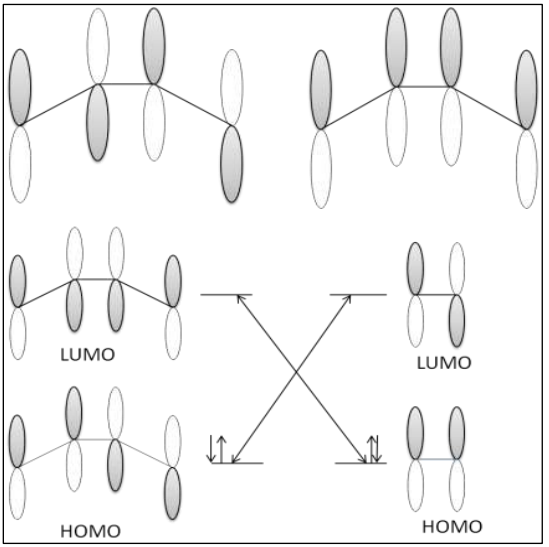

Fig 4: HOMO-LUMO structure of conducting polymers

Mechanism of Charge Transport Phenomenon of Conducting Polymers

The basic mechanism of the charge transport phenomenon of conducting polymers is very important. It has a great technical importance. The main three factors which help to increases the transport efficiency better with the consequence of:

Increasing the device speed.

a) Reducing the power loss.

b) Avoiding the excessive heating.

The packing of the molecules or polymer chains and the degree of order in the solid state, as well as on the impurities density and structural defects are important for the charge-transport properties of conjugated polymers. The polymers do not yield good crystals and they are composed of mixed crystalline and amorphous regions. According to the theoretical physicist, conducting polymers are shown as the limit of the finite linear π-conjugated molecule. As theorists' idealized from the materials perspective view, conducting polymers are considered as more complex in nature. Charges are inserted into (disordered) conjugated polymers and as a result induces local

distortions of the geometric structure are happened. It is also believed that at very high level of p-doping, the electronic transport properties of PT become like a metal which was reported by Sirringhaus *et al*. If we consider the broadening of the bipolaron states in the gap between upon increasing the dopant concentration, the lower and upper bipolaron bands will overlap with the VB and CB, respectively. A gradual change in the conductivity of the material and decrease of resistance is observed when p-type doping is increased at higher potential.

The one way to achieve high conductivities is the process of self-organization. This process explains the lamellar structure with 2D sheets which is built by strongly interacting conjugated segments in polymer main chain. Thus we observed room temperature mobilities of the material are up to 0.1 $cm^2\ V^{-1}\ s^{-1}$. The authors reported that the self-assembly properties of the polymer and superconductivity is very closely related to each other where an additional disorder was found to annihilate superconductivity. That is why we cannot observe superconductivity in chemically doped conjugated polymers. In this case, the disorder proposed by the impurities probably destroys the superconducting phase. The study of oligomer series and its properties are fundamental to understand about the properties, structure and relation between conducting polymers.

The phenomenon of charge transport in PAni is described by a quasi-1D conductor with 3D metallic states. The transfer rate of charge interchain happens inside the crystalline region of PAni which results in “metallic” bundles. Metallic bundles consist of an amorphous region or less ordered region where the hopping of charge through the less ordered region monopolize the macroscopic conductivity. The conduction mechanism of PAni is caused by 3D charge hopping between the chains of the PAni rather than 1D conducting chains, which was proved by high and low field ESR measurements. Both polaron and bipolaron play an important role in conduction in conducting polymers (polyaniline). At high oxidation states the polaronic conduction mechanism of PAni becomes insulating and spinless. Localization of polaron is caused by the formation of polaron pairs and as a result, spin disappears and conductivity decreases at a high doping level. Green protonated PAni has conductivity of the order of 10^0 S cm^{-1}. PAni was converted to non conducting emeraldine base when treated with alkali solution [109]. The conversion is shown in figure 5.

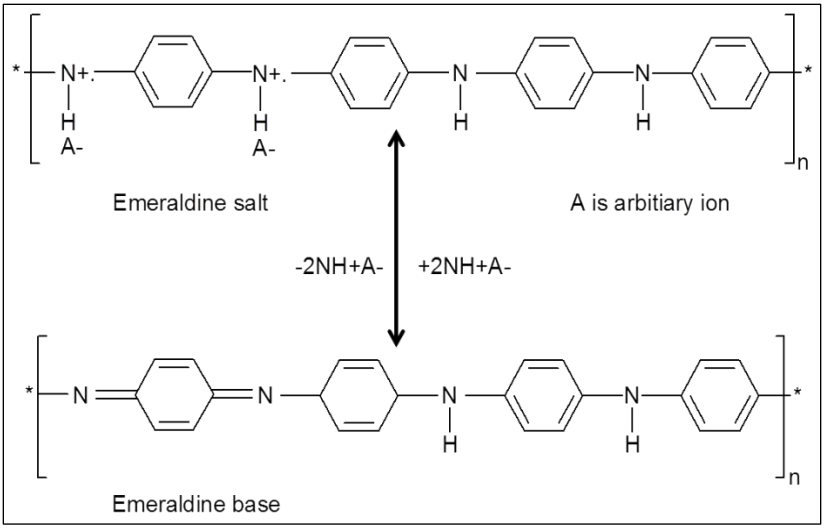

Fig 5: Conversion of EB to ES of polyaniline in presence of alkaline medium

The values of the conductivities of the various conducting polymer and their repeat unit are shown in the table below:

Table 1 [110]

Conducting polymer	Repeat unit of polymer	Orientation of chain	Value of Conductivity ($S.cm^{-1}$)
PAni	C_6H_4–NH	Low	400
PEDOT	$C_7H_4O_2S$	Low	300
PPV	C_6H_4–C_2H_2	High	10^4
PPy	C_5H_2N	Low	400
Polyacetylene	C_2H_2	High	10^4-10^5
Poly(3-methylthiophene)	C_5H_2S-CH_3	Low	400

Structure of Polyaniline and Protonation-Deprotonation Scheme

PAni contains reduced benzenoid units and oxidized quinoid units and known as a mixed oxidation state polymer. In each repeat unit there are two groups amine (−NH) and imine (−N=). This amine groups are separated by three benzene rings which is denoted as 1-3andone quinoid ring (4) is surrounded by imine groups. Quinoid ring contains two pairs of carbon atoms in the ring and four π-electrons which forms double bonds with the nitrogens. Thus the polymer structure is macroscopic in nature with a complicated and complex structure made up of many long chains of repeat units. The average oxidation state of PAni is denoted as (1-y) where y

denotes the existence of each of the three distinct PAni oxidation states. Thus PAni exists in three different oxidation states i.e. fully reduced leucoemeraldine (LE) where (1-y) = 0, half oxidized emeraldine base (EB) where (1-y) = 0.5 and fully oxidized pernigraniline (PE) where (1-y) = 1, which is displayed in figure 6. The most useful form of PAni is EB because of to its high stability at room temperature. Two benzenoid units and one quinoid unit is the composition of EB. The color of emeraldine salt is green and the emeraldine base is blue in color. EB salt is formed by doping EB base with dopants. The protonation helps to delocalize the units of EB. The emeraldine salt is highly electrically conducting if it is doped with acid. But Leucomeraldine and pernigraniline are poor conductors, even after doping with acid dopants. The degree of oxidation and degree of protonation are the two a variable in which properties of PAni is dependent [111, 112]. When emeraldine salt, the conductive form of the PAni is formed, the addition of an acid or a base causes switching of PAni between oxidation states which protonates and deprotonates the base (-NH-) sites in PAni [113]. EB form has the conductivity of ~10^{10} S/cm and can be protonated by 1M aqueous acid (pH~0) whose conductivity is around ~5 S/cm [114]. Highly resonance stabilized system occurs when protonation happens in every imine nitrogen and all the C_6H_4 rings and N atoms are chemically identical and it exists as polysemiquinone radical cation. The proximity of the semiquinone affiliation is believed to give rise to the polaron band which exhibits Pauli susceptibility [115, 116]. This phenomenon is complex which detects protonated amine species in the doped polymer. The protonation of imine nitrogens over amine sites in polymer is observed in acid-doped, EB.· Menardo *et al*. Established the titration of emeraldine hydrochloride with aqueous NaOH which yields two points of inflexion corresponding to pK_a values of 2.5 assigned to NH_2^+–sites and 5.5 assigned to –NH^+– species. Polyaniline is contained of ~14% protonated amines and ~32% protonated imines at pH~0 [117].

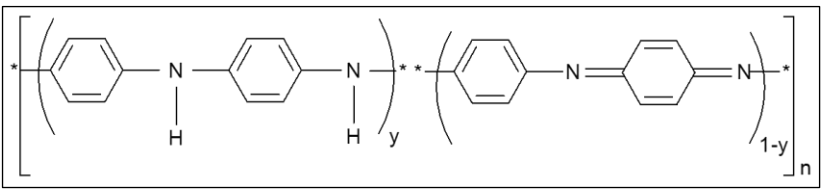

Fig 6: Various oxidation states of PAni (y= 1: Leucomeraldine; y=0.5: Emeraldine; y=0: Pernigraniline)

To determine the chemical properties which depends on various functional group by the chemical reactivity (E_r and E_{bar}) using the weak acid H_2CO_3which can protonate PAni [118]. The temperature dependence of reaction rates are described by the Arrhenius equation. The Arrhenius relation for protonation reaction is as follows:

$$v(T) = 10^{11} \exp(-\frac{E_{bar}}{kT}) \quad (4)$$

Where at the given temperature ν(T) is the rate constant and k, E_{bar}, and T are the Boltzmann's constant, energy barrier and thermodynamic temperature respectively. Introduction of functional groups deduce the values of E_{bar}, by including the doping of protonic acid. The chemical properties especially the chemical reactivity of PAni are very sensitive to derivatization at the polymer chain and doping of protonic acid increases.

Synthesis Mechanism of PAni

Several kinds of literature are reported on the structural and different aspects of aniline polymerization. The most important method of synthesis of PAni is the oxidative polymerization.

We synthesized PAni by chemical oxidation polymerization method which occurs in the presence of ammoniumpersulphate (APS). APS is used as an oxidizing agent in the aqueous medium for good polymerization reaction. Oxidant is used for polymerization method to withdraw a proton from the aniline monomer, without forming a strong co-ordination bond either with the substrate or with the final product. Oxidative degradation of the polymer is controlled by the smaller quantity of oxidant, whereas at high concentration of oxidant polymerization allows the fast oxidation of oligomer and PAni.

Electrochemical synthesis is an electro-organic process. Electrochemical synthesis is used to prepare a thin film. This method of synthesis is similar to the electrodeposition of metals.

Step 1:

The polymerization mechanism corresponds to polycondensationphenomenon as it goes by steps. The polymerization mechanism of PAni starts when aniline radical cation is formed by eliminating one electron from the aniline monomer [119] shown in figure 7.

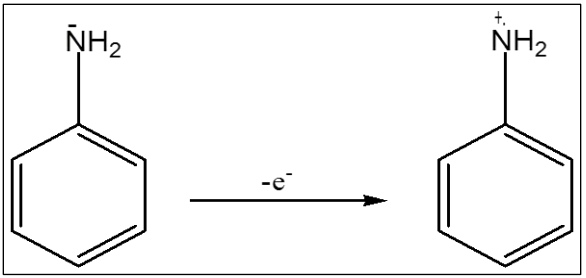

Fig 7: Formation mechanism of aniline radical cation

This aniline radical cation has three resonance forms, given in the figure below. Most reactive one is figure 8(b). Inductive effect is present in the most reactive resonance form and steric hindrance is absent.

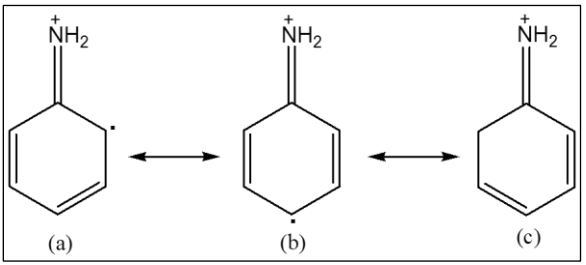

Fig 8: Resonance form of the aniline radical cation

Step 2:

In this step, a reaction occurs between the radical cation and resonance form (b) in an acidic medium. This is called head to the tail reaction. This reaction corresponds to the dimer formation [120, 121].

Step 3:

Here the dimer forms a new radical cation by oxidation process. According to the mechanism, proposed previously, a trimer or a tetramer is formed when a radical cation reacts with the radical cation monomer. The radical cation also reacts with the radical cation dimer to form a trimer or a tetramer [122], which is shown in the figure 9.

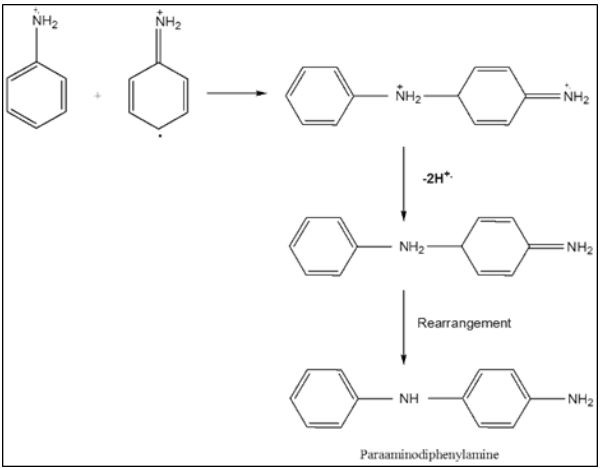

Fig 9: Formation of Dimer

Thus PAni is synthesized by forming a longer chain. It was supposed to be in an octamer form. Thus the path of polymerization is shown in figure 10.

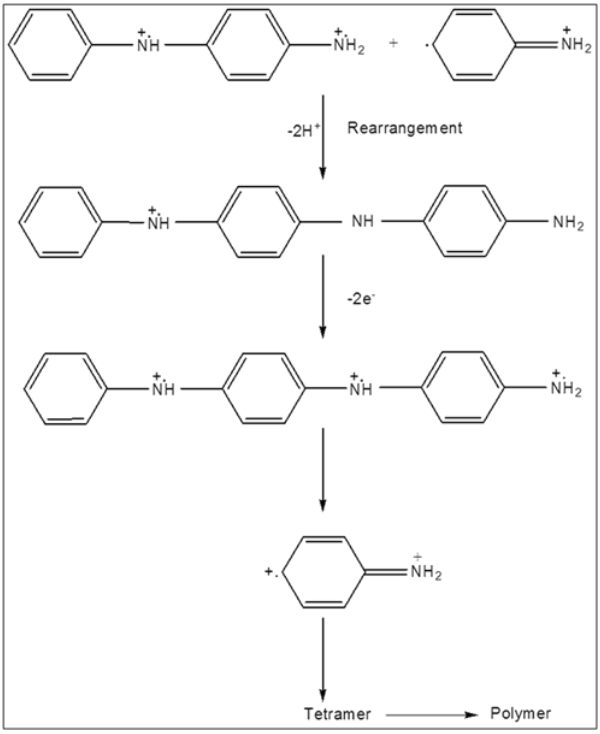

Fig 10: Path of polymerization

Conductivity Properties of Conducting Polymer (Polyaniline)

The most important property of conducting polymers is its conductivity. Conducting polymers has usually amorphous structure. In a few cases they have ordered domains. The mechanism of charge-transport in conducting polymers differs from that in the crystalline conducting materials. Charge carriers can reside openly in the energy bands between CB and VB's. The charge carriers are situated in the local doping energy levels (limited length of the conjugated polymer chain). But in case of ordered domains it is situated in narrow doping energy band. The conductivity of most of the conducting polymers increases due to doping or incorporating other materials with that particular polymer. In general, conductivity increases with decreasing band gap in undoped polymers [123-125]. Metals have zero band gap energy, while insulators like many polymers have a large band gap energy (1.5 to 4 eV). This large band gap energy block electron flow but careful design of the chemical structure of the polymer backbone, it may be possible to obtain band gap energy between 0.5 to 1 eV which is very low.

Emeraldine salt can be formed by doping (Protonated) emeraldine base form of PAni with hydrochloric acid, and conversely, we can get the emeraldine salt form back by dedoping with the base [126]. This doping processes cause conductivity variation from 10^{-10} to 10 Ω^{-1} cm. Zuo *et al*. studied the electric field and temperature dependent conductivity of PAni thin film. They claimed that the charging energy limited tunneling (CELT) studied by Sheng *et al*. satisfactorily described the mechanism of conductivity [127]. In this theory, it is stated that protonated polyaniline is modeled like a sphere which is of metal grain, where as an insulating region is formed for the unprotonated Polyaniline. Wang *et al*. show that Polyaniline behaves like a 1D disordered conductor, three-dimensional (3D) delocalized states are constituted by 1D intrachain localized states an interchain coupling, conform to Mott's variable range hopping (VRH) theory [128-130]. Temperature dependent conductivity of all conducting polymer follows the Mott's variable range hopping (VRH) model and behaves like that of semiconductors.

$$\sigma(T) = \sigma_0 e^{[-\frac{T_0}{T}]^{\frac{}{(n+1)}}} \quad (5)$$

Where σ_0 is a factor weakly related to temperature, n is the dimension number 1, 2, 3 indicating1D, 2D, and 3D VRH transportation respectively. For the 3D system we consider the equation [131, 132],

$$\sigma(T) = \sigma_0^{3d} \exp\left[-\left(\frac{T_0^{3d}}{T}\right)^{\frac{1}{4}}\right] \quad (6)$$

Where,

$$T_0^{3d} = \frac{C}{k_B N(E_F) L^3} \quad (7)$$

C is a constant, k_B is the Boltzmann constant, L is the effective conjugated chain length, and N (E_F) is the state density at the Fermi energy level.

In an article it is published that a granular rod model and the discussion of the temperature dependent conductivity, doping dependence, thermo-electric power and Pauli susceptibility of PAni [133]. The conductivity of PAni changes with the increase of oxidation and degree of protonation. This model is compared with the 3D VRH theory. Plester *et al*. also suggested a model which describes that the insulating, amorphous region surrounds conductivity, crystalline regions. They imply that the3D VRH theory model is adaptable with the Sheng CELT model. Zuppiroli *et al*. [134] restated that the employment of the CELT model of hopping conduction in disordered conducting polymers such as polyaniline. The diameter of conducting grains and the separation between the grains can be evaluated by using this model. Many researchers believe that there is so much disorder and defects state in conducting polymers, which is the conjugational defects, such as solitons and polarons. This solitons and polarons will lose much of their original characteristic properties and that is the most reasonable to start with classical models. Experiments have been related to the disordered hopping model from the last fifteen years. The temperature variation conductivity has an appropriate value and considered to provide information about the conduction mechanism. Most authors aspect a value near about ¼ to variable range hopping; and a value near to 1/2 is generally due to the presence of a Coulomb gap, either in the homogeneous system of localized interacting electrons or in the form of a charging energy in a granular metal-like system [135]. Detail explanation of protonation-induced interchain coupling theory is described by CELT model, thus they took polaronic clusters as conducting grains. Many other different experiments such as 3D VRH [136], 1D VRH with interchain coupling [137], amorphous regions connect crystalline regions, Efros-Schklovskii (ES) hopping conduction [138], CELT (granular metallic) model [139] and the localization interaction model are supported in the following years. From literature it is found that the charge transport of conducting polymers can be analyzed in a macroscopic scale, hence the

exact conductivity mechanism steps of the conducting polymer (PAni) is under argument. The conduction mechanism and various steps are shown in figure 11.

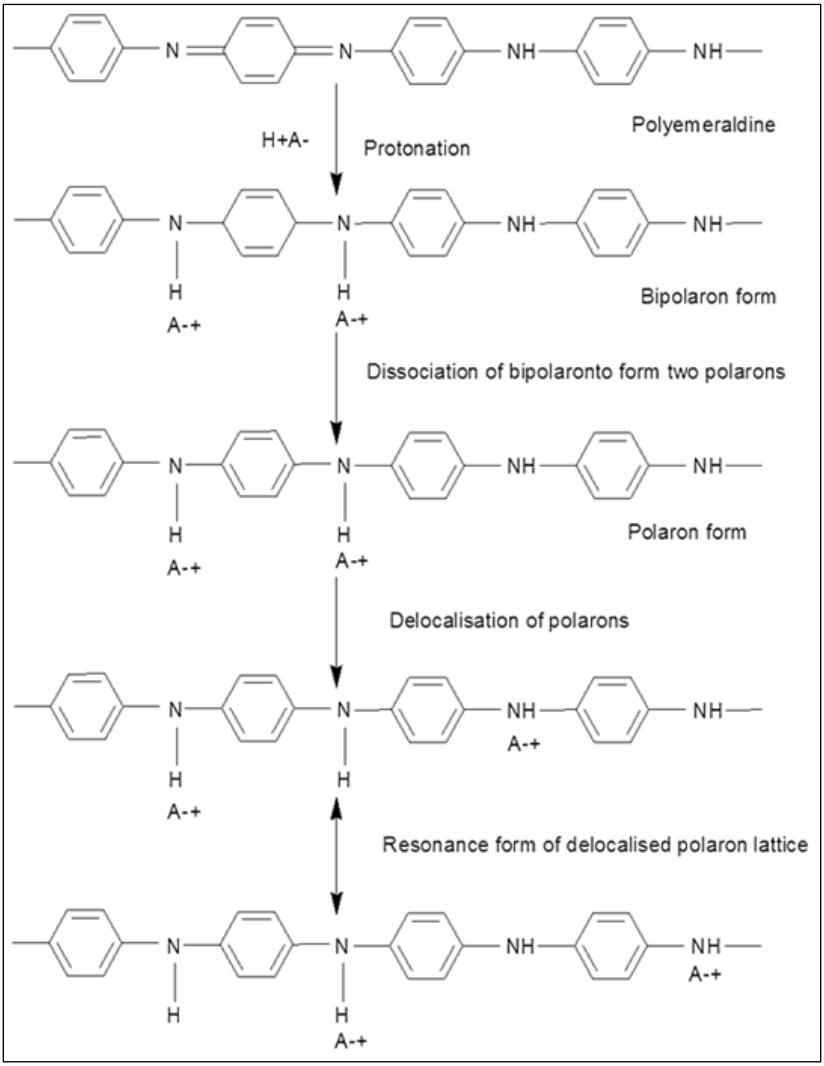

Fig 11: Conductivity mechanism of emeraldine salt form of PAni [140]

The main characteristics of Polyaniline among all conducting polymers are its high electron affiliation and low oxidation potential. The reduced polymers have to dope with n-type electron donors and oxidized polymers have to dope with p-type electron acceptors. In case of all conducting

polymers (here polyaniline), the concept of the valence band and conduction band does not work else the concept of HOMO and LUMO for the electron transfer from lowers to higher molecular orbital. The conventional inorganic compounds are compared with the semiconducting characteristics of conjugated polymers. To create the new and unfilled electronic energy states the additional charges exist within the energy gap of HOMO-LUMO. The role of dopant ion is to remove electrons or add electrons. In case of polyaniline, if the electron is relocated from the upper most valence band of the conducting polymer and the electron transfer to the lower level of conduction band, then according to the classical band theory the delocalization of the electron will not occur for the created vacancy hole in the valence band. The radical cation is localized when coulomb attraction is applicable for its opposite ion and it is also known as polaron. The concentration of the opposite ion is high enough. As the positive charge moves less enough to conduct electric charges, the dopants usually achieve polarons and bipolarons, which are responsible for the conduction of electricity in polyaniline. Dopants (electron acceptor) create the ionization potential of the conducting polymers chain to a positive polaron, which allows the electron to transfer from LUMO to HOMO [141].

Electron Transport Phenomenon and Proposed Conduction Model of Conducting PAni

Before we start to discuss the transport mechanism of Polyaniline, it is known that polyaniline which is not protonated have the band gap energy of ~ 4eV. The unprotonated PAni chain reveals a semiconductor like a band structure. This phenomenon of two electrons which is not overlapped and situated at a distance of size of the monomers seems to be connected with coulomb energy. Coulomb energy is mathematically expressed as,

$$U = \frac{e^2}{4\pi\epsilon_0\epsilon_r a} \tag{8}$$

Where,

e-electron charge.

ϵ_0-Vaccum permitivitty.

ϵ_r-Relative permittivity.

Polaron bands are formed in a protonated chain to establish the metallic properties when PAni is doped with an acid [142, 143]. Conjugated π electron consists of single and double bonds along the polymer backbone chain makes polymer capable of transporting electrical charge, this is the common

feature of conjugated polymer [144]. In the temperature dependent resistivity the PAni bulk has electrical properties which show semiconducting property rather than metallic manners [145]. Partially protonated model is considered as the protonated regimes, which is separated by unprotonated PAni forming conducting grains. This model describes the amorphous PAni nonstoichiometry, fully protonated PAni or connections between nanofibers. These all are denoted as insulators which separates the conducting grains. Conduction mechanism on macroscopic shell can be seen in single PAni nanofibers. Partially protonated PAni was implemented to study of the conduction mechanism of polyaniline. Using this partially protonated model, it can be simplified our inquiry and avoid the complicated and complex resultant of PAni, amorphous PAni and nonstoichiometry. From literature we find that the room temperature resistance is not enough to determine the protonation ratio in a simple way. Resistance cannot be accurately used to pin down the protonation ratio in room temperature. According to the CELT model the electron transport behaviours (resistance R denoted as a function of temperature T) were estimated and considered [146].

$$R = R_0 \exp[(\frac{T_0}{T})^{\frac{1}{p}}] \quad (9)$$

Where, R_0 and T_0 are parameters and p=2

In case of the CELT model there are other two theoretical models i.e. the ES hopping conduction and 1D Mott's VRH describes the electrical properties of single crystal PAni, sharing the same mathematical formula of above equation with p = 2.

$$R = R_0 \exp[(\frac{T_0}{T})^{\frac{1}{2}}] \quad (10)$$

At first in a single nanofibers we applied the ES hopping conduction to electron transport to explore the enough conditions required. At temperatures lower than the critical temperature T_C we can observe ES hopping conduction.

$$T_c = \frac{e^4 \xi g_0}{k_B(4\pi\epsilon_0\epsilon_r)^2} \quad (11)$$

Where ξ, e, g_0 , k_B, ϵ_0 and ϵ_r, are localization length, electron charge, density of states at Fermi level, Boltzmann constant, permittivity of vacuum and relative permittivity, respectively.

The coulomb interaction phenomenon is applicable in the two localized electron states when the temperature is above a critical value (T_c) and gives the occurrence of Mott's VRH model. The localization length ξ can be calculated using the parameter $T_0$and the relation.

$$\xi = \frac{2.8e^2}{4\pi\epsilon_0\epsilon_r k_B T_0} \quad (12)$$

The critical temperature is ≈35 K. The experimental temperature range is definitely higher than this critical temperature, indicating that the ES hopping conduction is incomplete to accept and to explain electron transport in PAni nanofibers. Therefore, in PAni nanofibers the possibility of considering the ES hopping model as an electron conduction mechanism is eliminated [147].

Further, we have found which model is appropriate for electron conduction mechanism, CELT model or 1D Mott's VRH model? We find that both the model suggest the same characteristics of temperature (with p=2) of resistivity in the low electric field regime. In the case of the high-field region, the differential resistance as a function of electric field E is declared as [148]:

$$R = R_T \exp\left(\left[\frac{E_0}{E}\right]^{\frac{1}{q}}\right) \quad (13)$$

Where, E_0 and q are constant parameters and R_T is a temperature-dependent parameter.

It is suggested that the values of exponent parameter q are to be 1 for the CELT model and 2 for 1D Mott's VRH model. In the high electric field, the resistance measurement is more difficult because a strong field is created in thin film devices in case of high voltage (100V). To get rid of this high voltage, we generally use nanoexperimental approach or nanofibers device approach and such a high electric field region is created by applying a voltage of 10V.

Sheng's CELT model explains that two parameters, T_0 and E_0 are used to consider thoroughly the mechanism of conductivity in a single PAni nanofibers. The basic matter which we assume for this model is that the intergrain distance "s" multiplied by the charging energy E_C of the grain is a constant. E_C, the charging energy of the grain is inversely proportional to the grain diameter "d", so this consideration explains that ratio of s/d is constant. The average values of (s+d) can be calculated from the equation given below,

$$s + d = \left(\frac{k_B T_0}{4eE_0}\right) \quad (14)$$

Additionally, the value of s/d can be calculated from the parameter T_0 and the relation [149] is given as,

$$T_0 = \frac{8U}{k_B\left(\frac{\frac{d}{s}+\left(\frac{d}{s}\right)^2}{2}\right)} \quad (15)$$

This relation is a generalized derivation form of the CELT model. We can find the most probable value of intergrain distance s mentioned above. To know more about CELT model we assume that the presence of protonated regimes (conducting grains) and unprotonated intergrain regimes in partially protonated PAni. We use hard sphere model to understand this model properly which is arranged in the fcc structure. We obtained a packing fraction of 74% when conducting grains are treated as a hard sphere. The relation between the CELT model and a real system of PAni nanofibers are described theoretically further. The electron transport pictures in high and low-electric-field regimes are shown in figure 12. In the high electric field, the electric-field-generated potential energy between grains is much larger than the thermal energy. This is the reason the field-induced tunnelling controls in the production of charge carriers between grains.

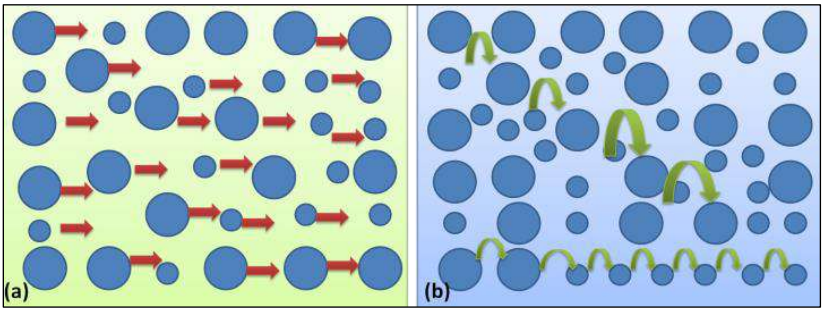

Fig 12: Conducting model in the PAni nanofibers in (a) high- and (b) low field region

The rate of tunneling is decreased exponentially with the intergrain distance, and thus an increase of electric potential energy happens which gives same effect as shortening the intergrain distance and also increases the tunneling rate (charge carriers). The charge transport phenomenon can take the direction along a different diameter of conducting grains. On the other hand, the thermally activated charge carriers dominate in the low field. The charge carriers transport through a hopping potential through large conducting grains (grey curve) at low temperature. But at a higher temperature, between smaller grains and the charge carriers more and more hopping channels are well established. This can hop through either the large or the small grain for high electric field regime (orange arrow).

Photo-Induced Absorption of Emeraldine Base (EB) and Leucomeraldine Base (LB) form of PAni

Here we discuss the photoinduced absorption theory of the two forms of the PAni (fully induced LB form and half oxidized form EB). Study of Conducting Polymer basically PAni gives the concept of defects state of polymer i.e. polarons, solitons, bipolarons. These defects states depend on a number of electrons and protons in the polymer chain backbone. LB, the fully reduced form of PAni acts as an insulator with large energy band gap (E_g~ 3.6 eV), originates from overlapping of molecular orbital's of the neighbouring phenyl rings and nitrogens. We can obtain the electronic states of the conducting polymer by removal of the protons of H_2 atoms, as well as electrons in the presence of amine (–NH–) group which makes the LB form chemically flexible. The half oxidized (1-y=0.5) EB form is also an insulator with la arge extrinsic gap (E_g~3.6 eV). Here the PAni forms polarons which can be described by the polaron energy band. The main aim of the photoinduced absorption is to show that the polarons are produced by photoexcitation of insulating EB form. Scientists show that the electronic structure and defects states in PAni determine the ground state and excited-state properties of materials. The photoinduced absorption spectra of EB in the IR and visible regions are reported for pumping into the π- π^* transition at 3.8 eV and compared to with the reported data for pumping near 2.5eV into the excitons band. Photoexcitation creates same type of defect states which shows the similarity of energy band.

To interpret the excited-state properties and ground state of PAni, we recommend a model which describes the photoinduced-absorption spectra. In this model, we acknowledge the removal, addition, or rearrangement of electrons through oxidation, reduction, or photoexcitation starting with leucoemeraldine base in its ground state level.

Different excited states are examined in this portion are schematically represented in Fig 13(a)-(e). They include:

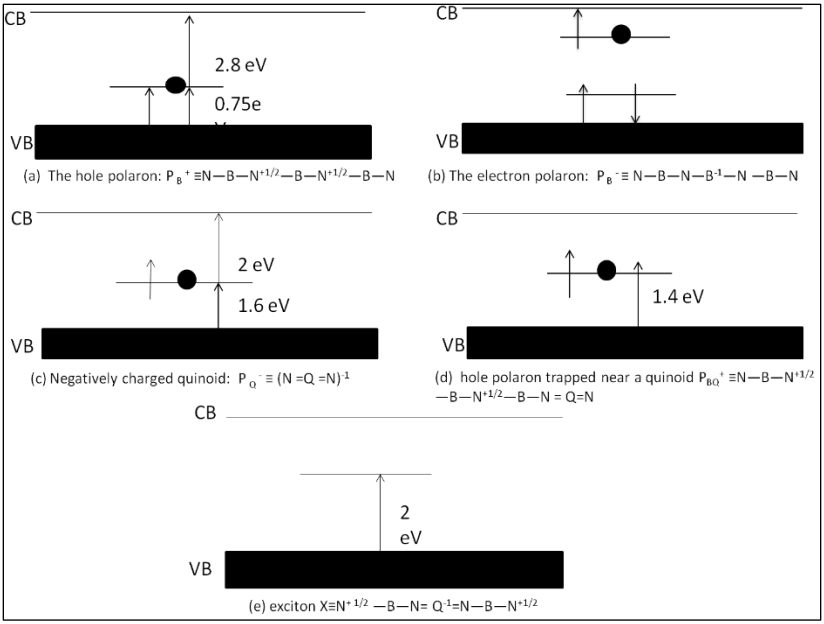

Fig 13: Schematic definition of defect states P_B^+, P_B^-, P_Q^+, P_{BQ}^+, and X with approximate energy level diagrams

In this notation, B act as a benzenoid site (—C_6H_4—), Qact as a quinoid site (=C_6H_4=) and N act as either an amine nitrogen (i.e. N—H) if adjoining to B or animine nitrogen (no H) if adjoining to Q. Additionally the charge distribution of the defects states will be more delocalized than indicated in the above schematicnotations. It is normal from theoretical calculations [150, 151] that ring-angle distortions and bond are important in all of the excited-state configurations. The energy of splitting of P_B^- is expected tobe not more than a few tenths eV.

Concept of Doping in Conducting Polymers

Charge transfer doping and the associated changes in the electronic properties of conjugated organic polymers such as polyacetylene, polythiophene, polypyrroleand polyaniline, are well known. Doping is very much important topic in the field of conducting polymers. Doping differentiates conducting polymers from all other various types of polymer. To gain high conductivities of CP, it is doped by different methods [152]. Generally, there are two forms of the conducting polymers i.e.

i) Undoped polymer

ii) Doped polymer

The neutral polymer backbone is converted to a charged π-conjugated system by doping process. Neutral form of the polymer is treated with small; not exactly amount of stoichiometric quantities of the chemical species. The structural, electrical, electronic, magnetic, optical, and properties of the polymer change drastically. Generally doped material has an electrical conductivity higher (~ 6-11 orders) in magnitude than that of the undoped material. The conductivity varies from 10^{-6} to 10^{-10} S/cm for undoped polymers, lying at the barrier region of the insulator and semiconductor (Figure 14) [153].

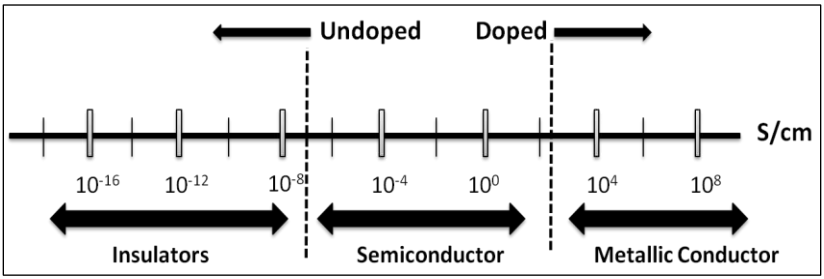

Fig 14: General conductivity range of doped and undoped conducting polymers

All conducting organic polymers are insulators or semiconductors in their neutral ("non-doped") forms. Doping and de-doping is basically a reversible process which keep the chemical structure unchanged and nature of the polymer's backbone. Chemical or electrochemical is the process by which the doping and undopingprocess carried out. By controllable adjustments of the doping level with the host, material detects the conductivity between undoped (insulating or semiconducting) and fully doped (highly conducting) form of the polymer. The "classical" method of "doping" involves redox doping, i.e., chemical or electrochemical partial oxidation ("p-doping"), or partial reduction ("n-doping") of the conjugated polymer backbone. Electron changes in the polymer backbone during this process. In p-type doping, a hole is created in the backbone of PAni when an electron transfers directly from HOMO to the dopant species. Conversely, in an n-type doping, electrons move to the LUMO of the PAni conducting polymer from the dopant species, resulting in increase in electron density. Therefore, by doping the density and mobility of charge carriers can be tuned [154-156]. Polyaniline consists of delocalized π electrons in its backbone in doped state, whereas in an undoped state, the PAni has a conjugated backbone, which after doping retained to its modified state or it may have a non-conjugated polymer chain backbone as in case of PAni. PAni becomes

conjugated after p doping. Here, we have illustrated the principle of conduction mechanism of CPs, which is also valid for PAni. The common electronic structure of every conducting polymer is based on double and single bond in the polymer skeleton. Localized σ-bond is denoted by both single and double bonds, forming a strong chemical bond. Additionally, localized π-bond is present in each double bond, which are weaker. The conjugated double bonds in the backbone of polymers is shown in figure 15.

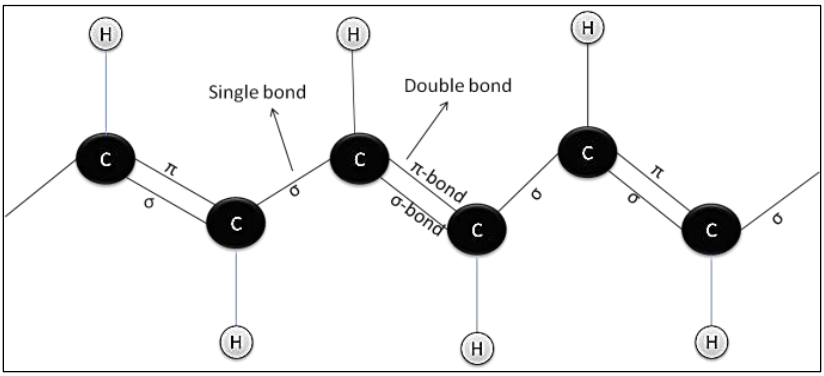

Fig 15: Conjugated double bonds of the backbone structure of polymers

There is bond between first and second carbon atoms which is known as the π-bond. This is transferred to the position between the second and third carbon atoms. The π-bond which is situated between the third and fourth carbon travels to the next carbon, and so on. As a result, the movement of electrons in the double bonds is observed along the carbon chain. The p_z-orbitals in the chain of π-bonds overlap continuously and the electrons in the π-bonds move along the carbon skeleton. Therefore, conjugated polymer double bonds allow the electrons to flow through the backbone of the polymer.

In principle, the bulk conductivity of conducting polymers should consist of contributions from intra-chain, inter-chain and inter-domain electron transportations (Dai *et al.*, 1999). The details of the electron transporting processes of conducting polymers and their relative importance are still under debate; some of the factors that influence conductivity have been recognized. The doping process influences the conductivity of conjugated polymers. Other factors include the orientation, crystallinity, and purity of the conjugated polymers. Vargaet. al. reported that the conductivity increases nearly 1000 times after doping PAni with silver [157]. At room temperature the conductivity value are 320 S/m for TSA-PAni composite, 15 S/m for CSA-PAni composite, and 3×10^{-6} S/m for TSPP-PAni. TSA and

CSA-PAni are, at least, seven times more conductive than undoped (~10^{-7} S/m) PAni [158]. Cao *et al*. in his study, discovered that at the highest doping level for $FeCl_3$, electrical conductivity was found to be 1.3×10^{-2} S cm^{-1}, and for $(FeCl_4^-)_y$ 0.58 S cm^{-1}. The low conductivity was attributed to the fact that only relatively low doping levels were possible [159]. Doping of HCl acid the conductivity increases to 10^5 times the undoped PAni. In the same article it was reported that doping with formic acid, iodine and Methylene blue, the conductivity increases upto 10^6, 10^4, 10^0 times respectively from the undoped version of PAni. The specific conductivity of the HCl doped PAni films varies linearly with humidity (35-70%). The specific conductivity of CSA doped PAni films remains constant with the variation of humidity, but increases non-linearly if the ranges goes below 30%. The increment of electrical conductivity with humidity can be generally attributed to the presence of water molecules in PAni matrices which induced a higher charge carrier mobility and a significant contribution from ionic conduction [160]. Dimitriev *et al*. reported that doping PAni by transition metal salts, controls the morphology and thus strongly contributes to the conductivity of the material [161]. PAni/V_2O_5 nanocomposite increases the conductivity up to 100 times compared to undoped PAni [162]. Some of the most commonly used doping methods are described below:

Chemical P-Doping

It is also named as oxidation doping, which refers to the doping process of the conjugated polymer main chain to form polarons. The oxidants I_2, Br_2, AsF_5, etc. can be used as p-dopant [163]. The conjugated polymer which is oxidized loses an electron and formsp-doped conjugated polymer chain, and the dopant gains an electron to become the counter anion after p-doping. The following reaction is a p-doping process:

$$CP + \frac{3}{2} I_2 \rightarrow (CP) + I_3^- \tag{16}$$

Where CP denotes the conducting polymer.

Chemical N-Doping

This is the process by which the conjugated polymer main chain form negative charge carriers. It is named as reduction doping. n-type dopant are some strong reductants, such as alkali metal vapor, $Na^+(C_{10}H_8)^-$, etc. To form main chain of an n-doped conjugated polymer, the conjugated polymer is reduced and gain electrons, whereas the dopant losses an electron to become the cation after n-doping. The following reaction is the n-doping process:

$$CP + Na^{+}(C_{10}H_{8})^{-} \rightarrow CP^{-}(Na^{+}) + C_{10}H_{8} \quad (17)$$

The main advantages of this type of doping are to obtain doping by exposing the sample vapor of the dopant or immersion into a solution with the dopant in a simple way and the disadvantages are

a) Performed very possible to prevent inhomogeneous doping.

b) Unstable doping levels obtained with respect to time.

c) Low reversibility occur after doping/de-doping.

Electrochemical P-Doping

Electrochemical doping is oxidation or reduction of the conjugated polymers on an electrode. The main chain of conjugated polymer missed an electron (gain a hole) accompanying the doping of anions from electrolyte solution when it is oxidized:

$$CP - e^{-} + A \leftrightarrow CP^{+}(A^{-}) \quad (18)$$

Where A−denotes the solution anion, $CP^{+}(A^{-})$ represents the conducting polymer with the main chain oxidized and anion doped.

Electrochemical N-Doping

The conjugated polymer main chain is decreased to gain an electron accompanying the doping of cations from electrolyte solution:

$$CP - e^{-} + M^{-} \leftrightarrow CP^{+}(M^{-}) \quad (19)$$

The main advantages of this doping process are

1) Doping level can be easily controlled by using an electrochemical cell with a controlled amount of current passed.

2) Doping/de-doping is highly reversible and clean polymer can be retrieved and the disadvantage is the unexpected structural distortion may cause electrical conductivity decay.

Redox Doping

The most extensively investigated conducting polymer is Trans-$(CH)_x$ which is known as the prototype conducting polymer. These polymers are capable of redox doping processes [164]. The bonding system of ¼of the prototype conducting polymer can be readily partially oxidized, “p doped”, by a variety of reagents such as iodine vapor or a solution of iodine inCCl_4,

$$(CH)_X + 1.5(xy)I_2 \rightarrow [CH^{+y}(I_3)^{-y}]_X \text{ [y≤~0.07]} \quad (20)$$

with a concomitant increase in conductivity from 10^{-5} S/cm to 10^{3} S/cm. Ifthe polymer is stretched to 5 to 6 fold before doping, the conductivity can be up to~10^{5} S/cm can be obtained [165]. Analogously, the polymer backbone can be partially decreased, "n-doped" by, for example, a solution of sodium naphthalen [166], in TetrahydrofuranTHF, viz,

$$(CH)_X + (my)Na^+(Npt)^- \rightarrow [Na^{+y}(CH)^{-y}]_X [y \leq \sim 0.1] \quad (21)$$

Large increase in conductivity values are observed, reported for iodine p-doping have not been obtained. This process populate the anti-bonding π^* system.

Non-Redox Doping

Non-redox doping process neither involves or adds nor removes an electron from the polymer chain backbone [167]. For instance, by a non-redox process emeraldine base can be doped [168] which is accomplished by simply protonating the imine nitrogen atoms of the polymer. Thus a polysemiquinone radical cation is produced in which both charges and spin are delocalized along backbone of the polymer. The conductivity of the polymer increases from 10^{-10} S/cm to~10^{0} S/cm. This protonic acid doping process has been drawn out to poly(heteroaromaticvinylenes) and its derivatives [169]. The main advantage and disadvantage are respectively number of electron generally does not change and low conductivity are observed for some CPs respectively.

Effect of Charges in Conducting Polymer Backbone Chains upon Doping

We can gain large range of conductivity by doping conducting polymers. The conductivity increases as the doping level increases gradually. Experimentally we see from that the conductivity ranges in between 10^{-3}–10^{3} S/cm of common doped conducting polymers, whereas without doping the intrinsic conjugated polymers such as PAni, which ranges in between 10^{-9}-10^{-6} S/cm. Thus, the conductivity of conjugated polymers increases by 6 to 9 fold after doping. The charges which are introduced into the backbone of the chain of polymers and oligomers through doping are generally stored in different states called solitons, polarons, and bipolarons. When an electric potential is applied it is believed that doping results in an electron imbalance and the extent π conjugated structure of the conductive polymer grants the new electron population to move along the backbone of polymer chain. Hence we can observe that charge carriers are mainly dependent on material and doping level [170]. When inorganic semiconductors are doped, the dopant

species occupy positions within the lattice of the host material, as a result, there is a presence of electron-rich or electron-deficient sites with no charge transfer occurring between the two sites [171]. The doping in organic conducting polymers results in partial oxidation and reduction in polymers rather than the creation of holes. Positively (or negatively) charged polymeric complex is formed when polymer is exposed to an oxidizing agent X (or reducing agent M^-) and of a counter ion which is the reduced X-(or the oxidized M^+) forms of the oxidant or reductant [172, 173]. In the case of conducting polymers the "doping process" may be more correctly classified as redox processes of the following general scheme:

$$Polymer + X \leftrightarrow (Polymer)^{p^+} + (X)^{p^-} \quad (22)$$

In the case of an oxidation (*p*-doping) process and

$$Polymer + M \leftrightarrow (Polymer)^{n^+} + (M)^{n^-} \quad (23)$$

For a reduction (*n*-doping) process

Where, X = I_2, Br_2, AsF_2,…….. and M= Na, Li……

The above reactions most likely occur in the case of unsaturated polymers as they can be easily removed or added to the polymeric chains to form poly-ions and, therefore, these are the types of polymers which assume high conductivity on doping [174].

Self-consistent polarization field is formed by the moving charges in a lattice which accompany together and can be treated as a quasi particle called the polaron. There are various characteristics of polaron such as effective mass, energy, total momentum etc. Charge appears on the organic polymer chain is possibly localized and a local distortion is occurred around the charge of the lattice. There is local upward shift of HOMO and downward shift of the LUMO which is observed due to the localized electronic states in the gap. A polaron is a charge carrier whose net spin is associated with a lattice distortion and localized electronic states are present in the gap. A polaron is just a radical ion. Charge deforms the lattice around it is the manifestation of a strong electron-phonon coupling. The positive polaron is denoted as P^+ with the negative polaron and a positive charge denoted as P^- with a negative charge. Oxidation of the conjugated polymer main chain forms P^+ and reduction of the conjugated polymer main chain forms P^-. In conjugated polymers polaron appear and creates two new polaron energy levels in the bandgap. P^+ and P^-acquire spin of 1/2. The mechanism of charge transport in conducting polymers and molecular single crystals result from the interplay between electronic and electronic vibration interaction, in the absence of physical and chemical defects.

Bipolarons are formed by the removal of the second electron from the conducting polymer chain and is associated with a strong local lattice distortion as a pair of like charge. Bipolaron is similar to the concepts of the cooper pair which is like BCS theory of the superconductivity. Double charges are occurred in bipolarons by coupling of two P^+ or two P^-on conjugated polymer main chain. The positive and negative bipolarons indicate to the hole pair or the electron pair. Energy is gained by the interaction with lattice when the bipolaron is formed. This energy is larger than the coulomb repulsion between the charges, confined in the same direction. Electron Spin Resonance (ESR) indicatesdifferent charge carriers in conducting organic polymer from those in the inorganic semiconductor. The variation in charge carriers is observed from low to high doping material [175].

At low doping, we observe that the polaron is formed with spin ½. The ESR signal saturates and then decreases at intermediate doping level, which consists the polaron to recombine to form spinless bipolaron. Although the system is highly conducting no ESR signals are observed at high doping level, indicating that the charge carriers in that region are spinless.

Soliton is a charge which is bounded by a boundary or domain wall. Soliton can also be defined as the system which leads to same energies one potential well to another. The main properties of the soliton are the solitary wave which propagates without deformation and dissipation. A neutralsoliton with spin ½ is a radical whereas charged solitons are spinless [176]. Soliton has electronic energy level at the middle of the bandgap energy of trans-polyacetylene. Positive soliton has zero electrons and there are couple of electrons on the soliton energy levels for negative soliton. Here we have shown the diagram (figure 16) of the mechanism of charge transport of polaron, bipolarons, and soliton through the energy band gap in polyacetylene.

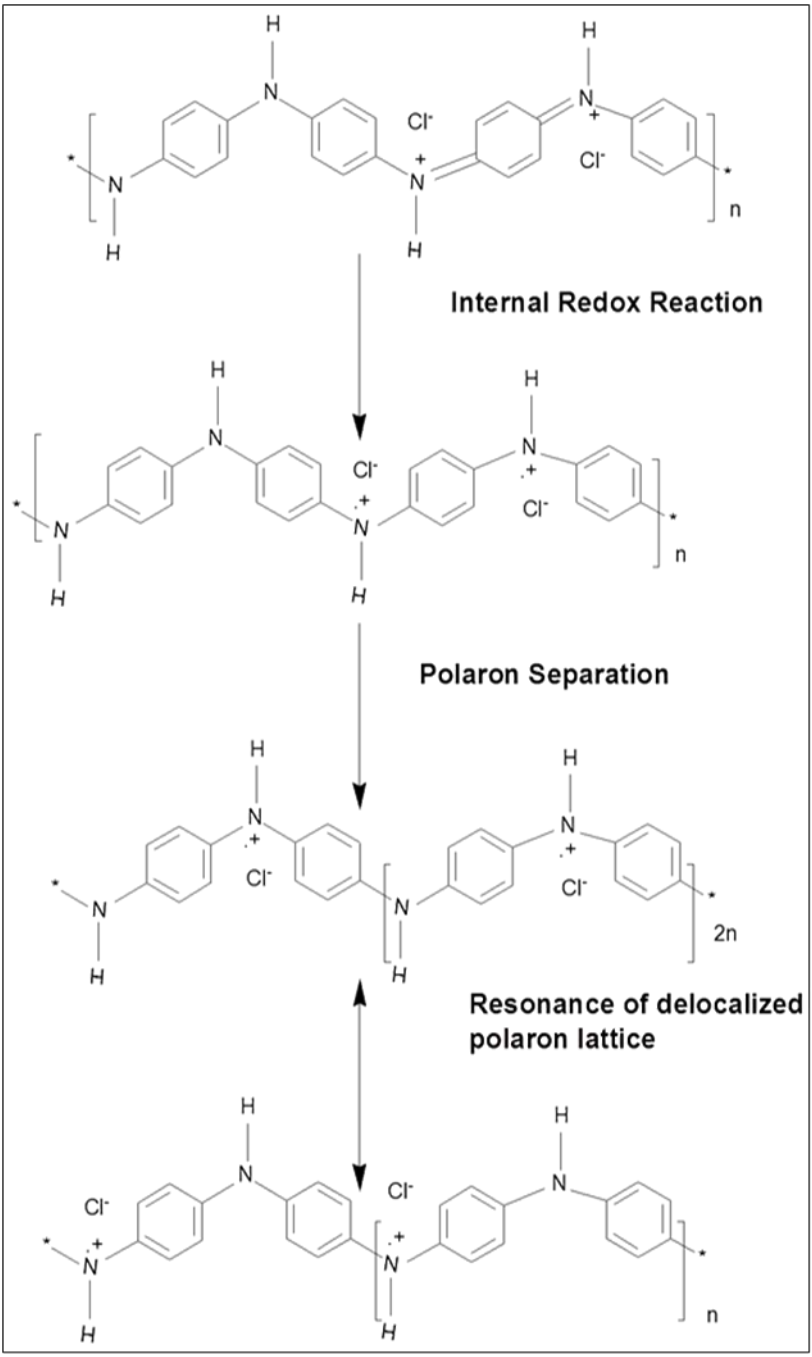

Fig 16: Charge transport mechanism in PAni through polaron, bipolaron [177]

Here we discuss the charge transport mechanism in PAni chain which was described as a quasi 1D conductor with 3D metallic states at first. The transfer rate of charge-interchain inside the crystalline region was presumed to result in metallic bundles. The amorphous region between the bundles, there is charges which hops and dominates the macroscopic conductivity. At high oxidation states PAni has its derivatives become insulating and spinless [178]. The polaron pairs having double charge are supposed not to be conducting, as the hopping probability of two charges in a single chain is too small [179].

Thus polaron pairs are formed and cause polaron localization and that is why spin disappeared and conductivity is decreased at a high doping level of PAni. According to the Mott's variable-range hopping model, the 3D conductivity of the protonated PAni is given as [180]:

$$\sigma = e^2 \nu [\frac{9N(E)}{8\pi\alpha kT}]^{\frac{1}{2}} \exp\{-[\frac{\lambda\alpha^3}{kTN(E)}]^{\frac{1}{4}}\} \quad (24)$$

Where σ is the dc conductivity which is function of temperature T; ν represent the hopping frequency, α is the inverse rate of the fall of the wave function and N(E) is the density of states (DOS) at the Fermi level [181], e denotes the electronic charge, k Boltzmann's constant and λ is a dimensionless constant whose value is ≈18.1. Recently many journals have reported the addition of various suitable substituent's in the PAni backbone [182-184]. The introducing of sulphonic acid (-SO_3Na), carboxylic groups (–COONa) and boronic acids (–BO_2H_2) at the phenyl rings and nitrogen sites are very cost effective for the doping to increase the conductivity of PAni. Doping of protonic acid is the unique property of PAni. But till now the derivation of the phenyl rings and nitrogen site in PAni at the atomic level on chemical and electronic properties are under research which can be used in practical applications. Varela-Álvarez *et al*. [185] reported that the changes of the chain length and number of monomers on the electronic properties of PAni. Wang *et al*. [186] evaluated the stability and electronic structure of HCl-protonated doped PAni and PAni-graphene composites. Romanova *et al*. [187] analysed interactions of PAni-water by introducing a polarisable continuum model by computational method.

Various Applications of PAni

PAni has dynamic evolution of applications in various fields. Followed by protonation and oxidation processes, PAni control its electronic structure and properties. Doping/dedoping process occurs in the presence of protonic acids as discussed above and keep the electrons number unchanged. An

unique electrochemical component is observed in PAni, in addition to redox doping. PAni is easy to synthesize and shows high stability in environment. An intrinsic conductivity is present in Polyaniline and has the ability to transform conducting to semiconducting form and finally dielectric form. The important application is discussed below:

Supercapacitor

This application is the trending one in the field of conducting polymer. It has high power and long stability. They are able to store energy much more than the normal traditional capacitors because the surface area of the electrodes are large enough with less distance between two charged layers. They are categorized into two main types: electrostatic double-layer supercapacitor (EDLC) and pseudocapacitor. In the conductive polymer electrolyte (conducting Polyaniline), EDLC stores the electrical energy by electrostatic adsorption and desorption of ions. In case of conducting polymer pseudocapacitors, the energy is stored, when the polymers are in doped state, inserting/extracting the electrolyte ions from the polymer's backbone. During the charging process the polycations attract the anions in the electrolyte to intercalate into the polymer backbone for electroneutrability. Usually, supercapacitors have lower energy density than batteries. More research are undergoing to improve supercapacitors and realizing the ideal case like high power and energy density, long stability etc. PAni based electrodes have high stability, high conductivity and power density and improved flexibility. Previous reports proposed that Pristine PAni electrode has high specific capacitance around 600 F g^{-1} in aqueous electrolyte due to its good pseudo capacitive properties [188, 189]. Wang Kai and co-workers reported that pure PAni with unique specialized structure rolled as an active material for supercapacitor, induces high capacitance of 950 Fg^{-1} by electrochemical polymerization method. Structure properties of PAni is highly responsible for excellent electrochemical performance. Incorporated carbon materials with PAni improves the properties of supercapacitor. It improves the properties due to its high stability, better conductivity and large surface to volume ratio. Many works reported that progress on PAni/Graphene by reducing GO to reduced-graphene-oxide (rGO) in order to enhance the conductivity.

Lithium-Ion Batteries (LIB)

Among secondary batteries, LIB is one of the rechargeable batteries, which is being developed day by day. These types of batteries are used in electronic devices owning to their high energy density, good security, and

long stability and long cycling life. Having higher energy density than supercapacitor LIB is used in potable electronics, electric vehicles and power grid applications. In electrochemical reaction, Li^+ ions transfer from the negative electrode via an electrolyte which allows for ionic movement to the positive electrode during discharge. Some Commercial LIB based cathodes are $LiCoO_2$, $LiFePO_4$, $LiMn_2O_4$ and $Li(Ni_{1/3}Co_{1/3}Mn_{1/3})O_2$ based materials as the cathodes for LIBs. These cathodes have very poor conductivity, inferior rate capability, short lifetime and voltage decay [190]. PAni is an excellent and promising material to make surface modification of these Li-based cathode materials, resulting by improved conductivity, long lifetime and stability [191]. Many research proved that PAni and PAni derived carbon materials are the promising cathode and anode for LIB's. Measurements of charge-discharge build up good capacity and long life cycling of the Li/PAni rechargeable cells which is demonstrated with the nano-structured doped PAni as the cathode., after which, the charge-discharge curves became steady and showed good reversibility with a discharge-plateau voltage of 3.0 V and a charge-plateau voltage of 3.4 V after the PAni electrode undergoes an induction process from unstable state to stable state. The reaction of Li/PAni batteries can be written as [192]:

$$\text{emaraldine base} + 2LiClO_4 \leftrightarrow 2Li + \text{emeraldine salt}$$

Now a days PAni doped graphite has attract our attention for commercially popular anode electrode, which has excellent properties like flat and low working potential, good cycling stability etc. It acquires the capacity of about 372 $mAhg^{-1}$. Increasing demands of energy density could not meet due to the limited diffusion rate of lithium into carbon materials. For these disadvantages, the anode materials are developed into three different types:

a) Intercalation layer-structured materials.
b) Alloy materials such as Si, Sn and SnO_2.
c) Conversion materials like transition metal oxides (Mn_xO_y, Fe_xO_y), metal sulphides (MoS_2) [193]

Li based cathode materials are being used to fabricate PAni modified electrodes for LIB's [194-196]. Karima Ferchichi *et al.* reported that the PAni/$LiCoO_2$ composite enhanced specific capacity of the pristine $LiCoO_2$ cathode from 136 $mAhg^{-1}$ to 167 $mAhg^{-1}$ by increment of the reaction reversibility and electronic conductivity by enhancing the mass ratio of $LiCoO_2$ to 4:1 in the composite. The conductivity of the PAni depends on the type of inorganic acid dopants. Cathodes like C-LFP/PAni composite which

is doped with HCl and H_3PO_4 gives a ca. 15% capacity increment at 0.2 C and 40% enhancement at 5 C compared to pure C-LFP, whereas H_2SO_4 is not a good dopant [197]. Dopant like polyethylene glycol (PEG) is used in PAni for modifying the performance of $LiFePO_4$, which is reported by Chunli Gong *et al.* [198]. PAni is also used as anode material for LIB's. Transition metal oxides like NiO, TiO_2, SnO_2 and Fe_2O_3 and metal sulphides like SnS_2, MoS_2 are used for fabricating anode material for LIB's [199-202]. An enhanced conductivity and stability can be obtained in NiO/PAni nanocomposite by connecting the NiO flakes and isolating them from electrolyte solution. Thus better reversibility is observed because of weaker polarization, better cycling process and discharge capacitance. The specific capacity of NiO/PAni nanocomposite is much better than pure NiO [203]. SnO2 is one of the promising LIB anode, because of its abundant theoretical specific capacity of about 891mAhg^{-1}. This is low cost, chemically stable environmental friendliness. But it has also some disadvantages occurs during lithiation and di-lithiation. So, PAni/SnO_2-Fe_2O_3 nanocomposite is prepared to overcome this problem [204].

Lithium Sulphur Batteries (LSBs)

In LSBs, lithium metal is used as anode and sulphur is used as cathode. These are rechargeable batteries with high specific energy (2600 Wh kg^{-1}), high specific capacitance (C_{th} = 1672 mAhg^{-1}), light weight, high abundance and low cost. During charge/discharge, low conductivity, low stability due to high solubility of intermediates (polysulfides Li_2S_x) in organic electrolyte and the large volume change are the main problems of these kinds of batteries. In order to neutralize these kinds of disadvantages, PAni is an ideal coating material with porous structure, low solubility in organic electrolyte and high flexibility to encapsulate sulphur in PAni matrix. When sulphur is incorporated in PAni matrix, PAni act as conductive shell. Ternary PAni@C/S nanocomposite sample is a perfect choice for the fabrication of LSBs, which has excellent electrochemical performance. Carbon nanotubes has high conductivity, good chemical and mechanical stability. PAni act as shell of sulphur coating of CNTs, which results in high capacity of sulphur. PAni shell was synthesized through an in-situ chemical oxidation resulting in high capacity, better rate capability and good cycling stability. Graphene oxide (GO) has2D structure and high specific surface area could also be used to cover PAni and sulphur. To enhance the stability the functional groups absorb polysulphides on the grapheme surface. Researcher reported that PAni coated sulphur shows high and stable capacity of 765 mAhg^{-1} [205]. To enhance the conductivity, bypiramidal structural sulphur is coated with PAni

and wrapped up with GO sheets. For enhancing the conductivity by carbon black is connected with S particles together, while the PAni shell could be an excellent sulphur host for high capacity.

Sodium-Ion Batteries (SIBs)

SIB is rechargeable batteries which has been developed for low cost and generous of Na salts. Here the energy storage of sodium ions behaves as Li ions. Recently several research groups has been developed suitable anodes based on PAni, with better electrochemical performance. To prepare advanced carbon anode for SIB, PAni is used as a precursor material. Hollow carbon nanowires (HCNWs) which was derived by pyrolization process from hollow PAni nanowire precursor, reported by Liu Jun *et al*. [206]. These structure of carbon nanowire is suitable for SIB anode due to its high conductivity and chemical/mechanical stability. Good electrochemical performance is observed in HCNWs, which is derived from PAni, with a high reversibility of 251 $mAhg^{-1}$ at 50 mAg^{-1} and good cycling stability over 400 cycles. For fabricating N-doped carbon materials with unique structures, PAni is used with nitrogen species. Cellulose is a good carbon materials for preparing electrodes for energy storage. Lina *et al*. and co-workers prepared N,S co-doped anode from cellulose and PAni microspheres [207]. In PS-PAni/rGO nanostructured hybrid materials PAni is used as SIB anode. Here Polystyrene (PS) is used as basic material for deposition of PAni. The spherical structure of PS with high surface area allows good dispersion of PAni and incorporating rGO enhance the stability of high capacity upto 155 $mAhg^{-1}$ and long-life time of 150 charge-discharge. In many hybrid anode system, PAni is widely used as coating layer material, including PAni/transition metal oxide. Zhan Xingxing and their co-workers reported that SnO2@PANi anode exhibits long cycle life and excellent rate performance [208]. The SnO_2@PAni composite gives high reversible capacity of 213.5 $mAhg^{-1}$ (after 400 cycles at 300 mAg^{-1}), than bare SnO_2particle anode with capacity of 14.4 $mAhg^{-1}$. The unique hollow structure and the PAni buffer layer decreases the pulverization of SnO_2 and agglomeration of the Sn particles during the discharge and charge process.

Chemical Sensor

A sensor is a kind of device by which an input parameter like, temperature, humidity, biological is converted into a measured signal. This output signal is based on optical and electrical properties. These types of sensor show reversible changes in conductivity, color and volume, which is suitable for sensing. But there is some disadvantage in these sensors, i.e. they

absorb organic compounds and moisture present in the environmental air and as a result they become unstable, low selectivity and low stability. These disadvantages are to be improved by tailoring their properties [209, 210]. CP sensors have been realized by exploiting conductometric, potentiometric, amperometric, voltammetric, gravimetric, pH-based, and incorporated-receptor-based sensing modes. Chemical sensor based on both amperometric and conductometric modes is reported by Forzani *et al.* [211]. PAni is used as dual mode sensor which is used to detect and analyze through individual changes in electrochemical current and conductance of the polymer. These sensor shows improved selectivity for the detection of the target. Many research are on going in developing metal/CP nanocomposites for selective chemical sensors. Pd/PAni nanocomposite which is used as selective methanol sensor, is reported by Athawale *et al*. [212]. The graphene/PAni film which contains numerous interfacial contacts between the highly conductive graphene and the semi conductive graphene, which provided unique anisotropic properties. Interestingly, the series connection-like configuration exhibited better sensing performance, particularly in terms of sensitivity. Due to its flexible, low-cost, and environmentally friendly properties, these fascinating studies on hybrid carbon nanomaterials and CPs provides excellent opportunities for sensors of next generation.

Fuel Cells

Metal electrocatalyst is supported by conducting polymers to enhance the conductivity, activity and stability. Among the conducting polymers, PAni supports as metal electrocatalyst due to its high flexibility and controllable morphologies. One of the suitable alternative sources of energy compared to fossil fuels is Hydrogen Evolution Reaction (HER) as it is derived from non-fossil sources [213]. Among the metal catalyst MoS2 shows excellent performance for HER. Except for MoS_2, Ni and Ni-Mo form composite with PAni matrix were also studied as surpassingly stable and catalytic systems. Moreover the synergistic effect of PAni between multiwall carbon nanotubes, electrocatalyst nanoparticles promote the electrical conductivity and stability. The CoFe2O4/PANi-MWCNT hybrid shows excellent activities and remarkably better durability which is much better than the $CoFe_2O_4$/MWCNT nanocomposite and pure $CoFe_2O_4$ NPs, indicating that the reaction sites of the electrode increased in the presence of PAni. PAni proved as a good supporter for Pt catalyst in methanol oxidation. Researcher investigated that PAni/CB/Pt nanocomposites plays a role of catalyst where CB has great importance in improving the polymeric degree and lower the defect density in the PAni backbone, leading to higher

catalytic activity due to exposure of more active sites and a faster charge transfer at the electrode/electrolyte interface due to enhanced conductivity. PAni is used to protect Pt/C catalysts as a conductive layer. Pt nanoparticles are used as anode and cathode material. The π conjugated structure of PAni leads to good environmental stability, high electrical conductivity in acidic environments. New design and synthesis process suggest the activity and durability issue of Pt/C@PAni core shell. Further Pt, PAni-decorated catalysts, including iron carbide, iron nitride, and manganese-based catalysts are found in various literature [214, 215]. VrGO nanosheets can cause mass transport and electron transport, but incorporating PAni with VrGO nanosheets not only enhance the conductivity, but also protect rGO from restacking and acidic environmental corrosion. When PAni act as an nitrogen containing carbon precursor, porous carbon materials in supercapacitor and battery application are fabricated. PAni derived N-doped porous carbon materials as an advanced catalyst support. Further it is recognized that co-doping of the transition metals can enhance the performance of metal free heteroatom doped carbon catalysts. Although, PAni plays an important role since it contributes N sites [216].

Visible Color Change of Polyaniline

The color change of conducting polymers is caused by doping/ de-doping process which is mediated by oxidation/reduction process. Reversible redox process usually effect the color changes of the polymer, this color change is called electrochromism. This is very important and interesting property of conducting polymers. These are very attractive properties for the application in various display devices such as electrochromic display, rear view mirror etc [217]. The energy gap of the conducting polymers and the dopants are responsible for the color change phenomenon. The ions are inserted into the conducting polymers by doping or de-doping process, this is the mechanism by which electrochromism happens. Due to doping process, the reorganization of the electronic structure takes place, and thus decreases the energy band gap of π-π^* transition. In case of pure conducting polymers the band gap is around 1.5 eV, thus strongly absorbs the visible light and high contrast colors are produced. But, the doped state of the polymer absorbs light of the near infrared region. Various redox states has various color of the conducting polymers.

Here in our discussions PAni is displayed to show the color change in various medium such as in acid, salt, organic-inorganic medium. Insertion of anions and the protonation-deprotonation process of PAni are reported by

many researchers. PAni changes color from transparent yellow to light blue, violet and finally dark greenish. That's why the absorption spectra of the PAni move to the visible region to near infrared region. This color changing property of the PAni depends on the redox property, chemical structure, reaction temperature, pH of the solution etc [218]. Speed of the magnetic stirrer and migration of the dopants with the polymer matrix causes the switching of the color change of PAni. The microstructural properties of the conducting polymers such as porosity can be controlled to enhance the color changing property [219].

Conclusions

The molecular structure, electron transport phenomenon in conducting polymers and its effect on charge transport due to doping was briefly reviewed in this article. The structure of PAni and its protonation/deprotonation scheme show that PAni is highly conducting and has high semiconducting properties. The steps of the synthesis process and the formation mechanism of dimer and tetramer finally results in construction of PAni. They form three resonance structure of the PAni which displays the inductive effect in the absence of steric hindrance. VRH theory and CELT model of the conductivity of conducting polymers are described briefly which shows the 3D delocalized states of polymers and mechanism process of conductivity respectively. From the CELT model, we get the concept of protonation induced intrachain coupling. Low band gap of the Undoped PAni by designing the chemical structure can increase the conductivity. Emeraldine base can transform emeraldine salt by doping HCl acid which causes the increment in conductivity. It is concluded that dopants generate polaron and bipolaron which carry electricity and increases the conductivity of the doped material. The HOMO-LUMO energy levels of conjugated polymers measure the oxidation and reduction potentials. HOMO-LUMO energy levels enhance the charge carriers to increase the efficiency of device fabrication. Photo induced absorption of conducting polymers (PAni) is also discussed in this context and we get the concepts of polaron, bipolarons from this. The charge distribution of the defects states are more Charge transport mechanism of solitons, polarons and bipolarons were observed in conducting polymers. Self-organization process explains the process of increasing the conductivity. High level of conductivity can be obtained by doping. Doping of conducting polymers causes drastic changes in electronic, electrical, magnetic, optical etc. properties. After doping the conductivity increases by about 6 fold to 9 fold. Besides, it is also concluded that at high doping level conductivity of PAni decreases due to the formation

and delocalization of polarons. Moreover, the energy storage application of PAni proves high stability and capacity, better conductivity when incorporating/doping it with metal or semiconductor, compared for better properties than pristine conducting PAni.

Conflicts of Interest

There are no conflicts to declare.

Acknowledgements

We are grateful to Indian Institute of Technology (Indian School of Mines), Dhanbad for financial support.

References

1. Maciulis, V.; Malinovskis, U.; Erts, D.; Ramanavicius, A.; Ramanaviciene, A.; Balevicius, S.; Juciute, S.; Plikusiene, I. Coatings, 10, 1018(2020).
2. Plikusiene, I.; Maciulis, V.; Graniel, O.; Bechelany, M.; Balevicius, S.; Vertelis, V.; Balevicius, Z.; Popov, A.; Ramanavicius, A.; Ramanaviciene, A. J. Mater. Chem. C, 9, 1345–1352(2021).
3. Filipovic, L.; Selberherr, S. Nanomaterials, 12, 3651(2022).
4. Maduraiveeran, G.; Jin, W. Mater. Sci. Engineer. B, 272, 115341(2021).
5. Heard, C.J.; Cˇ ejka, J.; Opanasenko, M.; Nachtigall, P.; Centi, G.; Perathoner, S. Adv. Mater., 31, 1801712(2019).
6. Wang, L.; Huang, L.; Tan, W.C.; Feng, X.; Chen, L.; Huang, X.; Ang, K.W. Small Methods, 2, 1700294(2018).
7. Kumar, S.; Pavelyev, V.; Mishra, P.; Tripathi, N.; Sharma, P.; Calle, F. Mater. Sci. Semicond. Process.,107, 104865(2020).
8. Jang, J.M.; Kim, S.D.; Choi, H.M.; Kim, J.Y.; Jung, W.G. Mater. Chem. Phys. , 113, 389–394(2009).
9. Chiu, H.Y.;Wi-Afedzi, T.; Liu, Y.T.; Ghanbari, F.; Lin, K.Y.A. J. Water Process Eng., 37, 101379(2020).
10. Yang, Z.; Lin, Y.; Jiao, F.; Li, J.; Wang,W.; Gong, Y.; Jing, X. Appl. Surf. Sci., 502, 144147(2020).
11. Tiwari, J.N.; Tiwari, R.N.; Kim, K.S. Prog. Mater. Sci., 57, 724–803(2012).

12. Nunes D, Pimentel A, Goncalves A, Pereira S, Branquinho R, Barquinha P, Fortunato E, Martins R Semicond Sci Technol, 34(4), 43001(2019).
13. Kumar S, Bukkitgar SD, Singh S, Singh V, Reddy KR, Shetti NP, Venkata Reddy C, Sadhu V, Naveen S, Chemistry Select, 4(18), 5322 (2019).
14. Palumbo G, Doyle D M, El-Sherik A M, Erb U and Aust K T Scr. Metall. Mater. 25, 679(1991).
15. Bakonyi I, Toth-Kada E, Tarnoczi T, Varga L K, Cziraki A, Gerocs I and Fogarassy B Nanostruct. Mater. 3, 155(1993).
16. Kyaw, H.H.; Al-Harthi, S.H.; Sellai, A.; Dutta, J. Beilstein J. Nanotechnol. 6, 2345(2015).
17. Ahmadzadeh-Raji, M.; Ghafar-Zadeh, E.; Amoabediny, G. , Sensors, 16, 1071(2016).
18. Khlyustova A., Cheng Y. and Yang R. J. Mater. Chem. B, 8, 6588(2020).
19. Ozaydin-Ince G., Dubach J. M., Gleason K. K. and Clark H. A. PANS. 108, 2656(2011).
20. Chan K. and Gleason K. K. Langmuir, 21, 11773(2005).
21. Dorval Dion C. A., Raphael W., Tong E. and Tavares J. R. Surf. Coat. Tech. 244, 98(2014).
22. Baxamusa S. H., Montero L., Dubach J. M., Clark H. A., Borros S. and Gleason K. K. Biomacromolecules, 9, 2857(2008).
23. Tiwari J.N., Tiwari R.N., Kim K.S. Prog. Mater. Sci., 57, 724(2012).
24. Joshi R.K., Schneider J.J. Chem. Soc. Rev. ;41, 5285(2012).
25. Young C., Wang J., Kim J., Sugahara Y., Henzie J., Yamauchi Y. Chem. Mater. ;30, 3379(2018).
26. Altintas Yildirim O. Mater. Sci. Semicond. Process. ;101, 238(2019).
27. Pei Y., Hu M., Xia Y., Huang W., Li Z., Chen S. Sens. Actuators B Chem. ;304, 127416(2020).
28. Soganci, T., Ayranci, R., Harputlu, E., Ocakoglu, K., Acet, M., Farle, M., ... & Ak, M. Sens Actuators B, 273, 1501(2018).

29. Han, S.T., Peng, H., Sun, Q., Venkatesh, S., Chung, K.S., Lau, S.C., Zh ou, Y., and Roy, V.A.L.: Adv. Mater. 29, 1700375 (2017).

30. Zhang, D., Zhang, K., Yao, Y.L., Xia, X.H., and Chen, H.Y.: Langmuir 20, 7303 (2004).

31. Choi, T., Kim, S.H., Lee, C.W., Kim, H., Choi, S-K., Kim, S-H., Kim, E., Park, J., and Kim, H.: 63, 325 (2015).

32. Ripka, P. and Janosek, M.: IEEE Sens. J. 10, 1108 (2010).

33. Lee, B., Roh, S., and Park, J.: Opt. Fiber Technol. 15, 209 (2009).

34. Hill, E.W., Vijayaragahvan, A., and Novoselov, K.: IEEE Sens. J. 11, 3161 (2011).

35. Tereshchenko, A., Fedorenko, V., Smyntyna, V., Konup, I., Konup, A., Eriksson, M., Yakimova, R., Ramanavicius, A., Balme, S., and Bechelany, M.: Biosens.Bioelectron. 92, 763 (2017).

36. Dominik, M., Lesniewski, A., Janczuk, M., NiedziolkaJoensson, J., Holdynski, M., Wachnicki, L., Godlewski, M., Bock, W.J., and Smietana, M.: Biosens. Bioelectron. 93, 102 (2017).

37. Comstock, D.J., Christensen, S.T., Elam, J.W., Pellin, M.J., and Hersam, M.C.: Adv. Funct. Mater. 20, 3099 (2010).

38. Fryčeka, R.; Jelínek, M.; Kocourek, T.; Fitl, P.; Vrňata, M.; Myslík, V.; Vrbová, M. Thin Solid Films , 495, 308(2006).

39. Houser, E.J.; Chrisey, D.B.; Bercu, M.; Scarisoreanu, N.D.; Purice, A.; Colceag, D.; Constantinescu, C.; Moldovan, A.; Dinescu, M. Appl. Surf. Sci., 252, 4871(2006).

40. Bloisi, F.; Vicari, L.; Papa, R.; Califano, V.; Pedrazzani, R.; Bontempi, E.; Depero, L.E. Mater. Sci. Eng. C , 27, 1185(2007).

41. Cristescu, R.; Mihaiescu, D.; Socol, G.; Stamatin, I.; Mihailescu, I.N.; Chrisey, D.B. Appl. Phys. A , 79, 1023(2004).

42. Stamatin, L.; Cristescu, R.; Socol, G.; Moldovan, A.; Mihaiescu, D.; Stamatin, I.; Mihailescu, I.N.; Chrisey, D.B. Appl. Surf. Sci. , 248, 422(2005).

43. Trojanowicz, M. Electrochem. Comm., 38, 47(2014).

44. Nasratun, M.; Said, H.A.; Noraziah, A.; Alla, A.N.A. Am. J. Appl. Sci., 6, 1653(2009).

45. György, E., Sima, F., Mihailescu, I. N., Smausz, T., Hopp, B., Predoi, D., ... & Petrescu, S. M. Mater. Sci. Eng. C, 30(4), 537(2010).
46. Aronne, A., Bloisi, F., Calabria, R., Califano, V., Depero, L. E., Fanelli, E., ... & Vicari, L. R. Appl. Surf. Sci., 336, 196(2015).
47. Caruso, F. Adv. Mater., 13(1), 11(2001).
48. Pandey, P., Datta, M., & Malhotra, B. D. Anal. Lett, 41(2), 159(2008).
49. Gupta, A. K., & Gupta, M. biomaterials, 26(18), 3995(2005).
50. Zhang, G., Liu, H., Qu, J., & Li, J. Energy Environ. Sci., 9(4), 1190(2016).
51. He, Q.; Zeng, Z.; Yin, Z.; Li, H.; Wu, S.; Huang, X.; Zhang, H. Small, 8, 2994(2012).
52. Lin, Y. C.; Dumcenco, D. O.; Huang, Y. S.; Suenaga, K. Nat. Nanotechnol., 9, 391(2014).
53. Zhang, D., Jiang, C., Li, P., & Sun, Y. E. ACS Appl. Mater. Interfaces., 9(7), 6462(2017).
54. Mutalik, C., Krisnawati, D. I., Patil, S. B., Khafid, M., Atmojo, D. S., Santoso, P., ... & Kuo, T. R. ACS Sustain. Chem. Eng., 9(23), 7904(2021).
55. Dong, H., Tang, S., Hao, Y., Yu, H., Dai, W., Zhao, G., ... & Ju, H. ACS Appl. Mater. Interfaces., 8(5), 3107(2016).
56. Wang, Y., & Ni, Y. Analytical chemistry, 86(15), 7463(2014).
57. Liu, T., Chao, Y., Gao, M., Liang, C., Chen, Q., Song, G., ... & Liu, Z. Nano Research, 9, 3003(2016).
58. Chao, J., Zou, M., Zhang, C., Sun, H., Pan, D., Pei, H., ... & Wang, L. Nanotechnology, 26(27), 274005(2015).
59. Wang, X., Chu, C., Shen, L., Deng, W., Yan, M., Ge, S., & Song, X. Sens Actuators B Chem, 206, 30(2015).
60. Ling, Y., Cao, T., Liu, L., Xu, J., Zheng, J., Li, J., & Zhang, M. J. Mater. Chem. B, 8(34), 7801(2020).
61. Zheng, J., Song, D., Chen, H., Xu, J., Alharbi, N. S., Hayat, T., & Zhang, M. Chin. Chem. Lett., 31(5), 1109(2020).
62. Wang, C., Du, J., Wang, H., Zou, C. E., Jiang, F., Yang, P., & Du, Y. Sens Actuators B Chem, 204, 302(2014).

63. Huang, M., Liu, C., Cui, P., Wu, T., Feng, X., Huang, H., & Wang, Y. Environ. Sci. Technol., 55(19), 13132(2021).

64. Qin, Z., Yue, Q., Liang, Y., Zhang, J., Zhou, L., Hidalgo, O. B., & Liu, X. J. Biotech., 284, 52(2018).

65. Wu, Q., Huang, L., Li, Z., An, W., Liu, D., Lin, J., & Wu, W. Nanoscale Res. Lett., 11, 1(2016).

66. Dabhane, H., Ghotekar, S., Tambade, P., Pansambal, S., Murthy, H. A., Oza, R., & Medhane, V. J. Environ. Chem. Ecotoxicol., 3, 209(2021).

67. Shivaji, K., Mani, S., Ponmurugan, P., De Castro, C. S., Lloyd Davies, M., Balasubramanian, M. G., & Pitchaimuthu, S. ACS Appl. Nano Mater., 1(4), 1683(2018).

68. Bharti, D. B., Bharati, A. V., & Wankhade, A. V. Luminescence, 33(8), 1445(2018).

69. Zucolotto, V. (2020). Specialty grand challenges in biosensors. Frontiers in Sensors, 1,

70. Ali, M. A.; Saion, E.; Yahya, N.; Kassim, A.; Dahlan, K. M.; and Hashim, S. (2007). Synthesis of Conducting Polyaniline Nanocomposites by Radiation Doping, Journal of Engineering Science and Technology, 2(1), 111-118.

71. Bitencourt, A. S.; Barros, U.; Maria, C. C.; and Leite, D. S. (2012). Multilayer Films Electrodes Consisted of Cashew Gum and Polyaniline Assembled by the Layer-by-Layer Technique, International Journal of Analytical Chemistry, 116, 1567-1577.

72. Catedral, M. D.; Tapia, A. K. G.; Sarmago, R. V.; Tamayo, J. P.; and del-Rosario, E. J. (2004). Effect of Dopant Ions on the Electrical Conductivity and Microstructure of Polyaniline (Emeraldine Salt), Journal of Science Diliman, 16(2), 41–46.

73. Da-Silva, J. E. P.; and Temperini, M. L. A.; and de-Torresi, S. I. C. (2005). Characterization of Conducting Polyaniline Blends by Resonance Raman Spectroscopy, J. Braz. Chem. Soc.,16(3A), 322-327.

74. Le, T. H., Kim, Y., & Yoon, H. (2017). Electrical and electrochemical properties of conducting polymers. Polymers, 9(4), 150.

75. G. Inzelt, Conducting polymers-A new era in electrochemistry, 2nd edn. In: F. Scholz (ed) Monographs in electrochemistry, Springer, Heidelberg, Berlin, Germany, 2012.

76. G. Inzelt, Charge transport in polymer modified electrodes, Encyclopedia of Electrochemistry, A.J. Bard, M. Stratmann (eds.) Functions and applications of modified electrodes Vol. 10, I. Rubinstein, J. Rusling, M. Fujihara (eds.), Weinheim, Wiley-VCH, 2007. Ch. 9, pp. 651-683.

77. Yi, N., &Abidian, M. R. (2016). Conducting polymers and their biomedical applications. In Biosynthetic Polymers for Medical Applications (pp. 243-276). Woodhead Publishing.

78. G. Inzelt, M. Pineri, J.W. Schultze, M.A. Vorotyntsev, Electrochimica Acta 45 (2000): 2403-2421

79. G. Inzelt, E. Csahok,V. Kertész, ElectrochimicaActa 46 (2001) 3955-3962.

80. E. Csahók, E. Vieil, G. Inzelt, Journal of Electroanalytical Chemistry 482 (2000) 168-177.

81. Shinde, S., &Kher, J. (2014). A Review on Polyaniline and Its Noble Metal Composites. Int. J. Innovative Res. Sci. Eng. Technol, 3, 16570-16576.

82. Kuzmany, H., Mehring, M., & Roth, S. (Eds.). (2012). Electronic Properties of Polymers and Related Compounds: Proceedings of an International Winter School, Kirchberg, Tirol, and February 23-March 1, 1985 (Vol. 63). Springer Science & Business Media.

83. Inzelt, G. (2008). Historical Background (Or: There Is Nothing New Under the Sun). Conducting Polymers: A New Era in Electrochemistry, 265-269.

84. Naarmann, H. (2000). Polymers, electrically conducting. Ullmann's Encyclopedia of Industrial Chemistry.

85. Cs. Visy, In situ combined electrochemical techniques for conducting polymers, Springer, Berlin, Heidelberg, 2017.

86. Kuzmany, H., Mehring, M., & Roth, S. (Eds.). (2012). Electronic Properties of Polymers: Orientation and Dimensionality of Conjugated Systems Proceedings of the International Winter School, Kirchberg, (Tyrol) Austria, March 9–16, 1991 (Vol. 107). Springer Science & Business Media.

87. Cheng, C. H., & Lonergan, M. C. (2004). A conjugated polymer pn junction. Journal of the American Chemical Society, 126(34), 10536-10537.

88. Boeva, Z. A., &Sergeyev, V. G. (2014). Polyaniline: Synthesis, properties, and application. Polymer Science Series C, 56(1), 144-153.

89. Chen, W., Rakhi, R. B., &Alshareef, H. N. (2013). Facile synthesis of polyaniline nanotubes using reactive oxide templates for high energy density pseudocapacitors. Journal of Materials Chemistry A, 1(10), 3315-3324.

90. Eftekhari, A. (Ed.). (2011). Nanostructured conductive polymers. John Wiley & Sons.

91. Guo, J., Guan, L., Wei, H., Khan, M. A., Zhang, X., Li, B., ...& Wei, S. (2016). Enhanced negative magnetoresistance with high sensitivity of polyaniline interfaced with nanotitania. Journal of The Electrochemical Society, 163(8), H664-H671.

92. Ravichandran, R., Sundarrajan, S., Venugopal, J. R., Mukherjee, S., & Ramakrishna, S. (2010). Applications of conducting polymers and their issues in biomedical engineering. Journal of the Royal Society Interface, 7(suppl_5), S559-S579.

93. Kim, Y., Le, T. H., Kim, S., Park, G., Yang, K. S., & Yoon, H. (2018). Single-walled carbon nanotube-in-binary-polymer nanofiber structures and their use as carbon precursors for electrochemical applications. The Journal of Physical Chemistry C, 122(8), 4189-4198.

94. Angelopoulos, M. (2001). Conducting polymers in microelectronics. IBM Journal of Research and Development, 45(1), 57-75.

95. Ivanov, S., Mokreva, P., Tsakova, V., &Terlemezyan, L. (2003). Electrochemical and surface structural characterization of chemically and electrochemically synthesized polyaniline coatings. Thin Solid Films, 441(1-2), 44-49.

96. Surwade, S. P. (2010). Synthesis of nanostructured polyaniline. University of Massachusetts Lowell.

97. Razak, A., Izwan, S., Wahab, I. F., Fadil, F., Dahli, F. N., Khudzari, M., ...&Adeli, H. (2015). A review of electrospun conductive polyaniline based nanofiber composites and blends: processing features, applications, and future directions. Advances in Materials Science and Engineering, 2015.

98. Owusu-Sekyere, K., Nkrumah, I., Nkum, R. K., & Singh, K. (2016). A Study of Optical Absorption of Polyanline thin films prepared by

Chemical Bath Deposition (CBD) Method. International Journal of Advanced Research in Engineering and Technology, 7(2).

99. Ma, Q., Wang, J., Dong, X., Yu, W., & Liu, G. (2015). Flexible ribbon-shaped coaxial electrical conductive nanocable array endowed with magnetism and photoluminescence. RSC Advances, 5(4), 2523-2530.

100. Hou, J., Tan, Z. A., Yan, Y., He, Y., Yang, C., & Li, Y. (2006). Synthesis and photovoltaic properties of two-dimensional conjugated polythiophenes with bi (thienylenevinylene) side chains. Journal of the American Chemical Society, 128(14), 4911-4916.

101. Chen, X., Yuan, C. A., Wong, C. K., Ye, H., Leung, S. Y., & Zhang, G. (2012). Molecular modeling of protonic acid doping of emeraldine base polyaniline for chemical sensors. Sensors and Actuators B: Chemical, 174, 210-216.

102. Gonzalez-Vazquez, J. P., Anta, J. A., &Bisquert, J. (2009). Random walk numerical simulation for hopping transport at finite carrier concentrations: diffusion coefficient and transport energy concept. Physical Chemistry Chemical Physics, 11(44), 10359-10367.

103. Rahman, M. A., Kumar, P., Park, D. S., & Shim, Y. B. (2008). Electrochemical sensors based on organic conjugated polymers. Sensors, 8(1), 118-141.

104. Masdarolomoor, F., Innis, P. C., & Wallace, G. G. (2008). Electrochemical synthesis and characterisation of polyaniline/poly (2-methoxyaniline-5-sulfonic acid) composites. ElectrochimicaActa, 53(12), 4146-4155.

105. Arkhipov, V. I., &Bässler, H. (1993). A model of weak-field quasi-equilibrium hopping transport in disordered materials. Philosophical magazine letters, 67(5), 343-349.

106. Mansurova, S., Stepanov, S., Camacho-Pernas, V., Ramos-Garcia, R., Gallego-Gomez, F., Mecher, E., &Meerholz, K. (2004). Measurements of deviation from Einstein relation in PVK-based photorefractive polymers by photoelectromotive-force technique. Physical Review B, 69(19), 193203.

107. Baranovskii, S. D., Cordes, H., Hensel, F., &Leising, G. (2000). Charge-carrier transport in disordered organic solids. Physical Review B, 62(12), 7934.

108. Ćirić-Marjanović, G., Trchová, M., &Stejskal, J. (2008). Theoretical study of the oxidative polymerization of aniline with peroxydisulfate: Tetramer formation. International Journal of Quantum Chemistry, 108(2), 318-333.

109. Koval'chuk, E. P., Whittingham, S., Skolozdra, O. M., Zavalij, P. Y., Zavaliy, I. Y., Reshetnyak, O. V., &Seledets, M. (2001). Co-polymers of aniline and nitroanilines. Part I. Mechanism of aniline oxidation polycondensation. Materials chemistry and physics, 69(1-3), 154-162.

110. 1Aleshin, A. N., Suh, D. S., & Park, Y. W. (2001). The influence of low-energy excitations on the metallic conductivity of perchlorate doped polyacetylene. Physica B: Condensed Matter, 305(3-4), 197-202.

111. Arora, R., Mandal, U. K., Sharma, P., &Srivastav, A. (2015). TiO2 and PVA Based Polyaniline Composite Materials-A Review. Materials Today: Proceedings, 2(4-5), 2767-2775.

112. Deore, B. A., Yu, I., & Freund, M. S. (2004). A switchable self-doped polyaniline: interconversion between self-doped and non-self-doped forms. Journal of the American Chemical Society, 126(1), 52-53.

113. Jotiram, K. P., Prasad, R. G. S. V., Jakka, V. S., Aparna, R. S. L., &Phani, A. R. (2012). Antibacterial Activity of Nanostructured Polyaniline Combined With Mupirocin. Nano Biomedicine & Engineering, 4(3).

114. Wang, Z.L.; He, X.J.; Ye, S.H.; Tong, Y.X.; Li, G.R. Design of polypyrrole/polyaniline double-walled nanotubes arrays for electrochemical energy storage. ACS Appl. Mater. Interfaces 2014, 6, 642–647.

115. Silva, C. H., Iliut, M., Muryn, C., Berger, C., Coldrick, Z., Constantino, V. R., ...&Vijayaraghavan, A. (2018). Ternary nanocomposites of reduced graphene oxide, polyaniline and hexaniobate: hierarchical architecture and high polaron formation. Beilstein journal of nanotechnology, 9(1), 2936-2946.

116. Scotto, J., Florit, M. I., & Posadas, D. (2018). About the species formed during the electrochemical half oxidation of polyaniline: Polaron-bipolaron equilibrium. ElectrochimicaActa, 268, 187-194.

117. Scott, J. C. (2010). History of conductive polymers. Nanostructured conductive polymers, 1-17.

118. Wang, R. X., Huang, L. F., &Tian, X. Y. (2012). Understanding the protonation of polyaniline and polyaniline–graphene interaction. The Journal of Physical Chemistry C, 116(24), 13120-13126.

119. Bansal, V., Bhandari, H., Bansal, M. C., &Dhawan, S. K. (2009). Electrical and optical properties of poly (aniline-co-8-anilino-1-napthalene sulphonic acid)—A material for ESD applications.

120. Koval'chuk, E. P., Whittingham, S., Skolozdra, O. M., Zavalij, P. Y., Zavaliy, I. Y., Reshetnyak, O. V., &Seledets, M. (2001). Co-polymers of aniline and nitroanilines. Part I. Mechanism of aniline oxidation polycondensation. Materials chemistry and physics, 69(1-3), 154-162.

121. R. Sainz, A.M. Benito, M.J. Martinez, J.F. Galindo, J. Sotres, A.M. Bar´o, B. Corraze, O. Chauvet, A.B. Dalton, R.H. Baughman and W.K. Maser, Nanotech., 16 (2005) 150-154.

122. Gizdavic-Nikolaidis, M. R., Jevremovic, M., Stanisavljev, D. R., &Zujovic, Z. D. (2012). Enhanced microwave synthesis: Fine-tuning of polyaniline polymerization. The journal of physical chemistry C, 116(5), 3235-3241.

123. Michira, I., Akinyeye, R., Somerset, V., Klink, M. J., Sekota, M., Al-Ahmed, A., ...&Iwuoha, E. (2007, September). Synthesis, characterisation of novel polyaniline nanomaterials and application in amperometric biosensors. In Macromolecular symposia (Vol. 255, No. 1, pp. 57-69). Weinheim: WILEY-VCH Verlag.

124. Shimano, J. Y., & MacDiarmid, A. G. (2001). Polyaniline, a dynamic block copolymer: key to attaining its intrinsic conductivity? Synthetic Metals, 123(2), 251-262.

125. Kaiser, A. B. (2001). Electronic transport properties of conducting polymers and carbon nanotubes. Reports on Progress in Physics, 64(1), 1.

126. Lange U., Roznyatovskaya N. V., Vladimir M. Mirsky V. M. (2008). Conducting polymers in chemical sensors and arrays. AnalyticaChimicaActa614, 1-26.

127. Lee K., Cho S., Park S. H., Heeger A. J., Lee C. W., Lee S. H. (2006). Metallic transport in polyaniline. Nature 441, 65-68.

128. Varela-Álvarez, A., &Sordo, J. A. (2008). A suitable model for emeraldine salt. The Journal of chemical physics, 128(17), 174706.

129. Venkateshvaran, D., Nikolka, M., Sadhanala, A., Lemaur, V., Zelazny, M., Kepa, M., Romanov, I. (2014). Approaching disorder-free transport in high-mobility conjugated polymers. Nature, 515(7527), 384.

130. Noriega, R., Rivnay, J., Vandewal, K., Koch, F. P., Stingelin, N., Smith, P., Salleo, A. (2013). A general relationship between disorder, aggregation and charge transport in conjugated polymers. Nature materials, 12(11), 1038.

131. Bakhshi, A. K., &Bhalla, G. (2004). Electrically conducting polymers: Materials of the twentyfirst century.

132. Podzorov, V. (2013). Conjugated polymers: long and winding polymeric roads. Nature materials, 12(11), 947.

133. Deb, K., Bera, A., &Saha, B. (2016). Tuning of electrical and optical properties of polyaniline incorporated functional paper for flexible circuits through oxidative chemical polymerization. RSC Advances, 6(97), 94795-94802.

134. Lee, K., Cho, S., Park, S. H., Heeger, A. J., Lee, C. W., & Lee, S. H. (2006). Metallic transport in polyaniline. Nature, 441(7089), 65.

135. Stejskal, J., & Gilbert, R. G. (2002). Polyaniline. Preparation of a conducting polymer (IUPAC technical report). Pure and Applied Chemistry, 74(5), 857-867.

136. Varela-Álvarez, A., &Sordo, J. A. (2008). A suitable model for emeraldine salt. The Journal of chemical physics, 128(17), 174706.

137. Tran, H. D., Wang, Y., D'Arcy, J. M., &Kaner, R. B. (2008). Toward an understanding of the formation of conducting polymer nanofibers. ACS nano, 2(9), 1841-1848.

138. Baker, C. O., Shedd, B., Innis, P. C., Whitten, P. G., Spinks, G. M., Wallace, G. G., &Kaner, R. B. (2008). Monolithic actuators from flash-welded polyaniline nanofibers. Advanced Materials, 20(1), 155-158.

139. Nicolas-Debarnot, D., &Poncin-Epaillard, F. (2003). Polyaniline as a new sensitive layer for gas sensors. AnalyticaChimicaActa, 475(1-2), 1-15.

140. Wallace, G. G., Teasdale, P. R., Spinks, G. M., & Kane-Maguire, L. A. (2008). Conductive electroactive polymers: intelligent polymer systems. CRC press.

141. Barbero C., Salavagione H.J., Acevedo D.F., Grumelli D.E., Garay F., Planes G.A., Morales G.M., Miras M.C. (2004). Novel synthetic methods to produce functionalized conducting polymers I. Polyaniline. ElectrochimicaActa49, 3671-3686.

142. Basavaraja, C., Veeranagouda, Y., Lee, K., Pierson, R., & Huh, D. S. (2009). Surface characterization and electrical behaviour of polyaniline–polymannuronate nanocomposites. Journal of Polymer Science Part B: Polymer Physics, 47(1), 36-45.

143. Freitas, J. M., Duarte, M. L., Darbre, T., &Abrantes, L. M. (2005). Electrochemical synthesis of a novel conducting polymer: The poly [(3-pyrrolyl)-octanoic acid]. Synthetic metals, 155(3), 549-554.

144. Duic L.J., Grigic S. (2001). The effect of polyaniline morphology on hydroquinone/quinone redox reaction. ElectrochimicaActa46, 2795–2803.

145. Basavaraja, C., Kim, N. R., & Jo, E. A. (2010). Biological templating of polyaniline and polypyrrole using E. coli. Macromolecular research, 18(3), 222-226.

146. Chen, X., Yuan, C. A., Wong, C. K., Ye, H., Leung, S. Y., & Zhang, G. (2012). Molecular modeling of protonic acid doping of emeraldine base polyaniline for chemical sensors. Sensors and Actuators B: Chemical, 174, 210-216.

147. Chaudhuri, D., Kumar, A., Nirmala, R., Sarma, D. D., Garcia-Hernandez, M., Chandra, L. S., &Ganesan, V. (2006). Transport and magnetic properties of conducting polyaniline doped with B X 3 (X= F, Cl, and Br). Physical Review B, 73(7), 075205.

148. Varela-Álvarez, A., &Sordo, J. A. (2008). A suitable model for emeraldine salt. The Journal of chemical physics, 128(17), 174706.

149. Ramohlola, K. E., Monana, G. R., Hato, M. J., Modibane, K. D., Molapo, K. M., Masikini, M., ... &Iwuoha, E. I. (2018). Polyaniline-metal organic framework nanocomposite as an efficient electrocatalyst for hydrogen evolution reaction. Composites Part B: Engineering, 137, 129-139.

150. Ide, K., Nomura, K., Hosono, H., &Kamiya, T. (2019). Electronic Defects in Amorphous Oxide Semiconductors: A Review. physica status solidi (a), 216(5), 1800372.

151. Andričević, P., Mettan, X., Kollár, M., Náfrádi, B., Sienkiewicz, A., Garma, T., ...&Horváth, E. (2019). Light-Emitting Electrochemical Cells of Single Crystal Hybrid Halide Perovskite with Vertically Aligned Carbon Nanotubes Contacts. ACS Photonics.

152. Nollau, A., Pfeiffer, M., Fritz, T., & Leo, K. (2000). Controlled n-type doping of a molecular organic semiconductor: Naphthalenetetracarboxylicdianhydride (NTCDA) doped with bis (ethylenedithio)-tetrathiafulvalene (BEDT-TTF). Journal of Applied Physics, 87(9), 4340-4343.

153. Cheng, Y. J., Yang, S. H., & Hsu, C. S. (2009). Synthesis of conjugated polymers for organic solar cell applications. Chemical reviews, 109(11), 5868-5923.

154. Bajpai, M., Srivastava, R., Dhar, R., & Tiwari, R. S. (2016). Review on optical and electrical properties of conducting polymers. Indian Journal of Materials Science, 2016.

155. Kim, Y., Le, T. H., Kim, S., Park, G., Yang, K. S., & Yoon, H. (2018). Single-walled carbon nanotube-in-binary-polymer nanofiber structures and their use as carbon precursors for electrochemical applications. The Journal of Physical Chemistry C, 122(8), 4189-4198.

156. De Albuquerque, J. E., Mattoso, L. H. C., Faria, R. M., Masters, J. G., & MacDiarmid, A. G. (2004). Study of the interconversion of polyaniline oxidation states by optical absorption spectroscopy. Synthetic Metals, 146(1), 1-10.

157. Varga, M., Prokes, J., Bober, P., &Stejskal, J. (2012). Electrical conductivity of polyaniline-silver nanocomposites. In WDS (Vol. 12, pp. 52-57).

158. Khalid, M., Tumelero, M. A., Brandt, I., Zoldan, V. C., Acuña, J. J., &Pasa, A. A. (2013). Electrical conductivity studies of polyaniline nanotubes doped with different sulfonic acids. Indian Journal of Materials Science, 2013.

159. Colak, N., &Sökmen, B. (2000). Doping of chemically synthesized polyaniline. Designed monomers and polymers, 3(2), 181-189.

160. Kiattibutr, P., Tarachiwin, L., Ruangchuay, L., Sirivat, A., &Schwank, J. (2002). Electrical conductivity responses of polyaniline films to SO2–N2 mixtures: effect of dopant type and doping level. Reactive and functional polymers, 53(1), 29-37.

161. Dimitriev, O. P. (2004). Doping of polyaniline by transition metal salts: effect of metal cation on the film morphology. Synthetic metals, 142(1-3), 299-303.

162. Islam, S., Lakshmi, G. B. V. S., Siddiqui, A. M., Husain, M., &Zulfequar, M. (2013). Synthesis, electrical conductivity, and dielectric behavior of polyaniline/V2O5 composites. International Journal of Polymer Science, 2013.

163. Gal, Y. S., Jin, S. H., Lim, K. T., Kim, S. H., &Koh, K. (2005). Synthesis and electro-optical properties of self-doped ionic conjugated polymers: poly [2-ethynyl-N-(4-sulfobutyl) pyridiniumbetaine]. Current Applied Physics, 5(1), 38-42.

164. Park, H. S., Ko, S. J., Park, J. S., Kim, J. Y., & Song, H. K. (2013). Redox-active charge carriers of conducting polymers as a tuner of conductivity and its potential window. Scientific reports, 3, 2454.

165. Abdelhamid, M. E., O'Mullane, A. P., & Snook, G. A. (2015). Storing energy in plastics: a review on conducting polymers & their role in electrochemical energy storage. Rsc Advances, 5(15), 11611-11626.

166. Qi, W.; Zhang, X.; Wang, H. Self-assembled polymer nanocomposites for biomedical application. Curr. Opin. Colloid Interface Sci. 2018, 35, 36–41.

167. Pasela, B. R., Castillo, A. P., Simon, R., Pulido, M. T., Mana-ay, H., Abiquibil, M., ...&Taaca, K. L. (2019). Synthesis and Characterization of Acetic Acid-Doped Polyaniline and Polyaniline–Chitosan Composite. Biomimetics, 4(1), 15.

168. Zhang, Y., de Boer, B., &Blom, P. W. (2009). Controllable Molecular Doping and Charge Transport in Solution-Processed Polymer Semiconducting Layers. Advanced Functional Materials, 19(12), 1901-1905.

169. Zhang, Y., &Blom, P. W. (2011). Electron and hole transport in poly (fluorene-benzothiadiazole). Applied Physics Letters, 98(14), 143-504.

170. Bitencourt, A. S.; Barros, U.; Maria, C. C.; and Leite, D. S. (2012). Multilayer Films Electrodes Consisted ofCashew Gum and Polyaniline Assembled by the Layer-by-Layer Technique, International Journal of Analytical Chemistry, 116, 1567-1577.

171. Catedral, M. D.; Tapia, A. K. G.; Sarmago, R. V.; Tamayo, J. P.; and del-Rosario, E. J. (2004). Effect of Dopant Ions on the Electrical

Conductivity and Microstructure of Polyaniline (Emeraldine Salt), Journal of Science Diliman,16(2), 41–46.

172. West, A. R. (2014). Solid state chemistry and its applications. John Wiley & Sons.

173. Hdeshmukh, S.; Kburghate, D.; and Akare, V. P. (2007). Electrical conductivity of polyaniline doped PVC– PMMA polymer Blends, Journal of Mater. Sci., 30(1), 51–56.

174. Razak, A., Izwan, S., Wahab, I. F., Fadil, F., Dahli, F. N., Khudzari, M., Adeli, H. (2015). A review of electrospun conductive polyaniline-based nanofiber composites and blends: processing features, applications, and future directions. Advances in Materials Science and Engineering, 2015.

175. Heeger, A. J. (2011). Nobel Lecture: Semiconducting and metallic polymers: The fourth generation of polymeric materials. Reviews of Modern physics, 73(3), 681-699.

176. D.A.Khan,A. Akhtar and S. A. Nabi, (2015) Investigation of the electrical conductivity and optical property of polyanilinebased nanocomposite and its application as an ethanol vapor sensor, New J. Chem., , 39, 3728–3735.

177. Bhowmik, K. L., Deb, K., Bera, A., Nath, R. K., & Saha, B. (2016). Charge transport through polyaniline incorporated electrically conducting functional paper. The Journal of Physical Chemistry C, 120(11), 5855-5860.

178. Wallace, G. G., Teasdale, P. R., Spinks, G. M., & Kane-Maguire, L. A. (2008). Conductive electroactive polymers: intelligent polymer systems. CRC press.

179. Bhowmik, K. L., Deb, K., Bera, A., Nath, R. K., &Saha, B. (2016). Charge transport through polyaniline incorporated electrically conducting functional paper. The Journal of Physical Chemistry C, 120(11), 5855-5860.

180. Chen, X. P., Jiang, J. K., Liang, Q. H., Yang, N., Ye, H. Y., Cai, M., Ren, T. L. (2015). First-principles study of the effect of functional groups on polyaniline backbone. Scientific reports, 5, 16907.

181. Chiou, N. R., Lu, C., Guan, J., Lee, L. J., & Epstein, A. J. (2007). Growth and alignment of polyaniline nanofibres with superhydrophobic, superhydrophilic and other properties. Nature nanotechnology, 2(6), 354.

182. Doan, T. C., Ramaneti, R., Baggerman, J., van der Bent, J. F., Marcelis, A. T., Tong, H. D., & van Rijn, C. J. (2012). Carbon dioxide sensing with sulfonated polyaniline. Sensors and Actuators B: Chemical, 168, 123-130.

183. Neethirajan, S., Freund, M. S., Jayas, D. S., Shafai, C., Thomson, D. J., & White, N. D. G. (2010). Development of carbon dioxide (CO2) sensor for grain quality monitoring. biosystems engineering, 106(4), 395-404.

184. Cao, T., Yang, S., Cao, J., Zhang, M., Huang, C., & Cao, W. (2001). Nanoassembly film of carboxylic polyaniline with photosensitive diazoresin and its photoelectric conversion properties. The Journal of Physical Chemistry B, 105(48), 11941-11944.

185. Varela-Álvarez, A., &Sordo, J. A. (2008). A suitable model for emeraldine salt. The Journal of chemical physics, 128(17), 174706.

186. Wang, R. X., Huang, L. F., &Tian, X. Y. (2012). Understanding the protonation of polyaniline and polyaniline–graphene interaction. The Journal of Physical Chemistry C, 116(24), 13120-13126.

187. Romanova, J., Petrova, J., Tadjer, A., &Gospodinova, N. (2010). Polyaniline–water interactions: A theoretical investigation with the polarisable continuum model. Synthetic Metals, 160(9-10), 1050-1054.

188. Zhou, H., Chen, H., Luo, S., Lu, G., Wei, W., &Kuang, Y. (2005). The effect of the polyaniline morphology on the performance of polyaniline supercapacitors. Journal of Solid State Electrochemistry, 9(8), 574-580.

189. Li, H., Wang, J., Chu, Q., Wang, Z., Zhang, F., & Wang, S. (2009). Theoretical and experimental specific capacitance of polyaniline in sulfuric acid. Journal of Power Sources, 190(2), 578-586.

190. Wang, D., Wang, X., Yang, X., Yu, R., Ge, L., &Shu, H. (2015). Polyaniline modification and performance enhancement of lithium-rich cathode material based on layered-spinel hybrid structure. Journal of Power Sources, 293, 89-94.

191. Lai, C., Zhang, H. Z., Li, G. R., &Gao, X. P. (2011). Mesoporous polyaniline/TiO2 microspheres with core–shell structure as anode materials for lithium ion battery. Journal of Power Sources, 196(10), 4735-4740.

192. Cheng, F., Tang, W., Li, C., Chen, J., Liu, H., Shen, P., & Dou, S. (2006). Conducting poly (aniline) nanotubes and nanofibers: controlled synthesis and application in lithium/poly (aniline) rechargeable batteries. Chemistry-A European Journal, 12(11), 3082-3088.

193. Goriparti, S., Miele, E., De Angelis, F., Di Fabrizio, E., Zaccaria, R. P., &Capiglia, C. (2014). Review on recent progress of nanostructured anode materials for Li-ion batteries. Journal of power sources, 257, 421-443.

194. Gao, X. W., Wang, J. Z., Chou, S. L., & Liu, H. K. (2012). Synthesis and electrochemical performance of LiV3O8/polyaniline as cathode material for the lithium battery. Journal of Power Sources, 220, 47-53.

195. Ferchichi, K., Hbaieb, S., Amdouni, N., Pralong, V., & Chevalier, Y. (2014). Pickering emulsion polymerization of polyaniline/LiCoO2 nanoparticles used as cathode materials for lithium batteries. Ionics, 20(9), 1301-1314.

196. Karthikeyan, K., Amaresh, S., Aravindan, V., Kim, H., Kang, K. S., & Lee, Y. S. (2013). Unveiling organic–inorganic hybrids as a cathode material for high performance lithium-ion capacitors. Journal of Materials Chemistry A, 1(3), 707-714.

197. Chen, W. M., Huang, Y. H., & Yuan, L. X. (2011). Self-assembly LiFePO4/polyaniline composite cathode materials with inorganic acids as dopants for lithium-ion batteries. Journal of electroanalytical chemistry, 660(1), 108-113.

198. C. Gong, F. Deng, C.-P. Tsui, Z. Xue, Y.S. Ye, C.-Y. Tang, X. Zhou, X. Xie, PANIePEG copolymer modified LiFePO4 as a cathode material for high performance lithium-ion batteries, J. Mater. Chem. A 2 (2014).

199. Huang, X. H., Tu, J. P., Xia, X. H., Wang, X. L., & Xiang, J. Y. (2008). Nickel foam-supported porous NiO/polyaniline film as anode for lithium-ion batteries. Electrochemistry Communications, 10(9), 1288-1290.

200. Jeong, J. M., Choi, B. G., Lee, S. C., Lee, K. G., Chang, S. J., Han, Y. K., Lee, C. S. (2013). Hierarchical hollow spheres of Fe2O3@ polyaniline for lithium-ion battery anodes. Advanced Materials, 25(43), 6250-6255.

201. Guo, J., Chen, L., Wang, G., Zhang, X., & Li, F. (2014). In situ synthesis of SnO2–Fe2O3@ polyaniline and their conversion to SnO2–Fe2O3@ C composite as fully reversible anode material for lithium-ion batteries. Journal of Power Sources, 246, 862-867.

202. Wang, G., Peng, J., Zhang, L., Zhang, J., Dai, B., Zhu, M., & Yu, F. (2015). Two-dimensional SnS2@ PAninanoplates with high capacity

and excellent stability for lithium-ion batteries. Journal of Materials Chemistry A, 3(7), 3659-3666.

203. Huang, X. H., Tu, J. P., Xia, X. H., Wang, X. L., & Xiang, J. Y. (2008). Nickel foam-supported porous NiO/polyaniline film as anode for lithium-ion batteries. Electrochemistry Communications, 10(9), 1288-1290.

204. Guo, J., Chen, L., Wang, G., Zhang, X., & Li, F. (2014). In situ synthesis of SnO2–Fe2O3@ polyaniline and their conversion to SnO2–Fe2O3@ C composite as fully reversible anode material for lithium-ion batteries. Journal of Power Sources, 246, 862-867.

205. Zhou, W., Yu, Y., Chen, H., DiSalvo, F. J., &Abruña, H. D. (2013). Yolk-shell structure of polyaniline-coated sulfur for lithium-sulfur batteries. Journal of the American chemical society, 135(44), 16736-16743.

206. Cao, Y., Xiao, L., Sushko, M. L., Wang, W., Schwenzer, B., Xiao, J., & Liu, J. (2012). Sodium ion insertion in hollow carbon nanowires for battery applications. Nano letters, 12(7), 3783-3787.

207. Xu, D., Chen, C., Xie, J., Zhang, B., Miao, L., Cai, J., ...& Zhang, L. (2016). A hierarchical N/S-codoped carbon anode fabricated facilely from cellulose/polyaniline microspheres for high-performance sodium-ion batteries. Advanced Energy Materials, 6(6), 1501929.

208. Zhao, X., Zhang, Z., Yang, F., Fu, Y., Lai, Y., & Li, J. (2015). Core–shell structured SnO2 hollow spheres–polyaniline composite as an anode for sodium-ion batteries. RSC Advances, 5(40), 31465-31471.

209. Yoon, H. Current trends in sensors based on conducting polymer nanomaterials. Nanomaterials 2013, 3, 524.

210. Huang, J.; Virji, S.;Weiller, B.H.; Kaner, R.B. Polyaniline nanofibers: Facile synthesis and chemical sensors. J. Am. Chem. Soc. 2003, 125, 314–315.

211. Forzani, E.S.; Li, X.; Tao, N. Hybrid amperometric and conductometric chemical sensor based on conducting polymer nanojunctions. Anal. Chem. 2007, 79, 5217–5224.

212. Athawale, A.A.; Bhagwat, S.V.; Katre, P.P. Nanocomposite of Pd-polyaniline as a selective methanol sensor. Sens. Actuators B 2006, 114, 263–267.

213. Y. Liu, J. Li, F. Li, W. Li, H. Yang, X. Zhang, Y. Liu and J. Ma, J. Mater. Chem. A, 4(2016)4472.

214. Wu, Z. Y., Xu, X. X., Hu, B. C., Liang, H. W., Lin, Y., Chen, L. F., & Yu, S. H. (2015). Iron carbide nanoparticles encapsulated in mesoporous Fe-N-doped carbon nanofibers for efficient electrocatalysis. Angewandte Chemie International Edition, 54(28), 8179-8183.

215. Xiao, M., Zhu, J., Feng, L., Liu, C., & Xing, W. (2015). Meso/Macroporous Nitrogen-Doped Carbon Architectures with Iron Carbide Encapsulated in Graphitic Layers as an Efficient and Robust Catalyst for the Oxygen Reduction Reaction in both Acidic and Alkaline Solutions. Advanced materials, 27(15), 2521-2527.

216. Peng, H., Liu, F., Liu, X., Liao, S., You, C., Tian, X., & Huang, P. (2014). Effect of transition metals on the structure and performance of the doped carbon catalysts derived from polyaniline and melamine for ORR application. ACS Catalysis, 4(10), 3797-3805.

217. Pages, H., Topart, P., & Lemordant, D. (2001). Wide band electrochromic displays based on thin conducting polymer films. Electrochimica Acta, 46(13-14), 2137-2143.

218. Le, T. H., Kim, Y., & Yoon, H. (2017). Electrical and electrochemical properties of conducting polymers. Polymers, 9(4), 150.

219. Schwendeman, I., Hwang, J., Welsh, D. M., Tanner, D. B., & Reynolds, J. R. (2001). Combined visible and infrared electrochromism using dual polymer devices. Advanced Materials, 13(9), 634-637.